Author:
Bates, Stephanie

Title:
Barium Uptake by Foraminifera: Understanding Past and Present Ocean Processes

Barium Uptake by Foraminifera: Understanding Past and Present Ocean Processes

Stephanie Lauren Bates

A dissertation submitted to the University of Bristol in accordance with the requirements for award of the degree of Doctor of Philosophy in the Faculty of Science

School of Earth Sciences

2013 – 2016

Abstract

Oceanic barium can provide multiple insights into the marine environment, an important facet of the climate system. Dissolved barium is removed from near-surface seawater in association with biological productivity and is returned at depth via remineralisation and barite dissolution, imparting a nutrient-like profile similar to that of carbonate alkalinity and silica. Due to the similarity in their distributions, seawater barium and alkalinity display a positive linear relationship globally and different water masses have distinct barium-alkalinity compositions. Benthic foraminiferal Ba/Ca ratios can thus be used as a proxy for past ocean circulation and alkalinity, but this may be complicated by additional environmental influences, particularly in non-pelagic settings. In addition, a specific barium partition coefficient may be required for each individual species. Glacial-interglacial changes have been successfully measured using benthic Ba/Ca ratios but many possible applications have yet to be explored to the same extent, such as comparisons between interglacial periods. Barium isotope ratios (δ^{138}Ba) can also be used to enhance our understanding of the marine environment, but because this is a relatively new technique there is still much to be learned regarding the oceanic distribution of barium isotopes and the relationship between seawater and foraminifer δ^{138}Ba is not yet known. An essential prerequisite to measuring either Ba/Ca or δ^{138}Ba ratios in foraminifera is the removal of particulate barite from their inner and outer surfaces. Although a cleaning technique has been established, this has sometimes increased foraminiferal Ba/Ca ratios, perhaps due to the preferential dissolution of low-barium calcium carbonate. During this project these topics were investigated using sediment cores from the southeast and southwest Atlantic Ocean dated to the Holocene and Marine Isotope Stage 5e (MIS 5e, part of the last interglacial period), as well as seawater and foraminifer samples of modern age from the tropical North Atlantic. Ba/Ca ratios in a continental shelf sediment core remain approximately constant despite apparent fluctuations in primary productivity, suggesting that the Ba/Ca proxy can reliably be used as a proxy for ocean circulation even in relatively shallow and productive regions. The effect of dissolution on Ba/Ca could not be assessed due to the absence of dissolution effects in this sediment core. New barium partition coefficients are presented for the benthic foraminifer species *Melonis barleeanus*, *Oridorsalis umbonatus* and *Uvigerina peregrina*. These are offset from one another, highlighting the potential importance of using species-specific partition coefficients. In other sediment cores from the southwest Atlantic, MIS 5e Ba/Ca ratios are on average significantly higher than those of the Holocene. This may be due to a 'stagnation event' in Antarctic Bottom Water (AABW) formation during MIS 5e which led to a build-up of dissolved barium in AABW. In samples from the tropical North Atlantic Ocean, seawater δ^{138}Ba appears to be controlled by conservative mixing at depths below ~500 m, with additional non-conservative controls in the upper ~500 m. δ^{138}Ba ratios in the planktic foraminifer *Orbulina universa* are consistently isotopically lighter than seawater, but the magnitude of this offset is variable. This variability may be due to morphotype-specific vital effects on δ^{138}Ba ratios. Although cleaning tests provide indirect evidence for barite removal, the impact of cleaning on Ba/Ca ratios remains variable and the cause of this variability remains an open question. Collectively, the findings presented here have implications for the uses of Ba/Ca and δ^{138}Ba ratios as palaeoceanographic proxies, as well as for the possible mechanisms of climatic variability in MIS 5e and the Holocene.

Dedication and Acknowledgements

To my parents,
Paul and Michelle

My wholehearted thanks are extended to all family, friends and colleagues who have supported and inspired me throughout my PhD studentship. First of all I thank my primary supervisor, Kate Hendry, whose unwavering patience and understanding, plentifully available guidance, insightful advice and friendly encouragement I have appreciated so much. I also thank my secondary supervisor Carrie Lear for her helpful involvement, as well as my viva panel, Laura Robinson and Alex Piotrowski. For first providing me with my PhD project I thank Cardiff University and its School of Earth and Ocean Sciences, especially my interviewers Ian Hall and Kate Hendry, and for hosting me from midway through the second year I thank the University of Bristol and its School of Earth Sciences.

For providing sediment core BC387-2 I thank Ros Rickaby and Simon Crowhurst, as well as the captain, crew and shipboard scientific party of cruise JR112 of the RRS *James Clark Ross*. I thank Jenny Roberts and Vicky Peck for providing samples from cores GC528 and GC642, with thanks also to the captains, crews and shipboard scientific parties of cruises JR244 and JR257 of the RRS *James Clark Ross*. For providing sediment and seawater samples from the tropical North Atlantic Ocean I thank Laura Robinson and Allison Jacobel, as well as the entire shipboard scientific party, captain and crew of cruise JC094 of the RRS *James Cook*.

I have many people to thank for helping me with foraminifer identification and laboratory work of various kinds. For their generous assistance I thank Anabel Morte-Ródenas, Carolyn Taylor, Carrie Lear, Chris Coath, Elaine Mawbey, Eleanor Heulwen John, Helena Pryer, Hong Chin Ng, James Chen, Kate Hendry, Kim Pyle, Kirsty Edgar, Lindsey Axe, Lindsey Owen, Maricel Williams, Mike Edwards, Paola Moffa-Sánchez, Pete Spooner, Simon Crowhurst, Suzie MacLachlan, Tristan Horner, Vanessa Fairbank and Vicky Peck. For providing swift and friendly data-collection services and for allowing me to reproduce their own data I thank Andy Cundy, Helena Pryer, Jenny Roberts, Mervyn Greaves, Sandra Nederbragt and Tristan Horner.

During the first year of my PhD studentship I travelled across the Atlantic Ocean via cruise JC094 and in the third year I visited Woods Hole Oceanographic Institution as a guest student. I thank Laura Robinson for authorising me to participate in this cruise, I thank Tristan Horner and Helena Pryer for hosting me so amiably at Woods Hole and I thank Kate Hendry for providing me with each of these fantastic opportunities.

Finally, I thank all of the wonderful friends who I've been fortunate enough to meet and spend time with during the course of these four years, I thank Mum and Dad for their perennial love and support, and I thank our dog Alfie for keeping me company during writing up.

This PhD project was funded by a Marie Curie Career Integration Grant awarded by the European Commission to Dr Kate Hendry. Cruise JR112 of the RRS *James Clark Ross* was funded by Antarctic Funding Initiative project AF14/02 of the Natural Environment Research Council. Cruises JR244 and JR257 of the RRS *James Clark Ross* were funded as part of the British Antarctic Survey's Polar Science for Planet Earth research programme. Cruise JC094 of the RRS *James Cook* was funded by the European Research Council.

Table of Contents

List of Figures

List of Tables

Chapter 1

Introduction

1.1 Barium and the climate system

A detailed understanding of Earth's climate system is essential for predicting the consequences of anthropogenic perturbations to the atmosphere. Due to the complexity of the climate system, this requires the study of many different Earth system components and the linkages between them, as well as how these may change through time. The ongoing collection of data relating to both the past and the present as well as the incorporation of these findings into climate models will continue to enhance our understanding. These efforts will in turn inform more accurate predictions, providing the means to both mitigate and adapt to future changes.

The oceans are of great importance to the climate system. This is partly due to their ability to rapidly equilibrate with the atmosphere and to transport these properties around the globe on relatively short timescales, in addition to their large volume which enables them to do this on a significant scale. For example, ocean circulation in the Atlantic Ocean and Southern Ocean forms a system of carbon dioxide storage-and-release which has been invoked to explain glacial-interglacial changes in atmospheric carbon dioxide concentrations (e.g. Sigman & Boyle 2000; Sigman et al. 2010). Many techniques have been developed which reveal past ocean conditions by using the predicted relationships between different measurements. One such approach is to use foraminiferal Ba/Ca as a proxy for past ocean circulation and alkalinity based upon the links between foraminiferal Ba/Ca, seawater dissolved barium concentrations and seawater alkalinity in the modern oceans. Barium has a nutrient-like profile in seawater (Figure 1.1) due to its uptake from near-surface waters via barite ($BaSO_4$) precipitation in association with organic matter remineralisation and the subsequent dissolution of this barite with depth (e.g. Dehairs et al. 1980; Bishop 1988; Horner et al. 2015; Cao et al. 2016). Although some barium is also removed by uptake into organic matter, calcium carbonate shells, acantharian celestite and adsorption to diatom frustules, mass balance calculations have shown that these are minor effects in comparison to barite cycling (Lea 1993; Horner et al. 2015). Barium is present in trace amounts in seawater, with an average concentration of approximately 100 nmol/kg (Broecker & Peng 1982; Elderfield & Schultz 1996). Riverine fluxes and hydrothermal vents provide the oceans with dissolved barium and it is lost from the oceanic reservoir via sedimentary burial. There is considerable uncertainty in the estimation of riverine and hydrothermal barium fluxes, largely due to desorption processes within rivers which add additional barium to seawater (Lea 1990) and particle scavenging in hydrothermal vent plumes which can render these a sink, rather than a source, of dissolved barium (Elderfield & Schultz, 1996). Consequently, the calculation of an oceanic residence time (τ_{res}) for barium has yielded inconsistent results, with estimates ranging from 8.8 x 10^3 years (Broecker & Peng 1982) and approximately 1 x 10^4 years (Chan et al. 1976) to 8.4 x 10^4 years (Goldberg 1963). A simple box model calculation shows that the range in riverine and hydrothermal flux estimates reported in the literature can even result in a residence time of up to 5 x 10^5 years (Figure 1.2).

Despite these uncertainties, barium is incorporated into the calcium carbonate shells of foraminifera in a predictable manner, such that Ba/Ca ratios measured in foraminifera can be used to

reconstruct seawater barium concentrations (Lea & Boyle 1989; Lea & Spero 1992; Lea & Spero 1994; Havach et al. 2001; Hönisch et al. 2011). Because different water masses have contrasting barium concentrations, these estimates can be used to infer changes in ocean circulation through the past (Hall & Chan 2004b; Lea & Boyle 1990a; Lea & Boyle 1990b; Lea 1990; Lea 1993; Lea 1995). Furthermore, due to the covariation of barium and alkalinity in seawater (e.g. Figure 1.1), Ba/Ca ratios can also be used to estimate seawater alkalinity (e.g. Lea 1993). Seawater alkalinity is dominantly controlled by the amount of carbonate (CO_3^{2-}), bicarbonate (HCO_3^-) and borate ($B(OH)_4^-$) ions in seawater (Chester & Jickells 2012). Because carbonate and bicarbonate ion concentrations are affected by ocean-atmosphere carbon dioxide exchange, estimates of seawater alkalinity can reveal how the oceans redistributed carbon in the past. Relatively recently, another barium-based technique for studying the oceans has been developed: barium isotope ratios ($\delta^{138}Ba$) (Horner et al. 2015; Cao et al. 2016). These may be partially controlled by both conservative mixing and non-conservative processes such as primary productivity and barite precipitation (Horner et al. 2015; Cao et al. 2016). Once the oceanic distribution of $\delta^{138}Ba$ is defined in greater detail, and if foraminiferal $\delta^{138}Ba$ can be used to infer that of seawater, foraminiferal $\delta^{138}Ba$ could become a new proxy for ocean circulation and primary productivity, both of which are important for the redistribution and storage of carbon in the oceans.

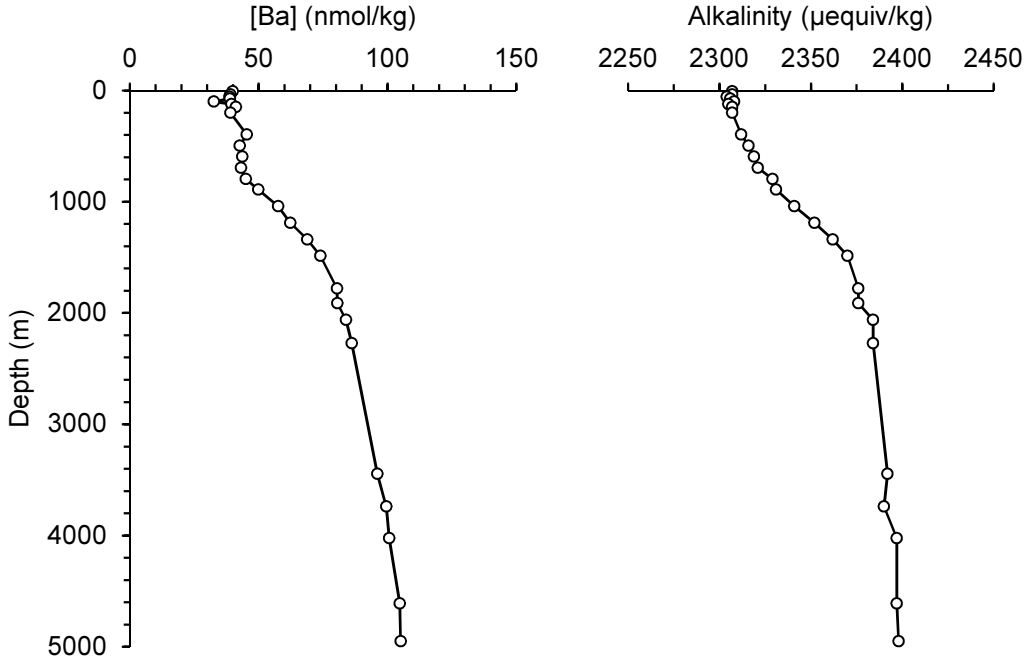

Figure 1.1. Seawater profiles of dissolved barium concentration and alkalinity for a site in the southwest Indian Ocean (Jeandel et al. 1996) demonstrating the similarity between the oceanic distributions of barium and alkalinity as well as the nutrient-like shape of the dissolved barium profile.

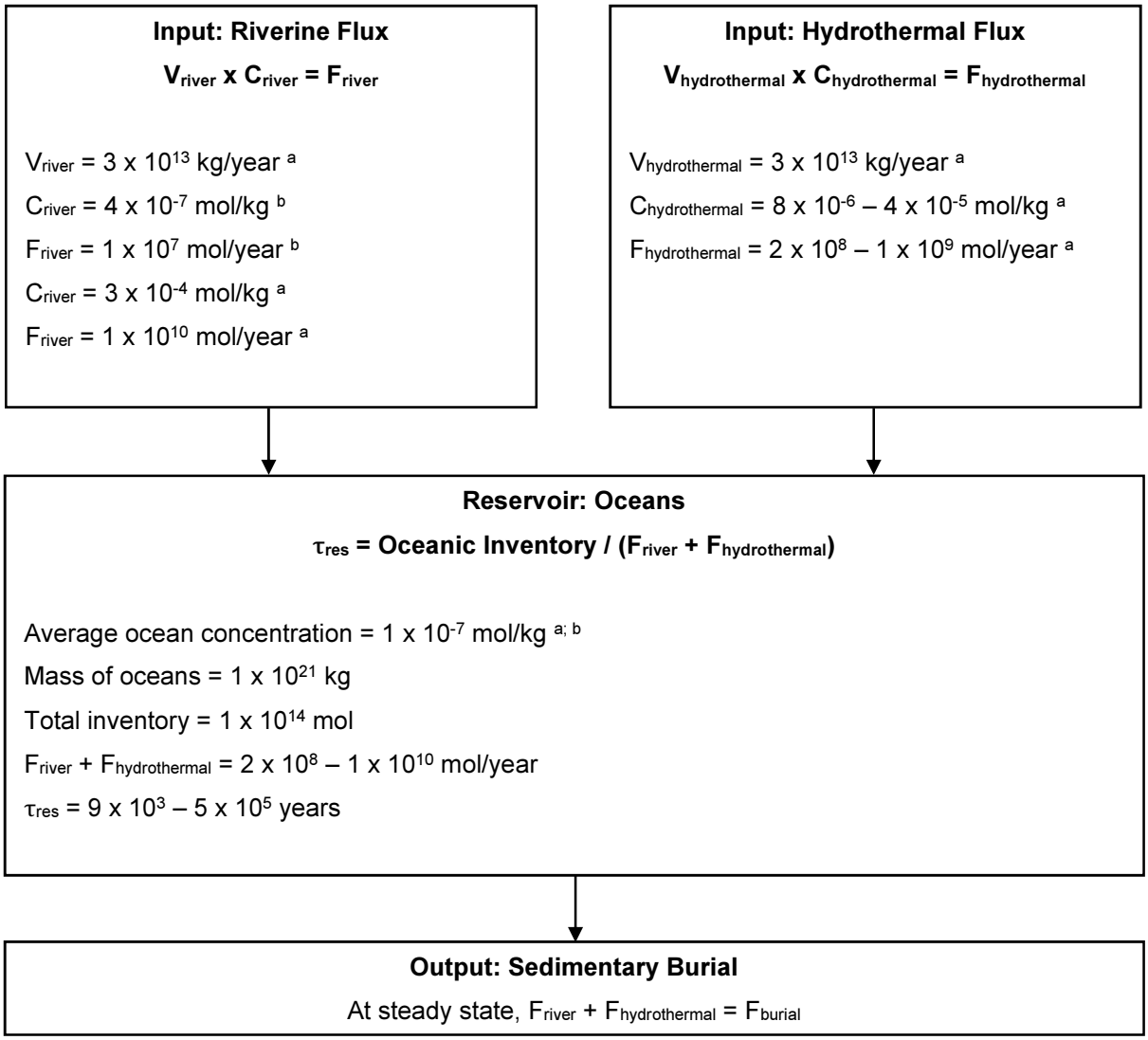

Figure 1.2. Box model for dissolved barium in seawater. All values are to one significant figure. 'V', 'C' and 'F' indicate volume, concentration and flux, respectively. τ_{res} = residence time. a) Elderfield & Schultz 1996; b) Broecker & Peng 1982.

1.2 Motivations for further study

However, there are potential caveats associated with each of these techniques. Because the removal of barium from seawater is largely facilitated by barite precipitation within sinking organic matter, rather than via uptake into calcium carbonate (e.g. Dehairs et al. 1980; Bishop 1988; Lea 1993; Horner et al. 2015), dissolved barium concentrations and seawater alkalinity are not mechanistically linked together. External influences which affect barium or alkalinity in different ways could therefore break down or change the relationship between them, rendering alkalinity estimates inaccurate. Productivity-associated barite precipitation may affect barium concentrations in the absence of concomitant effects on alkalinity, particularly in non-pelagic settings where inorganic carbon rain-rates are likely to differ from those in the open ocean, or in regions where the biological assemblage contains fewer carbonate-secreting organisms than usual (Rubin et al. 2003). A further concern is that, even if seawater barium and alkalinity retain their usual relationship, foraminiferal Ba/Ca ratios may be altered after deposition if their calcium carbonate becomes partially dissolved (McCorkle et al. 1995). Seawater barium and alkalinity reconstructions are also dependent on the availability of a barium partition coefficient for the species in use (Boyle 1981; Lea & Boyle 1989). Although these exist for several of the most commonly-used benthic foraminifera (Lea & Boyle 1989; Lea 1993; McCorkle et al. 1995; Havach et al. 2001), further measurements will facilitate the use of additional species and will allow for an assessment of intra-species variability in barium uptake. In planktic species a multi-species partition coefficient has been developed (Hönisch et al. 2011), but it is not known whether this approach is appropriate for benthic foraminifera.

Similarly, further development could significantly benefit the $\delta^{138}Ba$ proxy. The collection of additional seawater $\delta^{138}Ba$ measurements would produce a more detailed picture of $\delta^{138}Ba$ oceanic distributions, allowing for the mechanisms controlling these distributions to be defined. A clearer picture of $\delta^{138}Ba$ variability in the modern oceans would create a context for interpreting palaeoceanographic $\delta^{138}Ba$ measurements. Such measurements could be provided by foraminifera, but the relationship between foraminiferal $\delta^{138}Ba$ and that of seawater has yet to be investigated. Thus far, $\delta^{138}Ba$ in inorganically-precipitated carbonate is always isotopically lighter than that of the solution it precipitated from (von Allmen et al. 2010; Böttcher et al. 2012a; Pretet 2013), but this may or may not be true of living organisms such as foraminifera whose calcium carbonate is precipitated via biomineralisation (e.g. Elderfield et al. 1996; Erez 2003; de Nooijer et al. 2009).

The mechanism by which foraminiferal biomineralisation occurs and how this varies between species, or between morphotypes of the same species, is not yet well known (e.g. Khalifa et al. in press). Most species of foraminifera, including those used in this study, are known as ‘hyaline’. This term derives from their glassy transparent appearance, a feature resulting from the structure of their calcitic shells. They consist of radially-organised calcite crystals, with their longest axis (the c-axis) orientated perpendicular to the shell wall (Hansen & Reiss 1972; Bellemo 1974). Their shell walls are often punctuated by small openings, known as pores, up to approximately 10 μm in diameter (Hemleben et

al. 1989). Perforate hyaline foraminifera calcify their shells via a series of steps which have been observed through optical and electron microscopy, partly facilitated by the development of a technique which induces foraminifera to calcify upon a glass slide (Bentov 1997; Bentov et al. 2001; Bentov & Erez 2001; Erez & Bentov 1998; Erez & Bentov 2002; Erez et al. 1994; Erez et al. 2001; Erez et al. 2002). First, the foraminifer extends its ectoplasm into the area where the new shell chamber is to be precipitated and creates an organic sheet which is the template for the new calcite (e.g. Erez 2003; Figure 1.3). A primary layer of calcium carbonate is then deposited, which can consist of microspherulites of calcite embedded within the organic sheet (Erez 2003; Figure 1.3). Additional layers of radial calcite known as secondary calcite laminations are precipitated sequentially on top of this primary layer (Reiss 1957; Figure 1.3). Whilst these aspects of biomineralisation can be observed using microscopy, the mechanisms by which calcification ions and trace elements are transported from the ambient seawater to the site of calcification are more difficult to detect. Several studies have pointed towards the likely importance of seawater vacuolisation in this process (e.g. Erez 2003), whereby seawater is isolated within the foraminifer in one or several vesicles which are transported to the site of calcification (e.g. Erez 2003; Figure 1.3). A recent study has shown that these vesicles decrease in size as calcification progresses, providing supporting evidence for this theory (Khalifa et al. in press). However, although it is likely that this plays a role in most species (Erez 2003), the relative importance of this compared to other possible mechanisms of ion uptake and storage remains a subject of debate. Whilst Nehrke et al. 2013 do observe vesicles during biomineralisation, they conclude that these are not numerous enough to be the primary means of transporting ions to the site of calcification and instead invoke trans-membrane transport, whereby ions are transported across the cell membrane directly to the site of calcification at the time of biomineralisation (Nehrke et al 2013). Several authors have found evidence of granules (~0.5 – 1 μm) within the foraminiferal endoplasm near to the site of calcification, which may provide calcium ions for calcite precipitation (Bentov 1997; Bentov et al. 2001; Bentov & Erez 2001; Erez & Bentov 1998; Erez & Bentov 2002; Erez et al. 1994; Erez et al. 2001; Erez et al. 2002). The existence and relative importance of these different mechanisms for storing and transporting calcification ions, and how this might vary between different species, remains an active area of research.

Given that there is much still to be learned about biomineralisation, it is possible that different species of foraminifer, or perhaps different morphotypes of the same species, calcify their shells via significantly different processes. These differences might result in contrasting trace metal compositions, in the absence of any differences in seawater chemistry or other environmental conditions. Such offsets between species or morphotypes are known as vital effects. Vital effects on $\delta^{138}Ba$ have been observed in corals (Pretet 2013; Pretet et al. 2015), but foraminifera have not yet been tested. Although differences in foraminiferal Ba/Ca between species have been quantified by calculating partition coefficients (Lea & Boyle 1989; Lea & Boyle 1991; Lea & Spero 1992; Lea 1993; Lea & Spero 1994; McCorkle et al. 1995; Havach et al. 2001; Hall & Chan 2004b; Hönisch et al. 2011), it is not known whether these offsets result from different ambient barium concentrations, vital effects, or a

combination of both factors. If present, vital effects could lead to species- or morphotype-specific seawater-foraminifer $\delta^{138}Ba$ offsets and may overprint the influence of seawater $\delta^{138}Ba$.

Further to these concerns, both foraminiferal Ba/Ca and $\delta^{138}Ba$ measurements depend on the removal of barite prior to measurement. This is because barite contamination has the potential to skew results by providing excess barium to Ba/Ca ratios and by altering the overall $\delta^{138}Ba$ of a sample. A cleaning procedure for removing barite from foraminifera has therefore been developed (Lea & Boyle 1993). However, its impact on foraminifera is not certain because Ba/Ca ratios sometimes increase after cleaning (Lea & Boyle 1993; Martin & Lea 2002). It may be that barium is distributed heterogeneously within foraminiferal calcium carbonate and the cleaning procedure preferentially dissolves these low-barium regions of the shell (e.g. Lea & Boyle 1993), an effect which could vary widely between different species of foraminifera.

In addition to refining and developing barium-based oceanographic methods as described above, the existing proxies can be used to ask new questions. In previous studies, benthic foraminiferal Ba/Ca ratios have successfully revealed glacial-interglacial contrasts in ocean circulation (Hall & Chan 2004b; Lea & Boyle 1990a; Lea & Boyle 1990b; Lea 1990; Lea 1993; Lea 1995). For example, in Lea 1993 the Ba/Ca proxy is used to infer that deep ocean barium concentrations in the South Atlantic sector of the Southern Ocean were approximately 13 nM greater at the Last Glacial Maximum than during the Holocene. This equates to an alkalinity increase of ~20 μequiv/kg, which could account for approximately one third of the glacial-interglacial difference in atmospheric carbon dioxide concentrations (Lea 1993). In addition to glacial-interglacial insights, this proxy could be deployed to study other aspects of palaeoceanography such as comparisons between interglacial periods. Although the variability between interglacial periods is attributed ultimately to differences in solar insolation (e.g. Tzedakis et al. 2009; Rohling et al. 2010), the mechanisms which translated this forcing into climatic variability are yet to be strongly defined (e.g. Wanner et al. 2008; Tzedakis et al. 2009; Rohling et al. 2010). The Ba/Ca proxy could provide valuable additional insights into the differences between interglacial periods.

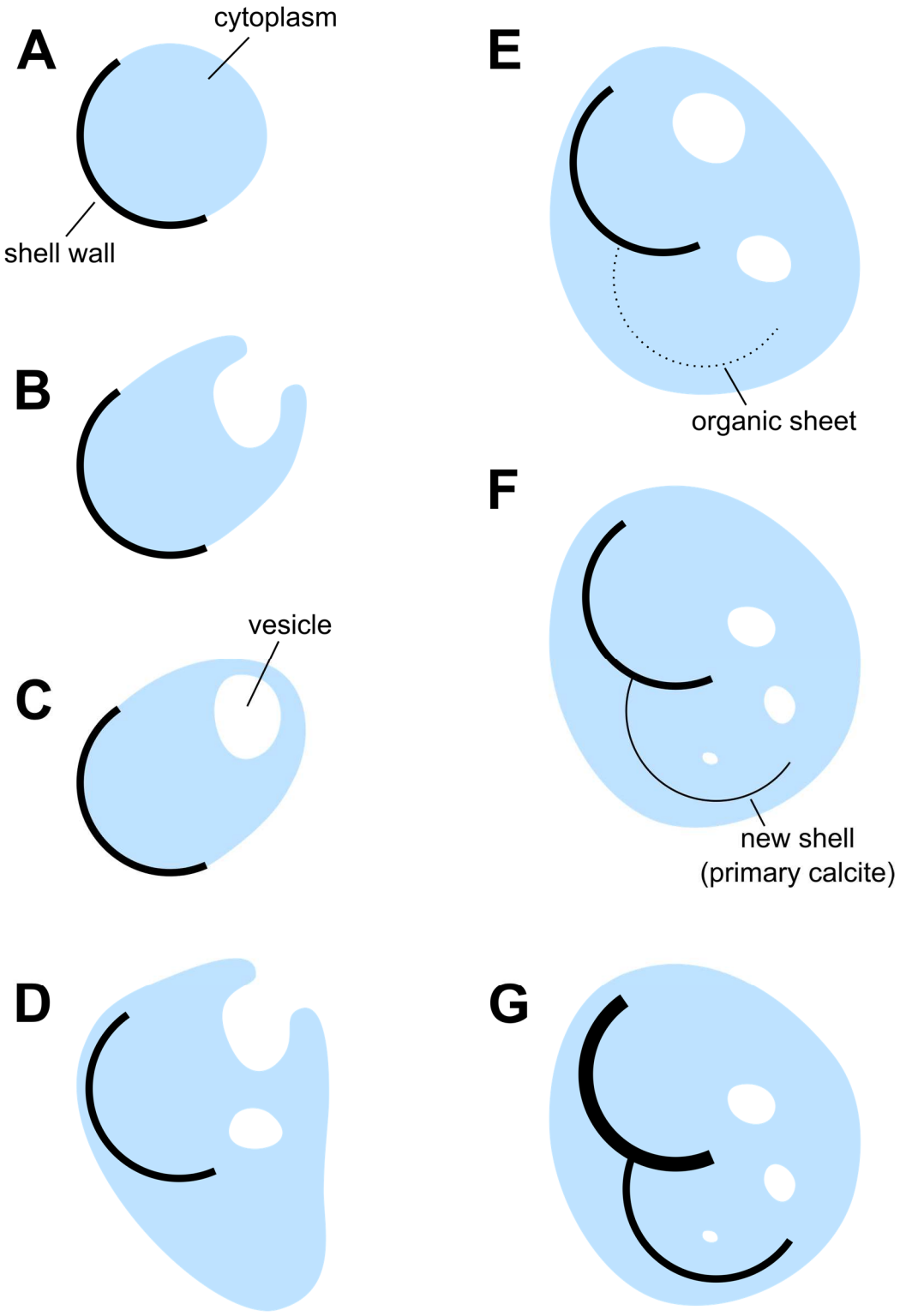

Figure 1.3. Schematic diagram of biomineralisation via seawater vacuolisation. A) Foraminifer cell; B) extension of cytoplasm to create vesicle; C) isolation of a vesicle of seawater within the cell; D) extension of cytoplasm into new shell area and continuing vesicle formation; E) formation of organic sheet; F) precipitation of primary calcite onto organic sheet, vesicles shrink as ions are used; G) precipitation of secondary calcite onto both new and old shell walls. Adapted from Erez (2003).

1.3 Thesis outline and setting

Here, the subjects outlined above are investigated using modern, Holocene and last interglacial samples of seawater, sediment and foraminifera from the tropical North Atlantic Ocean and the high-latitude southeast and southwest Atlantic Ocean (Figure 1.4). In the Atlantic, North Atlantic Deep Water (NADW), which forms mostly in the Greenland Sea and Labrador Sea, is transported southwards and Antarctic Bottom Water (AABW) moves northwards from its source regions in the high-latitude Southern Ocean (such as the Weddell Sea and Ross Sea) via thermohaline circulation (Brown et al. 2004). Antarctic Intermediate Water (AAIW) also flows northwards, overlying NADW (Brown et al. 2004). At shallower depths, the waters of the Atlantic are influenced by atmospheric conditions. For example, in the South Atlantic, Antarctic Surface Water (ASW) is subducted beneath Subantarctic Surface Water, forming AAIW, due to the relatively warmer temperatures of Subantarctic Surface Water (Brown et al. 2004). At low latitudes, relatively high temperatures and precipitation levels produce stable conditions in the upper water column, leading to weaker vertical mixing within near-surface waters than at higher latitudes (e.g. Kara et al. 2003). In addition to broad-scale thermohaline circulation and near-surface processes, Atlantic waters are affected by regional currents. The Deep Western Boundary Current flows southwards along the western edge of the North Atlantic, carrying Labrador Sea Water and NADW (Brown et al. 2004). In the Southern Ocean, the Antarctic Circumpolar Current flows from west to east encircling Antarctica at approximately 40ºS – 60ºS, whilst the Antarctic Coastal Current flows from east to west along the Antarctic coast (Brown et al. 2004). Ekman transport deflects the Antarctic Coastal Current towards Antarctica but in contrast deflects Antarctic Circumpolar Current waters away from the shore, resulting in a region of upwelling in-between these two currents known as the Antarctic Divergence (Brown et al. 2004). As NADW moves southwards towards Antarctica, some is upwelled and, also freshened by meltwater and precipitation inputs, becomes ASW (Brown et al. 2004). Downstream of the Drake Passage, the Malvinas Current (which is also known as the Falklands Current) branches off from the Antarctic Circumpolar Current and flows along the outer edge of the South American continental shelf (Piola & Gordon 1989; Peterson 1992; Piola & Matano 2009; Piola et al. 2010; Piola et al. 2013). A schematic drawing of the Malvinas Current and its relation to the sampling sites in the southwest Atlantic Ocean is provided in Figure 1.5. Maps showing the bathymetry of the sampling sites elsewhere in the Atlantic are also provided, in Figures 1.6 to 1.8.

In this study, the collection of Atlantic samples shown in Figures 1.4 to 1.8 is used to explore several different questions related to marine barium. First, in Chapter 2 'Trace Metal Methods' the techniques used to measure trace metal ratios such as Ba/Ca ratios in foraminifera are described, along with data quality assurance measures. In the following chapter, Chapter 3 'Evaluating the Ba/Ca Proxy', a sediment core of recent age from the southwest Atlantic (BC387) is used to investigate some of the potential caveats to the benthic Ba/Ca proxy: in a multi-proxy approach using trace metal ratios, oxygen and carbon isotope ratios, x-ray fluorescence and gamma-ray spectroscopy, the effects of productivity-associated barium cycling and post-depositional dissolution on foraminiferal Ba/Ca ratios are studied;

barium partition coefficients are measured in three species of benthic foraminifera; and cleaning tests are used to examine the impacts of the barite-removal cleaning technique. Chapter 4 'Foraminiferal Ba/Ca in the Holocene and Marine Isotope Stage 5e' presents a comparison of the Holocene with Marine Isotope Stage (MIS) 5e, which occurred during the last interglacial period, using the benthic foraminiferal Ba/Ca proxy and sediment cores from the southwest Atlantic Ocean (GC528 and GC642). Lastly, in Chapter 5 'Barium Isotope Ratios in Foraminifera and Seawater', new seawater δ^{138}Ba measurements from the tropical North Atlantic (seawater profiles CTD002, CTD005 and CTD006) are analysed alongside existing measurements from the southeast Atlantic (CTD013 and CTD025), towards building a whole-Atlantic picture of δ^{138}Ba distributions. Also presented are the first known δ^{138}Ba measurements of foraminifera (from sediment samples S0059, S0066, S0131, S0157 and S0177) as a first step towards developing these into a new palaeoceanographic proxy.

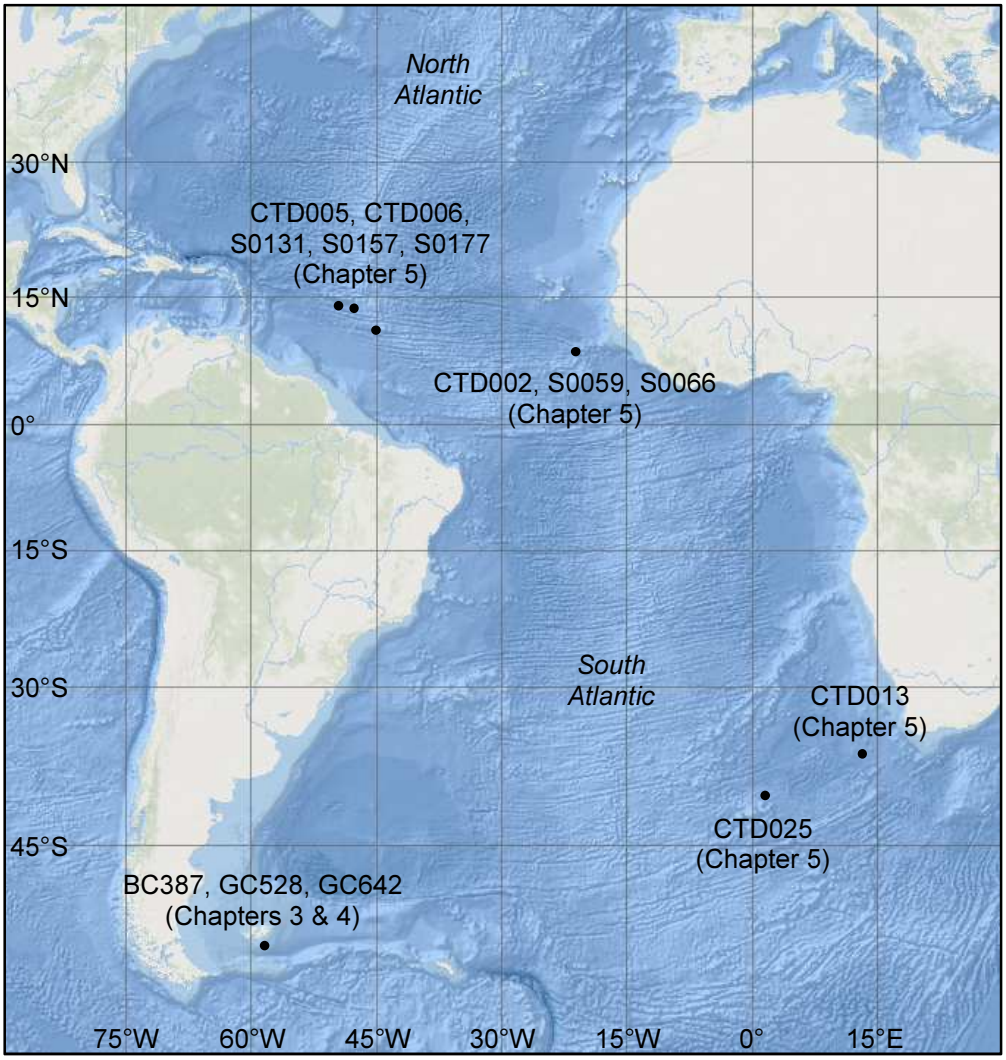

Figure 1.4. Map of all sample locations included in this thesis. Detailed views of these sample locations are shown in Figure 1.5, Figure 1.6, Figure 1.7 and Figure 1.8. Bathymetric base map from the National Centres for Environmental Information, National Oceanic and Atmospheric Administration, USA.

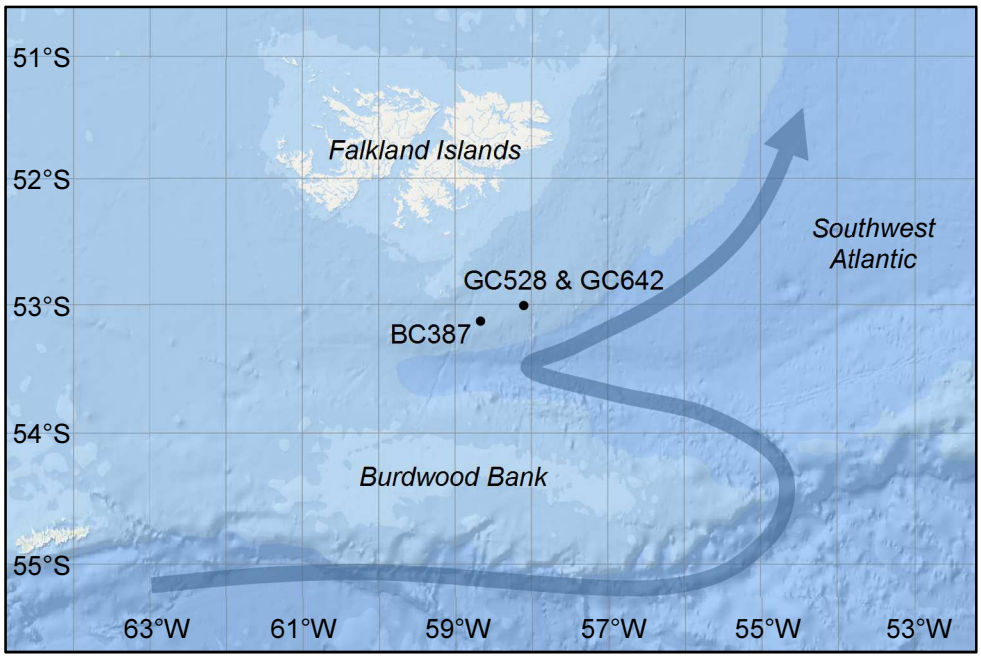

Figure 1.5. Detailed view of sample locations in the southwest Atlantic Ocean, with the approximate location of the Malvinas Current shown by an arrow. Bathymetric base map from the National Centres for Environmental Information, National Oceanic and Atmospheric Administration, USA.

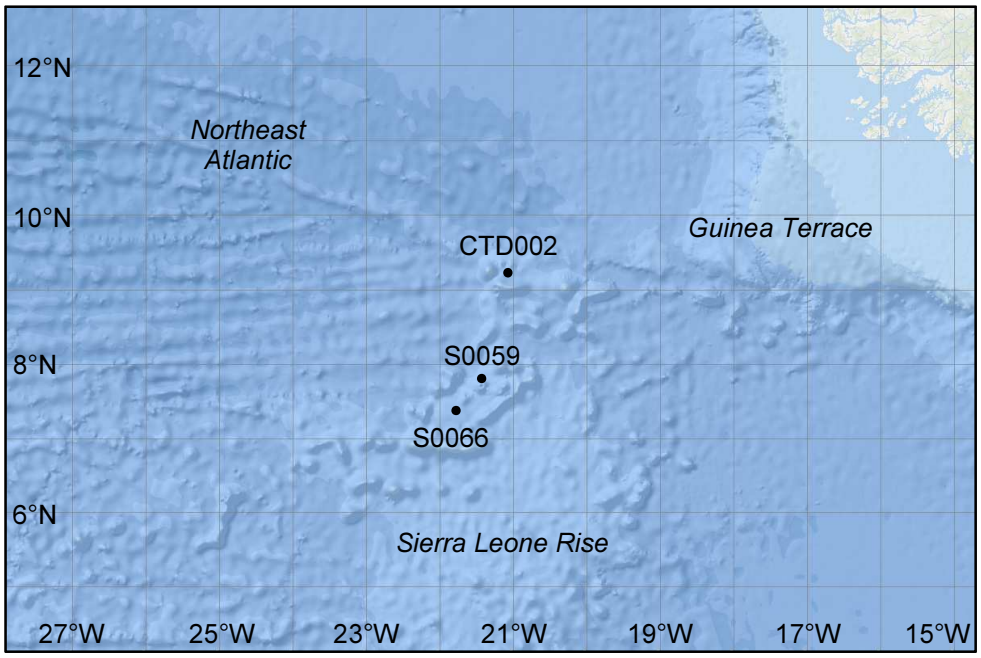

Figure 1.6. Detailed view of sample locations in the northeast Atlantic Ocean. Bathymetric base map from the National Centres for Environmental Information, National Oceanic and Atmospheric Administration, USA.

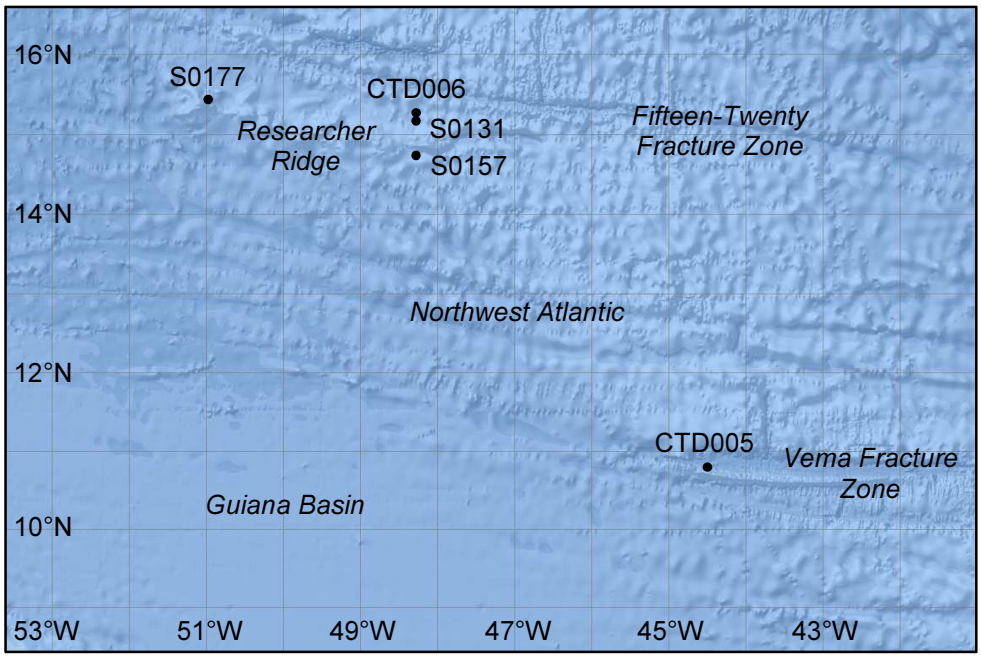

Figure 1.7. Detailed view of sample locations in the northwest Atlantic Ocean. Bathymetric base map from the National Centres for Environmental Information, National Oceanic and Atmospheric Administration, USA.

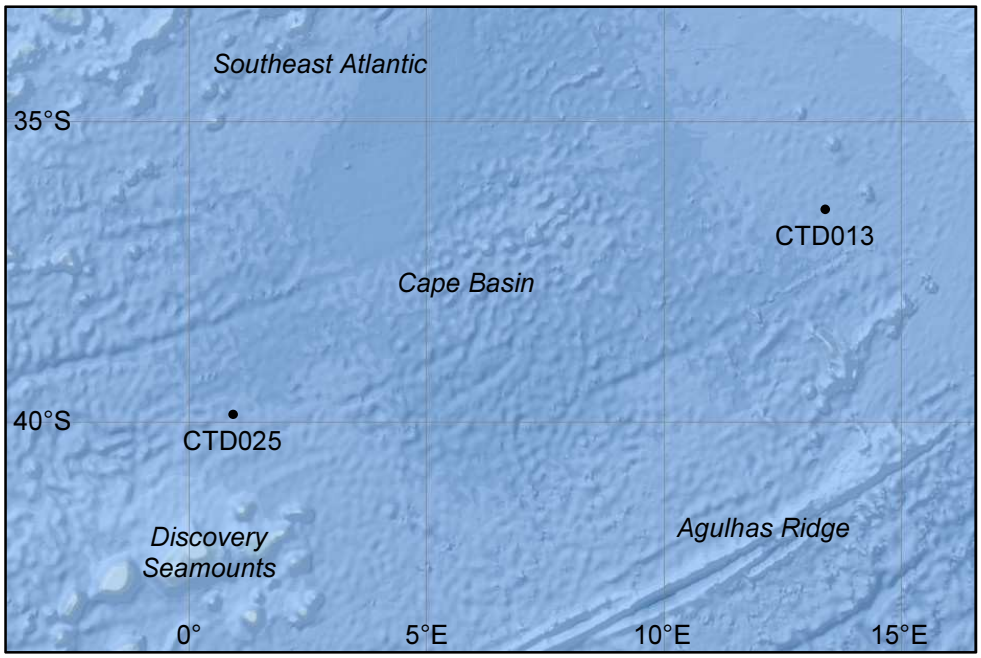

Figure 1.8. Detailed view of sample locations in the southeast Atlantic Ocean. Bathymetric base map from the National Centres for Environmental Information, National Oceanic and Atmospheric Administration, USA.

Chapter 2

Trace Metal Methods

2.1 Introduction

This chapter describes the methods used to gather the foraminiferal trace metal data which are presented in Chapters 3 to 5 (Ba/Ca, Mg/Ca and Sr/Ca ratios). Firstly, the cleaning procedure for foraminifera is described and secondly the procedure for data collection via mass spectrometry, including preparation of samples for analysis, instrumental set-up and tuning, sequence design and the calculation of trace metal ratios. Lastly, measures used to check data quality and method-validation tests are described.

2.2 Foraminiferal cleaning procedure

Under optical microscope, picked foraminifera were gently crushed between two glass slides cleaned in reverse osmosis purified (RO) water, to open as many of the chambers as possible to ensure maximum effectiveness of cleaning, yet without rendering the fragments too small to minimise sample loss. Glass slides were cleaned in-between samples to prevent cross-contamination. Visible contaminants were removed using a single-eyelash brush and the crushed foraminifer fragments were then placed into acid-cleaned 500 µl microcentrifuge vials by brushing them off the edge of the glass slide. The crushed fragments were then cleaned using the procedure described below in a clean laboratory reserved for working with carbonates at the Bristol Isotope Group in the School of Earth Sciences, University of Bristol.

The procedure for cleaning benthic foraminifera prior to trace metal analysis described here is similar to that of the School of Earth and Ocean Sciences, Cardiff University, except adapted to include a barite-removal step using DTPA (Lea & Boyle 1993). The Cardiff procedure was itself derived from: Boyle 1981; Boyle & Keigwin 1985; Barker et al. 2003; reversal of the order of the oxidation and reduction steps to prevent the precipitation of cadmium sulphide which causes high cadmium values; and the addition of a sample transfer stage (samples are placed into fresh clean vials) after the reducing step because of the loosening of sample vial lids caused by this step.

Systematic bias was avoided during cleaning by randomising the order of samples in the sample rack and by alternating the orientation of the sample rack in the ultrasonic bath. The sample rack used was a Nalgene tray capable of holding 24 microcentrifuge vials. All reagent storage bottles and pipette tips were acid-cleaned prior to use and at all stages in the procedure a freshly-cleaned pipette tip (rinsed in 3 M hydrochloric acid followed by Milli-Q water) was used whenever appropriate to avoid cross-contamination. The acids used for cleaning were reagent grade. Whenever a 1000 µl pipette was used, this was set to 600 µl for increased control. To prevent sample loss, samples were allowed to settle to the bottoms of the vials before pipetting out overlying solutions, and although as much of the overlying solution as possible was removed it was deemed acceptable to leave a small pool (of about 5 – 10 µl) covering the foraminifer fragments.

The cleaning procedure consists of: 1) a water and methanol step to remove clays; 2) checking for non-foraminiferal grains under the microscope and removal of these contaminants if present; 3) a reducing agent step to remove metal oxides; 4) an optional sample transfer to fresh vials; 5) an oxidising agent step to remove organic matter; 6) a DTPA step to remove barite; and 7) a final rinse of dilute acid to remove any remaining adsorbed contaminants. The procedure is described in full below.

2.2.1 Clay removal

2.2.1.1 Initial water rinse

The ultrasonication of samples in water was used to separate out clay material from the foraminifer fragments. The clays float in the water above the foraminifera and are thus removed along with the overlying solution.

Sample vials were first tapped firmly on their sides to move foraminifer fragments down to the bottoms of the vials. Approximately 500 µl Milli-Q water was then added to each vial, aiming at the sides of the vial in order to wash all fragments into the water. Vial lids were checked for fragments and these were also rinsed into the body of the vial by capping and inverting vials. Any air bubbles were removed by gently tapping the vials. The vials were then tapped again to ensure that all fragments had floated down to the bottoms of the vials. After allowing the fragments to settle the water was removed from each vial using a 1000 µl pipette.

The following steps were then performed three times (although repeats may be omitted if the sample is small or fragile, or further repeats added if clay contamination – a milky-white appearance to the overlying solution – is still seen after three rinses):

1. add approximately 250 µl Milli-Q water to each sample vial
2. ultrasonicate vials for 1 minute in an ultrasonic water bath
3. top up with Milli-Q water to approximately 500 µl
4. cap, invert and shake vials, tap out any bubbles
5. tap vials to settle samples to the bottoms of the vials
6. remove overlying water using a pipette

A further ultrasonication was then performed, whilst the foraminifer fragments were still in small pools of water (5 – 10 µl), then 500 µl Milli-Q water was added to each vial, the vials inverted, tapped to bring samples back down and the overlying water removed.

2.2.1.2 Methanol

Cleaning with methanol dislodges further clays because it has a lower viscosity than water. ~100 % Romil ultra-pure methanol was used. The following procedure was performed twice (although, as before, the number of repeats may be adjusted as required):

1. add approximately 250 µl methanol to each vial

2. ultrasonicate vials for 1 minute in an ultrasonic water bath
3. invert and shake vials
4. tap vials to settle samples to the bottoms of the vials
5. remove overlying methanol using a pipette

2.2.1.3 Final water rinse

A final water rinse was performed to remove any remaining methanol. This was achieved by performing the following steps twice:

1. add approximately 250 µl Milli-Q water to each vial
2. ultrasonicate vials for 1 minute in an ultrasonic water bath
3. top up with Milli-Q water to approximately 500 µl
4. cap, invert and shake vials, tap out any bubbles
5. tap vials to settle samples to the bottoms of the vials
6. remove overlying water using a pipette, then remove as much as possible of the remaining small pool of water using a 200 µl pipette

2.2.2 Checking for contaminants

Removing non-foraminiferal grains at this stage diminishes the risk of contamination from leaching them during the reducing step. Under an optical microscope, samples were checked for small black particles (silicate grains) and other contaminants. To remove contaminants, the sample fragments were expelled onto an RO water cleaned glass slide using the following technique:

1. take a 200 µl pipette tip and cut off about one quarter from the solution end, at an angle, using a disposable scalpel (creating an enlarged, oval-shaped aperture)
2. acid-clean the modified pipette tip twice (additional cleaning is required because it has come into direct contact with the metal scalpel)
3. using the modified pipette tip, add a small amount of Milli-Q water (approximately 50 µl) to the sample vial to float the foraminifer fragments
4. immediately (to avoid re-settling), use the modified pipette tip to remove the foraminifer fragments from the vial and transfer them onto a clean glass slide
5. repeat until all foraminifer fragments have been transferred to the glass slide

Contaminant grains were then removed using a single-eyelash brush. To prevent cross-contamination, glass slides were thoroughly cleaned in-between samples using RO water and a new modified pipette tip was used for each sample. When contaminants had been removed, the sample was placed back into its vial either by brushing the fragments off the edge of the glass slide into the vial or via pipetting using the technique described above.

2.2.3 Metal oxides removal (reducing step)

In this step, a reducing agent was used to remove metal oxides that might coat the foraminifer fragments. The original reducing agent recipe (Lea & Boyle 1993) consisted of 10 ml ammonium hydroxide, 10 ml of a citric acid ammonia mixture and 1200 µl hydrazine hydrate. Hydrazine is dangerously unstable at high concentrations, so suppliers provide hydrazine hydrate solutions which are approximately 55 – 65 % solutions of hydrazine. For safety reasons, it was deemed necessary to use a 55 % hydrazine hydrate (equal to 35 % hydrazine) solution. The recipe was adjusted to account for this, in order to keep the hydrazine concentration in the reducing agent the same as used by previous authors (Lea & Boyle 1993). The reducing agent recipe became 10 ml ~25 – 35 % Suprapur reagent grade ammonium hydroxide, 10 ml of a citric acid ammonia mixture (composed of 25 g AnalR reagent grade citric acid powder dissolved in 500 ml ~25 – 35 % Suprapur reagent grade ammonium hydroxide, mixed in an ice bath and stored under refrigeration) and 2160 µl 55 % ACROS Organics reagent grade hydrazine hydrate. Any change in the effectiveness of the reducing agent caused by altering the recipe in this way was deemed negligible (Dr M. Greaves, pers. com. 2014). The volume of reducing agent was always adjusted to the number of samples being cleaned to ensure the minimum possible amount of waste.

100 µl of reducing agent was added to each sample vial, which were then tightly shut. Depending on the equipment used, it may be necessary to clamp an acrylic sheet over the vial lids, using nylon screws to keep the acrylic cap flush with the vial lids, in order to prevent the vials from popping open in the hot water bath (which may result in sample loss). The sample vials were placed into a hot water bath at 70 – 90 ºC for 30 minutes. During this time, the following actions were performed every 2 minutes:

1. remove the rack of vials from the hot water bath
2. if applicable, tighten the screws on the acrylic plate if required
3. invert and shake vials
4. tap vials to settle samples to the bottoms of the vials
5. ultrasonicate the vials for a few seconds (this time the ultrasonic bath must be kept within an extracted fume hood)
6. again tap vials to re-settle samples to the bottoms of the vials
7. return the rack of sample vials to the hot water bath

Ultrasonication was used to agitate the reagent into all parts of the sample and discourage dissolved oxides from re-precipitating. After 30 minutes, the vials were removed from the hot water bath and carefully opened by peeling their lids off slowly (allowing gaseous build-up to be released slowly thus avoiding sample loss). As much of the reducing agent as possible was then removed from each sample vial using a 200 µl pipette. The samples were then rinsed with Milli-Q water in the following manner:

1. fill each sample vial with Milli-Q water
2. cap, invert and shake vials, tap out any bubbles
3. tap vials to settle samples to the bottoms of the vials
4. remove overlying water using a pipette
5. repeat steps 1 – 3 two times
6. add approximately 250 µl Milli-Q water to each sample vial
7. place vials in a hot water bath at 70 – 90 ºC for five minutes
8. remove vials from the hot water bath and remove overlying water using a pipette
9. repeat steps 1 – 3 two times
10. repeat steps 5 – 7 once

2.2.4 Sample transfer

Following the reducing step, it was sometimes necessary to place the samples into fresh vials because of the loosening of the sample vial lids caused by the reducing step. To perform sample transfers, a technique similar to that of Section 2.2.2 'Checking for contaminants' was used, as follows:

1. take a 200 µl pipette tip and cut off about one quarter from the solution end, at an angle, using a disposable scalpel (creating an enlarged, oval-shaped aperture)
2. acid-clean the modified pipette tip twice (additional cleaning is required because it has come into direct contact with the metal scalpel)
3. using the modified pipette tip, add a small amount of Milli-Q water (approximately 50 µl) to the sample vial to float the foraminifer fragments
4. immediately (to avoid re-settling), use the modified pipette tip to remove the foraminifer fragments from the vial and transfer them into a new vial
5. repeat until all foraminifer fragments have been transferred to the new vial

To prevent cross-contamination, a new modified pipette tip was used for each sample. After all samples were transferred, vials were tapped to settle samples to the bottoms of the vials and a 1000 µl pipette was used to remove the overlying solutions.

2.2.5 Organic matter removal (oxidising step)

In this step, an oxidising agent was used to remove organic matter from the samples. The oxidising agent consisted of 15 ml 0.1 M Fisher Chemical reagent grade carbonate-free NaOH mixed with 50 µl 30 % Romil ultra-pure H_2O_2 solution. 250 µl of oxidising agent was added to each sample vial. As in the reducing step, depending on the equipment used it may be necessary to clamp an acrylic sheet over the vial lids to prevent the vials from popping open in the hot water bath. The sample vials were placed into a hot water bath at 70 – 90 ºC for 10 minutes. Half way through this 10-minute period, the rack of sample vials was removed from the hot water bath, inverted, shaken, and then tapped firmly

on its side to re-settle the samples. At the end of the 10 minutes, sample vials were gently tapped to remove bubbles and then fragments allowed to re-settle. The oxidising agent was then removed from each sample vial using a 1000 µl pipette. Fresh oxidising agent was added to each vial (250 µl in each) and the process repeated once. The samples were then rinsed as follows:

1. fill each sample vial with Milli-Q water
2. cap, invert and shake vials, tap out any bubbles
3. tap vials to settle samples to the bottoms of the vials
4. remove overlying water using a pipette
5. repeat steps 1 – 4 once

2.2.6 Barite removal

Next, a solution of DTPA (Figure 2.1) was used to remove barite contamination. DTPA dissolves barite by chelating Ba^{2+} ions and is used in industry for cleaning barite from surfaces (Putnis et al. 2008). The DTPA solution is neutralised because this improves its effectiveness (Quattrini 1972) and to minimise calcium carbonate dissolution. To make this solution, 0.16 g of ACROS Organics reagent grade DTPA powder was dissolved in 200 ml Milli-Q water to make a 0.002 M DTPA solution, a concentration which prevents unacceptable sample loss whilst still removing barite (Lea & Boyle 1993), then 0.1 M Fisher Chemical reagent grade carbonate-free NaOH was added to this until the pH of the solution was approximately neutral (tested using indicator paper with a pH range of 1 – 14). 15 ml of 0.1 M NaOH was added. This was less than the predicted volume of NaOH to add which was 20 ml: 0.16 g of DTPA at 393.35 g/mol is 4.0676×10^{-4} mol DTPA; each DTPA molecule provides 5 H^+ ions to solution (Figure 2.1); moles of H^+ provided to solution = $5 \times 4.0676 \times 10^{-4} = 0.002$; 0.1 M NaOH provides 0.0001 mol OH^- per ml; to neutralise the H^+ from DTPA, 0.002 mol of OH^- are required; and this is provided by 20 ml of 0.1 M NaOH. The reason for a smaller requirement of NaOH than predicted could be that not all of the DTPA powder successfully dissolved. For this reason, the pH of the NaOH-DTPA solution was always checked before use so that if further DTPA dissolution had occurred additional NaOH could be added to maintain a neutral pH. The addition of 15 ml of NaOH indicates that the amount of DTPA powder which dissolved was approximately 0.118 g, resulting in a DTPA solution of 0.0015 M: 15 ml of 0.1 M NaOH provides 0.0015 mol OH^-; and 0.0015 mol H^+ would be provided by dissolution of 0.0003 mol DTPA (0.118 g). This is still an acceptable concentration for cleaning barite from foraminifera because a more dilute solution of DTPA is actually more effective at removing barite (Putnis et al. 2008) and because the use of a high-temperature water bath greatly increases the effectiveness of the DTPA solution (Putnis et al. 2008). The NaOH-DTPA solution was made in an acid-cleaned Teflon bottle to facilitate long-term storage.

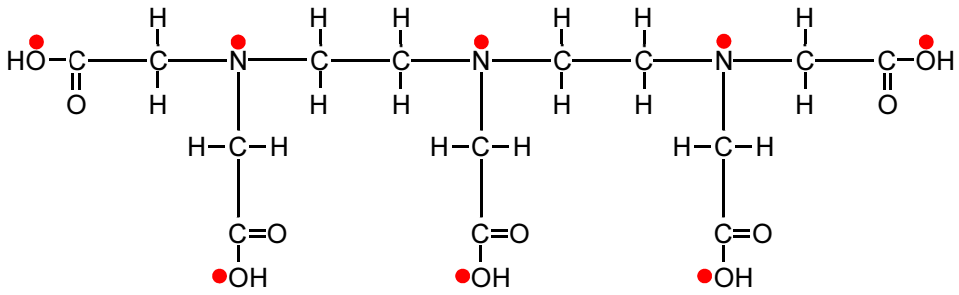

Figure 2.1. Chemical structure of diethylenetriaminepentaacetic acid (DTPA) ($C_{14}H_{23}N_3O_{10}$) with active sites for complexing cations marked by dots (Putnis et al. 2008). Each DTPA molecule acts as a ligand, forming a complex with one Ba^{2+} ion by wrapping around it (Housecroft & Constable 2010).

50 µl of this NaOH-DTPA solution was added to each sample vial. The sample vials were then placed in a hot water bath at 70 – 90 ºC for 10 minutes. As in the oxidising and reducing steps, depending on the equipment used it may be necessary to clamp an acrylic sheet over the vial lids to prevent the vials from popping open in the hot water bath. Within the 10 minute time period, every 2 minutes the rack of vials was removed, inverted, firmly tapped on its side to re-settle the samples, and returned to the hot water bath. Because DTPA dissolves calcium carbonate in addition to barite by chelating Ca^{2+} ions, it is important to rinse out the DTPA solution as quickly as possible after the 10 minute cleaning period is over to prevent unacceptable sample loss (Lea & Boyle 1993). To achieve this, samples were immediately rinsed with approximately 450 µl ~25 – 35 % Suprapur reagent grade ammonium hydroxide solution (Lea & Boyle 1993), followed by a Milli-Q water rinse to remove the ammonium hydroxide:

1. fill each sample vial with Milli-Q water
2. cap, invert and shake vials, tap out any bubbles
3. tap vials to settle samples to the bottoms of the vials
4. remove overlying water using a pipette
5. repeat steps 1 – 4 twice

2.2.7 Dilute acid rinse

The final stage of the cleaning procedure was a rinse with dilute nitric acid to remove any remaining adsorbed contaminants. This step may be adjusted as required depending on sample size and fragility. Because the samples were occasionally of very small size, the least aggressive possible version of this step was used. This involved modifying the original procedure by omitting ultrasonication, by not performing repeats and by using a 0.001 M solution of nitric acid rather than 0.002 M. In addition, only six samples were taken through this step at a time in order to reduce the contact time between acid and samples.

250 µl 0.001 M Romil ultra-pure nitric acid was added to each sample vial. The sample vials were then inverted, checked for bubbles, and firmly tapped to re-settle the samples, followed by removal of the nitric acid via pipette. Milli-Q water was then added to the vials and the same process repeated, to rinse the acid out of the sample vials. A 200 µl pipette was then used to carefully remove as much water as possible from each sample vial. Care was also taken to remove any water droplets from the vial lids. A new pipette tip was used for each sample vial to avoid cross-contamination. Samples were then dried down by placing them opened under a clean protective guard in a clean fume hood area, allowing any remaining water to evaporate over the course of a few hours. Sample vials were then firmly shut and the outsides of the vials dried before storage. At this stage, samples could be stored indefinitely until they were to be measured via mass spectrometry.

2.3 Measurement by mass spectrometry

2.3.1 Instrumental set-up and tuning

Samples were measured on a Thermo Finnigan Element 2 inductively coupled plasma mass spectrometer at the Bristol Isotope Group in the School of Earth Sciences, University of Bristol. Sample introduction was performed by a CETAC ASX-100 autosampler, Elemental Scientific MicroFlow PFA-50 self-aspirating Teflon nebuliser with ASX-100 stainless steel supported capillary, glass spray chamber and inbuilt peristaltic pump, with an Ar gas flow. The cones used were a platinum Thermo Finnigan sample cone and nickel Thermo Fisher 'H' skimmer cone.

Upon igniting the plasma, the Element was left to settle for 20 minutes to 1 hour before proceeding with tuning. A 1 ppb multi-element tuning solution was used to tune first the low, then medium and finally high resolution modes. In low resolution, torch position, sample gas flow rate (i.e. the gas which transports the sample from the spray chamber to the torch, the gas flow through the torch injector), auxiliary gas flow rate (i.e. plasma gas, the gas flow through the torch inner tube), and focus, x-deflection and y-deflection of low-resolution lenses (affecting the focus and deflection of the ion beam through the entrance slit) were tuned using Li, In, Ba and U. Typical sample gas and auxiliary gas flow rates were ~0.9 – 1.1 l/min and ~0.8 – 0.9 l/min, respectively. Oxide formation was also checked by measuring Ba, BaO, U and UO and calculating percentage oxides of U as (UO/U)*100 and of Ba as (BaO/Ba)*100. Typical percentages of oxides were approximately 3 % for U and 0.5 % for Ba. Tuning parameters were adjusted to gain an optimum balance between sensitivity and stability whilst maintaining sufficiently low oxides.

Once this had been achieved in low resolution, medium resolution mode was tuned using Na, K and Fe. Tuning was performed by adjusting the medium-resolution lenses until the Na, K and Fe peaks were flat-topped bell-shaped curves. High resolution mode was then tuned using Na, K and Fe, by adjusting the high-resolution lenses until flat-topped bell-shaped curves were achieved by the Na and Fe peaks and a separate peak could be seen attached to the K peak.

Next, mass calibrations were performed for the low, medium and high resolution modes in turn, and finally mass offsets were calculated and inserted into the method files to be used. Mass calibrations were performed every few weeks whereas mass offsets were updated before each run.

2.3.2 Data acquisition parameters

The method file for measurement of foraminiferal trace metal ratios is described in Table 2.1. The elements chosen for measurement were: Ba and Ca, for the measurement of Ba/Ca ratios, a primary objective of this project; Mg, because Mg/Ca ratios in foraminifera can be used as a proxy for temperature (e.g. Lear et al. 2002) so this could provide useful auxiliary data; Sr, because similarly Sr/Ca ratios can be used as a proxy for carbonate ion concentration (e.g. Yu et al. 2014) and temperature (e.g. Rosenthal et al. 2006; Cléroux et al. 2008); Mn, to check for contamination by metal oxides; and Al, to check for contamination by clays. The isotopes chosen for measurement were: ^{43}Ca, because ^{42}Ca, ^{43}Ca and ^{44}Ca are the most convenient for use in HR-ICP-MS due to their adequate abundances and relative lack of interferences (Halicz et al. 1999) compared to isotopes such as $^{40}Ca^{+}$ which is prone to isobaric interference by $^{40}Ar^{+}$ (Halicz et al. 1999) and of these, ^{43}Ca is least abundant allowing for samples to be run at 10 ppm Ca without overloading the detector in the mass spectrometer, which should only measure up to a limit of 10^7 cps (Figure 2.2); ^{138}Ba, because this is the most abundant stable isotope of Ba and hence the easiest to measure; ^{88}Sr for the same reason; ^{25}Mg, because Mg/Ca can be as high as 5 mmol/mol in foraminifera (e.g. Anand et al. 2003) so the use of a less-abundant isotope than ^{24}Mg reduces the risk of overloading the detector; ^{55}Mn, because this is the only stable isotope of Mn; and likewise for ^{27}Al. All isotopes were measured at low resolution because this resolution was sufficient to resolve interferences. Runs and passes were each set to 3. Passes are repeated scans which are averaged into one intensity per mass peak and runs are repeats of these which are also averaged and used to calculate a standard deviation (internal precision) (Figure 2.3).

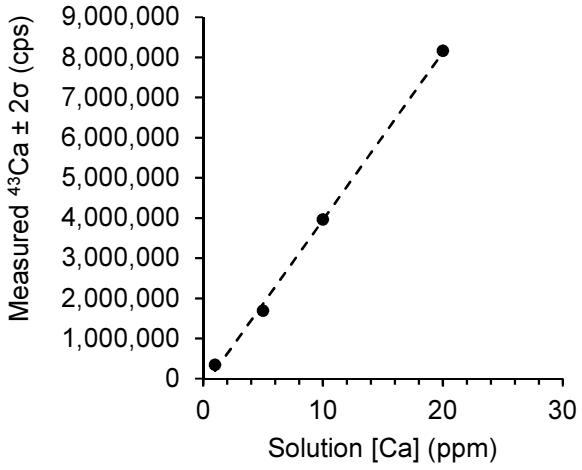

Figure 2.2. ^{43}Ca intensity in counts per second measured whilst varying calcium concentration with least-squares linear regression line (dashed line) of equation $y = (4.022 \times 10^5)*x$ with $R^2 = 0.998$. All of the error bars are smaller than the data points.

Table 2.1. Acquisition settings in the method file, with explanations. Values are the default settings provided by the Element 2 software.

Isotope	^{25}Mg	^{27}Al	^{43}Ca	^{55}Mn	^{88}Sr	^{138}Ba
Accurate mass (u)	24.9853	26.9810	42.9582	54.9375	87.9051	137.9047
Samples per peak	20	50	20	50	50	20
	The number of times to measure a peak within a scan, i.e. the number of vertical bars populating the mass peak (Thermo Finnigan 2001). The more times it is measured the better the precision will be but the longer the scanning time (Thermo Finnigan 2001).					
Mass window (%)	125	20	125	20	20	125
	The percentage of the mass peak, measured from the centre, used during scanning (data acquisition) (Thermo Finnigan 2001).					
Sample time (s)	0.0100	0.0100	0.0100	0.0100	0.0100	0.0100
	The time taken to acquire one sample (one vertical bar within a mass peak) (Thermo Finnigan 2001).					
Segment duration (s)	0.250	0.100	0.250	0.100	0.100	0.250
	The time taken to scan (i.e. acquire data from) each isotope's mass peak, resulting from samples per peak, mass window and sample time (Thermo Finnigan 2001).					
Integration window (%)	60	20	60	20	20	60
	The percentage of the mass peak, measured from the centre of the peak, used to calculate intensity (Thermo Finnigan 2001).					
Integration type	Average	Average	Average	Average	Average	Average
	Integration type 'average' means that the integrated intensity equals the sum of intensities in the peak window divided by number of samples in the window. Alternatives are 'peak top' (the maximum counts per second) or 'integral' (the sum of the intensities in the peak window) (Thermo Finnigan 2001).					
Scan type	EScan	EScan	EScan	EScan	EScan	EScan
	Scan type 'EScan' was used because this is the most appropriate scan type for general use (Thermo Finnigan 2001).					
Detection mode	Both	Both	Both	Both	Both	Both
	'Both' mode indicates that 'analogue' or 'counting' mode will be selected automatically depending on the counts per second detected: counting mode below 5 x 10^6 cps and analogue mode above this. The software automatically cross-calibrates the two modes (Thermo Finnigan 2001).					

Isotope	^{25}Mg	^{27}Al	^{43}Ca	^{55}Mn	^{88}Sr	^{138}Ba
Settling time (s)	0.048	0.001	0.027	0.014	0.030	0.001
	Time allowed for the magnet to stabilise after moving into position before measurements are taken. This is necessary because there is a small drift in the magnet after moving (Thermo Finnigan 2001).					

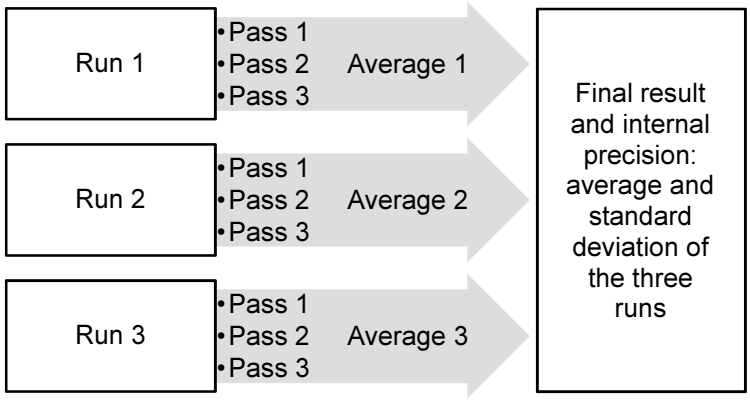

Figure 2.3. Schematic diagram of runs and passes.

2.3.3 Bracketing standard

A bracketing standard was created by adding aliquots of High-Purity Standards, Inc. single-element standard solutions to 40 ml 10,000 ppm Ca High-Purity Standards, Inc. standard solution. Volumes were calculated based on creating similar trace metal ratios in the bracketing standard to those found in foraminifera (Table 2.2). Aliquots were added whilst sequentially weighing the resulting solution and final trace metal ratios of the bracketing standard solution were calculated gravimetrically (Table 2.3). The bracketing standard was stored in an acid-cleaned Teflon bottle to facilitate long-term storage and was diluted to 10 ppm Ca using 0.075 M Romil ultra-pure nitric acid immediately prior to measurement.

Table 2.2. Example trace metal ratios in foraminifera.

Ba/Ca	Benthic: ~2 – 3.5 µmol/mol (e.g. Lea & Boyle 1990a) Planktic: ~1.3 – 2.6 µmol/mol (e.g. Hall & Chan 2004)
Mg/Ca	Benthic: ~0.6 – 1.1 mmol/mol (e.g. Rickaby et al. 2010) Planktic: ~3 – 5 mmol/mol (e.g. Anand et al. 2003)
Sr/Ca	Benthic: ~1.1 – 1.5 mmol/mol (e.g. Yu et al. 2014) Planktic: ~1.3 – 1.5 mmol/mol (e.g. Cléroux et al. 2008)
Al/Ca Mn/Ca	Measurements at Cardiff University, using their in-house bracketing standard, indicated that Al/Ca was on the order of 1 – 100 µmol/mol and that Mn/Ca was approximately 1 – 5 µmol/mol after using the cleaning technique outlined above.

Table 2.3. Formulation of the bracketing standard.

	High-Purity Standard added	Weight of solution added (g)	Volume of solution added (ml) [a]	Moles of element in solution [b]	X/Ca Ratio
Ca	40 ml of 10,000 ± 30 ppm solution	$4.130 \times 10^{1} \pm 1.000 \times 10^{-3}$	$4.001 \times 10^{1} \pm 7.755 \times 10^{-2}$	$9.984 \times 10^{-3} \pm 3.566 \times 10^{-5}$	Not applicable
Ba	480 µl of 10 ± 0.04 ppm solution	$4.760 \times 10^{-1} \pm 1.000 \times 10^{-3}$	$4.718 \times 10^{-1} \pm 1.363 \times 10^{-3}$	$3.435 \times 10^{-8} \pm 1.695 \times 10^{-10}$	$3.441 \times 10^{0} \pm 1.229 \times 10^{-2}$ µmol/mol
Mg	2183 µl of 1000 ± 3 ppm solution	$2.181 \times 10^{0} \pm 1.000 \times 10^{-3}$	$2.164 \times 10^{0} \pm 4.406 \times 10^{-3}$	$8.902 \times 10^{-5} \pm 3.228 \times 10^{-7}$	$8.916 \times 10^{0} \pm 3.185 \times 10^{-2}$ mmol/mol
Sr	1312 µl of 1000 ± 3 ppm solution	$1.318 \times 10^{0} \pm 1.000 \times 10^{-3}$	$1.305 \times 10^{0} \pm 2.767 \times 10^{-3}$	$1.489 \times 10^{-5} \pm 5.472 \times 10^{-8}$	$1.492 \times 10^{0} \pm 5.328 \times 10^{-3}$ mmol/mol
Al	27 µl of 1000 ± 3 ppm solution	$2.000 \times 10^{-2} \pm 1.000 \times 10^{-3}$	$1.970 \times 10^{-2} \pm 9.860 \times 10^{-4}$	$7.303 \times 10^{-7} \pm 3.661 \times 10^{-8}$	$7.315 \times 10^{1} \pm 2.612 \times 10^{-1}$ µmol/mol
Mn	210 µl of 10 ± 0.05 ppm solution	$2.120 \times 10^{-1} \pm 1.000 \times 10^{-3}$	$2.105 \times 10^{-1} \pm 1.077 \times 10^{-3}$	$3.832 \times 10^{-8} \pm 2.742 \times 10^{-10}$	$3.838 \times 10^{0} \pm 1.371 \times 10^{-2}$ µmol/mol

a) Calculated by: $volume_{ml} = solution\ mass_{ml} / density_{g/ml}$. Densities were provided by High-Purity Standards' Certificates of Analysis.

b) Calculated by: $element\ mass_{\mu g} = volume_{ml} \times concentration_{\mu g/ml\ i.e.ppm}$, followed by: $moles = mass_{g} / atomic\ mass_{g/mol}$.

2.3.4 Sequence design

Sample-standard bracketing was used to account for instrumental drift within runs. A typical sequence design is displayed in Figure 2.4. 'Wash out' blanks were run at the beginning of a sequence to avoid including high-RSD blank measurements, which were often seen at the beginning of a sequence, within the main run. Standards and samples were blank-corrected by the Element 2 software using the blank immediately preceding them. Blank solutions were 0.075 M Romil ultra-pure nitric acid and bracketing standard solutions were 10 ppm Ca dilutions of the bracketing standard described in Section 2.3.3 'Bracketing standard'. Sample solutions are described in Section 2.3.5 'Sample dissolution and measurement'. In addition to the blank, bracketing standard and sample solutions, a 'wash' solution of 0.075 M Romil ultra-pure nitric acid and a 'pre-wash' solution of 2 % reagent grade nitric acid were used and topped up before each run as necessary. All blank, bracketing standard and wash solutions were made fresh on the day of the run or on the day before. Appropriate solution take-up and wash times were estimated and set on the day of running using the tuning solution described in Section 2.3.1 'Instrumental set-up and tuning'. These were typically 1.5 and 2 minutes, respectively.

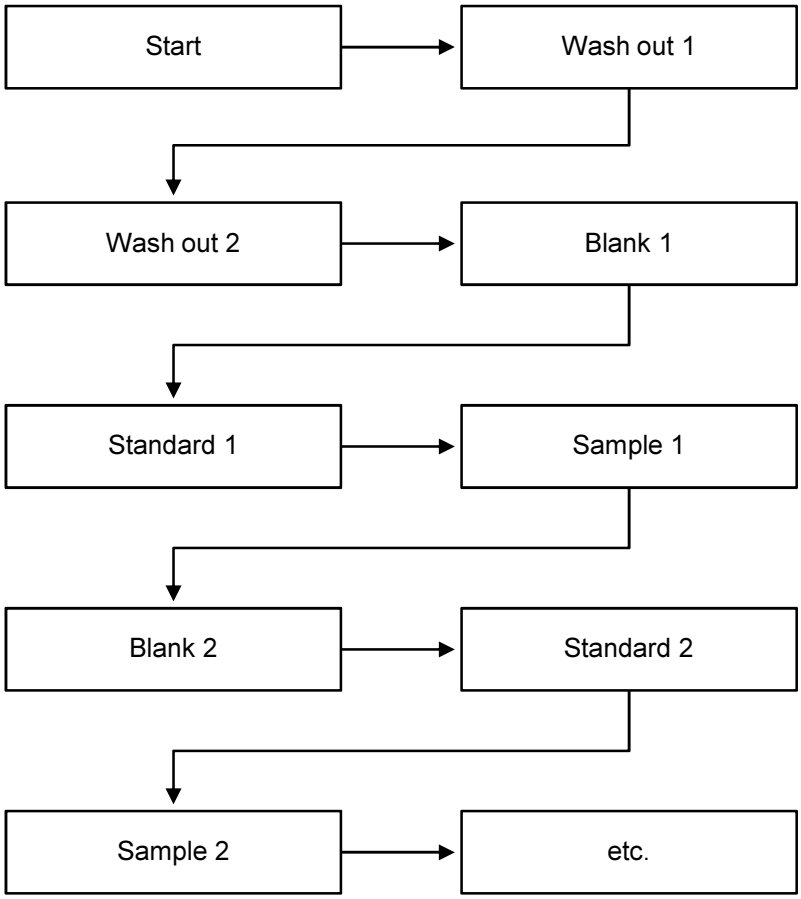

Figure 2.4. Schematic diagram of a typical sequence design.

2.3.5 Sample dissolution and measurement

Before measuring trace metal ratios in the samples, they were each diluted to the same calcium concentration as the bracketing standard in order to minimise matrix effects ('calcium-matching', e.g. Yu et al. 2005). A concentration of 10 ppm Ca was used primarily because this prevented ^{43}Ca intensities from overloading the detector (Figure 2.2). The relationship shown in Figure 2.2 predicts that 10^7 cps, the maximum allowable counts to prevent damaging the detector, would result from measuring a solution of approximately 25 ppm Ca. A concentration of 10 ppm Ca was used rather than this upper limit of 25 ppm Ca because fluctuations in instrument intensity between runs could cause this upper limit to vary. A lower concentration of 10 ppm was used to reduce the risk of overloading the detector. An alternative method of protecting the detector would be to use the less-abundant isotope ^{46}Ca, however this isotope is prone to isobaric interference from ^{46}Ti (Halicz et al. 1999). An added benefit of using 10 ppm rather than 80 or 100 ppm Ca as some previous authors have used (e.g. Yu et al. 2005; Harding et al. 2006; Marchitto 2006) was that this allowed for approximately 200 – 400 µg of foraminifera, a manageable picking amount, to be diluted to 1 or 2 ml for measurement, a convenient volume for using 2 ml autosampler vials in the CETAC ASX-100 autosampler whilst allowing for multiple measurements to be taken per sample. If 100 ppm were used, either the number of foraminifera to pick would increase or the overall sample volume would decrease, reducing the availability of full replicates or repeat measurements.

To begin measurement, samples were first dissolved by adding 200 µl 0.075 M Romil ultra-pure nitric acid to each sample and ultrasonicating in an ultrasonic bath for a few minutes or until CO_2 bubbles ceased forming and foraminifer fragments could no longer be seen. The dissolved samples were then centrifuged for 5 minutes at 5000 rpm using an Eppendorf MiniSpin microcentrifuge, to move any remaining particulates to the bottoms of the vials. 170 µl of each sample solution was then pipetted into a fresh acid-cleaned 500 µl microcentrifuge vial and set aside for later measurement. Of the remaining 30 µl, 20 µl was transferred into an acid-cleaned 2 ml autosampler vial and the remaining 10 µl was discarded along with the used microcentrifuge vial. 1980 µl 0.075 M Romil ultra-pure nitric acid was added to each autosampler vial to make the solutions up to 2 ml. These 2 ml calcium-matching solutions were then measured via HR-ICP-MS using the instrumental set-up, tuning, data acquisition parameters, bracketing standard and sequence design described above, with the exception that rather than measuring all isotopes in the method ^{43}Ca alone was measured. To reduce sample contamination, the time samples spent dissolved in vials was minimised by performing sample dissolution and calcium-matching on the day immediately before sample measurement. Calcium concentrations of the calcium-matching solutions were then calculated using the following equation:

$$\frac{[Ca]_{Ca\_match\_T}}{^{43}Ca_{Ca\_match\_T}} = \frac{[Ca]_{standard}}{^{43}Ca_{standard}} \qquad (2.1)$$

Which rearranges to:

$$[Ca]_{Ca\_match\_T} = \frac{^{43}Ca_{Ca\_match\_T} \times [Ca]_{standard}}{^{43}Ca_{standard}} \qquad (2.2)$$

Where $[Ca]_{Ca\text{-}match\text{-}T}$ is the calcium concentration of the calcium-matching solution in ppm, $^{43}Ca_{Ca\text{-}match\text{-}T}$ is the blank-corrected ^{43}Ca intensity of the calcium-matching solution in counts per second, $[Ca]_{standard}$ is the calcium concentration of the bracketing standard (10 ppm) and $^{43}Ca_{standard}$ is the blank-corrected ^{43}Ca intensity of the bracketing standard in counts per second.

Dilutions could then be calculated for diluting the remaining 170 µl of sample solutions, set aside earlier, to 10 ppm for measurement. The following equation was used to calculate these dilutions:

$$V_{sample\_170} = \frac{[Ca]_{new} \times V_{new} \times V_{Ca\_match\_20}}{[Ca]_{Ca\_match\_T} \times V_{Ca\_match\_T}} \qquad (2.3)$$

Where $V_{sample\text{-}170}$ is the volume of sample to use in the new dilution, $[Ca]_{new}$ is the target calcium concentration of the new dilution (10 ppm), V_{new} is the total volume of the new dilution (usually 2000 µl but this may be lowered if required to make $V_{sample\text{-}170} \leq 170$ µl), $V_{Ca\text{-}match\text{-}20}$ is the volume of sample used in the calcium-matching solution (20 µl), $[Ca]_{Ca\text{-}match\text{-}T}$ is the calcium concentration of the total calcium-matching solution (measured by HR-ICP-MS, see above) and $V_{Ca\text{-}match\text{-}T}$ is the total volume of the calcium-matching solution (2000 µl). The volume of sample designated by $V_{sample\text{-}170}$ was added to a new acid-cleaned 2 ml autosampler vial and then made up to the total volume designated by V_{new} by adding 0.075 M Romil ultra-pure nitric acid. $V_{sample\text{-}170}$ was rounded to 1 decimal place for enhanced pipetting accuracy. Once these dilutions had been made, the resulting sample solutions were ready for measurement of Ba/Ca, Mg/Ca, Sr/Ca, Al/Ca and Mn/Ca. Samples were measured via HR-ICP-MS using the instrumental set-up, data acquisition parameters, bracketing standard and sequence design described above. The derivation of the previous equation is described below:

$$\text{Concentration}_1 \times \text{Volume}_1 = \text{Concentration}_2 \times \text{Volume}_2 \qquad (2.4)$$

$$[Ca]_{Ca\_match\_20} \times V_{Ca\_match\_20} = [Ca]_{Ca\_match\_T} \times V_{Ca\_match\_T} \qquad (2.5)$$

$$[Ca]_{Ca\_match\_20} = \frac{[Ca]_{Ca\_match\_T} \times V_{Ca\_match\_T}}{V_{Ca\_match\_20}} \qquad (2.6)$$

Where $[Ca]_{Ca\text{-}match\text{-}20}$ is the calcium concentration of the 20 µl of sample that was used in the calcium-matching solution, $V_{Ca\text{-}match\text{-}20}$ is the volume of sample that was used in that same solution (20 µl), $[Ca]_{Ca\text{-}match\text{-}T}$ is the calcium concentration of the calcium-matching solution (measured via HR-ICP-MS) and $V_{Ca\text{-}match\text{-}T}$ is its total volume (2000 µl). Because the 20 µl of sample that was used in the calcium-matching solution was from the same source as the 170 µl of sample that was set aside to be used, their calcium concentrations are equal:

$$[Ca]_{Ca\_match\_20} = [Ca]_{sample\_170} \qquad (2.7)$$

Where $[Ca]_{sample\text{-}170}$ is the calcium concentration of the remaining 170 µl of sample that was set aside for measurement. Substituting this into the equation above gives:

$$[Ca]_{sample\_170} = \frac{[Ca]_{Ca\_match\_T} \times V_{Ca\_match\_T}}{V_{Ca\_match\_20}} \qquad (2.8)$$

The next step is to calculate the volume of this 170 µl of sample that should be used in the new dilution:

$$\text{Concentration}_1 \times \text{Volume}_1 = \text{Concentration}_2 \times \text{Volume}_2 \qquad (2.9)$$

$$[\text{Ca}]_{\text{sample\_170}} \times \text{V}_{\text{sample\_170}} = [\text{Ca}]_{\text{new}} \times \text{V}_{\text{new}} \qquad (2.10)$$

$$\text{V}_{\text{sample\_170}} = \frac{[\text{Ca}]_{\text{new}} \times \text{V}_{\text{new}}}{[\text{Ca}]_{\text{sample\_170}}} \qquad (2.11)$$

Where $V_{sample\text{-}170}$ is the volume of the remaining 170 µl of sample solution that should be used in the new dilution, $[Ca]_{new}$ is the target calcium concentration of the new dilution (10 ppm) and V_{new} is the target total volume of the new dilution (usually 2000 µl but this may be lowered if necessary to make $V_{sample\text{-}170} \leq 170$ µl). Substituting in for $[Ca]_{sample\text{-}170}$ gives:

$$\text{V}_{\text{sample\_170}} = ([\text{Ca}]_{\text{new}} \times \text{V}_{\text{new}}) \div \left(\frac{[\text{Ca}]_{\text{Ca\_match\_T}} \times \text{V}_{\text{Ca\_match\_T}}}{\text{V}_{\text{Ca\_match\_20}}}\right) \qquad (2.12)$$

Which rearranges to the final equation:

$$\text{V}_{\text{sample\_170}} = \frac{[\text{Ca}]_{\text{new}} \times \text{V}_{\text{new}} \times \text{V}_{\text{Ca\_match\_20}}}{[\text{Ca}]_{\text{Ca\_match\_T}} \times \text{V}_{\text{Ca\_match\_T}}} \qquad (2.13)$$

2.3.6 Calculation of trace metal ratios

This section describes how the raw data from HR-ICP-MS were processed into trace metal ratios. In order to avoid potential software artefacts ratios were calculated offline. Ratios were calculated by dividing the intensities of each isotope by that of ^{43}Ca:

$$\frac{\text{X}}{\text{Ca}} = \frac{\text{X}_{\text{intensity}}}{^{43}\text{Ca}_{\text{intensity}}} \qquad (2.14)$$

Where 'X' represents either ^{25}Mg, ^{27}Al, ^{55}Mn, ^{88}Sr or ^{138}Ba. This was done for both standards and samples. The uncertainty for X/Ca was calculated by propagation of internal precision (Figure 2.3) using the following equation:

$$\sigma_{\text{X/Ca}} = \left(\frac{\text{X}}{\text{Ca}}\right) \times \sqrt{\left(\frac{\sigma_{\text{X}}}{\text{X}}\right)^2 + \left(\frac{\sigma_{\text{Ca}}}{\text{Ca}}\right)^2} \qquad (2.15)$$

Where $\sigma_{X/Ca}$ is the propagated uncertainty for the X/Ca ratio, X/Ca is the ratio calculated using the previous equation, σ_X is the internal precision for isotope X, X is the intensity of isotope X, σ_{Ca} is the internal precision for ^{43}Ca and Ca is the intensity of ^{43}Ca. This was also done for both standards and samples.

Ratios were then converted from counts per second into concentration (mmol/mol) using the following equation:

$$\frac{\left(\frac{\text{X}}{\text{Ca}}\right)_{\text{SPL\_C}}}{\left(\frac{\text{X}}{\text{Ca}}\right)_{\text{SPL\_I}}} = \frac{\left(\frac{\text{X}}{\text{Ca}}\right)_{\text{STD\_C}}}{\left(\frac{\text{X}}{\text{Ca}}\right)_{\text{STD\_I}}} \qquad (2.16)$$

Which rearranges to:

$$\left(\frac{\text{X}}{\text{Ca}}\right)_{\text{SPL\_C}} = \frac{\left(\frac{\text{X}}{\text{Ca}}\right)_{\text{STD\_C}} \times \left(\frac{\text{X}}{\text{Ca}}\right)_{\text{SPL\_I}}}{\left(\frac{\text{X}}{\text{Ca}}\right)_{\text{STD\_I}}} \qquad (2.17)$$

Where $(X/Ca)_{SPL\text{-}C}$ is the X/Ca ratio of the sample in units of concentration (mmol/mol), $(X/Ca)_{STD\text{-}C}$ is the X/Ca ratio of the bracketing standard in units of concentration (mmol/mol) as calculated in Section 2.3.3 'Bracketing standard', $(X/Ca)_{SPL\text{-}I}$ is the X/Ca ratio of the sample in units of counts per second as calculated in the previous step and $(X/Ca)_{STD\text{-}I}$ is the X/Ca ratio of the bracketing standard in units of counts per second as calculated in the previous step. Each sample was paired with the standard immediately preceding it (see Section 2.3.4 'Sequence design'). Errors were propagated using the following equation:

$$\sigma_{\left(\frac{X}{Ca}\right)_{SPL\_C}} = \left(\frac{X}{Ca}\right)_{SPL\_C} \times \sqrt{\left(\frac{\sigma_{\left(\frac{X}{Ca}\right)_{SPL\_I}}}{\left(\frac{X}{Ca}\right)_{SPL\_I}}\right)^2 + \left(\frac{\sigma_{\left(\frac{X}{Ca}\right)_{STD\_I}}}{\left(\frac{X}{Ca}\right)_{STD\_I}}\right)^2 + \left(\frac{\sigma_{\left(\frac{X}{Ca}\right)_{STD\_C}}}{\left(\frac{X}{Ca}\right)_{STD\_C}}\right)^2} \qquad (2.18)$$

Where $\sigma_{(X/Ca)SPL\text{-}C}$ is the propagated uncertainty for the X/Ca ratio of the sample in units of concentration (mmol/mol), $(X/Ca)_{SPL\text{-}C}$ is the X/Ca ratio of the sample in the same units, σ values are uncertainties propagated from internal precision as described by Equation 2.15, 'SPL-I' indicates uncertainties and ratios of the sample in units of counts per second, 'STD-I' indicates uncertainties and ratios of the bracketing standard in units of counts per second and 'STD-C' indicates uncertainties and ratios of the bracketing standard in units of concentration (mmol/mol) which are provided in Section 2.3.3 'Bracketing standard'.

The different contributors of uncertainty to the total error are therefore: the standard deviation provided by the instrument (internal precision) for the ^{43}Ca intensity of the sample; that of the paired standard; the internal precision for the other isotope in the ratio 'X' (e.g. X = ^{138}Ba); that of the paired standard; and the error associated with the creation of the bracketing standard (Table 2.3). Of these, the Ca measurements in the sample and X measurements in the sample and standard contribute most of the uncertainty, because their relatively low concentrations in the measured solutions result in larger internal precision.

Mg/Ca and Sr/Ca values were maintained in units of mmol/mol. Ba/Ca, Al/Ca and Mn/Ca were converted to μmol/mol for ease of use. Their uncertainties were also converted to μmol/mol.

2.3.7 Challenges

The measurement of trace metal ratios via ICP-MS presented several challenges. On one occasion anomalously high barium levels were seen in bracketing standards during a run, causing the Ba/Ca of samples to be underestimated. Anomalous barium levels were also observed by other users of the laboratory during measurement when using the same mass spectrometer. Given that other users did not use the same clean laboratory facilities or sample containers and were measuring different blanks, standards and samples, the source of this excess barium may have been associated with the mass spectrometer itself. Testing the apparatus, for example by using different cones, capillaries, nebulisers and auto-samplers, did not elucidate the source of the excess barium. There were also no known

instances of other users running high-barium samples prior to measurement which may have resulted in residual barium contamination within the apparatus. In summary, the source of this excess barium has yet to be determined. In order to minimise the impact of these anomalously high barium levels in the bracketing standard on the results of this study, all Ba/Ca results from the run in question have been omitted. These discarded data are shown in Figure 2.5.

A further challenge experienced during measurement was difficulty in achieving and maintaining good signal stability. During tuning, it was often difficult to achieve acceptable signal stability despite following the procedures outlined in Section 2.3.1 'Instrumental set-up and tuning'. On occasion large swings in signal intensity occurred despite no changes to any of the tuning settings having been made. This inconsistent signal intensity occasionally caused very high RSD values on sample measurements; for example consecutive measurements of the same solution with all settings unchanged could give an RSD of 1.5 % followed seconds later by an RSD of 30 %. In an attempt to improve the signal stability different nebulisers were used, but these were found to have little effect or to cause only short-lived improvements. In case the poor stability was caused by solution contamination, wash times were increased and fresh solutions were made on the day of each run, but these measures brought little improvement. Changing the sample gas flow speed had an inconsistent impact on signal stability; sometimes raising the sample gas flow speed improved stability and other times the reverse was true. This difficulty in gaining good signal stability meant that running samples could be risky, as the signal stability could deteriorate within a run or during the time in-between sample dissolution and sample measurement. In addition to poor stability, sometimes poor signal intensities were observed, although this problem was remedied by replacement of the mass spectrometer's detector. The low signal intensities sometimes improved signal stability and other times worsened it. Initially, measurements of Li/Ca, Cd/Ca and U/Ca were planned, but because of these problems with signal stability and intensity the RSDs of the Li, Cd and U measurements were found to be too high for these data to be interpreted and they were thus omitted from the study.

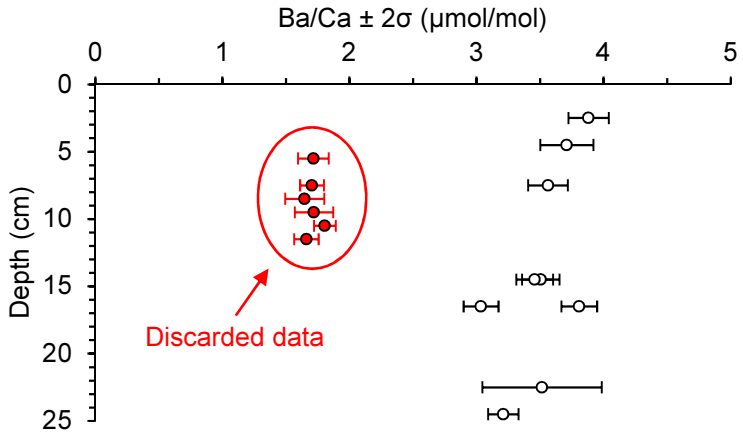

Figure 2.5. Ba/Ca data which were discarded due to high background Ba levels (red data points) alongside data which were not affected by this problem (white data points). All data are from *M. barleeanus* in sediment core BC387-2 (no other samples were affected). σ is internal precision.

2.4 Quality assurance

The trace metal ratios measured via HR-ICP-MS were screened in several ways to assure data quality. Data which did not meet these criteria were objectively discarded and data which satisfied all of these requirements are plotted within Chapters 3 to 5. The quality assurance measures are described below, as well as techniques used to check method reliability: consistency standards, repeat measurements and interlaboratory comparisons.

2.4.1 Data screening

2.4.1.1 Limit of detection

Before calculating trace metal ratios, raw intensity data were checked to ensure that all data were above the limit of detection of the instrument, defined as:

$$\text{limit of detection} = \text{BI} + 3\sigma_{\text{BI}} \qquad (2.19)$$

Where BI is the intensity of the blank and σ_{BI} is the internal precision for this value (Harris 2010). Intensity data which were below the limit of detection were discarded and not used to calculate trace metal ratios. In this case, '< LoD', standing for 'below limit of detection', was noted down in place of a trace metal ratio.

2.4.1.2 Contamination

Elevated Mn/Ca and Al/Ca ratios can indicate contamination by metal oxides and clays, respectively. Samples with a high risk of contamination can be removed by using cut-off limits for Mn/Ca (Boyle 1983) and Al/Ca (Ni et al. 2007). A sample was considered contaminated and its data discarded if its Mn/Ca ratio was above 3 μmol/mol (for sediment core BC387-2) or 40 μmol/mol (for sediment cores GC528 and GC642) or if its Al/Ca ratio was above 50 μmol/mol (GC528) or 60 μmol/mol (GC642 and BC387-2). The cut-off limits were tailored to each sediment core in order to conserve as much data as possible whilst preventing positive correlations between Mn/Ca or Al/Ca and Ba/Ca, Mg/Ca or Sr/Ca (see Section 2.4.2 'Correlations with Al/Ca, Mn/Ca and matrix effect').

2.4.1.3 Matrix effects

Matrix effects are differences in measured trace metal ratios caused by differences in the solution matrix. In dissolved foraminifer solutions, calcium ions are most abundant and so matrix effects can be assumed to be dependent only on the amount of calcium ions (e.g. Lear et al. 2002). Here, 'matrix effect' is defined as the percentage difference in ^{43}Ca intensity between a sample and its paired standard, relative to the standard. Matrix effects were calculated using the following equation:

$$\text{matrix effect (\%)} = \left(\frac{\text{Ca}_{\text{SPL}} - \text{Ca}_{\text{STD}}}{\text{Ca}_{\text{STD}}}\right) \times 100 \qquad (2.20)$$

Where Ca_{SPL} is the blank-corrected ^{43}Ca intensity of the sample and Ca_{STD} is the blank-corrected ^{43}Ca intensity of its paired standard. Internal precision was propagated using the following equation:

$$\sigma_{\text{matrix effect}} = \left| \text{matrix effect} \times \sqrt{\left(\frac{\sqrt{{\sigma_{SPL}}^2 + {\sigma_{STD}}^2}}{Ca_{SPL} - Ca_{STD}}\right)^2 + \left(\frac{\sigma_{STD}}{Ca_{STD}}\right)^2} \right| \qquad (2.21)$$

Where $\sigma_{\text{matrix effect}}$ is the propagated uncertainty for the matrix effect, σ_{SPL} is the internal precision of the ^{43}Ca intensity of the sample, σ_{STD} is the internal precision of the ^{43}Ca intensity of the standard, Ca_{SPL} is the ^{43}Ca intensity of the sample and Ca_{STD} is the ^{43}Ca intensity of the standard.

A perfect matrix effect would be zero, but due to the limiting factors of pipettor accuracy and instrumental drift it is more feasible to achieve matrix effects of –15 to 15 % (Dr A. Morte-Ródenas, pers. com. 2014). Because some data of interest fell outside of this range, the cut-off limit was widened to ± 25 % such that only trace metal data with matrix effects larger than 25 % or smaller than –25 % were discarded.

2.4.2 Correlations with Al/Ca, Mn/Ca and matrix effect

To check for significant relationships between trace metal data and contaminants or matrix effects, which may indicate that data are biased by these factors, Ba/Ca, Mg/Ca and Sr/Ca are plotted against Al/Ca, Mn/Ca and matrix effect (Figure 2.6; Figure 2.7; Figure 2.8) and correlation coefficients calculated (Table 2.4).

There are no significant relationships between Ba/Ca, Mg/Ca or Sr/Ca and Mn/Ca or Al/Ca (Table 2.4), confirming that the data are not significantly biased by contamination from clays or metal oxides. To test whether the matrix effect cut-off limit of ± 25 % was acceptable, trace metal data were also plotted against matrix effects and product moment correlation coefficient values calculated (Figure 2.6; Figure 2.7; Figure 2.8; Table 2.4). No significant relationships were found between trace metal data and matrix effects (Table 2.4), suggesting that increasing the range of matrix effects from ± 15 % to ± 25 % has not significantly impacted the trace metal data, lending confidence to the inclusion of these data.

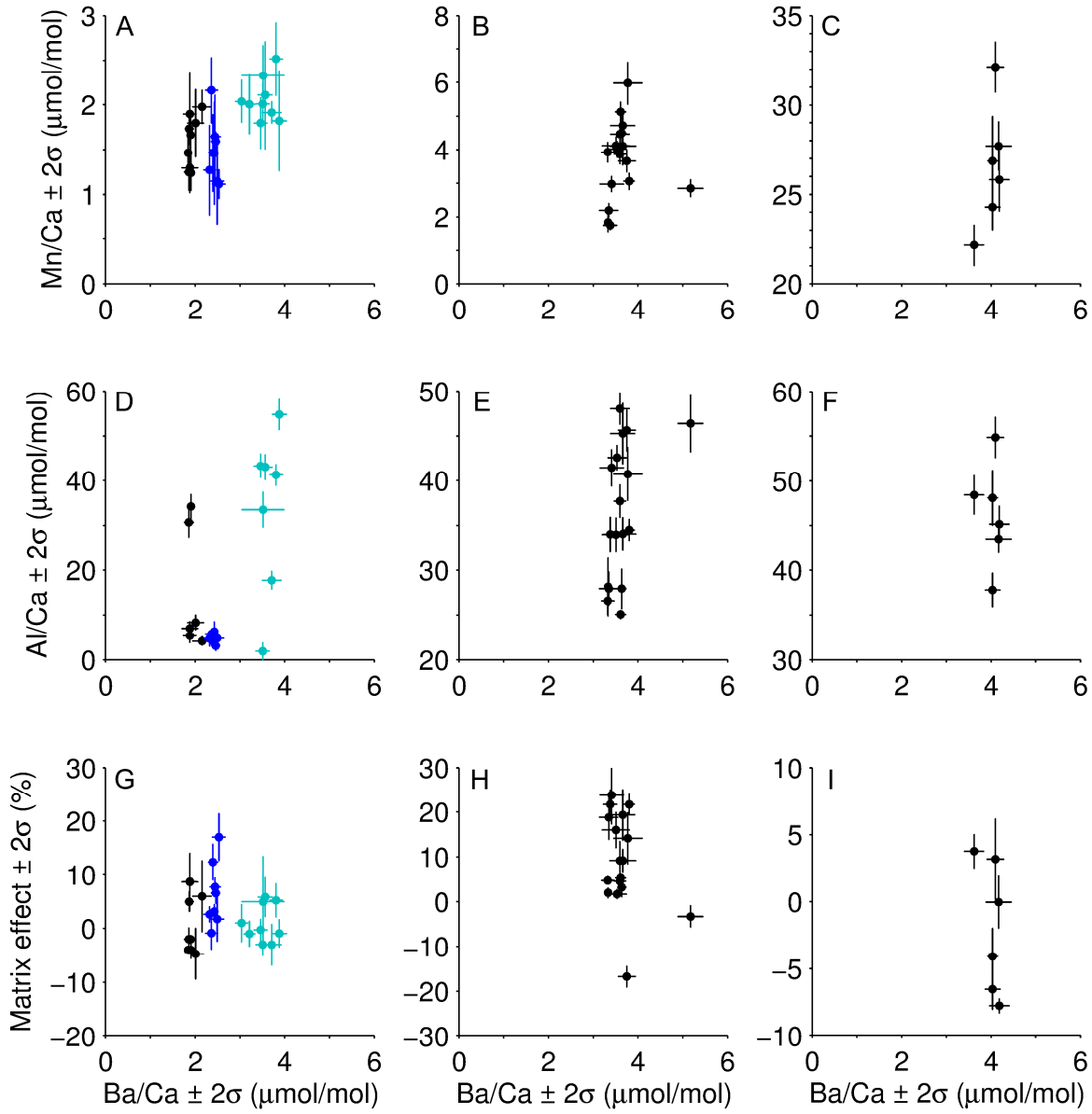

Figure 2.6. Foraminiferal Ba/Ca plotted against Mn/Ca for sediment cores BC387-2 (A; light blue = *Melonis barleeanus*, dark blue = *Uvigerina peregrina*, black = *Oridorsalis umbonatus*), GC528 (B) and GC642 (C) and likewise against Al/Ca (D, E and F) and against matrix effect (G, H and I). Product moment correlation coefficients and their p-values for this figure are provided in Table 2.4.

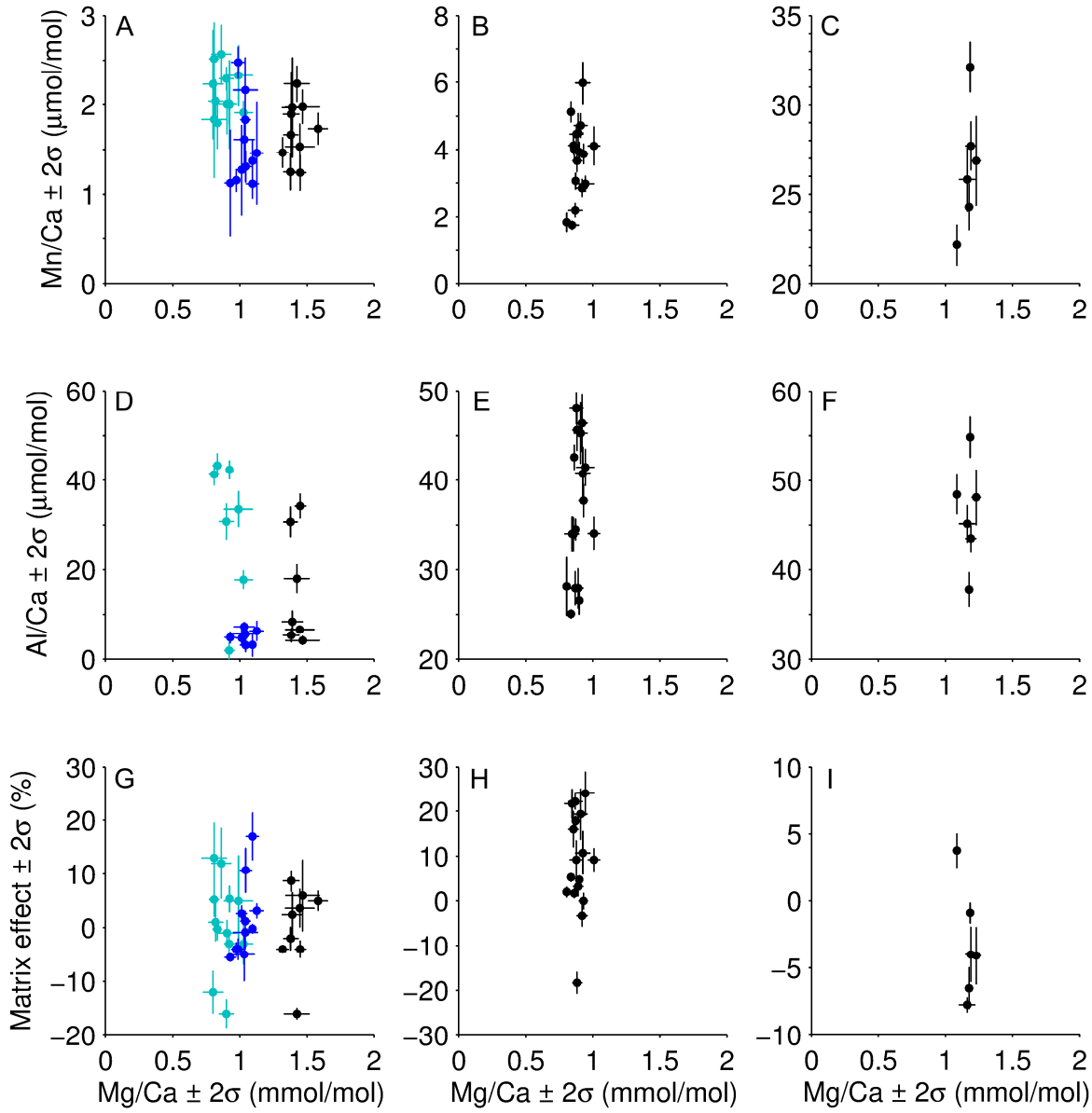

Figure 2.7. Foraminiferal Mg/Ca plotted against Mn/Ca for sediment cores BC387-2 (A; light blue = *Melonis barleeanus*, dark blue = *Uvigerina peregrina*, black = *Oridorsalis umbonatus*), GC528 (B) and GC642 (C) and likewise against Al/Ca (D, E and F) and against matrix effect (G, H and I). Product moment correlation coefficients and their p-values for this figure are provided in Table 2.4.

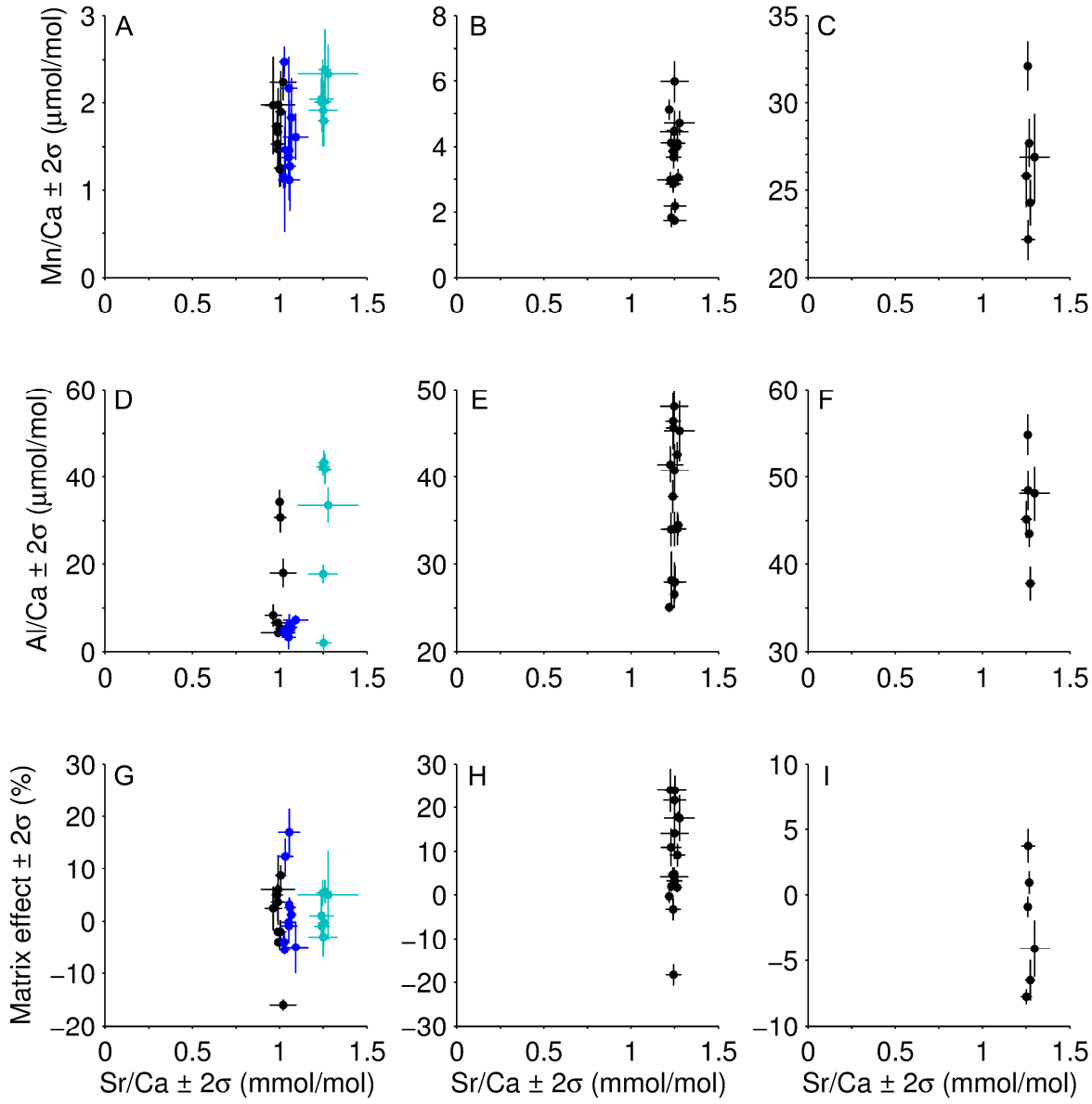

Figure 2.8. Foraminiferal Sr/Ca plotted against Mn/Ca for sediment cores BC387-2 (A; light blue = *Melonis barleeanus*, dark blue = *Uvigerina peregrina*, black = *Oridorsalis umbonatus*), GC528 (B) and GC642 (C) and likewise against Al/Ca (D, E and F) and against matrix effect (G, H and I). Product moment correlation coefficients and their p-values for this figure are provided in Table 2.4.

Table 2.4. Product moment correlation coefficients (R) and their p-values (p). The two parameters used to calculate R and p are displayed as horizontal and vertical labels.

Sediment core,		Mn/Ca		Al/Ca		Matrix effect	
species		R	p	R	p	R	p
BC387-2	Ba/Ca	0.12	0.75	0.39	0.38	0.09	0.81
M. bar.	Mg/Ca	–0.10	0.76	–0.49	0.26	–0.11	0.73
	Sr/Ca	0.64	0.08	0.20	0.71	0.50	0.21
BC387-2	Ba/Ca	0.58	0.10	–0.46	0.36	0.12	0.76
O. umb.	Mg/Ca	0.16	0.67	–0.1	0.82	0.26	0.47
	Sr/Ca	0.03	0.93	0.36	0.42	–0.51	0.13
BC387-2	Ba/Ca	–0.46	0.26	–0.24	0.61	0.52	0.18
U. per.	Mg/Ca	–0.03	0.93	0.03	0.94	0.59	0.06
	Sr/Ca	0.04	0.92	–0.67	0.07	0.04	0.92
GC528	Ba/Ca	0.05	0.86	0.46	0.06	–0.34	0.18
M. bar.	Mg/Ca	0.31	0.23	0.33	0.20	0.03	0.92
	Sr/Ca	0.09	0.75	0.27	0.30	0.23	0.37
GC642	Ba/Ca	0.63	0.18	–0.16	0.77	–0.52	0.29
M. bar.	Mg/Ca	0.60	0.20	–0.04	0.94	–0.61	0.20
	Sr/Ca	–0.05	0.93	–0.13	0.81	–0.08	0.87

R = 1 indicates a perfect positive linear relationship, R = –1 indicates a perfect negative linear relationship and R = 0 indicates no linear relationship.

The relationship described by R is significant at a 95 % significance level if p is less than 0.05: no significant relationships are present.

M. bar. = Melonis barleeanus, *O. umb. = Oridorsalis umbonatus*, *U. per. = Uvigerina peregrina.*

2.4.3 Short- and long-term precision

2.4.3.1 Creation of consistency standard

A consistency standard to monitor long and short-term precision was created by cleaning and then dissolving foraminifera into a solution that could be sampled, diluted and measured as required. This approach was taken rather than creating a powdered standard which could be dissolved when needed because of the potential contamination introduced by the powdering process, which involves close contact with metal surfaces in a non-trace-metal-clean environment (Dr K. Hendry, pers. com. 2014). Cleaning the foraminifera after powdering would be unviable because foraminifer powder would rapidly dissolve and be lost during the cleaning procedure.

To make the consistency standard, sediment sample S0157 collected during cruise JC094 of the RRS *James Cook* was used because excess sediment was available from this sample and because this sediment is rich in foraminifera. Further details of the collection of this sediment sample are provided Section 5.3.1 'Sample collection'. A mixed selection of different species of planktic and benthic foraminifera were picked from the 355 – 425 μm size fraction, with individual weights of approximately 30 μg. The use of a mixture of different foraminifera gave the consistency standard a composition roughly similar to that of a typical foraminifer sample. These were crushed and cleaned using the same procedures as for samples as described in Section 2.2 'Foraminiferal cleaning procedure'. The cleaned foraminifera were then dissolved in 0.075 M Romil ultra-pure nitric acid using the technique described in Section 2.3.5 'Sample dissolution and measurement' and combined into one solution, which was stored in an acid-cleaned Teflon bottle for long-term storage.

Prior to the first time the consistency standard was measured, it underwent calcium-matching as described in Section 2.3.5 'Sample dissolution and measurement'. Calcium-matching dictated that a 10 ppm Ca solution of consistency standard would result from 13 μl of consistency standard made up to a total volume of 2 ml.

2.4.3.2 Short-term precision

In each sample run, short-term precision, defined here as the precision within each run, was monitored by measuring the consistency standard several times within each run and calculating the standard deviation of these measurements. The standard was measured at the start, middle and end of relatively long runs, or only at the start and end if the run was relatively short. These measurements are displayed in Figure 2.9 and Figure 2.10. Ba/Ca or Sr/Ca are not shown for some runs, where data quality assessment was failed (see Section 2.4.3.3 'Long-term precision'). Within each run, consistency standard measurements remain constant within ± 2σ. The short-term precision per run is displayed in Table 2.5. These range from 0.01 – 0.07 for Ba/Ca, 0.01 – 0.15 for Mg/Ca and < 0.01 – 0.06 for Sr/Ca (Table 2.5).

Table 2.5. Short-term precision.

Ratio	Date of run	Sediment core measured	σ	μ	n
Ba/Ca	29th March 2015	BC387-2	0.01	1.06	2
	19th April 2015	BC387-2	0.06	1.16	3
	18th November 2015	GC528 and GC642	0.03	1.36	3
	23rd November 2015	GC528 and GC642	0.07	1.61	3
	4th February 2016	BC387-2	0.04	1.21	3
Mg/Ca	29th March 2015	BC387-2	0.01	4.43	2
	19th April 2015	BC387-2	0.10	4.51	3
	24th May 2015	BC387-2	0.03	4.51	2
	26th June 2015	BC387-2	0.07	4.56	3
	11th July 2015	BC387-2	0.05	4.43	3
	18th November 2015	GC528 and GC642	0.04	4.50	3
	23rd November 2015	GC528 and GC642	0.15	4.45	3
	4th February 2016	BC387-2	0.07	4.47	3
Sr/Ca	29th March 2015	BC387-2	< 0.01	1.26	2
	19th April 2015	BC387-2	< 0.01	1.26	3
	24th May 2015	BC387-2	0.06	1.21	2
	26th June 2015	BC387-2	0.01	1.27	3
	18th November 2015	GC528 and GC642	0.01	1.27	3
	23rd November 2015	GC528 and GC642	0.05	1.28	3
	4th February 2016	BC387-2	< 0.01	1.27	3

σ = short-term precision, μ = mean, n = number of samples used in calculation. σ and μ are in units of μmol/mol for Ba/Ca and mmol/mol for Mg/Ca and Sr/Ca. Data used to calculate these values are displayed in Figure 2.9 and Figure 2.10.

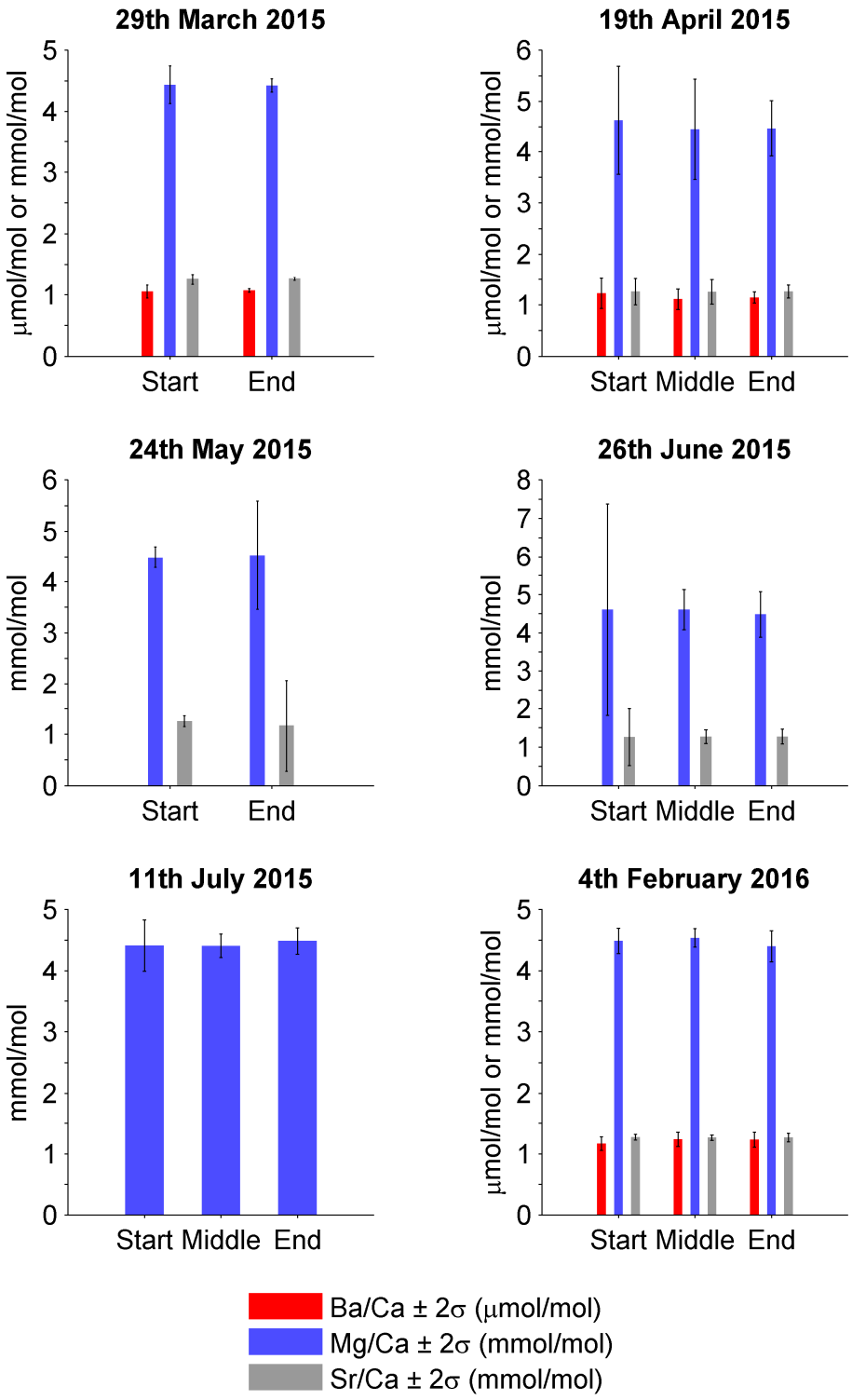

Figure 2.9. Consistency standard measurements from the start, middle and end of runs on the dates shown. These runs measured samples from sediment core BC387-2 (for core details see Section 3.3.1 'Sediment collection and oceanographic setting'). No mid-run measurement was made when a run was relatively short. Ba/Ca and Sr/Ca data are omitted where Ba/Ca and Sr/Ca results were discarded in order to maintain acceptable long-term consistency. The short-term precision per run is provided in Table 2.5.

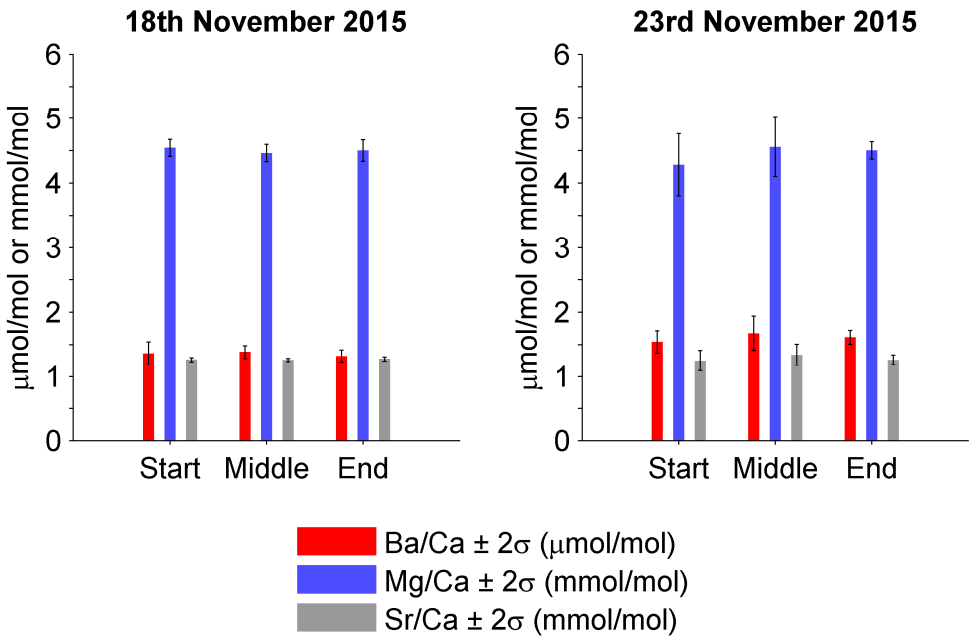

Figure 2.10. Consistency standard measurements from the start, middle and end of runs on the dates shown. These runs measured samples from sediment cores GC528 and GC642 (for core details see Section 4.3.1 'Sediment collection and oceanographic setting'). The short-term precision per run is provided in Table 2.5.

2.4.3.3 Long-term precision

Long-term precision, across several days to months, was monitored by calculating the standard deviation across consistency standards from all runs, per trace element ratio (Figure 2.11; Figure 2.12; Figure 2.13). Data were averaged per run before calculating the long-term precision. (Figure 2.11, Figure 2.12 and Figure 2.13 show the un-averaged data, with each date representing one run). The long-term precision across all measurements is σ = 0.19 µmol/mol for Ba/Ca, σ = 0.04 mmol/mol for Mg/Ca and σ = 0.02 mmol/mol for Sr/Ca (Table 2.6). Long-term precision per sediment core is provided in Table 2.6. Each run from which foraminiferal trace metal data were collected is represented by at least one accompanying consistency standard measurement within the long-term precision calculation. Foraminifer sample data were discarded and their accompanying consistency standard measurements omitted from the long-term precision calculation if trace element data were found to be anomalously high, likely reflecting contamination, or if their uncertainties were very large, which could be caused by instrumental instability or very low sample concentrations. This was assessed per trace element ratio.

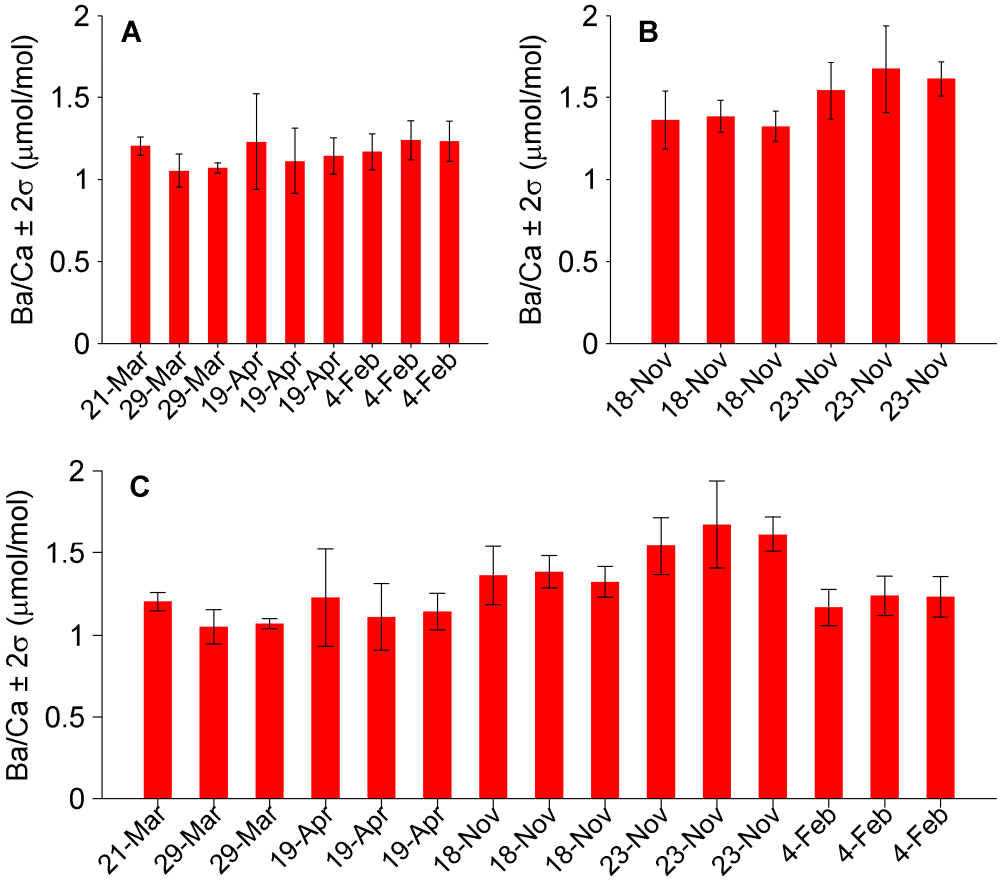

Figure 2.11. Long-term Ba/Ca measurements in consistency standards: A) runs where samples from sediment core BC387-2 were measured; B) runs where samples from sediment cores GC528 and 642 were measured; and C) measurements from all runs. Details of sediment core BC387-2 are provided in Section 3.3.1 'Sediment collection and oceanographic setting' and details of sediment cores GC528 and GC642 are provided in Section 4.3.1 'Sediment collection and oceanographic setting'. The dates shown are all in the year 2015, except for 4th February which is in the year 2016. Each date represents one run. Long-term precision, calculated by averaging each run and then calculating the standard deviation across these averages, is provided in Table 2.6.

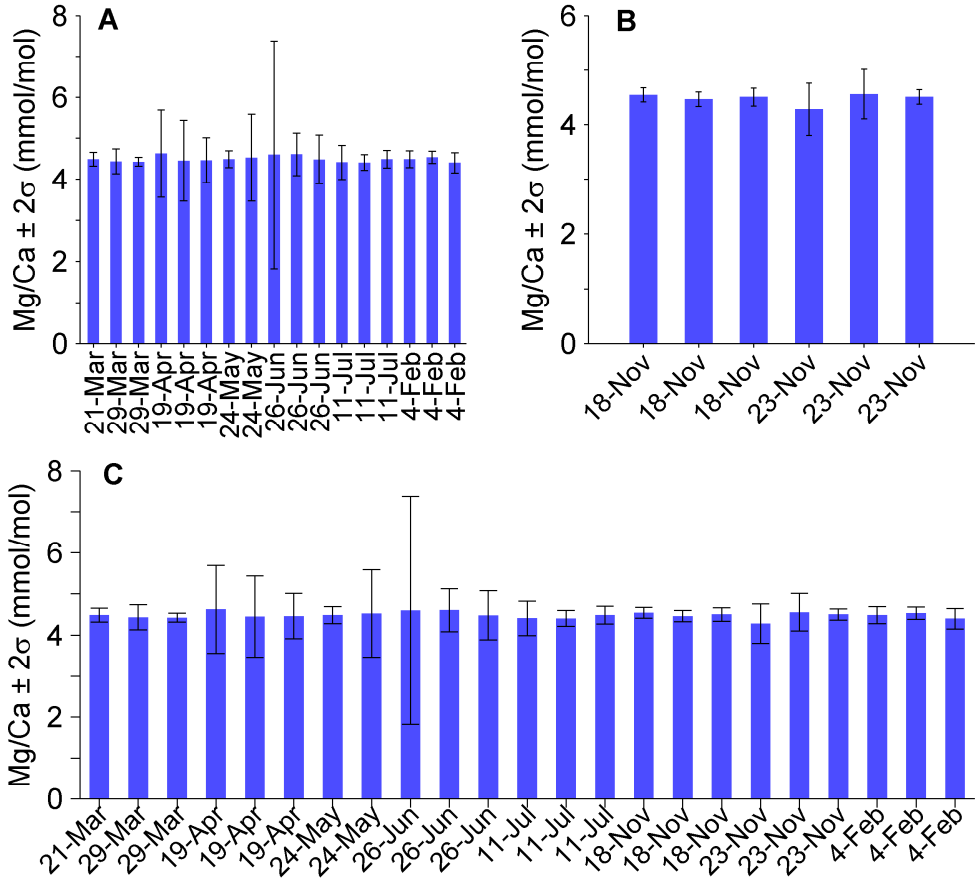

Figure 2.12. Long-term Mg/Ca measurements in consistency standards: A) runs where samples from sediment core BC387-2 were measured; B) runs where samples from sediment cores GC528 and 642 were measured; and C) measurements from all runs. Details of sediment core BC387-2 are provided in Section 3.3.1 'Sediment collection and oceanographic setting' and details of sediment cores GC528 and GC642 are provided in Section 4.3.1 'Sediment collection and oceanographic setting'. The dates shown are all in the year 2015, except for 4th February which is in the year 2016. Each date represents one run. Long-term precision, calculated by averaging each run and then calculating the standard deviation across these averages, is provided in Table 2.6.

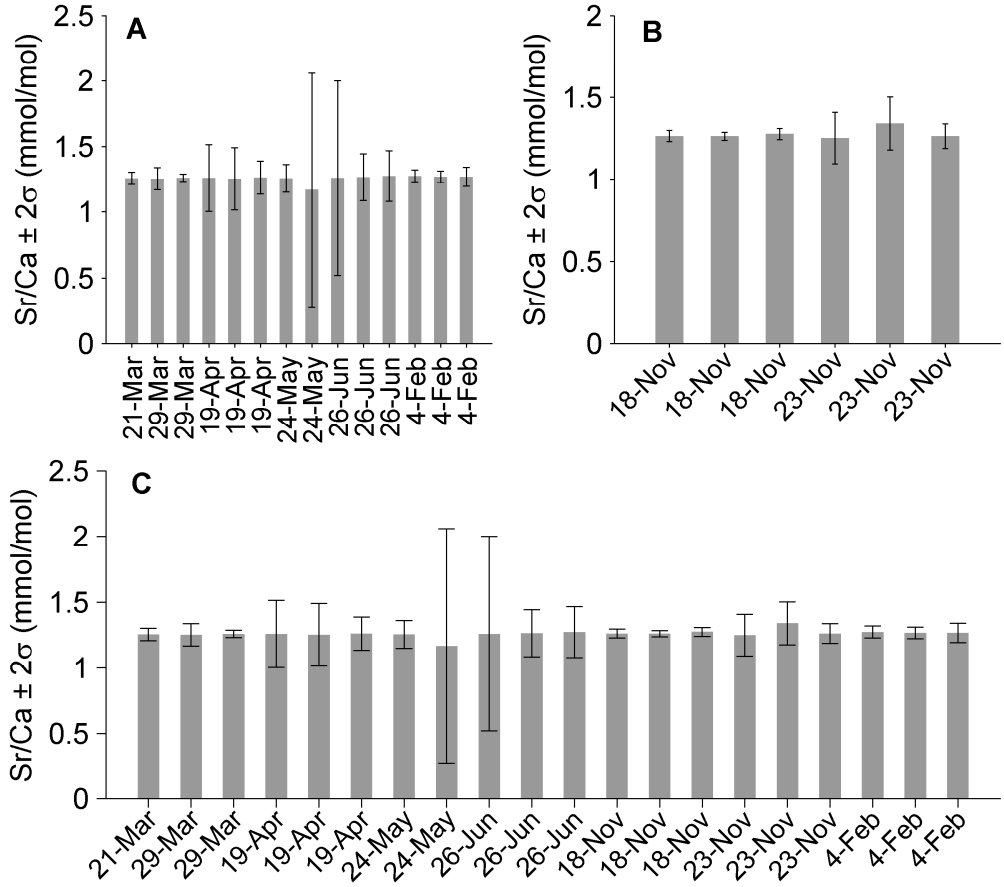

Figure 2.13. Long-term Sr/Ca measurements in consistency standards: A) runs where samples from sediment core BC387-2 were measured; B) runs where samples from sediment cores GC528 and 642 were measured; and C) measurements from all runs. Details of sediment core BC387-2 are provided in Section 3.3.1 'Sediment collection and oceanographic setting' and details of sediment cores GC528 and GC642 are provided in Section 4.3.1 'Sediment collection and oceanographic setting'. The dates shown are all in the year 2015, except for 4th February which is in the year 2016. Each date represents one run. Long-term precision, calculated by averaging each run and then calculating the standard deviation across these averages, is provided in Table 2.6.

Table 2.6. Long-term precision.

Ratio	Sediment core measured during runs	σ	μ	n
Ba/Ca	All	0.19	1.27	6
	BC387-2	0.07	1.16	4
	GC528 and GC642	0.18	1.48	2
Mg/Ca	All	0.04	4.48	9
	BC387-2	0.05	4.49	7
	GC528 and GC642	0.04	4.48	2
Sr/Ca	All	0.02	1.26	8
	BC387-2	0.02	1.25	6
	GC528 and GC642	0.01	1.28	2

σ = long-term precision, μ = mean, n = number of samples used in calculation.

σ and μ are in units of μmol/mol for Ba/Ca and mmol/mol for Mg/Ca and Sr/Ca.

Data were averaged per run before calculating these values. Un-averaged data are shown in Figure 2.9, Figure 2.10, Figure 2.11, Figure 2.12 and Figure 2.13.

Details of sediment core BC387-2 are provided in Section 3.3.1 'Sediment collection and oceanographic setting' and details of sediment cores GC528 and GC642 are provided in Section 4.3.1 'Sediment collection and oceanographic setting'.

2.4.4 Counting statistics

The uncertainty from counting statistics shows the maximum possible precision achievable given the count rate of the detector. The uncertainty of the count rate is as shown:

$$\mathrm{I} \pm \text{absolute uncertainty} = \mathrm{I} \pm \frac{\sqrt{\mathrm{I}}}{\sqrt{\mathrm{t}}} = \mathrm{I} \pm \left(\mathrm{I} \times \sqrt{\frac{1}{\mathrm{It}}} \right) \qquad (2.22)$$

$$\mathrm{I} \pm \text{relative uncertainty} = \mathrm{I} \pm \frac{1}{\sqrt{It}} = \mathrm{I} \pm \frac{1}{\sqrt{\text{counts per second}}} \qquad (2.23)$$

Where I is count rate, t is time in seconds and count rate multiplied by time = counts per second. The maximum possible counts per second detected was 10^7 cps; this would contribute a relative uncertainty of approximately 3.1 x 10^{-2} % to the overall uncertainty. The minimum counts detected was approximately 50,000 cps (typical cps at the top of the ^{138}Ba peak when instrumental sensitivity was relatively low); this would contribute approximately 4.5 x 10^{-1} % to the overall relative uncertainty. Given that typically the internal precision of a ratio is 1 – 5 %, counting uncertainty is only a minor contribution to the overall uncertainty.

2.4.5 Full replicates

Full replicates of samples are repeat measurements from the same sediment horizon using different batches of foraminifera of the same size fraction and species. In Chapters 3 to 5, wherever repeat measurements are plotted these are full replicates.

2.4.6 Interlaboratory comparison

Interlaboratory comparisons were made between: the Bristol Isotope Group in the School of Earth Sciences, University of Bristol and the School of Earth and Ocean Sciences, Cardiff University (BRIS and CARD); and between the Bristol Isotope Group in the School of Earth Sciences, University of Bristol and the WHOI Plasma Facility and Department of Marine Chemistry and Geochemistry, Woods Hole Oceanographic Institution (BRIS and WHOI). Interlaboratory precision was calculated as the standard deviation of full replicates of foraminifera samples measured at these different institutions: *Orbulina universa* from size fraction 355 – 425 μm for the BRIS-WHOI comparison; and *Oridorsalis umbonatus* from size fraction 250 – 355 μm for the BRIS-CARD comparisons. The *O. universa* foraminifera were picked from sediment sample S0157 and the *O. umbonatus* foraminifera were picked from sediment core BC387-2. Collection details and locations of these samples are provided in Section 5.3.1 'Sample collection' and Section 3.3.1 'Sediment collection and oceanographic setting', respectively. All foraminifer samples were cleaned using the procedures described in Section 2.2 'Foraminiferal cleaning procedure' prior to measurement. Samples measured at BRIS and WHOI were cleaned at the School of Earth Sciences, University of Bristol and CARD samples were cleaned at the School of Earth and Ocean Sciences, Cardiff University using an identical cleaning procedure. A summary of techniques and instruments used to collect data and calculate uncertainties at the different institutions is presented in Table 2.7. Mg/Ca and Sr/Ca were not measured at WHOI, so only Ba/Ca is compared. The measured data are displayed in Figure 2.14. All measurements agree within ± 2σ (uncertainties propagated from internal precision in the case of BRIS and CARD data and representative uncertainty for the WHOI data; Table 2.7). The interlaboratory precision is 0.02 μmol/mol for Ba/Ca (both BRIS-WHOI and BRIS-CARD), 0.03 mmol/mol for Mg/Ca and 0.01 mmol/mol for Sr/Ca.

Table 2.7. Instruments and techniques used to measure Ba/Ca ratios at three institutions.

	BRIS	CARD	WHOI
Instrument	Thermo Finnigan Element 2 HR-ICP-MS	Thermo Scientific Element XR HR-ICP-MS	Thermo Neptune MC-ICP-MS
Measurement technique	As described in Section 2.3 'Measurement by mass spectrometry'	Similar to BRIS, using Cardiff's in-house bracketing standard and method file. Calculation of trace metal ratios identical to BRIS	Ba content determined by double-spiking method of Horner et al. 2015 and ratioed to Ca using total weight of foraminifer sample [b]
Uncertainty calculation	As described in Section 2.3.6 'Calculation of trace metal ratios'	Identical to BRIS except without uncertainties on bracketing standard composition [a]	No error bar is shown because the internal precision resulting from this technique was sufficiently small as to be negligible (Dr T. Horner, pers. com. 2015) [b]

BRIS = Bristol Isotope Group in the School of Earth Sciences, University of Bristol; CARD = School of Earth and Ocean Sciences, Cardiff University; WHOI = WHOI Plasma Facility and Department of Marine Chemistry and Geochemistry, Woods Hole Oceanographic Institution. a) These are negligible compared to other contributors to the overall error. b) A detailed description of this method is provided in Section 5.3.3 'Foraminifer methods'.

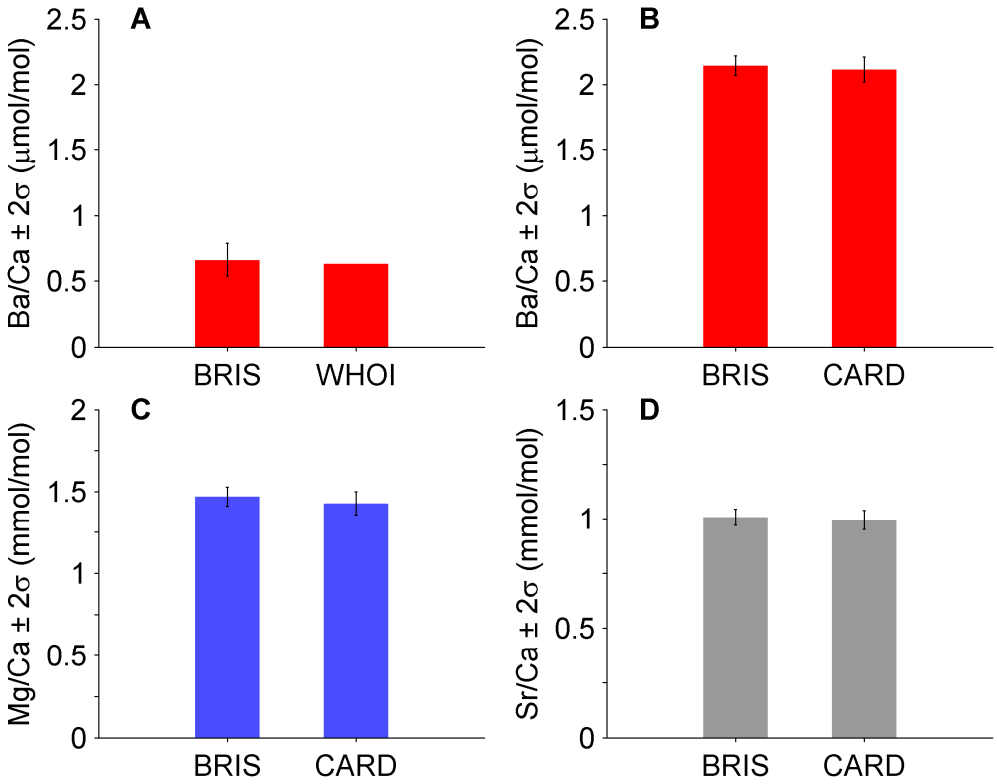

Figure 2.14. Interlaboratory comparisons of foraminiferal trace metal ratios: A) Ba/Ca (*Orbulina universa*); B) Ba/Ca; C) Mg/Ca and D) Sr/Ca (B – D: *Oridorsalis umbonatus*). 'BRIS' = the Bristol Isotope Group in the School of Earth Sciences, University of Bristol, 'CARD' = the School of Earth and Ocean Sciences, Cardiff University and 'WHOI' = the Department of Marine Chemistry and Geochemistry, Woods Hole Oceanographic Institution. No error bar is shown for the WHOI Ba/Ca ratio (A) because the internal precision resulting from this technique was sufficiently small as to be negligible (Dr T. Horner, pers. com. 2015).

2.5 Conclusions

In this chapter the full method for cleaning foraminifer samples prior to the measurement of trace metal ratios has been described, which builds upon the cleaning procedure of the School of Earth and Ocean Sciences, Cardiff University by including a barite-removal step using DTPA (Lea & Boyle 1993). Also described are the mass spectrometry methods used to measure trace metal ratios during this project, along with some of the challenges associated with these methods. Elsewhere in this thesis, where trace metal data are presented their methods sections will refer back to this chapter. Lastly, the measures taken to ensure data quality during this project have been described. These measures minimise the risk of contamination by clays or metal oxides and ensure that matrix effects are limited. It has also been demonstrated that despite the challenges encountered during sample measurement, short- and long-term precisions are acceptable across this study and the measurement techniques compare well with those of other institutions. Overall, these measures give confidence in the trace metal data which are presented and interpreted in this thesis.

Chapter 3

Evaluating the Ba/Ca Proxy

3.1 Abstract

Benthic foraminiferal Ba/Ca ratios have been used as a proxy for seawater barium concentration and alkalinity, but this proxy may be compromised by factors such as post-depositional dissolution of foraminifera, local perturbations in barium cycling, differences in barium uptake between species and contamination by marine barite. In this chapter, these potential caveats are investigated using box core sediments from the southwest Atlantic Ocean. Foraminiferal Sr/Ca ratios and XRF data indicate that post-depositional dissolution is not prevalent in the sediment core studied here, so the impact of dissolution on foraminiferal Ba/Ca cannot be considered. However, stable isotope data in combination with foraminiferal Ba/Ca suggest that Ba/Ca ratios remain constant in this core despite down-core fluctuations in productivity. This suggests that the Ba/Ca proxy remains robust despite local variability in barium cycling. In addition, new barium partition coefficients are calculated for three species of benthic foraminifera: *Melonis barleeanus*, *Oridorsalis umbonatus* and *Uvigerina peregrina*. A simple modelling study shows that these values are highly sensitive to the barium concentration used in their calculation and that this effect is greater for higher foraminiferal Ba/Ca values. In addition, scanning electron microscopy and cleaning studies are used to investigate barite contamination and its removal. Whilst the impact of cleaning barite from foraminifera on their Ba/Ca ratios is variable, as found by previous authors, scanning electron microscopy suggests that the barite cleaning technique is effective at removing barite. Overall, these findings lend confidence to the use of Ba/Ca as a proxy for seawater barium concentrations.

3.2 Introduction

Ba/Ca ratios in the calcium carbonate of benthic foraminifera have been used to reconstruct seawater barium concentrations and thus used as a proxy for ocean circulation and seawater alkalinity (Hall & Chan 2004b; Lea & Boyle 1990a; Lea & Boyle 1990b; Lea 1990; Lea 1993; Lea 1995). Further studies of the potential caveats of this proxy may contribute towards improving its accuracy in determining past oceanic conditions, thus improving its value as a palaeoclimatological tool. Questions have been raised about the appropriateness of this proxy in shelf environments where the relationship between barium and carbonate cycling may be different to that of the global ocean on average (Rubin et al. 2003). It is also necessary to ascertain whether each species of foraminifer records bottom water [Ba] or porewater [Ba] and to accurately determine the uptake rate of barium into foraminiferal calcium carbonate for each species. Studies of post-depositional effects on Ba/Ca ratios would also be beneficial, including the effect of dissolution on foraminiferal Ba/Ca and the impact of contamination by marine barite. In this chapter, these potential caveats are investigated using three species of benthic foraminifera (*Melonis barleeanus*, *Oridorsalis umbonatus* and *Uvigerina peregrina*) in a sediment core from the southwest Atlantic, as a contribution towards evaluating the use of Ba/Ca as a proxy for seawater [Ba] and alkalinity.

3.3 Methods

3.3.1 Sediment collection and oceanographic setting

Box core BC387 was collected during cruise JR112 of the RRS *James Clark Ross* on 13th December 2004 (Prof R. Rickaby, pers. com. 2013). The box corer was deployed opportunistically during a detour from the expected route caused by sea ice (Brandon 2005). BC387 was collected from a water depth of 586 m at 53º9.0'S, 58º39.0'W, near the Falkland Islands in the South Atlantic Ocean (Figure 3.1). Upon recovery of the box core, five sub-cores were taken from it using piston core tube linings trimmed to 75 cm, of which BC387 sub-core 2 (hereafter referred to as BC387-2) was one (Prof R. Rickaby, pers. com. 2013). BC387-2 comprised approximately 26 cm of sediment. Subsequent to the cruise it was stored intact at 4 ºC in the Oast House repository of the University of Cambridge.

The collection site of BC387-2 is located close to Burdwood Bank, a highly-productive region (Schejter et al. 2016). Typical seafloor temperatures are 4 – 5 ºC (Schejter et al. 2016). This site is to the north of the Antarctic Circumpolar Current (ACC), in the Subantarctic Zone (Brown et al. 2004). A branch of the ACC known as the Falklands Current or Malvinas Current flows northwards over the sample site, following the contours of the continental shelf (Piola & Gordon 1989; Peterson 1992; Piola & Matano 2009; Piola et al. 2010; Piola et al. 2013). The influence of this current extends to approximately 2000 m (Peterson 1992), hence the sample site (which is at 585.59 m water depth) is bathed in waters of similar properties to those of the upper ACC (Peterson 1992), namely Antarctic Surface Water (ASW) (Brown et al. 2004). ASW derives from the freshening of upwelled North Atlantic Deep Water via precipitation and the addition of meltwater (Brown et al. 2004).

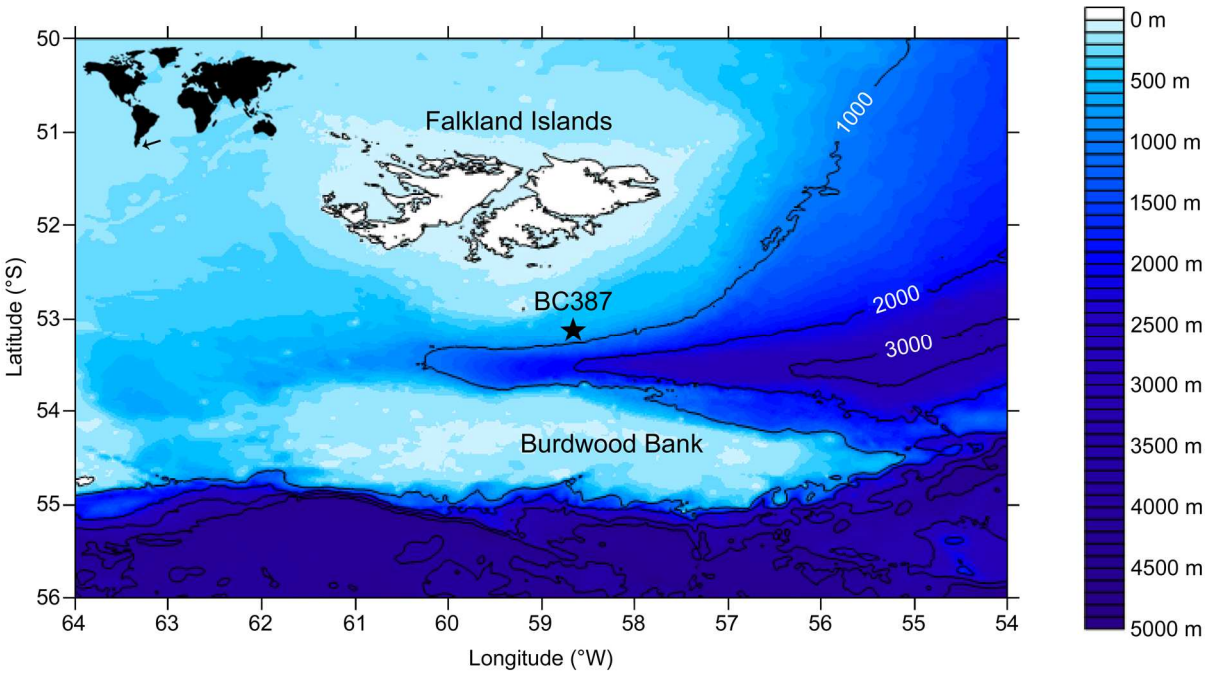

Figure 3.1. Location of box core BC387.

3.3.2 Foraminifer picking

Sediment core BC387-2 was extruded into 1 cm slices with the assistance of the Sedimentary Laboratory at the Godwin Laboratory for Palaeoclimate Research, University of Cambridge. At the School of Earth and Ocean Sciences, Cardiff University, a portion of each of the 1 cm sediment slices was separated into coarse (> 63 µm) and fine (< 63 µm) grain-size fractions by wet sieving and gravity settling, then oven-dried at 45 ºC for several days until completely dry. Foraminifera were picked from sieved grain-size fractions using a wetted brush (reverse-osmosis purified (RO) water was used) under an optical microscope.

Three species were picked: *Melonis barleeanus*, *Oridorsalis umbonatus* and *Uvigerina peregrina*. These species were chosen because they are all benthic, and hence appropriate for investigating the Ba/Ca proxy for seawater [Ba] and alkalinity which relies on benthic foraminifera, yet have differing morphologies and habitats. *M. barleeanus* is planispiral and lives entirely infaunally at 1 – 6 cm below the sediment-water interface (Corliss 1985; Corliss 1991; Buzas et al. 1993), whereas *O. umbonatus* is trochospiral and lives at 0 – 4 cm (Rathburn & Corliss 1994) and *U. peregrina* is triserial can live at 0 – 10 cm (Loubere & Gary 1990; Corliss 1991; Buzas et al. 1993) although it is most abundant at depths 0.5 – 1 cm (Tachikawa & Elderfield 2002). These microhabitats should be considered susceptible to change rather than immutable (e.g. Buzas et al. 1993) because infaunal benthic foraminifera may migrate to different depths depending on where the most favourable conditions for growth are found (Tachikawa & Elderfield 2002). Several morphotypes of *U. peregrina* were present, but despite these morphological variations *U. peregrina* is genetically a single species (Schweizer et al. 2005; Schweizer 2006) and therefore random selections of individuals of all morphotypes were

measured, rather than separating them by morphotype prior to measurement. A further consideration was that these three species were all available in sufficient quantities for analysis in size fraction 250 – 355 µm, which is more convenient for picking than smaller size fractions. Although epifaunal species would have been preferable for reconstructing bottom water properties, these were not available in sufficient quantities for analysis.

3.3.3 Trace metals

Ba/Ca, Mg/Ca and Sr/Ca ratios were measured at sediment depths between 0 and 24 or 25 cm for each of the three species (*M. barleeanus*, *O. umbonatus* and *U. peregrina*), using the methods detailed in Chapter 2 'Trace Metal Methods'. These methods comprised: a cleaning procedure to remove clays, metal oxides, organic matter and barite from foraminifer samples; measurement of isotope intensities via inductively coupled plasma mass spectrometry using a Thermo Finnigan Element 2; offline calculation of trace metal ratios; and conversion to units of concentration via measurements of a custom-made bracketing standard. All replicates shown are full replicates (a completely separate set of foraminifera). In addition, some samples were cleaned with the barite removal step omitted, facilitating the comparison of DTPA-cleaned with non-DTPA-cleaned foraminifera.

3.3.4 Temperatures

Mg/Ca ratios were used to calculate temperature estimates. Several calibrations exist for converting *U. peregrina* and *Uvigerina* spp. Mg/Ca ratios into temperatures (Elderfield et al. 2010). The most applicable calibrations for *U. peregrina* at the BC387-2 site are those which encompass the temperature range of bottom waters at this site (approximately 4 – 5 ºC (Schejter et al. 2016)) and which used reductive cleaning prior to measurement. These are Equation 3.1 (Bryan & Marchitto 2008) and Equation 3.2 (Elderfield et al. 2006):

$$\frac{\mathrm{Mg}}{\mathrm{Ca}} = 0.86 \pm 0.04 + (0.071 \pm 0.005 \times \mathrm{T}) \qquad (3.1)$$

$$\frac{\mathrm{Mg}}{\mathrm{Ca}} = 0.91 \pm 0.06 + (0.065 \pm 0.011 \times \mathrm{T}) \qquad (3.2)$$

Melonis barleeanus Mg/Ca ratios can be converted into temperatures using the calibration of Kristjánsdóttir et al. 2007 (Equation 3.3):

$$\frac{\mathrm{Mg}}{\mathrm{Ca}} = 0.658 \pm 0.07 \times \mathrm{e}^{0.137 \pm 0.020 \times \mathrm{T}} \qquad (3.3)$$

Mg/Ca ratios from *Oridorsalis umbonatus* may be converted into temperatures using the following equations of Lear et al. 2015 (Equation 3.4 and Equation 3.5), assuming a modern seawater Mg/Ca value of 5.2 mol/mol (Dickson 2002; Horita et al. 2002; Coggon et al. 2010):

$$\frac{\mathrm{Mg}}{\mathrm{Ca}} = 0.66 \pm 0.08 \times 5.2^{0.27 \pm 0.06} \times \mathrm{e}^{0.114 \pm 0.02 \times \mathrm{T}} \qquad (3.4)$$

$$\frac{\mathrm{Mg}}{\mathrm{Ca}} = 1.21 \pm 0.04 + (0.12 \pm 0.004 \times \mathrm{T} \times 5.2^{-0.003 \pm 0.02}) \qquad (3.5)$$

3.3.5 Oxygen and carbon isotope ratios

Approximately 50 – 60 µg of foraminifera per measurement were crushed between two RO water cleaned glass slides under an optical microscope and then placed in acid-cleaned 500 µl microcentrifuge vials. Foraminifer fragments were then ultrasonicated for 5 minutes in approximately 400 – 500 µl methanol and rinsed twice with Milli-Q water. Sample vials were left open under a clean protective guard in a clean fume hood area to dry down completely before measurement. $\delta^{18}O$ and $\delta^{13}C$ were measured at the School of Earth and Ocean Sciences, Cardiff University using a Thermo Scientific Kiel IV Carbonate Device with Thermo Scientific MAT 253 isotope ratio mass spectrometer. This instrument has a long-term precision of $\sigma = 0.050$ ‰ for $\delta^{18}O$ and $\sigma = 0.022$ ‰ for $\delta^{13}C$ ($n = 202$) using a Carrara marble standard (Dr S. Nederbragt, pers. com. 2015). All isotope ratios were calculated relative to Vienna Pee Dee Belemnite (VPDB).

3.3.6 Scanning electron microscopy and energy-dispersive x-ray spectroscopy

SEM micrographs of foraminifera (*M. barleeanus*, *O. umbonatus* and *U. peregrina*) were taken at the British Ocean Sediment Core Research Facility in the National Oceanography Centre, University of Southampton using a Hitachi TM1000 Tabletop Microscope. This microscope does not require samples to be coated. Samples were mounted on specimen stubs by attaching them to carbon adhesive discs (Leit tabs) using a wetted brush. SEM micrographs were taken of uncrushed foraminifera that were: a) uncleaned; b) cleaned but without performing the barite removal step; and c) fully cleaned using the procedure detailed in Section 2.2 'Foraminiferal cleaning procedure'. EDS spectra were collected using the aforementioned Hitachi TM1000 Tabletop Microscope with Hitachi SwiftED-TM attachment. Spectra were measured on cross-hair targeted areas of uncleaned *M. barleeanus* and *O. umbonatus*, using a 240 s acquisition time. Surfaces of barite-like particles were targeted in addition to the calcium carbonate surfaces of the foraminifera. Several repeat measurements were acquired per site to ensure that spectra were reproducible. SEM images were taken of the areas targeted by EDS, showing the exact placement of the cross-hairs.

3.3.7 X-ray fluorescence

At the Sedimentary Laboratory in the Godwin Laboratory for Palaeoclimate Research, University of Cambridge, subsamples of each of the 1 cm slices of BC387-2 were assembled into a U-channel and bulk elemental composition measured by x-ray fluorescence using an Avaatech XRF Core Scanner. The XRF scanner also obtained colour data and an image. Colour data were used to crop the dataset to the sediment area (Figure 3.2). Care was taken to crop edge effects out of the data. XRF scanner positions were linearly converted into sediment depths, using the assumption that the U-channel was perfectly assembled into 1 cm horizons. The XRF data were collected at 0.25 cm resolution, however because 1 cm sediment slices were assembled onto the U-channel prior to scanning the true

resolution is 1 cm. The data were therefore averaged into 1 cm horizons, treating the data as repeat measurements per 1 cm. The elements measured at each energy level (10, 30 and 50 kV) are displayed in Figure 3.3. When an element was measured at multiple energies, the data with higher counts were used. This was 30 kV in all cases (Fe, Cu, Br, Rb, Sr, Zr and Pb). Silver measurements were discarded due to the presence of silver in the detector of the XRF scanner. Overall, these selection criteria precipitate the suite of elements displayed in Figure 3.4. XRF ratios were calculated by dividing pre-averaged elemental data.

3.3.8 Gamma-ray spectroscopy

Portions of un-sieved bulk sediment from every other 1 cm sediment horizon between 0 and 11 cm, horizon 14 – 15 cm and horizon 24 – 25 cm were oven-dried at 45 ºC and then gently disaggregated using an agate pestle and mortar at the School of Earth and Ocean sciences, Cardiff University. ^{210}Pb, ^{214}Pb, ^{7}Be and ^{137}Cs activities in the sediments were measured using a Canberra well-type ultra-low background high-purity germanium gamma ray spectrometer (Prof A. Cundy, pers. com. 2013) at the School of Environment and Technology, University of Brighton. Spectra were accumulated and analysed using a 16K channel integrated multichannel analyser and the Genie 2000 system, using a count time of 150,000 seconds (Prof A. Cundy, pers. com. 2013). The detection limits for ^{210}Pb and ^{137}Cs were typically approximately 15 and 5 Bq/kg, respectively (Prof A. Cundy, pers. com. 2013). The data were calibrated and checked using the radionuclide standard QCYK8163 held in bentonite clay and International Atomic Energy Agency reference material 135 (Prof A. Cundy, pers. com. 2013).

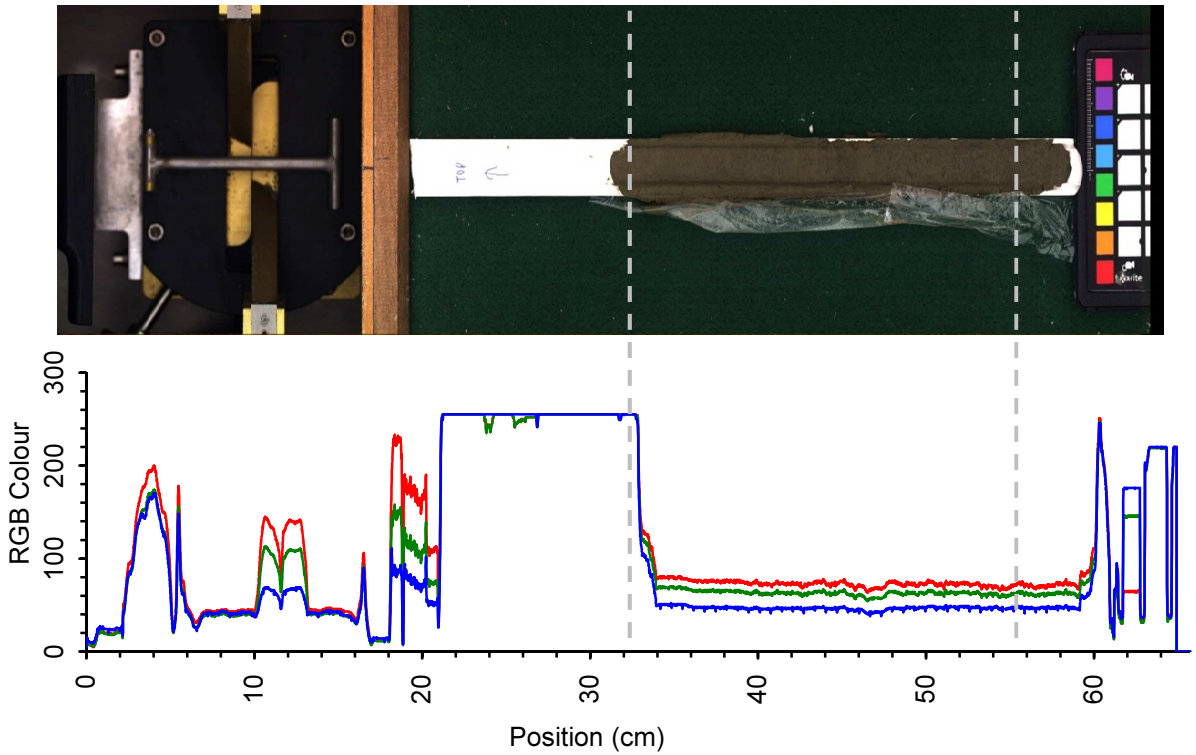

Figure 3.2. Image of sediment core BC387-2 and RGB colour data. The colour data were used to crop the XRF data to the sediment core region whilst removing edge effects from the data.

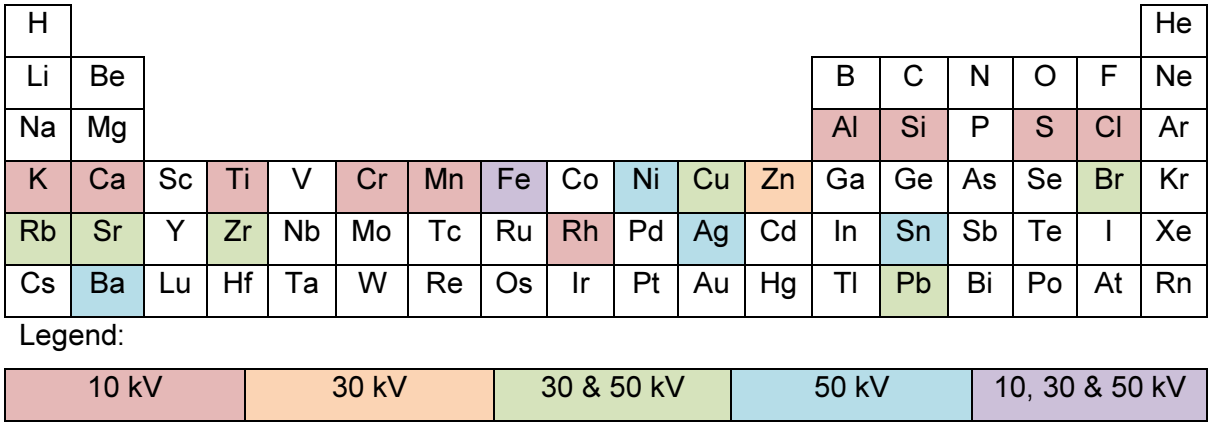

Figure 3.3. Truncated periodic table displaying the elements measured at each energy level by x-ray fluorescence.

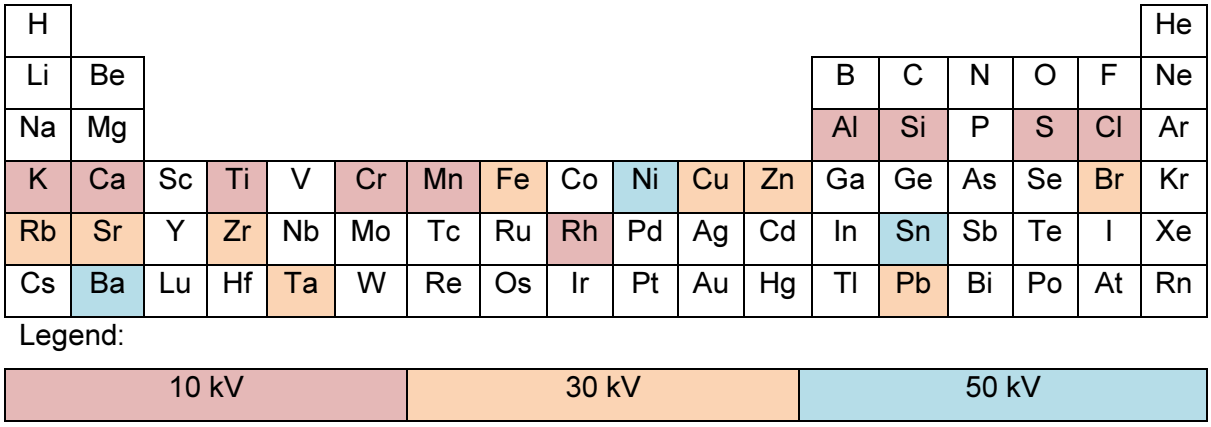

Figure 3.4. Truncated periodic table displaying the elements measured by x-ray fluorescence that may be used in analysis.

3.4 Results

3.4.1 Foraminifer results

Ba/Ca, Mg/Ca and Sr/Ca of fully-cleaned *O. umbonatus*, *M. barleeanus* and *U. peregrina* are presented in Figure 3.5 (A, B and C). Trace metal data of non-DTPA-cleaned foraminifera are plotted alongside their fully-cleaned equivalents in Figure 3.6. All plotted trace metal data satisfy the requirements stipulated in Section 2.4 'Quality assurance' which ensure that data are not adversely affected by matrix effects or contamination by clays and metal oxides. The long-term precision is σ = 0.19 µmol/mol for Ba/Ca, σ = 0.04 mmol/mol for Mg/Ca and σ = 0.02 mmol/mol for Sr/Ca (see Section 2.4.3 'Short- and long-term precision'). Mg/Ca-derived temperatures calculated using Equations 3.1 to 3.5 are displayed in Figure 3.5 (D). The Mg/Ca data used to calculate these temperatures are displayed in panel B of the same figure. $\delta^{18}O$ and $\delta^{13}C$ for each species (*O. umbonatus*, *M. barleeanus* and *U. peregrina)* are presented in Figure 3.5 (E and F).

3.4.2 X-ray fluorescence

The full suite of XRF data is provided in Appendix A. Selected XRF ratios (Fe/Al, Cu/Al and S/Al which correlate positively with diagenesis and Ca/Al, Si/Al and Ba/Al which correlate positively with productivity) are presented in Figure 3.5 (G).

3.4.3 Scanning electron microscopy and energy-dispersive x-ray spectroscopy

SEM micrographs are presented as composites containing images of the three species *O. umbonatus*, *M. barleeanus* and *U. peregrina.* Figure 3.7 shows uncleaned foraminifera and a more magnified view of these, whilst Figure 3.8 shows non-DTPA-cleaned foraminifera alongside fully-cleaned foraminifera.

Representative EDS spectra, along with SEM images showing the targeted sites, are presented for: a) the surface of a potential barite particle; and b) the shell surface of the *O. umbonatus* specimen that this barite-like particle was located upon (Figure 3.9). Repeat measurements were taken from the same position to ensure that the EDS spectra are representative; these are provided in Appendix B. Additional EDS spectra were collected from the same foraminifer, from a specimen of *M. barleeanus* and from several barite-like particles of similar size and appearance to the particle shown in Figure 3.9. These results agree closely with those presented in Figure 3.9 and are also included in Appendix B.

3.4.4 Gamma-ray spectroscopy

Measured ^{210}Pb and ^{214}Pb activities are displayed in Table 3.1. ^{7}Be and ^{137}Cs were below detection limits in all cases, the implications of which are discussed below.

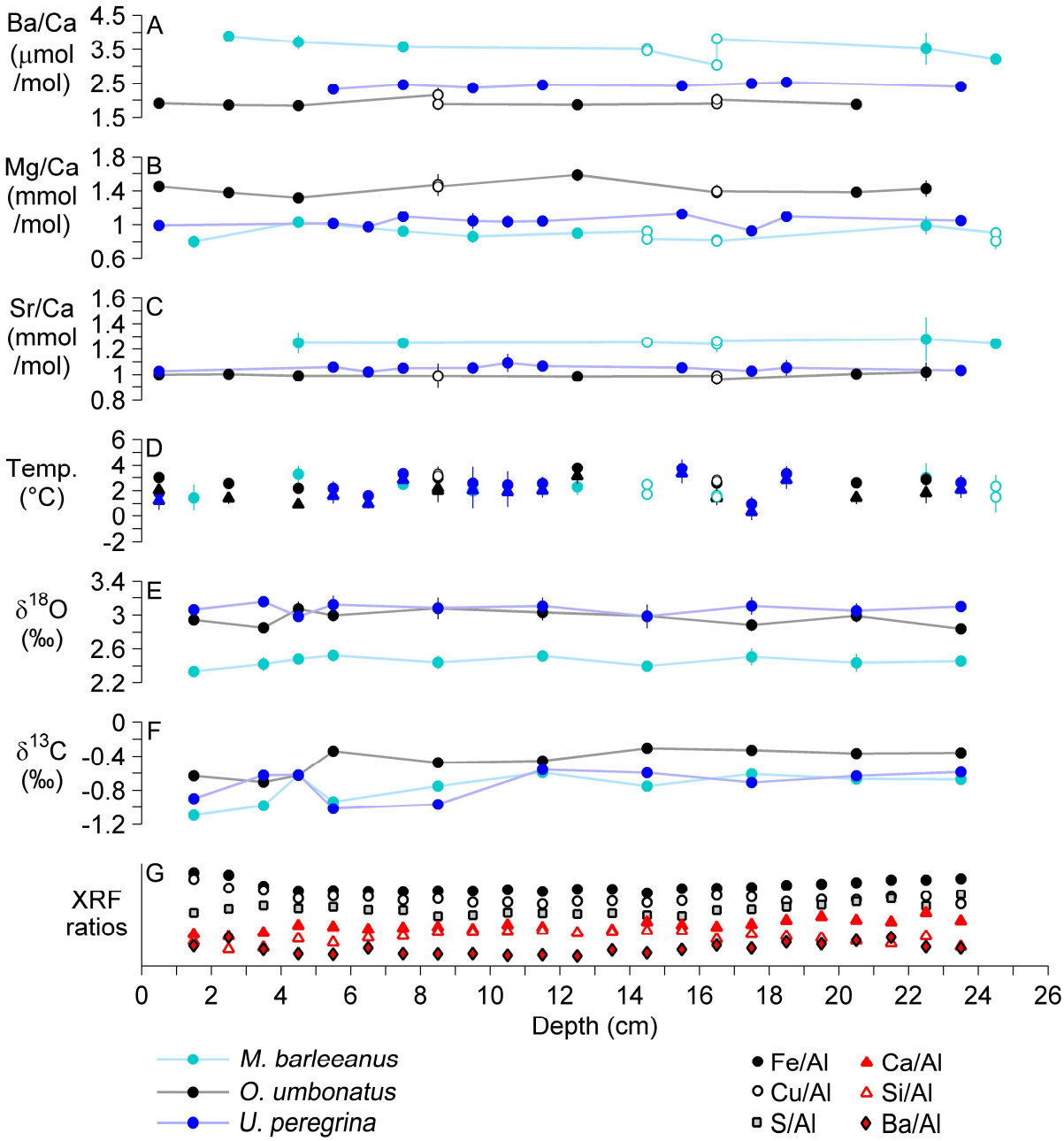

Figure 3.5. A) Ba/Ca; B) Mg/Ca; C) Sr/Ca; D) Mg/Ca-derived temperatures, using the temperature calibrations of Kristjánsdóttir et al. 2007 (*M. barleeanus*, light blue circles), Lear et al. 2015 (*O. umbonatus*, black circles for their exponential equation and black triangles for their linear equation), Bryan & Marchitto 2008 (*U. peregrina*, dark blue circles) and Elderfield et al. 2006 (*U. peregrina*, dark blue triangles); E) $\delta^{18}O$; F) $\delta^{13}C$; and G) XRF ratios. All data are from sediment core BC387-2. Vertical error bars are ± 2σ (internal precision). XRF ratios are normalised and offset for visual clarity. Open symbols (A to D) are full replicates.

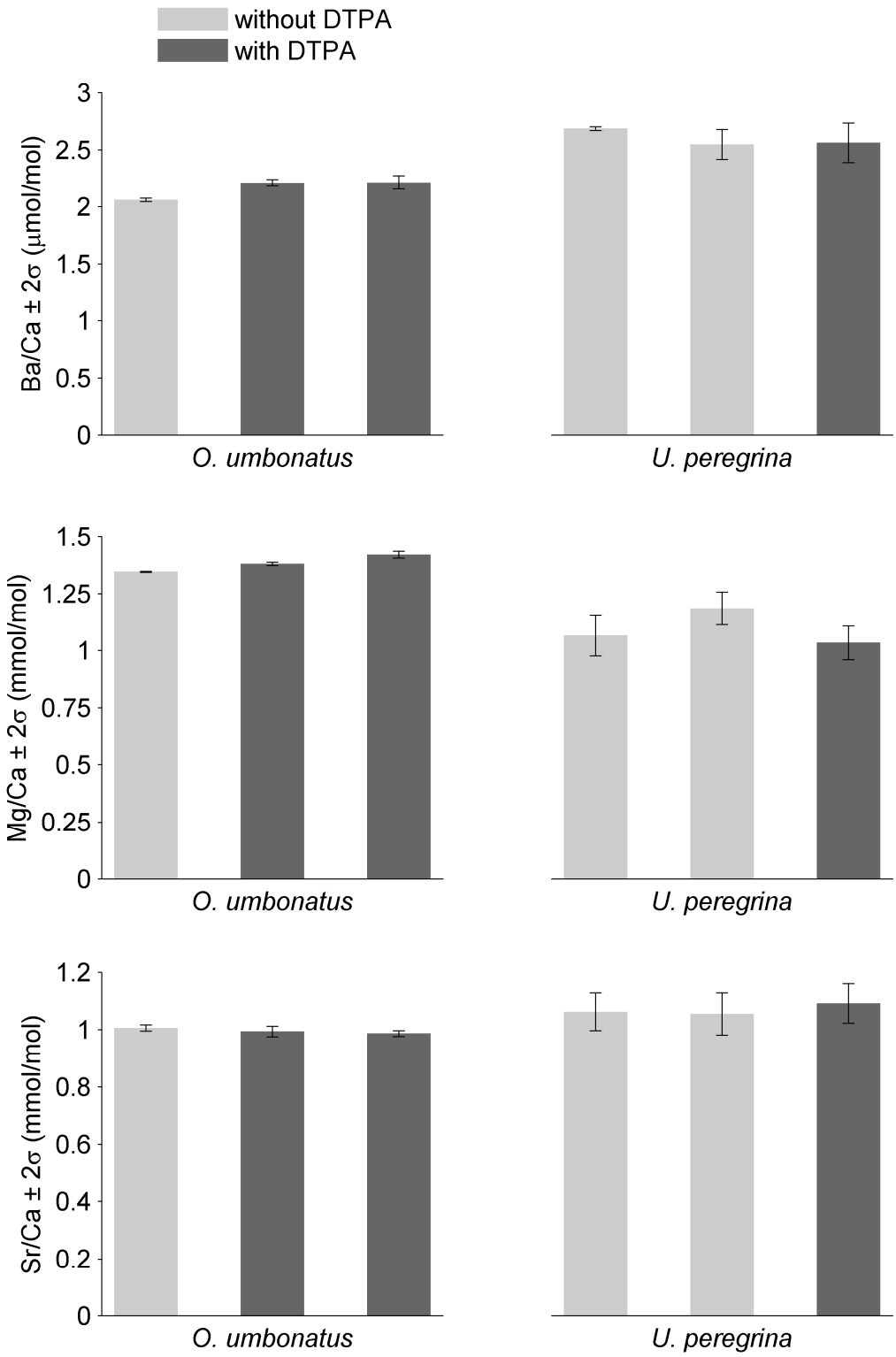

Figure 3.6. Ba/Ca, Mg/Ca and Sr/Ca of foraminifera cleaned: a) whilst omitting the DTPA step that removes barite ('without DTPA'); and b) using the full cleaning procedure ('with DTPA'). All repeat measurements shown here are full replicates.

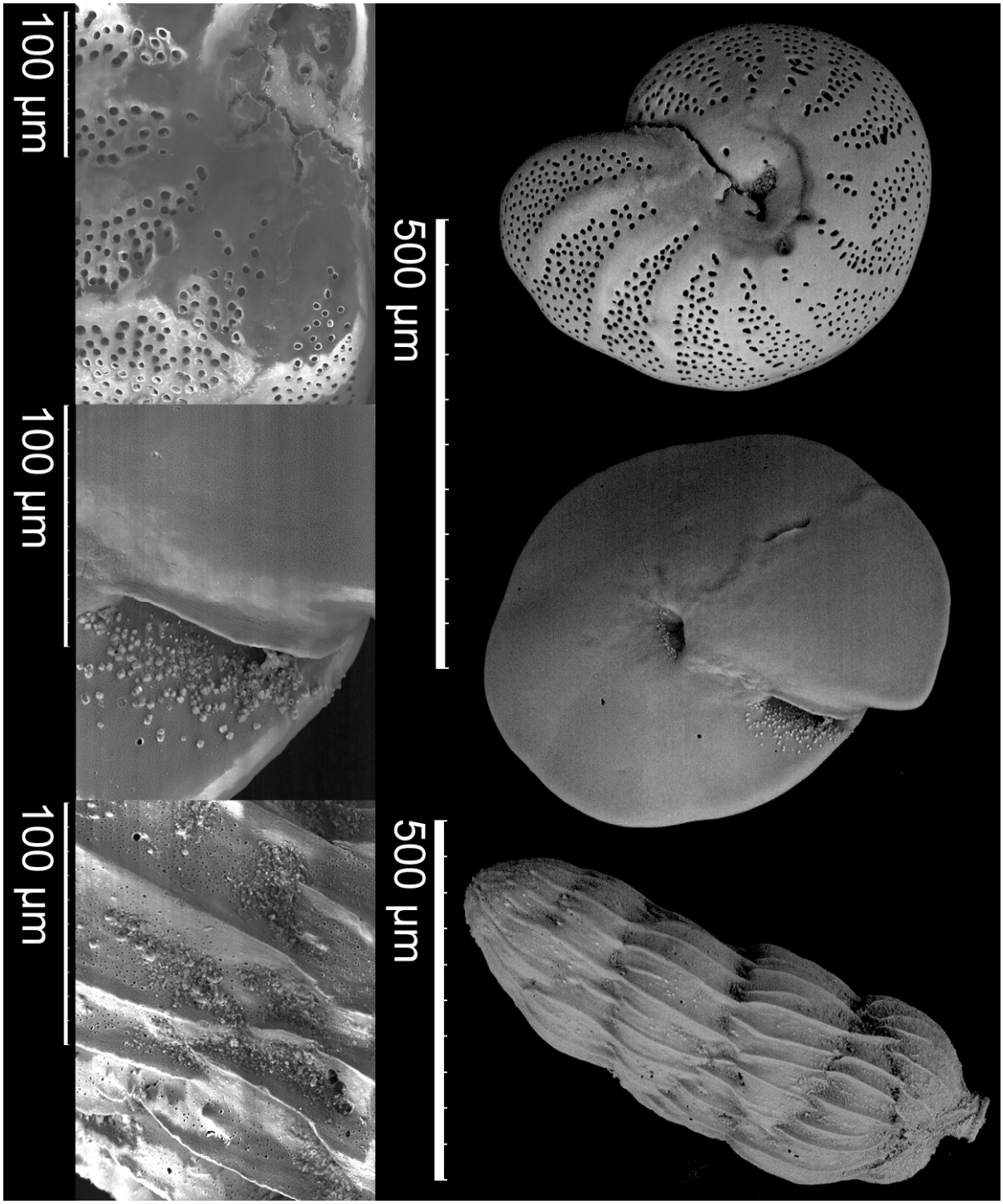

Figure 3.7. SEM images of uncleaned foraminifera. The species are (from top to bottom) *Melonis barleeanus*, *Oridorsalis umbonatus* and *Uvigerina peregrina*. The images on the left are higher-magnification images of the same species. Additional SEM images are provided in Appendix C.

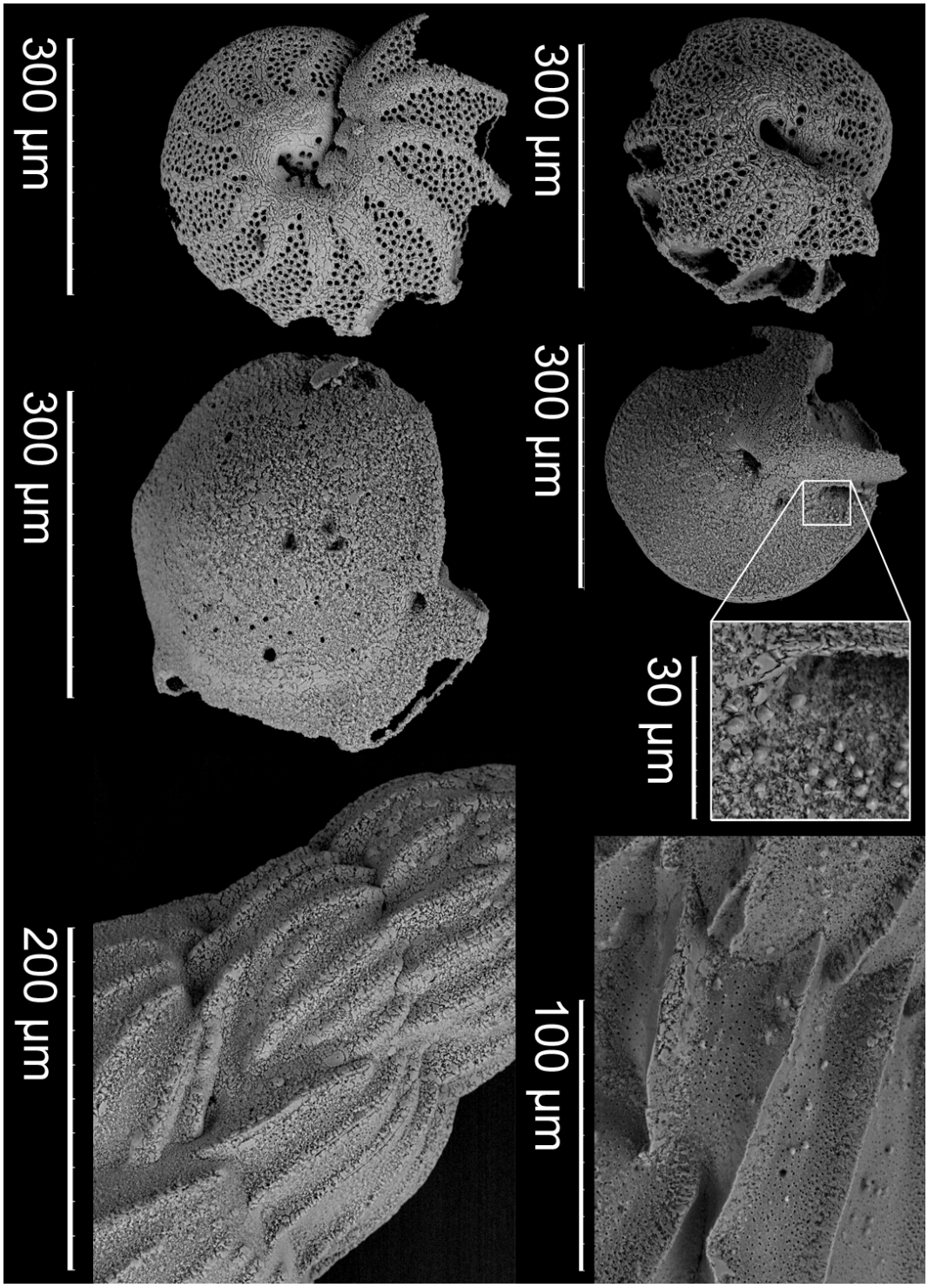

Figure 3.8. SEM images of foraminifera that have been cleaned: a) whilst omitting the DTPA step that removes barite (right); and b) using the full cleaning procedure (left). The species are (from top to bottom) *Melonis barleeanus*, *Oridorsalis umbonatus* and *Uvigerina peregrina*. Additional SEM images are provided in Appendix C.

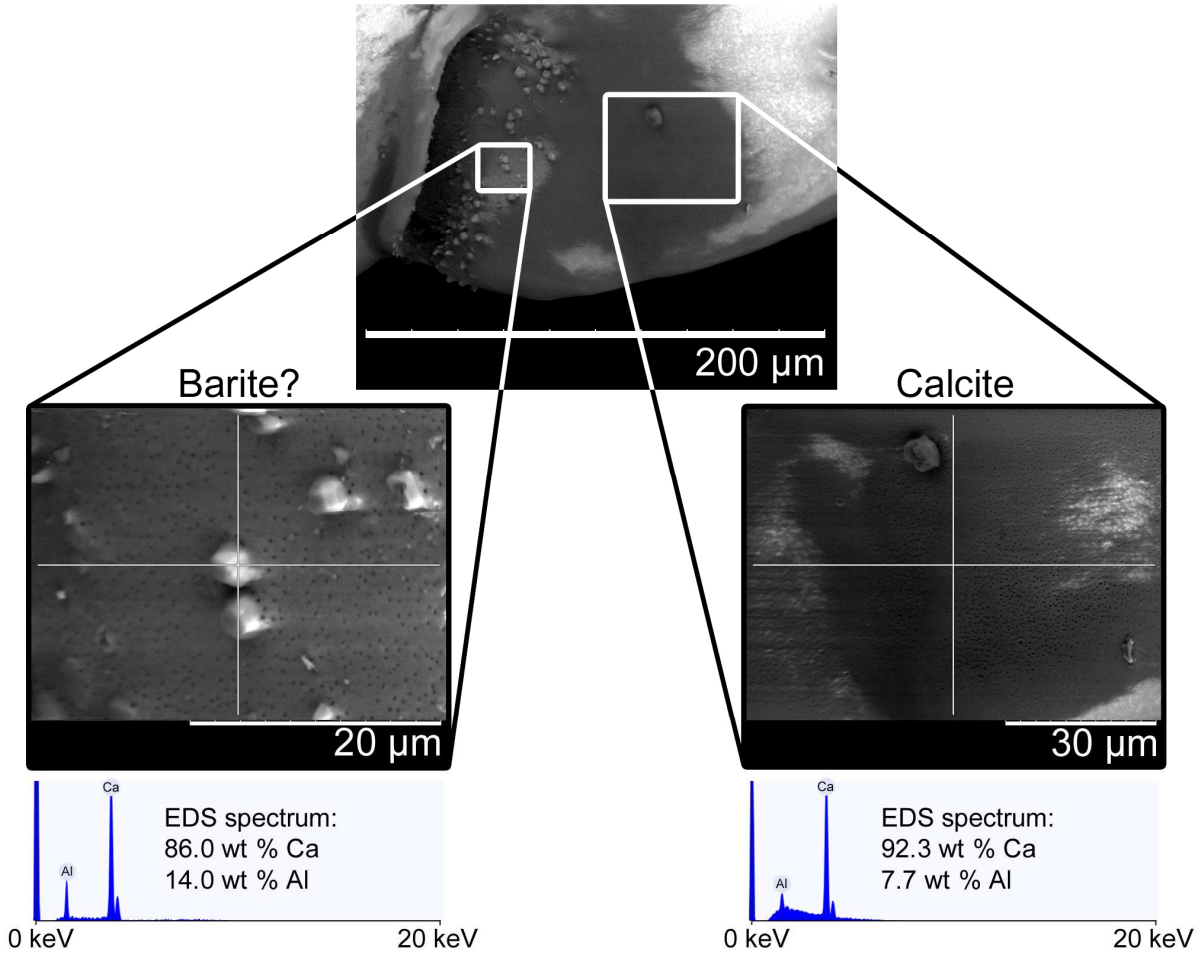

Figure 3.9. EDS spectra of a particle with the appearance of barite (left) and the calcium carbonate shell of the same *O. umbonatus* specimen (right), accompanied by SEM images showing the EDS-targeted locations (indicated by cross-hairs). wt % = weight %.

Table 3.1. Activities of radionuclides in sediment core BC387-2.

Depth (cm)	Sed. Weight (g)	^{210}Pb (Bq/kg)	^{214}Pb (Bq/kg)	^{137}Cs (Bq/kg)	^{7}Be (Bq/kg)
0 – 1	3.00	97 ± 12	27 ± 2.3	BDL	BDL
2 – 3	3.01	72 ± 8.6	24 ± 2.1	BDL	BDL
4 – 5	3.15	67 ± 6.4	29 ± 1.3	BDL	BDL
6 – 7	3.02	52 ± 4.1	34 ± 1.0	BDL	BDL
8 – 9	3.06	32 ± 3.0	32 ± 0.8	BDL	BDL
10 – 11	3.00	24 ± 2.6	34 ± 0.9	BDL	BDL
14 – 15	3.04	14 ± 2.6	28 ± 0.8	BDL	BDL
24 – 25	3.05	21 ± 2.7	31 ± 0.9	BDL	BDL

BDL = below detection limit. Sed. weight = weight of sediment used in measurement.

3.5 Discussion

3.5.1 BC387-2 age model

^{210}Pb and ^{214}Pb activities were used to create an age model for core BC387-2. ^{210}Pb is generated within the sediment by the decay of ^{226}Ra. When this 'supported' Pb is subtracted away from the total amount, this reveals the remaining 'unsupported' ^{210}Pb (also known as 'excess' ^{210}Pb) which must have been supplied by the water column via sedimentation. The accumulation of this excess ^{210}Pb can be used to estimate a sedimentation rate and thereby construct an age model for a sediment core, using the following equation to calculate age:

$$\text{age (years)} = \frac{\text{depth (cm)}}{\text{sedimentation rate } \left(\frac{\text{cm}}{\text{year}}\right)} \qquad (3.6)$$

The activity of supported ^{210}Pb in the sediment core was estimated by the average ^{210}Pb within the core region where ^{210}Pb has become roughly constant with depth. The three deepest values (at sediment horizons 10 – 11, 14 – 15 and 24 – 25 cm) were used, yielding an average ^{210}Pb of 20 ± 2.6 Bq/kg (Table 3.1). ^{214}Pb was used to verify this value. Because ^{214}Pb is also a daughter of ^{226}Ra, it should be present in sediment in the same amounts as supported ^{210}Pb. In reality ^{214}Pb provides only a rough estimate of what supported ^{210}Pb should be, because samples were not kept in air-tight conditions during analysis and so radioactive equilibrium is unlikely to have been preserved (Prof A. Cundy, pers. com. 2013). The ^{214}Pb activities are roughly similar to 20 Bq/kg, and therefore corroborate the above estimate of supported ^{210}Pb activity (Table 3.1).

Unsupported ^{210}Pb activity was calculated by first subtracting 20 Bq/kg (the activity of supported ^{210}Pb) from all ^{210}Pb values (Table 3.2). Next, the activities were adjusted to the time of sediment core collection, to account for the ongoing radioactive decay of ^{210}Pb in the sediment from the time of collection to the time of analysis (Table 3.2). To back-calculate the activity of ^{210}Pb in the sediment at the time of its collection, the following equation was used:

$$N(t) = N_0 e^{-\lambda t} \qquad (3.7)$$

Where N(t) = the quantity of ^{210}Pb remaining in the sediment, N_0 = the initial quantity of ^{210}Pb i.e. at the time of sediment collection, λ = the decay constant of ^{210}Pb and t = the time elapsed from collection to analysis. BC387-2 was collected 13th December 2004, and the ^{210}Pb measurements made during December 2013, therefore t = 9 years.

A sedimentation rate for BC387-2 is estimated using the model of Henderson et al. 1999, which takes into account the effect of bioturbation on sediments. The model is described by the following equation:

$$A = A_0 e^{\left(\frac{w-\sqrt{w^2+4D\lambda}}{2D}\right)z} \qquad (3.8)$$

Where A = unsupported ^{210}Pb, A_0 = unsupported ^{210}Pb at the sediment-water interface, w = sedimentation rate, D = mixing rate, λ = the decay constant of ^{210}Pb and z = depth from the sediment-water interface. In this model, mixing rate and sedimentation rate are varied to provide the best possible

fit of a theoretical curve ('A') to the ^{210}Pb data (using the time-adjusted excess ^{210}Pb, shown in Table 3.2). Mixing rate was varied between 0.01 and 400 in steps of 0.01 (units of cm^2/year). 400 cm^2/year was used as an estimate of an extreme upper limit for a mixing rate (Teal et al. 2008), an increment of 0.01 was used because this is the minimum step that can be used whilst maintaining two significant figures, and a lower threshold of 0.01 cm^2/year was used because a negative mixing rate is illogical and a value of zero is not possible in this model (mixing rate being within the denominator of a fraction), therefore 0.01 is the minimum possible value at two significant figures. Simultaneously, for each value of D in turn, sedimentation rate was varied from 0.01 to 1 in steps of 0.01 (units of cm/year). 1 cm/year was used as the upper limit because 0.1 cm/year is approximately the maximum expected sedimentation rate for a coastal or continental shelf region (Ruddiman 2001), so a value of 1, being an order of magnitude higher than that, should provide an extreme upper estimate. The minimum value and increment for sedimentation rate were selected using the same criteria as for the mixing rate. As the mixing rate and sedimentation rate were varied, the coefficient of determination (R^2) was calculated between the resultant theoretical ^{210}Pb curves (A) and the measured ^{210}Pb data. The combination of mixing rate and sedimentation rate which produced the best possible fit of 'A' to the measured data (denoted by the R^2 value closest to 1) was taken as the best estimate of mixing rate and sedimentation rate for this core. These values were found to be a mixing rate of 0.3 cm^2/year and a sedimentation rate of 0.16 cm/year, with R^2 of approximately 0.975.

To gauge an estimate of uncertainty for these values, age-depth relationships from the sedimentation rates of the top five R^2 values are plotted (Figure 3.10). This range in sedimentation rate from 0.07 to 0.18 cm/year creates an age difference of approximately 220 years at the base of the core (ages ranging from approximately 140 to 360 years at sediment depth 25 – 26 cm). An alternative visualisation of the range of possible sedimentation rates is provided by plotting the highest R^2 value found per sedimentation rate (Figure 3.11). From this it can be seen that for sedimentation rates of 0.01 to 0.21 cm/year the maximum R^2 appears to remain constant. In this plateau region of the curve, the R^2 values differ by a maximum of 5.1×10^{-5}, which is arguably negligible. From this it could be argued that the sedimentation rate is best represented by the range 0.01 – 0.21 cm/year, rather than a specific value from within that range. This range in sedimentation rates produces sediment ages of approximately 120 – 2500 years at the base of the core.

From these observations it can be concluded that, although there is considerable uncertainty involved in assigning precise ages to this sediment core using this method, it is likely to be entirely late Holocene in age. The nearby sediment core GC528 (53º0.8'S, 58º2.4'W, depth = 598 m) (Roberts et al. 2016) has a sedimentation rate of approximately 0.01 cm/year (Roberts et al. 2016), suggesting that the true age of BC387-2 lies closer to the older end of the predicted range. Because the best possible age estimate of this sediment core is debateable, data are plotted against depth rather than age.

The activities of ^{137}Cs and ^{7}Be were measured in addition to ^{210}Pb and ^{214}Pb, but were below detection limits in all cases (Table 3.1). ^{137}Cs is an anthropogenic radioisotope created by nuclear bomb

detonations and can be used to date sediments by providing a tie-point to the mid-1960s, when most ^{137}Cs fallout was generated. This can be used to corroborate the sediment age provided by ^{210}Pb. In gamma-ray spectroscopy, detection limits depend on sample mass and counting time (Prof A. Cundy, pers. com. 2013) so it is possible that ^{137}Cs could be measured in BC387-2 given a larger sample mass and/or counting time. However, ^{137}Cs is present only in very small amounts in the Southern Hemisphere so it may be that ^{137}Cs is not measurable in this region without great effort (e.g. Henkel et al. 2011; Tsumune et al. 2011). For this reason and because ^{137}Cs measurement was not a priority for this study re-measurement was not undertaken. ^{7}Be is a cosmogenic nuclide that can be used to date sediments in the same way as unsupported ^{210}Pb (its supply rate being indicative of sedimentation rate). This too can be used to corroborate ^{210}Pb-derived ages. ^{7}Be likely fell below detection limit because of its short half-life of 53 days: over the nine years that BC387-2 has been in storage, it is likely that ^{7}Be has decayed away sufficiently such that it is now too scarce to be measured. Whilst ^{137}Cs and ^{7}Be would have provided beneficial information, their measurement was not essential due to the alternative verification method provided by ^{214}Pb so the ^{210}Pb-derived sediment ages remain legitimate without ^{137}Cs or ^{7}Be verification.

Table 3.2. Calculated values of time-adjusted excess ^{210}Pb in sediment core BC387-2.

Depth (cm)	Total ^{210}Pb (Bq/kg)	Excess ^{210}Pb (Bq/kg)	Time-adjusted excess ^{210}Pb (Bq/kg)
0 – 1	97 ± 12	77 ± 15	100 ± 20
2 – 3	72 ± 8.6	52 ± 11	69 ± 15
4 – 5	67 ± 6.4	47 ± 9.0	62 ± 12
6 – 7	52 ± 4.1	32 ± 6.7	42 ± 9.0
8 – 9	32 ± 3.0	12 ± 5.6	16 ± 7.0
10 – 11	24 ± 2.6	4.0 ± 5.2	5.0 ± 7.0
14 – 15	14 ± 2.6	–6.0 ± 5.2	–8.0 ± 7.0
24 – 25	21 ± 2.7	1.0 ± 5.3	1.0 ± 7.0

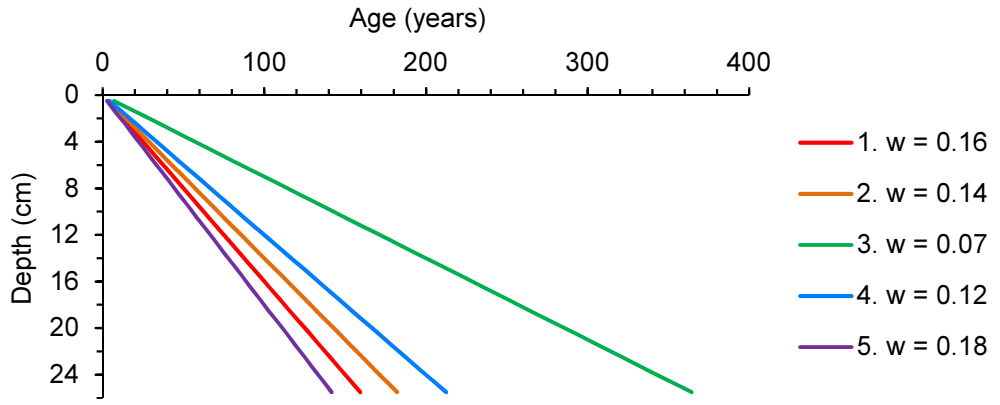

Figure 3.10. Age-depth relationships from the 'top five' sedimentation rates (the ones which provided the five highest R^2 values). 'w' is sedimentation rate in units of cm/year. Sedimentation rates numbered 1 to 5 correspond to the five highest R^2 values found, number 1 being the highest.

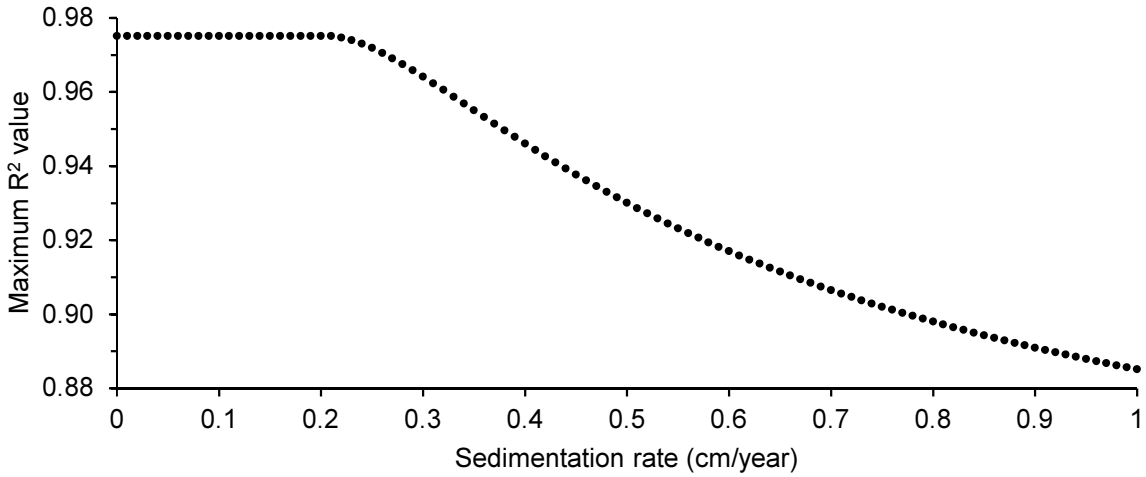

Figure 3.11. The maximum R^2 value for each sedimentation rate.

3.5.2 Barite contamination and its removal

Before measuring foraminiferal Ba/Ca ratios for estimating seawater [Ba], it is necessary to remove barite from the foraminifera so that its barium content does not elevate the measured Ba/Ca ratios. Despite seawater being undersaturated with respect to barite in much of the world's oceans (Monnin et al. 1999), barite is preserved beneath this depth as evidenced by the presence of barite particles in sediments. Increases in porewater [Ba] have been observed beneath the sediment-water interface, suggesting that barite dissolution occurs within sediments (Figure 3.12; Paytan & Kastner 1996; McManus et al. 1998), but once porewaters reach saturation with respect to barite the dissolution of barite ceases (Paytan & Kastner 1996). It may be that this dissolution is insufficient to completely remove barite from foraminifera, or that, as in shallower depths, microenvironments within decaying organic matter provide areas where barite is preserved and/or precipitated. Barite precipitation is

thought to occur inorganically, except for in rare cases such as in certain species of agglutinated foraminifera (Bertram & Cowen 1997). Barite removal is achieved by using DTPA to chelate Ba^{2+} ions thus dissolving barite (further details are provided in Section 2.2.6 'Barite removal'). However, DTPA also chelates Ca^{2+} ions, so care must be taken during this process or else extensive sample loss may occur (Lea & Boyle 1993). Here, the effect of DTPA on foraminiferal surfaces is investigated using scanning electron microscopy, to see whether DTPA adversely deteriorates the structure of foraminifer shells in comparison to the damage caused by the rest of the cleaning procedure. Additionally, Mg/Ca and Sr/Ca data from non-DTPA-cleaned foraminifera are compared to those of fully-cleaned foraminifera to investigate whether the use of DTPA significantly affects Mg/Ca or Sr/Ca. This is followed by an analysis of the effect of DTPA on Ba/Ca ratios and visible barite removal.

Figure 3.7 and Figure 3.8 show SEM images of uncleaned, non-DTPA-cleaned and fully-cleaned foraminifera (*M. barleeanus*, *O. umbonatus* and *U. peregrina*). The surfaces of non-DTPA-cleaned foraminifera are visually identical to the surfaces of fully-cleaned foraminifera, indicating that the addition of a DTPA step into the cleaning procedure (as described in Section 2.2 'Foraminiferal cleaning procedure') did not result in significant sample degradation.

Martin & Lea 2002 write that increasingly aggressive cleaning results in progressively lower Mg/Ca in *Uvigerina* sp. and *C. wuellerstorfi*, attributing this to either the removal of contamination or the preferential dissolution of Mg-rich areas of calcium carbonate, but do not see further decreases with the addition of a DTPA step into the cleaning procedure. Here these findings are replicated for *U. peregrina*, which shows no decrease in Mg/Ca when DTPA is used compared to when it is not used (Figure 3.6). Mg/Ca ratios of fully-cleaned samples are higher than those of a non-DTPA cleaned sample of *U. peregrina*. This could be because there are Mg-containing contaminants attached to barite which are removed along with barite dissolution, or could be natural variability from one sample to another (the difference between replicates is similar to the difference between the non-DTPA cleaned sample and the fully-cleaned samples). *O. umbonatus* does not show any change in Mg/Ca when DTPA is used (Figure 3.6). These findings confirm that the addition of a DTPA step into the procedure did not adversely affect Mg/Ca ratios.

The effect of cleaning on Sr/Ca ratios was also investigated by Martin & Lea 2002, who found no difference in Sr/Ca when cleaning intensity was increased. Similarly, no change in Sr/Ca of *U. peregrina* or *O. umbonatus* can be seen when non-DTPA cleaning was used versus the full cleaning procedure (Figure 3.6). This lends confidence that the use of DTPA does not systematically alter Sr/Ca ratios.

As well as ensuring that DTPA does not dissolve calcium carbonate too aggressively or affect other trace metal ratios, it would be beneficial to confirm that all of the barite had been removed from foraminifera before measuring Ba/Ca. Previous authors have found that the use of DTPA does decrease Ba/Ca (Lea & Boyle 1993; Martin & Lea 2002) which is to be expected given barite removal, but also report variable, and sometimes increasing, responses of Ba/Ca to DTPA cleaning (Lea & Boyle 1993;

Martin & Lea 2002). The data presented here suggest that Ba/Ca can have a variable response to DTPA cleaning, in agreement with previous authors. In *U. peregrina* Ba/Ca remains the same within ± 2σ upon addition of DTPA, whereas in *O. umbonatus* Ba/Ca increases by ~0.08 – 0.23 μmol/mol when DTPA is used (Figure 3.6). This increase could be due to natural variability between samples or the preferential removal of low-Ba/Ca regions of calcium carbonate. Although Lea & Boyle 1991 and Lea & Boyle 1993 found via sequential dissolution experiments that no such heterogeneity exists in *Globigerinoides conglobatus*, *Oridorsalis* spp., *Uvigerina* spp. or *Cibicides wuellerstorfi*, these data by the assertion of the authors themselves is open to interpretation, particularly the latter three species (Lea & Boyle 1993) and other species have not yet been tested. Further sequential dissolution experiments on different species and laser ablation studies which are able to target different regions of individual foraminifer shells (e.g. Hathorne et al. 2003) could elucidate this further.

Barite can have several different morphologies, occurring on benthic foraminifera as rhombic crystals (Bertram & Cowen 1997). In the SEM micrographs, which are shaded according to atomic mass, rhombic crystals which have the visual appearance of barite can be seen (Figure 3.7; Figure 3.8; Figure 3.9; Dr A. (S.) Turchyn, pers. com. 2015). They are bright which could be due to the higher atomic mass of barite (233 g/mol) compared to that of the surrounding calcium carbonate (100 g/mol). Their location near the foraminiferal aperture is interesting because this supports the idea that barite precipitates within organic matter microenvironments within benthic foraminifera. Energy-dispersive x-ray spectroscopy was used to investigate whether these particles are indeed barites, but the resulting spectra show little difference between barite-like particles and the background calcium carbonate shell (Figure 3.9). If these were barites their EDS spectra should have peaks in Ba and S (e.g. Riedinger et al. 2006). This could be because the electron beam did not penetrate the surface of the barites. It might also be that these apparent barite particles are pseudomorphs which are composed of calcium carbonate but have retained the visual appearance of the rhombic barite crystals they once were. Further investigation using a technique such as Raman spectroscopy could elucidate the composition of these barite-like particles and thus confirm whether or not they are crystals of barite.

If these particles are indeed barites, the SEM micrographs of uncleaned foraminifera (Figure 3.7) show that barite is present upon *O. umbonatus* and *U. peregrina* but not *M. barleeanus* prior to cleaning and at least some of this barite remains after cleaning without DTPA (Figure 3.8), confirming the need to clean foraminifera with DTPA prior to analysis. In SEM micrographs of DTPA-cleaned foraminifera (Figure 3.8) barite can no longer be seen. Although this does not prove that DTPA has removed all of the barite, it is a good indication that the DTPA cleaning step is effective and necessary. The apparent lack of barite on *M. barleeanus* could be due to the way this species calcifies, with new chambers growing over old ones such that the outer surface is the most 'fresh' (Lipps 1993).

Even if the use of DTPA always resulted in Ba/Ca decreasing, this would still not absolutely confirm that all barite is always removed before measurement because the extent of barite contamination may vary from one individual to another, yet it is not feasible to perform this test on

every individual foraminifer before measurement. However, scanning electron microscopy can provide supporting evidence for barite removal. This could be performed on a few foraminifera from each site or at certain depth intervals under the assumption that other nearby foraminifera would contain similar amounts of barite.

3.5.3 Foraminiferal uptake of barium: D_{Ba} values

Before foraminiferal Ba/Ca can be used to calculate seawater [Ba], it is necessary to determine the relationship between Ba/Ca and ambient seawater [Ba] using a partition coefficient. The Ba/Ca ratio of foraminiferal calcium carbonate has a positive linear relationship with the barium concentration of the water in which they grew, which was first noted by Lea & Boyle 1989 who measured Ba/Ca in the benthic species *Uvigerina* spp., *C. wuellerstorfi* and *C. kullenbergi*. Other species of benthic and planktic foraminifera have also been confirmed to record ambient barium concentrations in this way (Lea & Spero 1992; Lea & Spero 1994; Havach et al. 2001; Hönisch et al. 2011). Because the process of biomineralisation, including the method by which Ba^{2+} ions are transported into the calcium carbonate lattice, is not yet fully understood (e.g. Elderfield et al. 1996; Erez 2003; de Nooijer et al. 2009), a practical way of measuring barium uptake is to use a partition coefficient (D_{Ba}), defined as:

$$D_{Ba} = \frac{\left(\frac{Ba}{Ca}\right)_f}{\left(\frac{Ba}{Ca}\right)_{sw}} \qquad (3.9)$$

Where $(Ba/Ca)_f$ is the Ba/Ca of foraminiferal calcium carbonate and $(Ba/Ca)_{sw}$ is the dissolved Ba/Ca ratio of the ambient seawater. Partition coefficients are assigned the notation 'D' because they were originally known as distribution coefficients, which was later changed to partition coefficient to avoid confusion with thermodynamic distribution constants although the use of the notation 'D' remained (Morse & Bender 1990; Lea & Spero 1992). The concept of using a partition coefficient in this way was first introduced by Boyle 1981. The barium concentration of seawater can then be calculated from $(Ba/Ca)_{sw}$ by assuming a value for the calcium concentration of seawater and using the following equation:

$$[Ba]_{sw} = \left(\frac{Ba}{Ca}\right)_{sw} \times [Ca]_{sw} \qquad (3.10)$$

Where $[Ba]_{sw}$ and $[Ca]_{sw}$ are the dissolved barium and calcium concentrations of the ambient seawater and $(Ba/Ca)_{sw}$ is the dissolved Ba/Ca ratio of the ambient seawater. D_{Ba} values should be defined as accurately as possible because relatively small variations in the D_{Ba} value used can cause substantial differences in resulting seawater [Ba] and alkalinity estimates (Figure 3.13).

Although the use of D_{Ba} values mitigates the need to fully understand biomineralisation before the Ba/Ca proxy can be used, an improved knowledge of this process would nonetheless benefit our understanding of how this and other foraminifera-based proxies should be interpreted. Authors such as Pingitore 1986 have hypothesised that foraminiferal barium uptake is an abiotic process whereby Ba^{2+} ions are incorporated into the calcium carbonate lattice by adsorption followed by entrapment within

the lattice during growth. Alternatively, several authors propose that Ba^{2+} ions substitute for Ca^{2+} ions within the calcium carbonate lattice (e.g. Lea 1990; Lea & Boyle 1991; Lea & Spero 1992). Although the larger ionic radius of the Ba^{2+} ion should prevent solid solution formation (Shannon 1976; Pingitore & Eastman 1984; Pingitore 1986), it is nonetheless possible because the amount of barium in ocean waters, and hence in foraminiferal calcium carbonate, is so small that it does not significantly impact lattice structures (Lea & Spero 1992). The lack of agreement between D_{Ba} values of inorganic and foraminiferal carbonates, the former being up to an order of magnitude larger than the latter (Kitano et al. 1971), has led to a broad consensus that Ba^{2+} uptake likely occurs via substitution into the calcium carbonate lattice during biomineralisation (e.g. Lea & Spero 1992). However, the specific biomineralisation mechanisms of different species are a topic of ongoing study (e.g. Khalifa et al. in press). Biomineralisation may occur as inorganic-style precipitation induced by the foraminifer, for example via seawater vacuolisation whereby a pocket of seawater is isolated within the foraminifera and calcium carbonate is calcified from this internal pool (e.g. Erez 2003; Bentov & Erez 2006; Bentov et al. 2009), or a more strongly biologically-mediated calcification process such as trans-membrane transport (e.g. Nehrke et al. 2013). Barium has no known function in foraminifer shells so its uptake may be an accidental by-product of obtaining Ca^{2+} and CO_3^{2-} ions for calcification. It has been hypothesised that a Ca^{2+} ion pump within foraminifera might accidentally admit small quantities of other ions such as Ba^{2+} (Erez 2003; de Nooijer et al. 2009).

Because the barium uptake process is not fully understood, it is important to determine D_{Ba} values for each individual species as it is not known how vital effects might differ from one species to another. D_{Ba} values have been determined for several species of foraminifer via laboratory culture experiments and core-top calibrations (Table 3.3). Intraspecific variation in barium uptake has been confirmed to be negligible in some species (Lea & Spero 1992; Lea & Spero 1994) and so each of these D_{Ba} values may be thought of as representative per species, although extending these studies of intraspecific variation to other species would be beneficial. Some authors have merged data from multiple planktic species into one D_{Ba}, rather than using a unique D_{Ba} per species (Lea & Boyle 1991; Lea & Spero 1994; Hönisch et al. 2011). The consistency of D_{Ba} values amongst these individual species validates this approach, which allows for samples containing mixed species to be analysed, increasing the amount of material available for use. Lea & Boyle 1989 applied this technique to the benthic species *Uvigerina* spp., *C. wuellerstorfi* and *C. kullenbergi* and found "no evidence for significant differences in individual D values for each species" (Lea & Boyle 1989). However, these authors also acknowledge that there is variation in D_{Ba} amongst these three species and that "the uncertainty in D for each species can be improved by further analyses from high-sedimentation-rate cores, ultimately allowing us to determine whether different benthic species have different effective distribution coefficients" (Lea & Boyle 1989). Therefore, whether or not the approach of using one D_{Ba} value for multiple species is applicable to benthic foraminifera is still an open question.

As a contribution to this ongoing work, separate D_{Ba} values for the three benthic species *O. umbonatus*, *M. barleeanus* and *U. peregrina* are calculated using the core-top Ba/Ca data of this study (Figure 3.5; Figure 3.14). Assuming a seawater barium concentration of 75 – 85 nM which is typical for this region at depths of approximately 600 m (Figure 3.15) and a seawater Ca concentration of 10.3 mM (Dickson and Goyet, 1994) yields a seawater Ba/Ca of approximately 7.28 – 8.25 nmol/mmol or µmol/mol. D_{Ba} values were therefore calculated using the following equation:

$$D_{Ba} = \frac{\left(\frac{Ba}{Ca}\right)_f}{\left(\frac{Ba}{Ca}\right)_{sw}} = \frac{\left(\frac{Ba}{Ca}\right)_f}{7.28 \text{ to } 8.25} \qquad (3.11)$$

Where foraminiferal Ba/Ca is in units of µmol/mol. Ba/Ca ratios from as near the core-top as possible were used (Figure 3.14). Seawater [Ba] was varied from 75 to 85 nM in steps of 1 nM and a D_{Ba} value calculated each time, resulting in the D_{Ba} values shown in Figure 3.16. The D_{Ba} values calculated using 75 and 85 nM [Ba] are presented in Table 3.4. Upper and lower limits on D_{Ba} values were calculated using ± 2σ on the foraminiferal Ba/Ca data used in the equation. Although sample limitations prevented the measurement of *M. barleeanus* or *U. peregrina* from the 0 – 1 cm sediment horizon, Ba/Ca ratios remain approximately constant down-core (Figure 3.5) so this has minimal impact on the D_{Ba} values calculated. This is evidenced by the consistency of *O. umbonatus* D_{Ba} values calculated from samples ranging from depths 0 – 5 cm (Table 3.4). The resulting D_{Ba} values are typical of benthic foraminifera, which vary between approximately 0.2 and 0.4 (Table 3.3). No D_{Ba} values have previously been measured for *O. umbonatus* or *M. barleeanus*. The *U. peregrina* D_{Ba} value agrees well with previously-measured D_{Ba} values for this species which are 0.34, 0.32 and 0.31 (Table 3.3). The change in D_{Ba} caused by varying seawater [Ba] from 85 to 75 nM is approximately 0.06 for *M. barleeanus*, 0.03 for *O. umbonatus* and 0.04 for *U. peregrina* (Table 3.4; Figure 3.16). These uncertainties are large given the sensitivity of seawater [Ba] and alkalinity estimates to the D_{Ba} value used (Figure 3.13). Defining a more precise estimate of seawater [Ba] for this site would therefore reduce the uncertainty on these D_{Ba} values. Some previous authors have taken a similar approach to this study by using estimates of seawater [Ba] rather than [Ba] measured in water samples taken from directly above the sediment (e.g. Lea & Boyle 1989). Here it is demonstrated that this approach should be treated with caution as the true uncertainty on D_{Ba} values may be underestimated.

A further consideration is that infaunal and epifaunal benthic foraminifera may be influenced by porewater [Ba] and fluxes of dissolved barium emanating from sediments into bottom waters. If these processes sufficiently overprinted bottom water [Ba] variations, the foraminiferal Ba/Ca would no longer be a proxy for ocean circulation changes and would instead record changes in sedimentary processes through time. Additionally, the presence of sedimentary influences on [Ba] could mean that a different seawater [Ba]-alkalinity calibration should be used for infaunal or epifaunal foraminifera, rather than the global average relationship between seawater [Ba] and alkalinity (Lea 1993) which may not be applicable to sediment porewaters or under the influence of significant sedimentary fluxes.

Porewater [Ba] can vary by up to approximately 100 nM within the top 25 cm of sediment, with the most rapid changes in concentration occurring in the top few centimetres (Figure 3.12; Paytan & Kastner 1996; McManus et al. 1998). This has been attributed to in situ barite dissolution within sediments which ceases once saturation with respect to barite is reached (Paytan & Kastner 1996). If the seawater [Ba] used to calculate D_{Ba} was an underestimation of the true ambient [Ba] within porewaters, the resulting D_{Ba} value would be overestimated. Figure 3.17 demonstrates the effect that this magnitude of variability in ambient [Ba] could have on calculated D_{Ba} values: depending on foraminiferal Ba/Ca, when ambient water [Ba] is varied from 50 to 150 nM the resulting D_{Ba} changes by approximately 0.1 – 0.4, which is large in terms of reconstructing past seawater [Ba] and alkalinity (Figure 3.13).

In addition to environmental controls, Ba/Ca and thus calculated D_{Ba} values may be affected by vital effects. The Ba/Ca ratios of *M. barleeanus* are offset from those of the other two species by approximately 1 – 1.5 μmol/mol (Figure 3.5). This may be due to differences in ambient [Ba] in the habitats of the different species, but might also be a permanent offset which occurs even when foraminifera are grown under the same conditions, caused by differing vital effects on Ba/Ca in the different species. The presence of vital effects on $\delta^{18}O$ and Sr/Ca in this core suggests that vital effects may also be responsible for the Ba/Ca offsets observed: *M. barleeanus* $\delta^{18}O$ is offset from that of *U. peregrina* by approximately 0.6 ‰ (Figure 3.5), in agreement with the offset measured by Hoogakker et al. 2010 of 0.55 ± 0.37 ‰; and *M. barleeanus* Sr/Ca is offset from that of *U. peregrina* by approximately 0.2 mmol/mol (Figure 3.5), in agreement with the offset measured by Rosenthal et al. 1997 of ~0.2 – 0.3 mmol/mol. The constancy of the Ba/Ca offset between *M. barleeanus* and the other species down-core (Figure 3.5) is also suggestive of vital effects, rather than environmental controls which are susceptible to change over time. The possible existence of vital effects on benthic foraminiferal Ba/Ca highlights the importance of calculating a D_{Ba} value per individual species and supports the hypothesis that Ba uptake occurs via the process of biomineralisation rather than abiotically.

Given these uncertainties, the D_{Ba} values measured here are only tentatively interpreted, although their similarity to previously-published D_{Ba} values increases their credibility. The D_{Ba} values of different species do not overlap with each other (Figure 3.16) suggesting that it is appropriate to use a species-specific D_{Ba} value for each species rather than combining them into one 'benthic infaunal D_{Ba}'. These offsets in D_{Ba} between species could be because of: a) vital effects that differ between species; b) these species inhabiting different microenvironments with differing ambient [Ba]; or c) a combination of both factors. To determine the extent to which Ba/Ca is affected by vital effects and environmental conditions, the mechanisms behind species-specific D_{Ba} values could be explored further by taking paired measurements of infaunal and epifaunal foraminiferal Ba/Ca, porewater [Ba] and sedimentary flux [Ba] using benthic landers, as well as continuing research into how barium uptake occurs during biomineralisation.

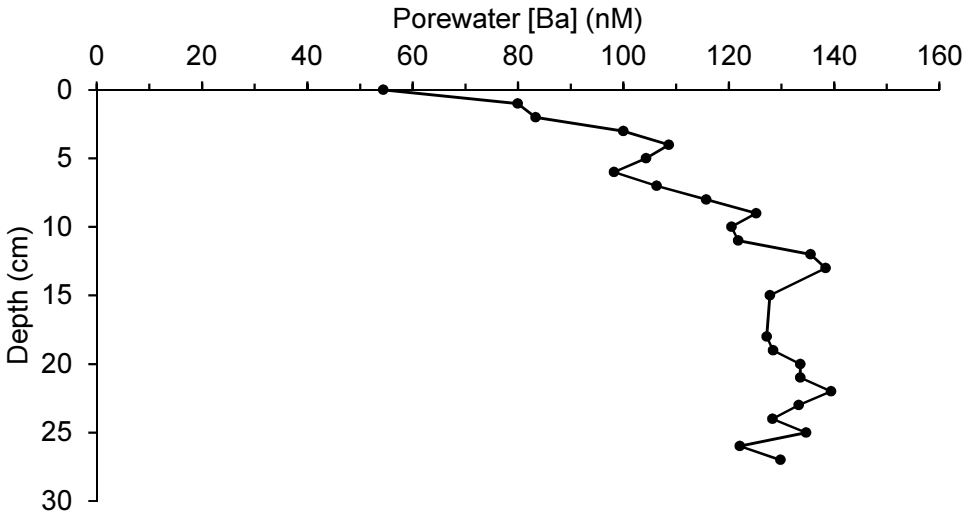

Figure 3.12. Porewater [Ba] in sediment core JC089-07-6M-F, normalised relative to 50 nM, an approximated bottom water [Ba] for its deep Atlantic location (Dr M. Greaves, pers. com. 2015). This approximation means that absolute values may not be accurate, but the relative change in porewater [Ba] down-core is conserved (Dr M. Greaves, pers. com. 2015).

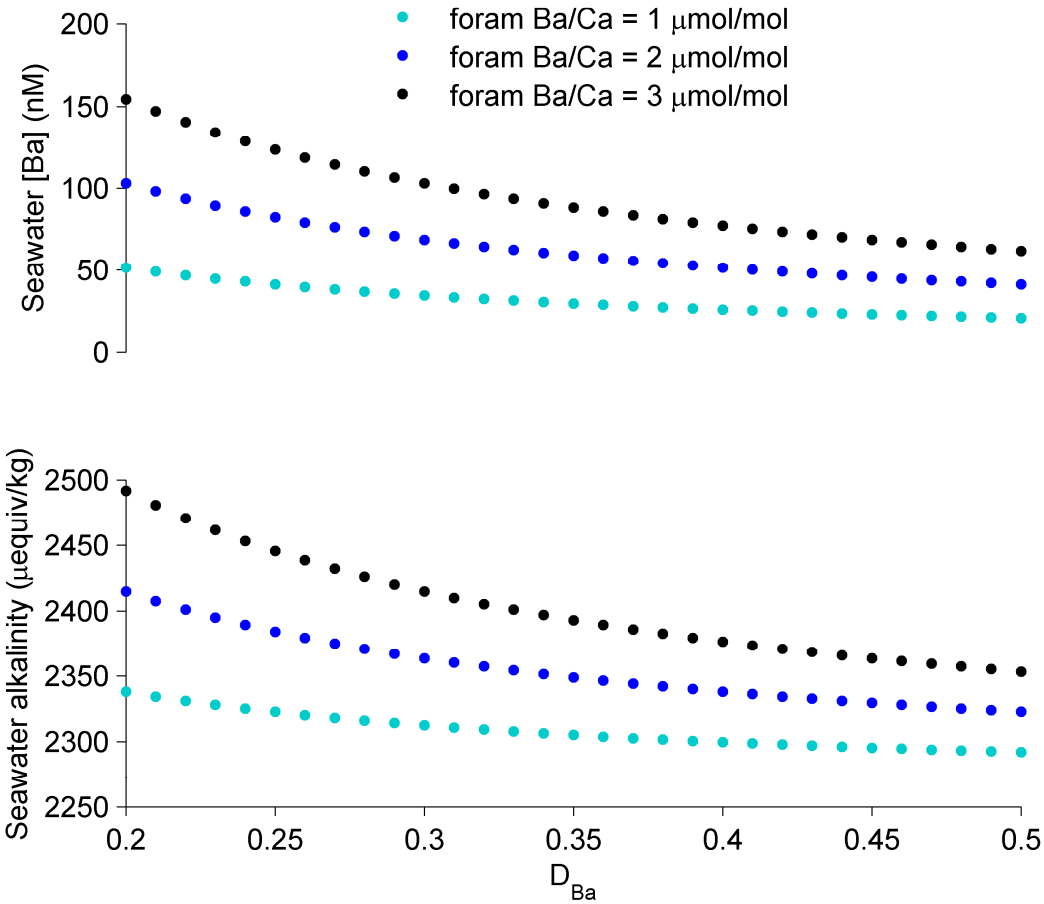

Figure 3.13. The effect of varying D_{Ba} on resultant seawater [Ba] and alkalinity estimates.

Table 3.3. Compilation of previously-measured barium partition coefficients (D_{Ba} values).

Planktic species	D_{Ba}	C or L [a]	Reference
Globoquadrina dutertrei, Globigerinoides sacculifer, Orbulina spp.*, Globigerinoides ruber, Globigerinoides conglobatus* (combined)	0.19 ± 0.05	C	Lea & Boyle 1991
Orbulina universa	Not forced through zero: 0.15 ± 0.01 (intercept is 0.22 ± 0.21) Forced through zero: 0.16 ± 0.01	L	Lea & Spero 1992
Orbulina universa, also applicable to *Globigerinoides sacculifer*	Not forced through zero: 0.134 ± 0.008 (intercept is 0.14 ± 0.08) Forced through zero: 0.147 ±0.004	L	Lea & Spero 1994
Neogloboquadrina pachyderma sinistral	0.22 ± 0.02	C	Hall & Chan 2004b
Globigerina bulloides	0.17 ± 0.04	L	Hönisch et al. 2011
Orbulina universa	0.17 ± 0.02	L	Hönisch et al. 2011
Applicable to spinose planktic species and *Neogloboquadrina* (but not *Globorotalia*)	0.149 ± 0.05	L	Hönisch et al. 2011 (also used data from Lea & Spero 1994)
Benthic species	D_{Ba}	C or L [a]	Reference
Cibicides wuellerstorfi, *Cibicides kullenbergi* and *Uvigerina* spp. (combined)	0.37 ± 0.06	C	Lea & Boyle 1989
Uvigerina spp.	0.34	C	Lea & Boyle 1989
Cibicides wuellerstorfi	0.37	C	Lea & Boyle 1989
Cibicides kullenbergi	0.41	C	Lea & Boyle 1989
Uvigerina spp.	0.31 ± 0.04	C	Lea 1993
Uvigerina spp.	0.32 ± 0.06	C	Lea 1993 (also used data from Lea & Boyle 1989)

Benthic species	D_{Ba}	C or L [a]	Reference
Cibicides wuellerstorfi	0.313 to 0.221	C	McCorkle et al. 1995
Cibicides pachyderma	0.5 ± 0.1	L	Havach et al. 2001
Uvigerina peregrina	0.24 ± 0.06	L	Havach et al. 2001
Bulimina marginata	0.24 ± 0.07	L	Havach et al. 2001
Ammonia beccarii	0.20 ± 0.04	L	Havach et al. 2001

a) L = measured via laboratory culture experiment, C = measured via core-top calibration.

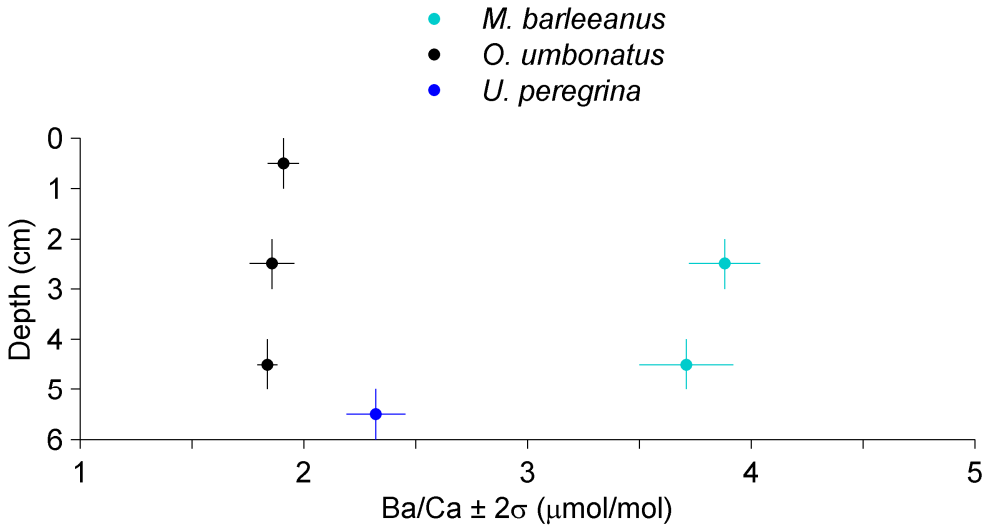

Figure 3.14. Ba/Ca measured in benthic foraminifera from sediment core BC387-2 at core-top and shallow sediment depths. These data were used to calculate the barium partition coefficients (D_{Ba}) shown in Table 3.4 and Figure 3.16.

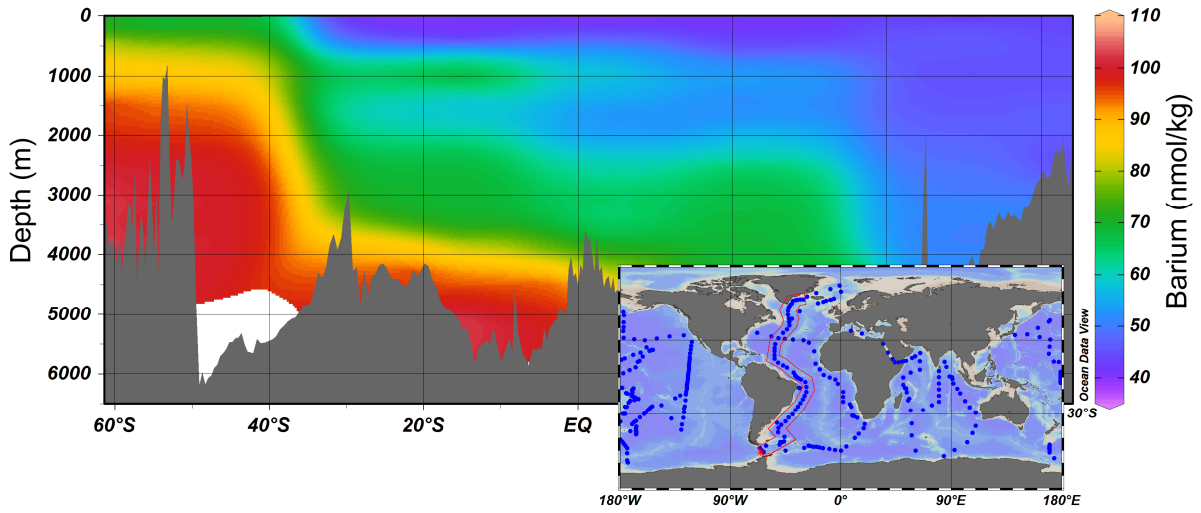

Figure 3.15. GEOSECS seawater barium concentrations in the western Atlantic Ocean.

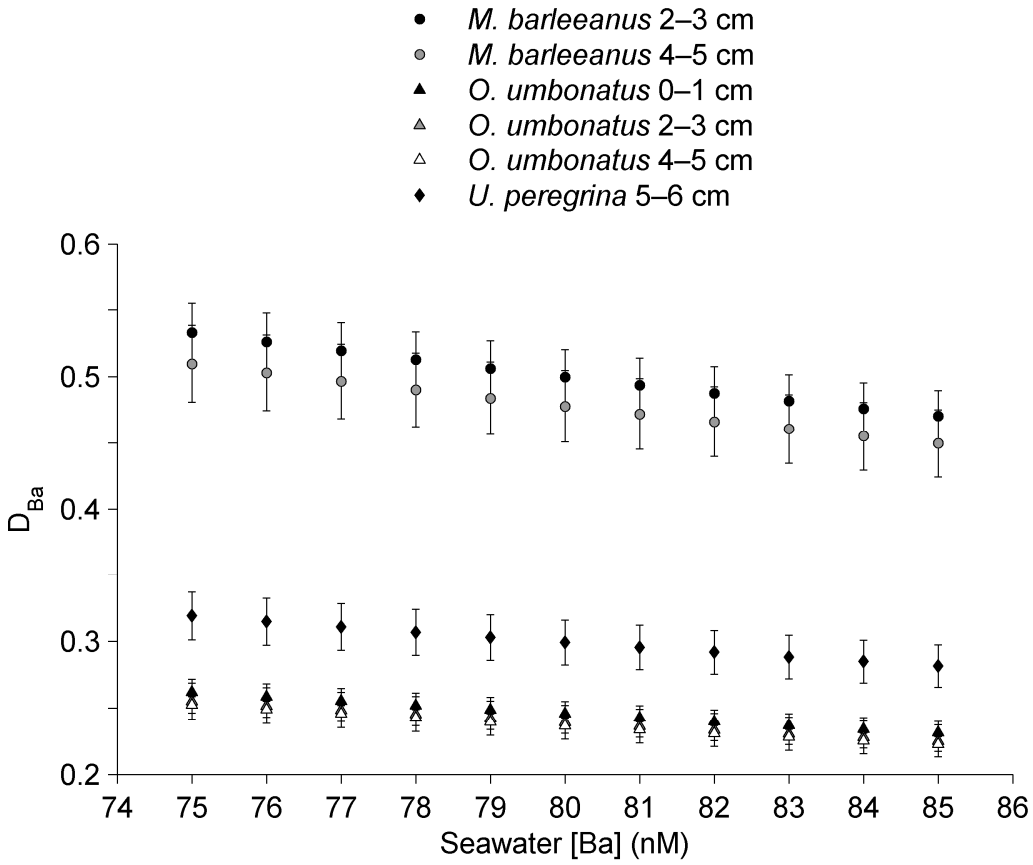

Figure 3.16. D_{Ba} values calculated whilst the varying seawater [Ba] between 75 and 85 nM and using core-top (0 – 1 cm) and shallow (2 – 6 cm) Ba/Ca ratios. Upper and lower error bounds are computed using ± 2σ Ba/Ca values. These data are tabulated in Table 3.4.

Table 3.4. Calculated D_{Ba} values. These data are plotted in Figure 3.16.

		$[Ba]_{sw}$ = 75 nM		$[Ba]_{sw}$ = 85 nM	
Species	Depth (cm)	D_{Ba}	2σ	D_{Ba}	2σ
M. barleeanus	2 – 3	0.53	0.02	0.47	0.02
	4 – 5	0.51	0.03	0.45	0.03
O. umbonatus	0 – 1	0.26	0.01	0.23	0.01
	2 – 3	0.26	0.01	0.23	0.01
	4 – 5	0.25	0.01	0.22	0.01
U. peregrina	5 – 6	0.32	0.02	0.28	0.02

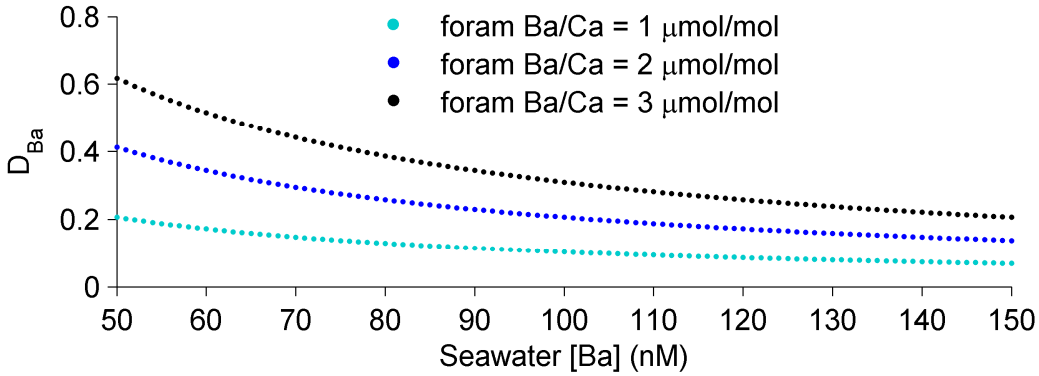

Figure 3.17. Graph showing the effect on calculated D_{Ba} values of varying the ambient barium concentration used to calculate D_{Ba} from 50 to 150 nM.

3.5.4 Environmental influences on Ba/Ca ratios

Here, down-core data from sediment core BC387-2 are used to assess the impacts of post-depositional dissolution of foraminifera, changes in primary productivity at the core site and temperature on benthic foraminiferal Ba/Ca ratios. To use foraminiferal Ba/Ca as a proxy for seawater [Ba], it is important to ensure that the data have not been significantly affected by factors other than ambient seawater barium concentrations, or that if these effects do exist that they are corrected for. Ba/Ca ratios may decrease during diagenesis via preferential loss of Ba from the calcium carbonate lattice during dissolution (McCorkle et al. 1995). Small-scale variability in barium cycling, such as that caused by local primary productivity, may render globally-constructed [Ba]-alkalinity calibration curves (e.g. Lea 1993) inapplicable to certain locations, particularly at relatively shallow depths and in highly-productive regions. It is for this reason that Rubin et al. 2003 suggest that the Ba/Ca-alkalinity proxy is not applicable to shallow marine environments, but open-ocean areas only. Here, down-core Ba/Ca data from three species of benthic foraminifera are paired with Mg/Ca, Sr/Ca, $\delta^{18}O$, $\delta^{13}C$ and XRF data to investigate whether post-depositional dissolution of foraminifer shells or fluctuations in the amount of primary productivity have significant impacts on benthic foraminiferal Ba/Ca. In addition, Mg/Ca-derived temperatures are used to investigate whether temperature has an effect on Ba/Ca ratios in these three species.

3.5.4.1 Post-depositional dissolution

A lack of evidence for post-depositional alteration of foraminifera in this sediment core means that the impact of dissolution on Ba/Ca cannot be assessed here. Due to preferential dissolution of Sr-rich areas of calcium carbonate, foraminiferal Sr/Ca ratios decrease with increasing post-depositional alteration (e.g. Brown & Elderfield 1996). The Sr/Ca ratios of all three species remain approximately constant down-core (Figure 3.5), suggesting that significant dissolution has not taken place. SEM images of uncleaned foraminifera do not reveal any signs of significant dissolution, with 'fresh' glassy surfaces and unaltered morphologies (Figure 3.7). Furthermore, XRF Fe/Al, Cu/Al and S/Al ratios,

which are indicative of diagenetic activity (Croudace & Rothwell 2015), also do not show any large variations down-core. In summary, it seems that significant post-depositional dissolution did not occur within BC387-2, which means that the impact of carbonate dissolution on foraminiferal Ba/Ca ratios cannot be studied using this core. This lack of dissolution could be due to the relatively young age of this core (see Section 3.5.1 'BC387-2 age model') or its shallow depth (586 m) compared to the lysocline (~4500 m). Further investigations would be beneficial because sedimentary dissolution studies which use benthic foraminifera are relatively rare (Edgar et al. 2013). McCorkle et al. 1995 found that with increasing water depth from 2 to 4 km, Ba/Ca ratios of the benthic foraminifer *C. wuellerstorfi* fell by approximately 25 % despite no concurrent decrease in seawater barium concentrations. They hypothesise that this was caused by a 'dissolution effect' in sediments, whereby barium was preferentially lost from the calcium carbonate due to its relative enrichment in areas of the shell more prone to dissolution (McCorkle et al. 1995). However, this result has not been replicated by other authors who find no change in Ba/Ca between different areas of foraminifer shells (Lea & Boyle 1991; Lea & Boyle 1993) or between different water depths (Lea & Boyle 1991). Further studies of dissolution effects on Ba/Ca would therefore be beneficial, particularly on high-resolution cores from locations often used in palaeoclimate work (Edgar et al. 2013).

3.5.4.2 Productivity

Sediment core BC387-2 contains evidence that productivity has been variable at this site in the absence of concomitant changes in Ba/Ca, suggesting that productivity has a negligible effect on benthic foraminiferal Ba/Ca ratios. In all three of the foraminifer species measured, down-core variability in $\delta^{13}C$ can be seen (Figure 3.5), particularly at depths 3.5 – 5.5 cm (Figure 3.5). This suggests that productivity has been variable at this site, with lighter $\delta^{13}C$ values indicating enhanced productivity (e.g. Schmiedl & Mackensen 2006). Because organic matter is isotopically light, the degradation of organic matter in sediment porewaters causes the $\delta^{13}C$ of porewaters to become lighter (e.g. Schmiedl & Mackensen 2006). The greater the organic matter supply, the lighter the $\delta^{13}C$ of sediment porewaters becomes. This is imprinted onto the $\delta^{13}C$ of benthic foraminiferal calcium carbonate. Benthic foraminiferal $\delta^{13}C$ is not significantly affected by diagenesis so down-core changes in $\delta^{13}C$ are conserved over time (Edgar et al. 2013). Although $\delta^{13}C$ is a water mass tracer in addition to indicating productivity changes, because this core is entirely Holocene in age (as shown in Section 3.5.1 'BC387-2 age model') water mass changes are unlikely to have occurred down-core. Therefore, these $\delta^{13}C$ variations are likely caused by variability in productivity. The shifts to heavier $\delta^{13}C$ values seen in *M. barleeanus* and *O. umbonatus* at 3.5 – 5.5 cm and in *U. peregrina* at 1.5 – 3.5 and 8.5 – 11.5 cm (Figure 3.5) may be due to reduced productivity in the overlying water column at these times resulting in reduced productivity in sediments due to a diminished food supply, whereas the lighter $\delta^{13}C$ values at 1.5 – 3.5 cm in *M. barleeanus* and *O. umbonatus* and at 5.5 – 8.5 cm in *U. peregrina* (Figure 3.5) would

be indicative of enhanced productivity at these times, possibly due to an increased food supply from the overlying water column. Changes in the amount of organic matter supply to sediments may affect these species at different times and to varying extents due to their different habitats and because foraminifera may migrate to take advantage of food sources opportunistically (Tachikawa & Elderfield 2002; Fontanier et al. 2006). This could explain why the $\delta^{13}C$ variations are not synchronous across all three species. *U. peregrina* has been known to migrate large vertical distances within sediments, up to 10 cm from the sediment-water interface (Loubere & Gary 1990), which may explain why the $\delta^{13}C$ fluctuations of this species have a greater magnitude than those of *M. barleeanus* or *O. umbonatus* (Figure 3.5). Sedimentary Ca/Al, Si/Al and Ba/Al ratios from XRF, indicative of carbonate, silica and barite production and hence overall productivity (Croudace & Rothwell 2015), do not show strong variations, remaining approximately constant down-core (Figure 3.5). These parameters therefore do not provide strong supporting evidence for down-core productivity variations. This may be because XRF ratios are not necessarily applicable in relatively shallow margin settings where lithogenic inputs have a greater impact on sediment composition than in the open ocean. Furthermore, XRF ratios are semi-quantitative, with changes in sediment texture, water content, porosity, grain size and surface roughness affecting results (Croudace & Rothwell 2015). Given these considerations, the productivity variations indicated by $\delta^{13}C$ are likely to be real, despite the lack of supporting evidence from XRF. In spite of these down-core productivity variations, Ba/Ca ratios remain approximately constant (Figure 3.5) and there is no significant correlation between Ba/Ca ratios and $\delta^{13}C$ (Figure 3.18; Table 3.5). The lack of a relationship between $\delta^{13}C$ and Ba/Ca suggests that productivity does not have a significant impact on benthic foraminiferal Ba/Ca, despite the link between productivity and barite cycling. This may be because barite precipitated in association with near-surface productivity has been sufficiently remineralised at these depths and/or because productivity-related barite precipitation only negligibly affects seawater barium concentrations in comparison to the total inventory of dissolved barium in seawater. The lack of a correlation between productivity and Ba/Ca supports the use of Ba/Ca ratios as a proxy for ocean circulation. Furthermore, this suggests that benthic Ba/Ca ratios may be a reliable proxy for ocean circulation even in relatively shallow and highly-productive settings, such as the BC387-2 collection site (Figure 3.1; Schejter et al. 2016), where near-surface processes are more likely to affect benthic environments.

3.5.4.3 Temperature

The down-core Ba/Ca ratios and Mg/Ca-derived temperatures measured in this sediment core provide no evidence for a temperature effect on foraminiferal Ba/Ca ratios. The calculated temperatures agree well across the three species (Figure 3.5) and with the known seafloor temperatures at this location, which are approximately 4 – 5 ºC (Schejter et al. 2016). Fluctuations in temperature occur down-core, particularly at 6.5 – 7.5 cm and 1.5. – 18.5 cm in *U. peregrina* (Figure 3.5), yet Ba/Ca ratios

remain approximately constant throughout the sediment core (Figure 3.5), suggesting that Ba/Ca ratios are not significantly affected by temperature changes. Furthermore, when Ba/Ca is plotted against temperature, no significant relationships are found (Figure 3.18; Table 3.5). These results are in agreement with those of previous authors who find that foraminiferal Ba/Ca is unaffected by temperature (Lea & Spero 1994; Hönisch et al. 2011). In laboratory culturing experiments, Lea & Spero 1994 find no temperature effect on *Orbulina universa* Ba/Ca with a temperature range of 22 – 29 ºC and Hönisch et al. 2011 also find Ba/Ca in this species to be aunaffected by temperature at 18 – 26 ºC. No other studies have thus far tested the effect of temperature on foraminiferal Ba/Ca. The results of this study extend the tested temperature range to colder temperatures and increase the number of species tested to include three benthic species. The continued lack of evidence for a temperature effect on Ba/Ca is encouraging in regards to the use of Ba/Ca as a proxy for seawater [Ba], which would benefit from an absence of complicating factors such as temperature effects. Further laboratory culturing experiments would be highly beneficial both for testing the findings presented here and for further extending the range of temperatures and species tested.

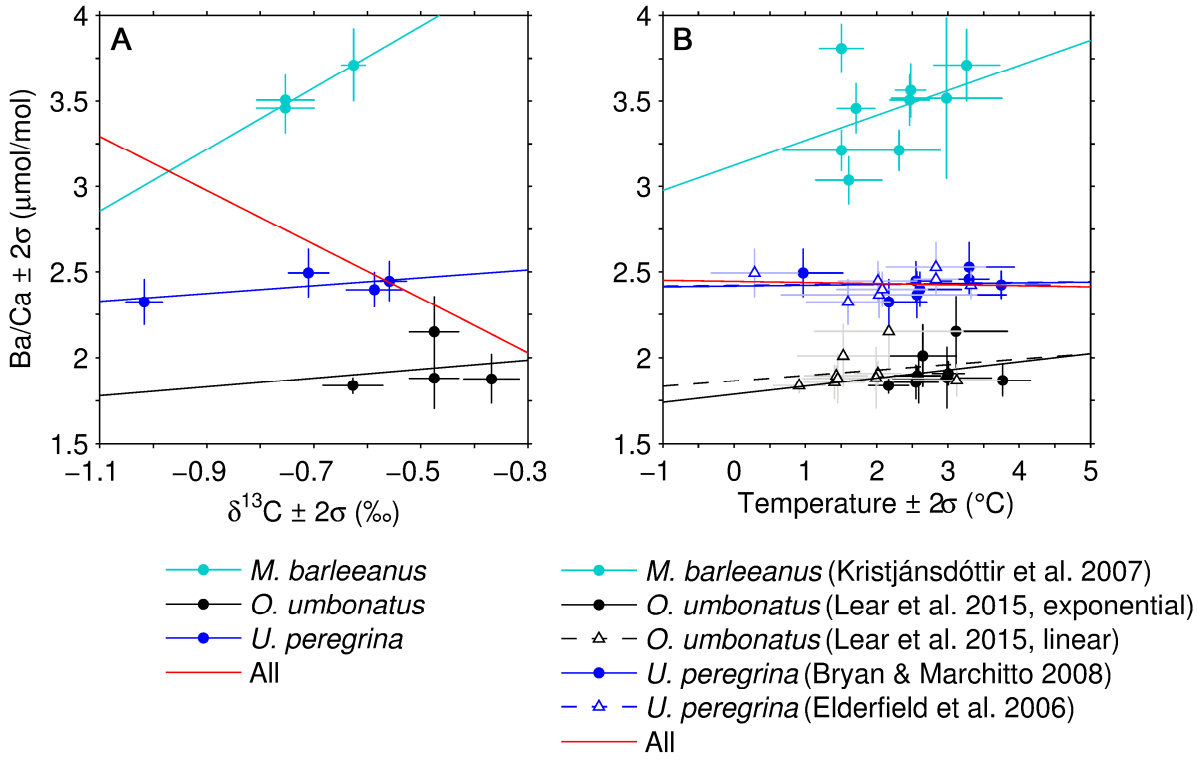

Figure 3.18. Foraminiferal Ba/Ca ratios plotted against $\delta^{13}C$ (A) and Mg/Ca-derived temperature (B) with least-squares linear regression lines. No significant relationships are found (equations, correlation coefficients and p-values are provided in Table 3.5).

Table 3.5. Equations of the least-squares linear regression lines plotted in Figure 3.18, along with product moment correlation coefficients (R) and their p-values (p). In all cases the 'y' parameter, which was plotted against the 'x' parameter, was foraminiferal Ba/Ca.

'x' parameter	Equation of regression line	R	p
M. barleeanus $\delta^{13}C$	y = 1.80x + 4.84	0.98	0.11
O. umbonatus $\delta^{13}C$	y = 0.26x + 2.06	0.19	0.81
U. peregrina $\delta^{13}C$	y = 0.23x + 2.58	0.67	0.33
All $\delta^{13}C$	y = –1.58x + 1.55	–0.40	0.22
M. barleeanus temperature [a]	y = 0.15x + 3.12	0.38	0.31
O. umbonatus temperature [b]	y = 0.05x + 1.79	0.22	0.57
O. umbonatus temperature [c]	y = 0.03x + 1.86	0.20	0.60
U. peregrina temperature [d]	y = 0.01x + 2.42	0.06	0.89
U. peregrina temperature [e]	y = 0.01x + 2.42	0.06	0.89
All temperature	y = –0.01x + 2.44	–0.01	0.96

a) temperature calculated from Mg/Ca using the equation of Kristjánsdóttir et al. 2007

b) temperature calculated from Mg/Ca using the exponential equation of Lear et al. 2015

c) temperature calculated from Mg/Ca using the linear equation of Lear et al. 2015

d) temperature calculated from Mg/Ca using the equation of Bryan & Marchitto 2008

e) temperature calculated from Mg/Ca using the equation of Elderfield et al. 2006

R = 1 indicates a perfect positive linear relationship, R = –1 indicates a perfect negative linear relationship and R = 0 indicates no linear relationship.

The relationship described by R is significant at a 95 % significance level if p is less than 0.05: no significant relationships are present.

3.6 Conclusions

In this chapter, several potential caveats to the Ba/Ca proxy for seawater [Ba] and alkalinity have been considered. Firstly, the effectiveness of DTPA in cleaning barite from foraminifera was assessed. It is impractical to ensure the total removal of barite from all foraminifera prior to measurement, but the evidence presented here indicates that barite removal from foraminifera is successfully achieved by the DTPA cleaning step described in Section 2.2.6 'Barite removal'. The variable effect of DTPA cleaning on Ba/Ca ratios might be due to there being variable amounts of barite contamination present on foraminifera prior to cleaning, or due to heterogeneous Ba distributions in foraminifer shells. Sequential dissolution experiments or laser ablation studies targeting various regions of the shell (e.g. Hathorne et al. 2003) could aid in answering this question.

A second factor which influences the accuracy of seawater [Ba] and alkalinity estimates made from Ba/Ca ratios is the measurement of D_{Ba} values (barium partition coefficients). Here, new D_{Ba} values for *O. umbonatus*, *M. barleeanus* and *U. peregrina* are presented. Although the D_{Ba} values for *Uvigerina* compare well between this study and those found by previous studies (Figure 3.19), the D_{Ba} values of different species are offset from one another (Figure 3.19). Furthermore, the spread in D_{Ba} values is greater amongst benthic species than planktic species (Figure 3.19). This suggests that for benthic foraminifera it may be particularly important to use D_{Ba} values on a 'per-species' basis rather than applying a collective D_{Ba} value as in the case of some planktic foraminifera. Differences in D_{Ba} values between species may be caused by contrasting ambient [Ba] at their habitation depths within sediments, species-specific vital effects, or a combination of both of these factors. This could be assessed further by using laboratory culturing experiments, or by pairing foraminiferal sample collections with porewater measurements.

In order to use Ba/Ca ratios to accurately reconstruct seawater [Ba] and hence as a proxy for ocean circulation or alkalinity, it is necessary to ensure that Ba/Ca ratios are controlled solely by ambient barium concentrations, or if other controls do exist that they are accounted for by calibration curves. Mg/Ca-derived temperatures have been used to investigate the effect of temperature on Ba/Ca ratios in this core. In agreement with previous authors, no temperature effects are found. Ba/Ca ratios might, however, be influenced by post-depositional dissolution. Post-depositional dissolution of foraminifera appears to be minimal in this core, so the effect of this on Ba/Ca ratios cannot be thoroughly evaluated here and future studies would therefore be beneficial. Lastly, given that barite cycling is linked to productivity, it might be expected that seawater [Ba] and hence foraminiferal Ba/Ca would be affected by changes in productivity in the overlying water column. However, despite $\delta^{13}C$ evidence for variable productivity at this site, Ba/Ca ratios remain approximately constant throughout sediment core BC387-2, suggesting that productivity-driven changes in seawater [Ba] in the overlying water column have a negligible impact on benthic foraminiferal Ba/Ca ratios. Given that this is a relatively shallow site in a highly-productive region, this finding endorses the use of benthic foraminiferal Ba/Ca ratios as a proxy for ocean circulation and alkalinity.

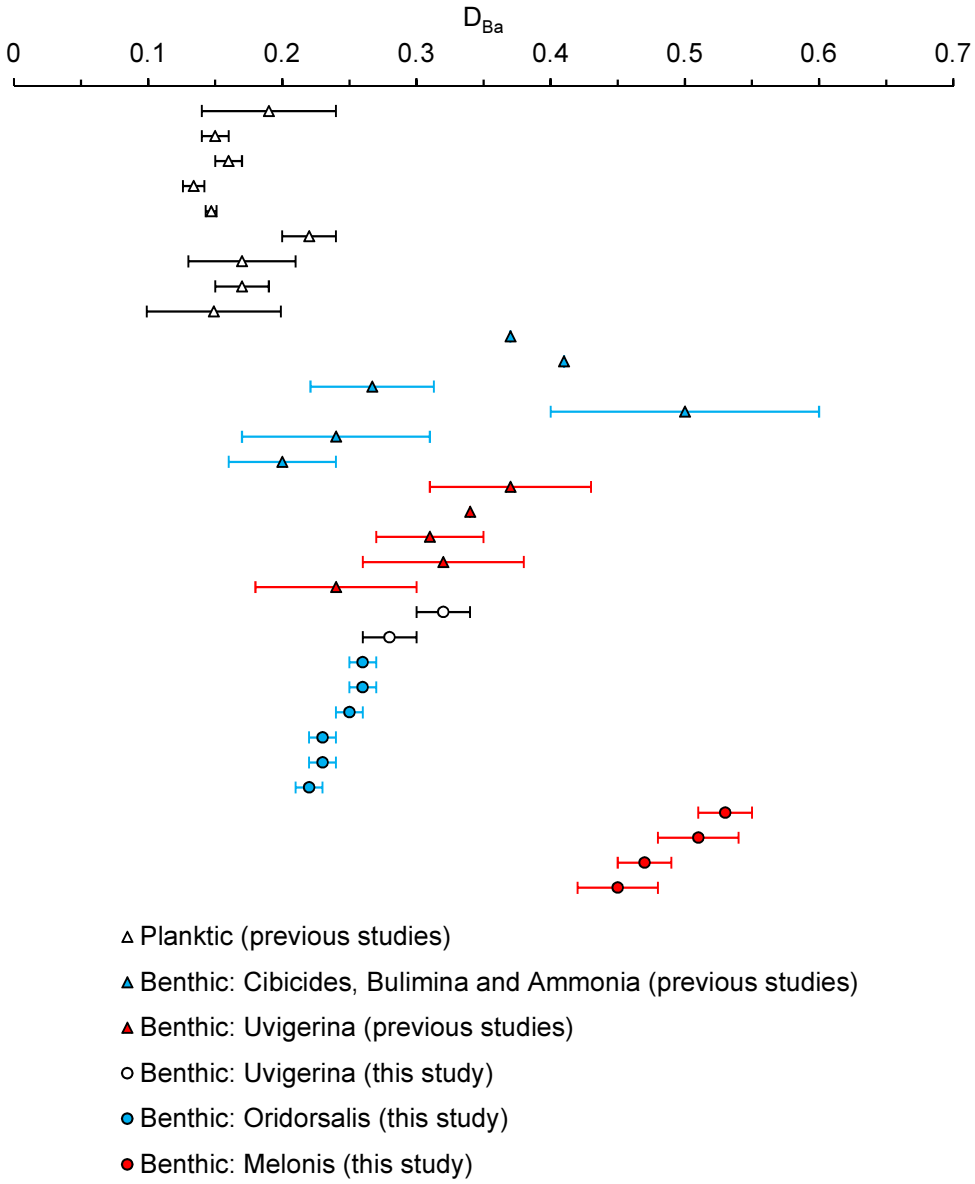

Figure 3.19. D_{Ba} values for planktic and benthic foraminifera measured in previous studies (as shown in Table 3.3, where references for these data are provided) and this study (tabulated in Table 3.4). Error bars on the previously-published data are shown as provided in those studies. Error bars on the data of this study were calculated as described in Section 3.5.3 'Foraminiferal uptake of barium: D_{Ba} values'.

Chapter 4

Foraminiferal Ba/Ca in the Holocene and Marine Isotope Stage 5e

4.1 Abstract

A full understanding of the mechanisms governing climatic variability is vital for predicting and therefore mitigating future climate change. Comparisons of the Holocene with the previous interglacial period can be useful in this regard, because the previous interglacial period had higher atmospheric carbon dioxide concentrations than the pre-industrial Holocene and was warmer than present so may provide an analogue for the future. In glacial-interglacial cycles, deep Atlantic carbon storage and release has been invoked as a dominant control over atmospheric carbon dioxide changes. In contrast, a recent study has suggested that a slow-down in Southern Ocean deep water formation caused an increase in deep water carbon storage during the last interglacial, a time of relatively high atmospheric carbon dioxide concentrations compared to the Holocene. Here, these differences in ocean circulation between the last interglacial period and the Holocene are investigated further using benthic foraminiferal Ba/Ca ratios, a proxy for ocean circulation and seawater alkalinity. This study finds that Ba/Ca ratios, and by inference seawater dissolved barium concentrations and seawater alkalinity, were significantly higher in Southern Ocean waters during the last interglacial period compared to the Holocene. This finding supports the hypothesis that a slow-down in Southern Ocean deep water formation, known as a stagnation event, resulted in enhanced oceanic carbon storage in the last interglacial compared to the Holocene, although the timing of this event could be clarified. The presence of surplus atmospheric carbon dioxide in the last interglacial compared to the Holocene cannot therefore be attributed to weakened deep water carbon storage, unlike in glacial-interglacial cycles, suggesting that the mechanism of climatic change between the last interglacial and the Holocene (and therefore, perhaps between the present and the future) was different to that driving glacial-interglacial change. Furthermore, the stagnation event mechanism only invokes a relatively minor change in water mass formation, which contrasts with the substantial water mass reorganisations involved in the glacial-interglacial mechanism. These contrasts between glacial-interglacial and Holocene-MIS 5e variability have implications for predictions of future climate change.

4.2 Introduction

The ongoing anthropogenically-driven increase in atmospheric carbon dioxide concentrations (pCO_{2atm}) and associated warming of global temperatures poses many risks, including sea level rise, increased severity and frequency of extreme weather events, ecological disruptions, reduced crop yields and movement of water resources (IPCC 2013; IPCC 2014). A complete as possible understanding of the mechanisms controlling climatic variability will aid in predicting the effects of anthropogenic climate change and thereby our ability to mitigate them. Insights can be gained by studying climate fluctuations within the current interglacial period, the Holocene, and by comparing this epoch to previous interglacial periods throughout the Quaternary. Marine Isotope Substage 5e (MIS 5e) occurred at the height of the previous interglacial period (Shackleton et al. 2003). Temperatures were approximately 2 ºC warmer in the last interglacial than in the Holocene (Otto-Bliesner et al. 2006; Kaspar et al. 2005), pCO_{2atm} was up to ~20 ppmv greater (Figure 4.1; Lüthi et al. 2008; Petit et al. 1999) and eustatic sea level was ~9 m higher due to ice sheet collapse (O'Leary et al. 2013). These contrasts may have originated from differences in solar insolation driven largely by orbital precession (Berger & Loutre 1991). Studying MIS 5e can provide a window into a possible future scenario which may occur when the climate is warmed as a result of anthropogenic greenhouse gas emissions. Furthermore, understanding the mechanisms which caused the Holocene climate to differ from that of MIS 5e could elucidate the mechanisms of future climate change.

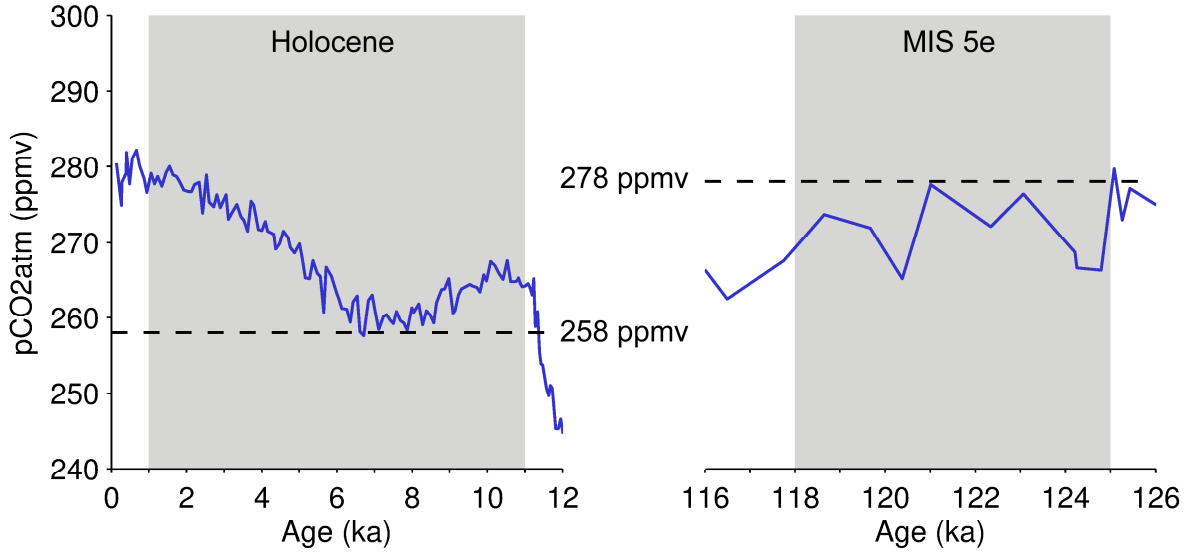

Figure 4.1. Composite pCO_{2atm} record from the EPICA Dome C and Vostok ice cores (Lüthi et al. 2008; Petit et al. 1999). The grey bars are the Holocene and MIS 5e intervals measured by this study.

The Holocene can be divided into several sub-epochs, such as the relatively warm mid-Holocene Climatic Optimum (~3.360 – 9.070 ka) and the cooler climatic reversal (9.070 – 11.460 ka) and Neoglacial (~0.100 – 3.360 ka) (Domack et al. 2001). Intra-Holocene climatic variations such as

these are thought to be driven by changes in solar insolation (e.g. Wanner et al. 2008; Nielsen et al. 2004). Similarly, differences between interglacials are attributed to differing solar insolation at these times (e.g. Tzedakis et al. 2009; Rohling et al. 2010). However, the precise feedback mechanism translating insolation variability into changes in specific components of the climate system such as atmospheric carbon dioxide concentration, sea level and temperature remains a subject of debate, both within and between interglacials (e.g. Tzedakis et al. 2009; Wanner et al. 2008; Rohling et al. 2010).

In glacial-interglacial cycles, ocean circulation changes and their impact on oceanic carbon storage are thought to be a critical component of climatic variability, so these may also play an important role in changes within and between interglacials. Ice core records show that atmospheric carbon dioxide concentrations are consistently ~80 – 100 ppmv lower in glacial periods (~180 – 200 ppmv) than in interglacial periods (~280 ppmv) (e.g. Barnola et al. 1987; Kawamura et al. 2003; Lüthi et al. 2008; Petit et al. 1999; Siegenthaler et al. 2005). The global carbon cycle can be separated into two cycles: a longer-term cycle involving the processes of chemical weathering, hydrothermal activity and volcanism; and a shorter-term cycle involving the terrestrial biosphere, soils (including permafrost) and oceans (dominated by inorganic carbon but also containing organic carbon in the marine biosphere and methane clathrates) (Archer 2010). Of these, it is the shorter-term cycle which must control the glacial-interglacial change in pCO_{2atm}, the longer-term cycle being too slow to supply and remove 80 – 100 ppmv CO_2 from the atmosphere on glacial-interglacial timescales (Archer 2010). According to a variety of terrestrial evidence and modelling studies, the terrestrial biosphere and soils experienced a decrease in carbon storage during the Last Glacial Maximum (LGM) relative to the Holocene (e.g. Adams et al. 1990; Beerling 1999; Ciais et al. 2012; Crichton et al. 2013; Crowley 1995; Prentice et al. 1993; Van Campo et al. 1993). This is supported by benthic foraminiferal $\delta^{13}C$ data which show that the oceans' inorganic carbon was isotopically lighter during glacials than in interglacial periods (e.g. Cortese et al. 2007), indicating that in glacial periods a smaller amount of isotopically light (organic) carbon was locked away from the ocean-atmosphere system (Archer 2010). This means that isotopically light carbon presents a source of carbon to the ocean-atmosphere system in glacial periods and vice versa, which is the opposite of that required to explain the lower pCO_{2atm} of glacial periods (Archer 2010). This excludes all of the organic carbon pools (the terrestrial and marine biosphere, methane clathrates and soils) from having contributed to the glacial pCO_{2atm} sink (Archer 2010). In fact, because the organic carbon pool was smaller at the LGM than in the Holocene, this adds a further 15 – 45 ppmv CO_2 on top of the 80 – 100 ppmv that must be sourced in order to reach the interglacial concentration (Archer 2010). The remaining candidate for the glacial-interglacial variation in pCO_{2atm} is the inorganic carbon pool in the oceans, so it may be deduced that some oceanic mechanism involving inorganic carbon storage must be an important factor in the glacial-interglacial pCO_{2atm} variation (Archer 2010). The large size of the oceanic carbon pool and the oceans' ability to equilibrate with the atmosphere over the required timescales lend weight to this argument (Archer 2010). The Southern Ocean may have particular importance because it is the region of Antarctic Bottom Water (AABW) formation and is thus

the window to the deep ocean, where an appropriate amount of carbon could be stored on the required timescales for glacial-interglacial variability (e.g. Sigman et al. 2010; Burke & Robinson 2012). Furthermore, this region is rich in nutrients which are incompletely utilised by primary productivity and is therefore capable of sequestering greater amounts of carbon from the atmosphere through enhanced biological uptake of carbon and export of this carbon to depth (e.g. Sigman et al. 2010).

Given the importance of ocean circulation in glacial-interglacial climate variability, and considering that the timescales involved in glacial-interglacial variability are similar to those of changes within and between interglacials (namely, millennial-scale changes) it is likely that this is also an important factor in interglacial variability. Changes in carbon storage caused by ocean circulation can be traced using Ba/Ca ratios in benthic foraminifera. This is because dissolved barium and carbonate alkalinity have strikingly similar oceanic distributions, caused by their similar uptake and regeneration sites and subsequent redistribution by oceanic circulation (e.g. Lea 1993). This proxy has successfully been used to study glacial-interglacial variability, showing that deep Atlantic barium storage (and by inference, carbonate alkalinity and thus carbon) was greater during glacial periods (Hall & Chan 2004b; Lea & Boyle 1990a; Lea & Boyle 1990b; Lea 1990; Lea 1993; Lea 1995).

Here, the Ba/Ca proxy for ocean circulation and carbon storage is used to investigate both intra-Holocene and Holocene-MIS 5e variability in sediment cores from the southern frontier of the South Atlantic Ocean at approximately 53 ºS, which is bathed in waters derived from the Southern Ocean. The aims of this study are to contribute towards our understanding of intra-Holocene variability and Holocene-MIS 5e contrasts in the Southern Ocean, by using the Ba/Ca proxy to investigate how ocean circulation distributed barium (and by inference, carbon) during these times. A full understanding of Southern Ocean circulation during interglacial periods is important for piecing together the complete picture of interglacial climatic variability.

4.3 Methods

4.3.1 Sediment collection and oceanographic setting

Sediment cores GC528 and GC642 were collected via gravity corer during cruises JR244 and JR257 of the RRS *James Clark Ross* (Dr J. Roberts, pers. com. 2015). Together, these two cores cover the past ~230 kyr (Dr J. Roberts, pers. com. 2015). GC528, which contains the Holocene section, was first obtained and then the older sediments of GC642 were collected from a site approximately 3 km away and 20 m upslope where sediments were more condensed (Dr J. Roberts, pers. com. 2015). Locations, depths (~600 m) and collection dates for these cores are provided in Table 4.1. The sampling sites are located on the Falkland Plateau (Figure 4.2), adjacent to Burdwood Bank, a highly-productive region (Schejter et al. 2016). Typical seafloor temperatures are 4 – 5 ºC (Schejter et al. 2016). This site is positioned to the north of the Antarctic Circumpolar Current (ACC), in the Subantarctic Zone (Brown et al. 2004).

Between the subtropical high at ~30 ºS and the subpolar low at ~60 ºS the prevailing winds are westerlies (Brown et al. 2004). These westerly winds blow clockwise around Antarctica, generating the westerly-flowing ACC via geostrophic flow (Brown et al. 2004). ACC surface waters – Antarctic Surface Water (ASW) – are deflected away from Antarctica by Ekman transport and at the Antarctic Polar Front (also known as the Antarctic Convergence) which encircles Antarctica at ~50 – 60 ºS, these waters subduct beneath Sub-Antarctic Surface Water, becoming Antarctic Intermediate Water (Brown et al. 2004). The Malvinas Current (also known as the Falklands Current) branches off from the ACC downstream of the Drake Passage, following the contours of the South American continental shelf (Piola & Gordon 1989; Peterson 1992; Piola & Matano 2009; Piola et al. 2010; Piola et al. 2013). This current carries Antarctic Surface Water to the core site (Figure 4.2; Figure 4.3) which would otherwise be bathed in Sub-Antarctic Surface Water. ASW derives from upwelled North Atlantic Deep Water (NADW), freshened by inputs of meltwater and precipitation (Figure 4.3; Brown et al. 2004). Like the ACC, the Malvinas Current is a geostrophic flow (Vivier & Provost 1999). The mean horizontal flow of the Malvinas Current is barotropic (Vivier & Provost 1999), meaning that its density and hence flow path is determined by pressure, and horizontally-flowing jets within the Malvinas Current have been observed at depths up to approximately 2000 m (Piola et al. 2013). In contrast, its vertical structure is controlled by a combination of both barotropic and baroclinic (wherein density is determined by both pressure and temperature) flows (Vivier & Provost 1999). This was determined using current meters moored at various depths within the Malvinas Current (Vivier & Provost 1999).

Table 4.1. Details of sediment cores GC528 and GC642 (Dr J. Roberts, pers. com. 2015).

	Latitude	Longitude	Depth	Collection date
GC528	53º0.6'S	58º2.4'W	598 m	29/01/11
GC642	53º0.0'S	58º5.1'W	578 m	30/03/12

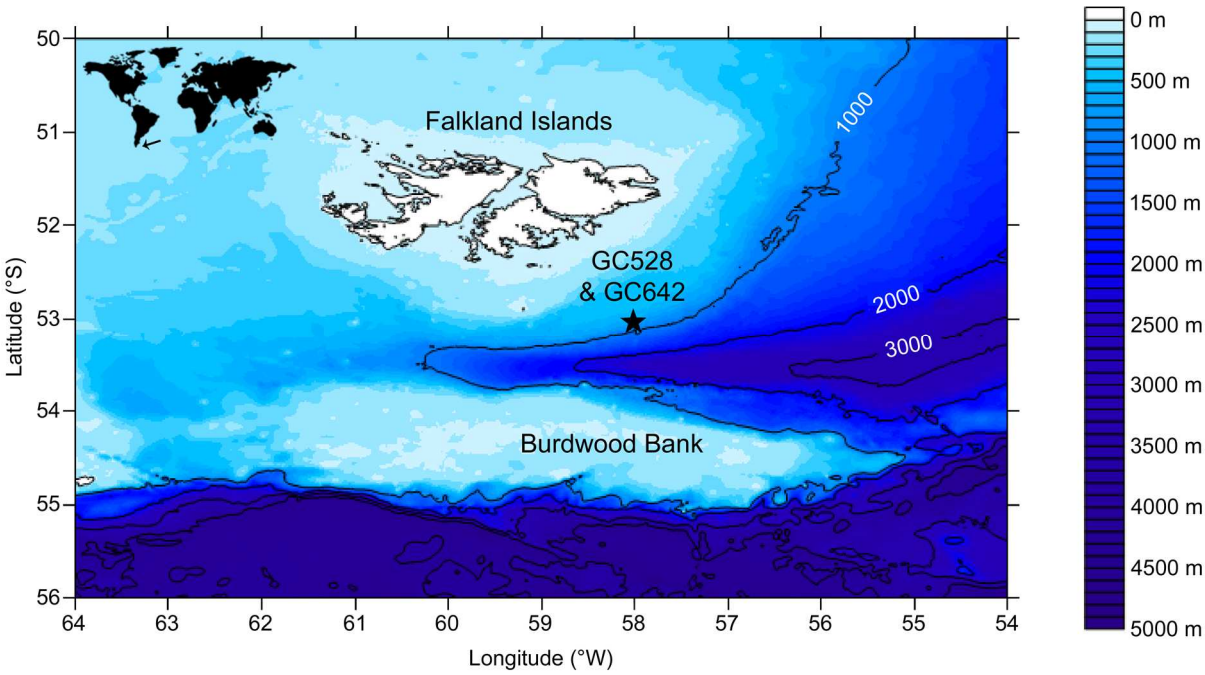

Figure 4.2. Location of sediment cores GC528 and GC642.

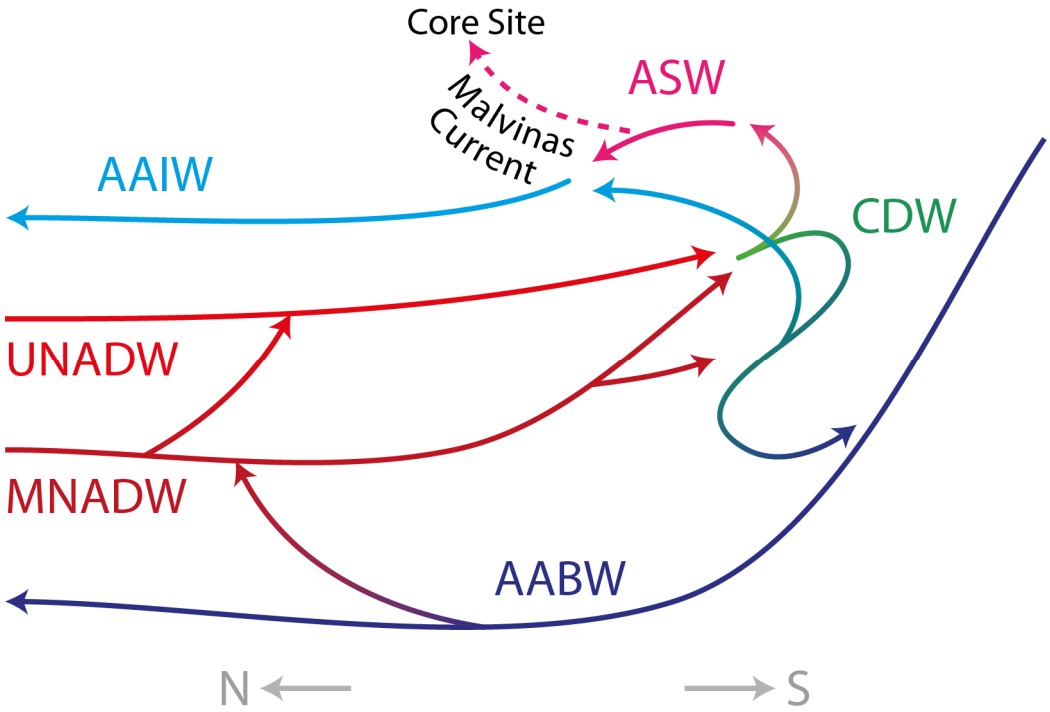

Figure 4.3. Schematic diagram of thermohaline circulation in the southwest Atlantic Ocean and the Atlantic sector of the Southern Ocean (adapted from Curry & Webster 1999). ASW = Antarctic Surface Water, AAIW = Antarctic Intermediate Water, CDW = Circumpolar Deep Water, UNADW = Upper North Atlantic Deep Water, MNADW = Middle North Atlantic Deep Water and AABW = Antarctic Bottom Water. Not to scale.

4.3.2 Age models

An age model for sediment core GC528, produced using radiocarbon dating of *Uvigerina bifurcata,* has been published by Roberts et al. 2016. Reservoir age constraints were provided by paired U-Th/^{14}C dating of corals (Burke & Robinson 2012). Full details are available in the supplementary information of Roberts et al. 2016. An age model for sediment core GC642 was produced via alignment of benthic foraminiferal $\delta^{18}O$ with the 'LR04' benthic $\delta^{18}O$ stack (Lisiecki & Raymo 2005) (Dr J. Roberts, pers. com. 2015).

4.3.3 Foraminifer picking

Foraminifera were picked from pre-dried sediment samples, provided by Dr J. Roberts, at sediment depths corresponding to the Holocene (0 – 11.7 ka) and the 'plateau' section of MIS 5e which comprises the warmest section of the last interglacial (approximately 116 – 127 ka; Shackleton et al. 2003). *Melonis barleeanus* were picked from the 250 – 355 μm size fraction under optical microscope using a brush wetted with reverse-osmosis purified (RO) water. Epifaunal species would have been preferable for reconstructing bottom water properties, but these were not sufficiently available.

4.3.4 Trace metals

Ba/Ca, Mg/Ca and Sr/Ca ratios were measured using the methods detailed in Chapter 2 'Trace Metal Methods'. These methods comprised: a cleaning procedure to remove clays, metal oxides, organic matter and barite from foraminifer samples; measurement of isotope intensities via inductively coupled plasma mass spectrometry using a Thermo Finnigan Element 2; offline calculation of trace metal ratios; and conversion to units of concentration via measurements of a custom-made bracketing standard. In addition to screening for contamination, Mn/Ca ratios can be used as a proxy for bottom water oxygenation (Koho et al. 2015; McKay et al. 2015) so these are included alongside the other trace metal ratios.

4.3.5 Seawater barium concentration and alkalinity

Seawater [Ba] was calculated from foraminiferal Ba/Ca using the following equation:

$$[\mathrm{Ba}]_{\mathrm{sw}} = \frac{\left(\frac{\mathrm{Ba}}{\mathrm{Ca}}\right)_{\mathrm{f}}}{\mathrm{D}_{\mathrm{Ba}}} \times [\mathrm{Ca}]_{\mathrm{sw}} \qquad (4.1)$$

Where $[Ba]_{sw}$ is the barium concentration of seawater, $(Ba/Ca)_f$ is the foraminiferal Ba/Ca ratio, D_{Ba} is the barium partition coefficient for *Melonis barleeanus* and $[Ca]_{sw}$ is the calcium concentration of seawater. The D_{Ba} value for *M. barleeanus* was calculated in Chapter 3 'Evaluating the Ba/Ca Proxy'. In order to encompass the uncertainty arising from the calculation of the D_{Ba} value, the minimum and maximum computed D_{Ba} values of 0.42 and 0.55 were used, resulting in an upper and lower estimate of seawater [Ba] per Ba/Ca measurement. The seawater calcium concentration was set to 10.3 mM (Dickson & Goyet 1994). Errors were propagated from internal precision (σ) using Equation 4.2.

$$\sigma_{[Ba]_{sw}} = \frac{\sigma_{\left(\frac{Ba}{Ca}\right)_f}}{D_{Ba}} \times [Ca]_{sw} \qquad (4.2)$$

Alkalinity was estimated from seawater [Ba] using Equation 4.3 (Lea 1993):

$$Alk_{sw} = \left(\frac{[Ba]_{sw}}{\rho_{sw}} + 1515\right) \times \frac{1}{0.67} \qquad (4.3)$$

Where Alk_{sw} is seawater alkalinity in µequiv/kg, $[Ba]_{sw}$ is seawater barium concentration in nM and ρ_{sw} is seawater density in kg/l. Seawater density was calculated from estimated local temperature (4 – 5 ºC; Schejter et al. 2016) and salinity (34.2; Figure 4.4) (Maidment 1993), producing a density value of ρ_{sw} = 1.03 kg/l. Errors were calculated by propagating internal precision (σ) using Equation 4.4.

$$\sigma_{Alk_{sw}} = \frac{\sigma_{[Ba]_{sw}}}{\rho_{sw}} \times \frac{1}{0.67} \qquad (4.4)$$

4.3.6 Temperatures

Temperatures were calculated from *M. barleeanus* Mg/Ca ratios using Equation 4.5 (Kristjánsdóttir et al. 2007), where Mg/Ca is the foraminiferal Mg/Ca ratio and T is the estimated bottom water temperature. This equation rearranges to Equation 4.6. Temperature uncertainties were calculated by propagating Mg/Ca internal precision, which was itself calculated using the method described in Section 2.3.6 'Calculation of trace metal ratios'. This error propagation was performed using Equation 4.7.

$$\frac{Mg}{Ca} = 0.658 \pm 0.07 \times e^{0.137 \pm 0.020 \times T} \qquad (4.5)$$

$$T = \left(\ln \frac{\frac{Mg}{Ca}}{0.658 \pm 0.07}\right) \times \frac{1}{0.137 \pm 0.020} \qquad (4.6)$$

$$\sigma_T = \frac{\sigma_{Mg/Ca}}{0.658} \times \frac{1}{Mg/Ca} \times \frac{1}{0.137} \qquad (4.7)$$

4.3.7 Statistical analyses

To statistically compare the Holocene and MIS 5e data, two-tailed T-tests were used to determine whether the means of the two populations are significantly different. Either a T-test for two populations of equal variance (Student's T-test) or a T-test for two populations of unequal variance (Welch's T-test) was used, depending on the result of a prior F-test. These tests were performed at 95 % and 99 % confidence levels. The F-statistic was calculated by dividing the larger variance of the two populations by the variance of the other population. This was then compared with a critical value taken from an F-test table using the degrees of freedom of each of the two populations, where degrees of freedom is sample size minus one. For Student's T-test, the T-statistic was calculated using Equation 4.8 and compared with a critical value taken from a T-test table using the degrees of freedom number calculated by Equation 4.9. For Welch's T-test, the T-statistic was calculated using Equation 4.10 and compared with a critical value taken from a T-test table using the degrees of freedom number calculated

using Equation 4.11. In these equations, t is the T-statistic, D.F. is the degrees of freedom number, μ_1 and μ_2 are the means of the two populations, σ_1 and σ_2 are their standard deviations and n_1 and n_2 are the populations' sample sizes.

$$t = \frac{\mu_1 - \mu_2}{\sqrt{\frac{\left((n_1-1)\times\sigma_1^2\right)+\left((n_2-1)\times\sigma_2^2\right)}{n_1+n_2-2}} \times \sqrt{\frac{1}{n_1}+\frac{1}{n_2}}} \qquad (4.8)$$

$$D.F. = n_1 + n_2 - 2 \qquad (4.9)$$

$$t = \frac{\mu_1 - \mu_2}{\sqrt{\frac{\sigma_1^2}{n_1}+\frac{\sigma_2^2}{n_2}}} \qquad (4.10)$$

$$D.F. = \frac{\left(\frac{\sigma_1^2}{n_1}+\frac{\sigma_2^2}{n_2}\right)^2}{\frac{\left(\frac{\sigma_1^2}{n_1}\right)^2}{n_1-1}+\frac{\left(\frac{\sigma_2^2}{n_2}\right)^2}{n_2-1}} \qquad (4.11)$$

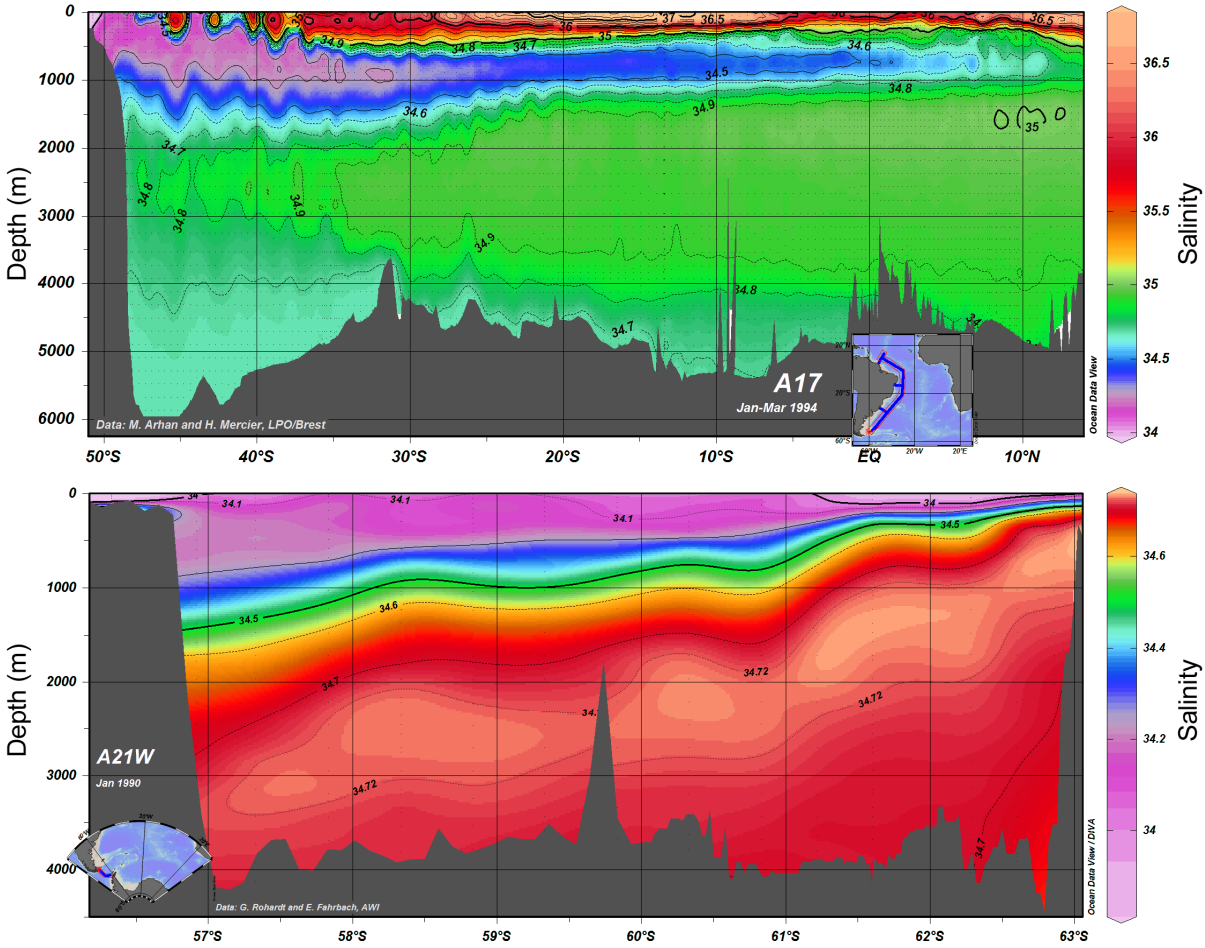

Figure 4.4. Salinity in the vicinity of the core site. Figures by eWOCE Gallery.

4.4 Results

Foraminiferal trace metal ratios (Ba/Ca, Mg/Ca, Sr/Ca and Mn/Ca) for both the Holocene and MIS 5e are presented in Figure 4.5, along with seawater barium concentration and alkalinity reconstructions and Mg/Ca-derived temperatures. The Holocene temperature data measured by Roberts et al. 2016 in the same sediment core (GC528) are also plotted for comparison with the results of this study. The mean values of each of these parameters in the Holocene and MIS 5e are provided in Table 4.2. The results of the statistical analyses (F-tests for and T-tests) are provided in Table 4.3.

Table 4.2. Mean values in the Holocene and MIS 5e.

	Holocene	MIS 5e
Ba/Ca ± 2σ (μmol/mol)	3.65 ± 0.05	4.03 ± 0.08
Ba/Ca ± 2σ (μmol/mol) [a]	3.56 ± 0.05	Not applicable
Mg/Ca ± 2σ (mmol/mol)	0.89 ± 0.01	1.17 ± 0.01
Temperature ± 2σ (ºC)	2.20 ± 0.12	4.21 ± 0.14
Mn/Ca ± 2σ (μmol/mol)	3.71 ± 0.08	26.49 ± 0.66
Sr/Ca ± 2σ (mmol/mol)	1.25 ± 0.01	1.27 ± 0.02

a) Omitting the peak value of ~5 μmol/mol. σ = internal precision.

Table 4.3. Results of F-tests and T-tests comparing the Holocene data to the MIS 5e data.

	F-test result: variances are equal or unequal?		T-test result: means are significantly different?	
Confidence level	95 %	99 %	95 %	99 %
Ba/Ca	Equal	Equal	No	No
Ba/Ca [a]	Unequal	Unequal	Yes	Yes
Mg/Ca	Equal	Equal	Yes	Yes
Temperature	Equal	Equal	Yes	Yes
Mn/Ca	Equal	Equal	Yes	Yes
Sr/Ca	Unequal	Unequal	Yes	No

a) Omitting the peak value of ~5 μmol/mol.

For two populations of equal variance, Student's T-test was used.

For two populations of unequal variance, Welch's T-test was used.

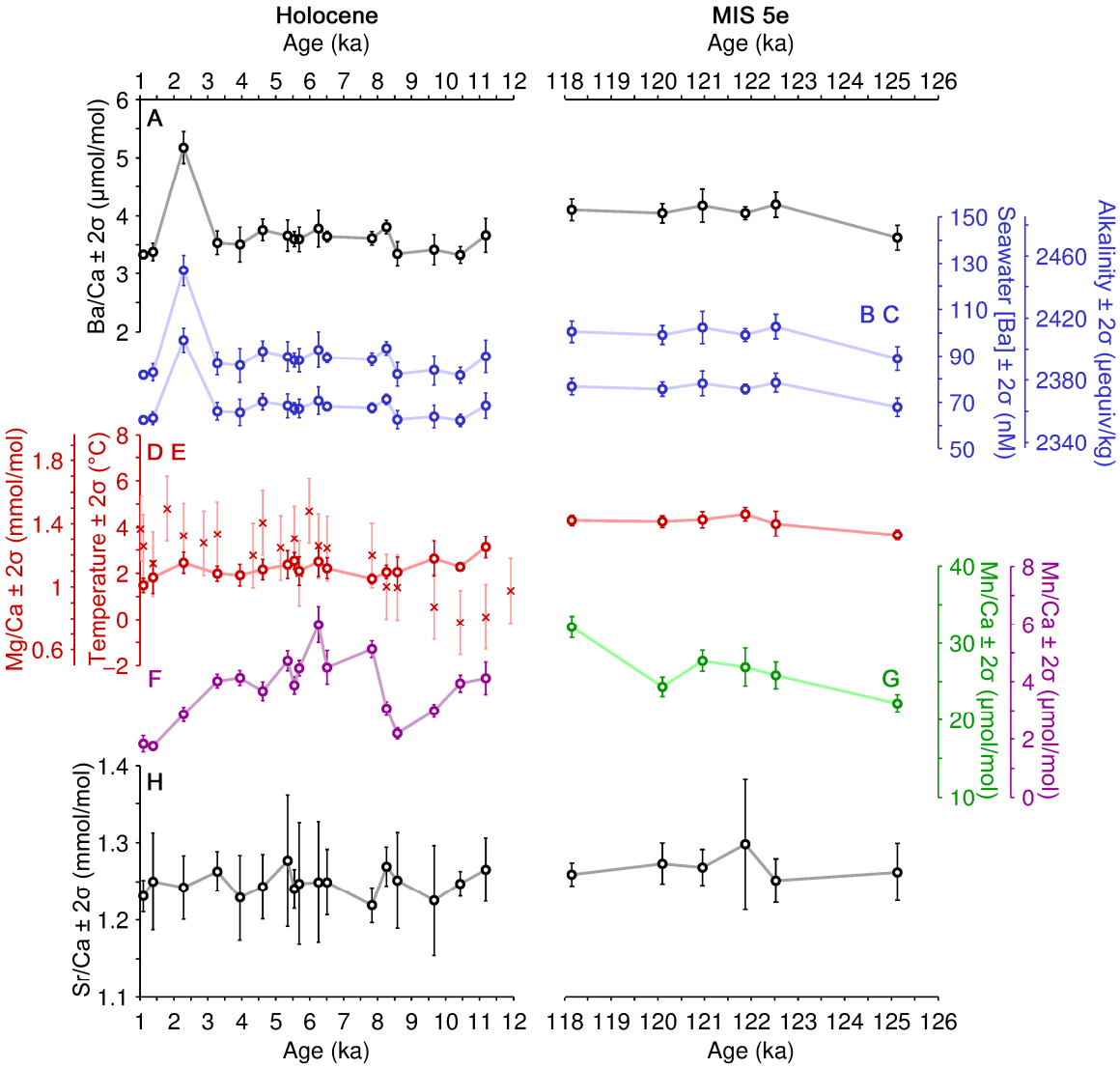

Figure 4.5. *M. barleeanus* data from the Holocene (GC528) and MIS 5e (GC642): A) Ba/Ca; B) seawater [Ba] calculated from Ba/Ca using two different barium partition coefficients; C) seawater alkalinity estimated from seawater [Ba] using the equation of Lea 1993; D) Mg/Ca and E) Mg/Ca-derived temperatures from *M. barleeanus* using the temperature calibration of Kristjánsdóttir et al. 2007 (circle symbols) and from *Uvigerina* spp. with ± 1.4 ºC uncertainties (Roberts et al. 2016) (cross symbols) (the Mg/Ca axis does not apply to the cross symbols); F) and G) Mn/Ca with different vertical axes for the Holocene (F) and MIS 5e (G); and H) Sr/Ca. ± 2σ errors for seawater [Ba], alkalinity and temperature were propagated from Ba/Ca and Mg/Ca uncertainties. All data are plotted using the age model of Roberts et al. 2016.

4.5 Discussion

4.5.1 Sr/Ca ratios: testing for dissolution

Foraminiferal Sr/Ca ratios are affected by post-depositional alteration of foraminifera and so can be used to check that samples have not been compromised by this. Dissolution of foraminiferal calcium carbonate within sediments decreases its Sr/Ca ratio (Brown & Elderfield 1996) because areas of foraminifer shells which are relatively rich in strontium are more susceptible to dissolution (Brown & Elderfield 1996). Although the T-test results show that mean Sr/Ca is significantly higher in MIS 5e than in the Holocene at a 95 % confidence level (Table 4.2; Table 4.3), at a 99 % confidence level it is not significant (Table 4.3). Furthermore, the maximum mean difference is only 0.05 mmol/mol higher (Table 4.2) and by visual inspection, Sr/Ca stays approximately constant down-core across the Holocene and MIS 5e within ± 2σ (Figure 4.5). In summary, across both the Holocene and MIS 5e Sr/Ca ratios remain approximately constant, suggesting that the foraminiferal trace metal ratios have not been significantly altered by post-depositional dissolution.

4.5.2 Mn/Ca ratios as a proxy for bottom water oxygenation

Mn/Ca ratios in benthic foraminiferal calcium carbonate can be used as a proxy for bottom water dissolved oxygen concentration (Koho et al. 2015; McKay et al. 2015). Mn is incorporated into foraminiferal calcium carbonate in proportion to the dissolved Mn concentration of ambient water (Koho et al. 2015; McKay et al. 2015). If metal oxides are removed from foraminifera prior to measurement using a reductive cleaning technique, their Mn/Ca ratio is therefore indicative of the ambient Mn concentration in which they grew. Because porewater Mn concentrations are themselves affected by the amount of dissolved oxygen present, due to redox reactions, benthic foraminiferal Mn/Ca can be used as a proxy for bottom water oxygenation (Koho et al. 2015; McKay et al. 2015). The mechanism behind this proxy is explained below.

When bottom waters are oxygenated, deeper low-oxygen sediments are overlain by shallower high-oxygen sediments, because sediment oxygenation decreases with depth from the sediment-water interface due to organic matter remineralisation (Koho et al. 2015). In shallower high-oxygen sediments, Mn oxides precipitate and are buried; whereas in the deeper low-oxygen sediments, this buried Mn is reduced back to aqueous Mn^{2+} (Koho et al. 2015). The aqueous Mn^{2+} then diffuses back upwards towards the sediment-water interface, until it reaches the high-oxygen sediment layer and is re-oxidised (Koho et al. 2015). This cycle continues and, because more Mn is increasingly added to the sediment from the water column, the burial of Mn oxides exceeds the upward transport of Mn^{2+} such that there is a net increase of Mn^{2+} within the deeper low-oxygen sediment layer (Koho et al. 2015). The more oxygenated the shallower sediments are, the more Mn is oxidised and buried and the greater the build-up of Mn^{2+} in deeper sediments (Koho et al. 2015). Therefore, in deep-dwelling foraminifera that live in the low-oxygen part of the sediment, higher Mn/Ca (resulting from higher ambient Mn^{2+}) is indicative of greater bottom water oxygenation (Koho et al. 2015). When bottom waters have low

oxygen, there is no high-oxygen sediment layer and Mn either does not precipitate as an oxide or if it does is immediately reduced back to aqueous Mn^{2+} which escapes into the water column, such that no build-up of Mn^{2+} occurs in the deeper sediments and foraminifera therefore record lower Mn/Ca ratios (Koho et al. 2015). In summary, in deeper-dwelling foraminifera that inhabit the low-oxygen sediment layer, higher Mn/Ca indicates greater oxygenation of bottom waters and lower Mn/Ca indicates lesser oxygenation of bottom waters (Koho et al. 2015).

In shallow-dwelling foraminifera, when bottom waters are more oxygenated there is greater precipitation of Mn oxides resulting in lower porewater Mn concentrations (Koho et al. 2015; McKay et al. 2015). Correspondingly, when bottom waters are less oxygenated there is less precipitation of Mn oxides so porewater Mn concentrations are higher (Koho et al. 2015; McKay et al. 2015). This means that, in contrast to deeper-dwelling species, in shallower-dwelling foraminifera high Mn/Ca indicates lesser oxygenation of bottom waters and low Mn/Ca indicates greater oxygenation of bottom waters (Koho et al. 2015; McKay et al. 2015). The relationship between bottom water oxygenation and foraminiferal Mn/Ca is therefore opposite for deeper-dwelling versus shallower-dwelling foraminifera. It is consequently important to consider the habitat of the species in use, in order to assess which of these two interpretations is more appropriate for that species.

Melonis barleeanus is categorised as an infaunal species (Corliss 1985) but its sub-categorisation as either shallow, intermediate or deep infaunal is less certain, with peak abundances recorded at depths ranging from approximately 1 to 4 cm (Corliss 1985; Corliss 1991; Buzas et al. 1993). This is because foraminifera may migrate to different depths within sediments due to factors such as food supply, leading to uncertainties in their habitat classification (Tachikawa & Elderfield 2002). Koho et al. 2015 consider *M. barleeanus* an 'intermediate to deep infaunal' species for which the 'deep-dwelling' version of the Mn/Ca proxy is appropriate. However, the *M. barleeanus* Mg/Ca-derived temperatures agree well with those measured in *Uvigerina* spp. (Figure 4.5), a species which can vary widely in habitat depth (Loubere & Gary 1990) but has most often been observed in the top 0.5 cm of sediment (Corliss 1991; Buzas et al. 1993). Therefore, perhaps in these sediments *M. barleeanus* should be classified as 'shallow infaunal' and its Mn/Ca interpreted using the 'shallow-dwelling' version of the proxy. Using this interpretation, the high Mn/Ca ratios measured at ~4 – 7 ka (Figure 4.5) are consistent with the mid-Holocene Climatic Optimum at ~3.360 – 9.070 ka (Domack et al. 2001), a time of high productivity (Domack et al. 2001) and hence reduced oxygenation. In the following discussion, the 'shallow-dwelling' version of the Mn/Ca proxy will be used to interpret *M. barleeanus* Mn/Ca ratios.

4.5.3 Comparison of the Holocene with MIS 5e

Enhanced deep ocean carbon storage during glacial periods is widely accepted as an important factor in glacial-interglacial pCO_{2atm} change (e.g. Archer 2010; Sigman et al. 2010). Given that during the last interglacial pCO_{2atm} was up to ~20 ppmv greater than in the pre-industrial Holocene (Figure 4.1, Lüthi et al. 2008; Petit et al. 1999), it might be expected that less carbon was stored in the deep ocean during MIS 5e than in the Holocene. ASW derives from upwelled North Atlantic Deep Water (NADW), which is itself influenced by AABW (Figure 4.3). An increase in barium (and by inference, carbon) storage within AABW should therefore cause ASW barium concentration to also increase. However, at this site (which is bathed in ASW) Holocene Ba/Ca ratios are significantly lower on average than those of MIS 5e (Figure 4.5; Table 4.2; Table 4.3) suggesting that seawater barium concentrations were lower during the Holocene (Figure 4.5). Using the Ba/Ca proxy for seawater alkalinity of Lea 1993, this finding implies that seawater alkalinity was not significantly higher in the Holocene than in MIS 5e (Figure 4.5) and therefore cannot support the hypothesis that during the Holocene a greater amount of carbon was stored in the ocean than at MIS 5e. This suggests that the mechanisms controlling Holocene-MIS 5e contrasts are different to those driving glacial-interglacial changes.

A possible explanation for the lower Ba/Ca ratios of the Holocene compared to MIS 5e is that during MIS 5e there was a slow-down in the production of AABW (a 'stagnation event') (Hayes et al. 2014). When porewater dissolved oxygen concentrations decrease, either due to increased inputs of organic matter (the remineralisation of which uses oxygen) or decreased oxygen concentrations in overlying bottom waters, a greater amount of aqueous U(VI) is reduced to less-soluble U(IV) within sediments (Klinkhammer & Palmer 1991). Concentrations of authigenic uranium (aU) in sediments can therefore provide insights into bottom water oxygenation and primary productivity (Klinkhammer & Palmer 1991). In sediments from ODP Site 1094 in the Atlantic sector of the Southern Ocean, Hayes et al. 2014 observe a peak in aU at ~127 ka, indicating that porewater oxygen concentrations were lower at this time (Figure 4.6; Hayes et al. 2014). This aU peak at ~127 ka occurs in the absence of a concomitant increase in biological productivity, measured via biogenic opal flux, or lateral transport of organic matter to the site, examined using the focusing factor (Hayes et al. 2014). This suggests that a decrease in bottom water dissolved oxygen concentrations was responsible for this enhanced deposition of uranium (Hayes et al. 2014). Hayes et al. 2014 attribute this low-oxygen event to a slow-down in AABW formation. Their hypothesis is supported by sortable silt evidence from the Agulhas basin: sortable silt size is low at ~127 ka (Figure 4.6; Krueger et al. 2012), suggesting that AABW flow was slowed-down at this time (Hayes et al. 2014; Krueger et al. 2012). This resulted in an oxygen minimum and increased carbon storage within AABW because primary productivity, which uses oxygen, and the 'biological pump', which exports carbon from the surface to depth, continued despite the slow-down of AABW export, leading to greater oxygen depletion and carbon accumulation (Hayes et al. 2014). Hayes et al. 2014 suggest that this stagnation event was caused either by increased meltwater inputs into the areas of AABW production or by a strengthening of NADW formation. In contrast to the glacial-

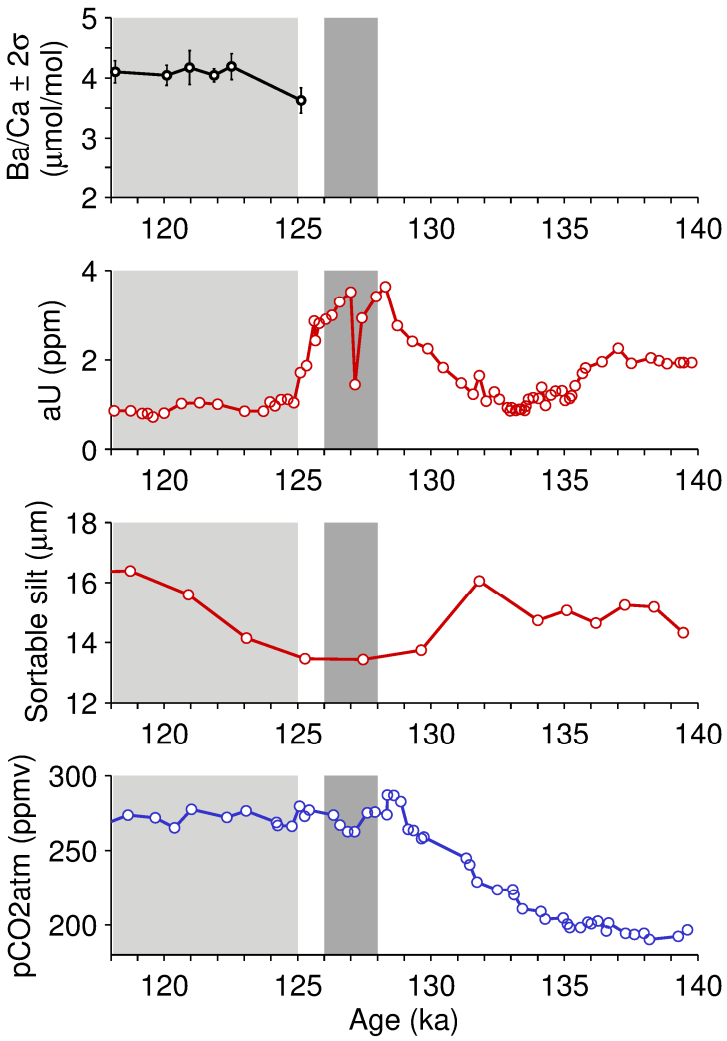

Figure 4.6. Foraminiferal Ba/Ca ratios in sediment core GC642 (this study); authigenic uranium (aU) at ODP Site 1094 in the Atlantic sector of the Southern Ocean (Hayes et al. 2014); sortable silt size in sediment core PS2561-2 from the Agulhas basin (Krueger et al. 2012); and pCO_{2atm} from Antarctic ice cores (Lüthi et al. 2008; Petit et al. 1999). Light grey bars show the age range of the MIS 5e data measured by this study (118 – 125 ka) and dark grey bars show approximate age of the stagnation event (127 ± 1 ka; Hayes et al. 2014).

interglacial hypothesis for enhanced AABW formation and carbon storage during glacial periods, the stagnation event mechanism does not invoke a physical change in the configuration of water masses, which must occur over longer timescales. Instead, it constitutes a change in water mass chemical properties, brought about by a relatively minor change in water mass formation.

Because barium distributions are also affected by the biological pump due to uptake of barium into organic matter and its subsequent remineralisation (e.g. Chan et al. 1977; Jeandel et al. 1996), such an event could also increase barium concentrations within AABW. A high-barium signal in AABW could be transferred to ASW via mixing with NADW, which forms ASW via upwelling (Figure 4.3). The significantly higher Ba/Ca ratios of MIS 5e compared to the Holocene might therefore be a result

of this stagnation event during MIS 5e. In contrast, in the Holocene AABW formation remained strong, preventing this build-up of carbon and barium and leading to lower seawater barium concentrations in AABW and ASW than during MIS 5e, on average.

It is not entirely clear whether the stagnation event coincides with the MIS 5e data measured in this study or precedes them. Hayes et al. 2014 date this event to 127 ± 1 ka, which does not overlap with the ages of the MIS 5e data measured in this study (~118 – 125 ka). However, the aU peak only returns to its pre-stagnation event value at approximately 125 ka (Figure 4.6), such that the oldest data point measured here overlaps with the tail-end of the stagnation event (at 125.13 ka). If AABW properties were conveyed to ASW on a ~1000-year timescale, the signature of the stagnation event should continue to be seen for ~1000 years after the end of the event, affecting Ba/Ca ratios during the earliest part of the record (~125 – 124 ka) followed by a return to 'normal' conditions afterward, replicating aU variability (Figure 4.6). This is not seen; the Ba/Ca data remain approximately constant during ~118 – 125 ka (Figure 4.6), suggesting that the stagnation event did not coincide with the data collected by this study. Alternatively, it may be more appropriate to define the timing of the stagnation event using a direct indicator of flow rate, such as sortable silt size. The minimum in sortable silt size observed during the MIS 5e stagnation event extends for a longer time than the aU peak, only recovering its pre-stagnation event values at approximately 119 ka (Figure 4.6). This may indicate that the stagnation event lasted for a longer time than suggested by aU alone, possibly meaning that the MIS 5e data measured in this study are entirely contained within the stagnation event. In this case, the potential slight increase in Ba/Ca from 125 to 122.5 ka (Figure 4.6) might be due to the attainment of maximum-stagnation conditions at ~122.5 ka. Another alternative interpretation can be proposed using atmospheric carbon dioxide data. If the MIS 5e stagnation event involved enhanced oceanic carbon storage it may be expected to cause a pCO_{2atm} decrease. Such a decrease (of approximately 13 ppmv) can be seen at ~128 – 127 ka, with pCO_{2atm} recovering to its previous value at ~126 ka (Figure 4.6). This is in exact agreement with the 127 ± 1 ka timing given by Hayes et al. 2014. If pCO_{2atm} is the best indicator of the timing of the stagnation event, this would suggest that the event has ended by ~125 ka, such that the data measured in this study do not overlap with it.

A discrepancy in timing between the stagnation event and the MIS 5e data of this study can be reconciled if the effects of the stagnation event persist after the event itself has ended. The end of the stagnation event could be defined as a return of AABW formation to its normal strength. Subsequent to this, the elevated alkalinity and barium concentration of AABW would dissipate gradually through mixing with other water masses and ventilation to the atmosphere. The return to pre-stagnation event alkalinity and barium concentrations might therefore lag behind the end of the stagnation event by approximately 1000 years, the timescale of ocean ventilation via thermohaline circulation. If AABW formation was fully re-invigorated by ~125 ka, it might not be feasible to attribute the elevated barium concentrations recorded at the core site, which persist until at least ~118 ka, to the stagnation event. However, the minimum in sortable silt size observed by Krueger et al. 2012 does not regain its pre-

stagnation value until ~119 ka (Figure 4.6), suggesting that AABW formation did not fully recover until this time. Taking into account the ~1000 year lag between the end of the event and the complete dissipation of its influence from the oceans, this would facilitate ongoing elevated barium concentrations at the site until approximately ~118 ka, in agreement with the observed Ba/Ca ratios (Figure 4.6).

This stagnation event mechanism contrasts with the glacial-interglacial mechanism that involves greater carbon storage within AABW during glacials and the subsequent release of this carbon during interglacials. In essence, this glacial-interglacial mechanism involves a change in the positions and compositions of water masses, with substantially greater AABW formation and higher Ba concentrations in AABW during glacial periods, whereas the stagnation event mechanism only involves a change in the compositions of water masses, their positions remaining approximately the same (Figure 4.7; Table 4.4). This is consistent with the much greater magnitude of the climatic variability between glacial and interglacial periods than between MIS 5e and the Holocene: glacial-interglacial cycling involves large-scale 'switches' in circulation with substantial expansion and contraction of AABW (and carbon storage therein), whereas Holocene-MIS 5e variability involves smaller-scale (geographically and temporally) changes. The two mechanisms are also different in the sense that in the glacial-interglacial mechanism, colder climate conditions result in a higher barium concentration in AABW, whereas in the stagnation event mechanism the opposite is true: it is the warmer conditions of MIS 5e which result in higher barium concentrations (Figure 4.7; Table 4.4). If such a stagnation event mechanism is responsible for the Holocene-MIS 5e differences, this suggests that the mechanisms controlling climatic variability between interglacial periods are significantly different to those controlling climatic variability between glacial and interglacial periods. Figuratively speaking, it shows that the Holocene and MIS 5e are not comparatively a 'miniature glacial' and 'miniature interglacial', respectively.

Table 4.4. Summary of the described contrasts between the glacial-interglacial mechanism and the stagnation event mechanism.

Glacial-interglacial mechanism	Stagnation event mechanism
Glacial • *Colder* than interglacial • *Greater* C and Ba storage in AABW than during interglacial	Lack of Stagnation/Re-invigoration • *Colder* than MIS 5e • *Lesser* C and Ba storage in AABW than during a stagnation
Interglacial • *Warmer* than glacial • *Lesser* C and Ba storage in AABW than during glacial	Stagnation (MIS 5e) • *Warmer* than Holocene • *Greater* C and Ba storage in AABW than during a re-invigoration or compared to if a stagnation had not occurred

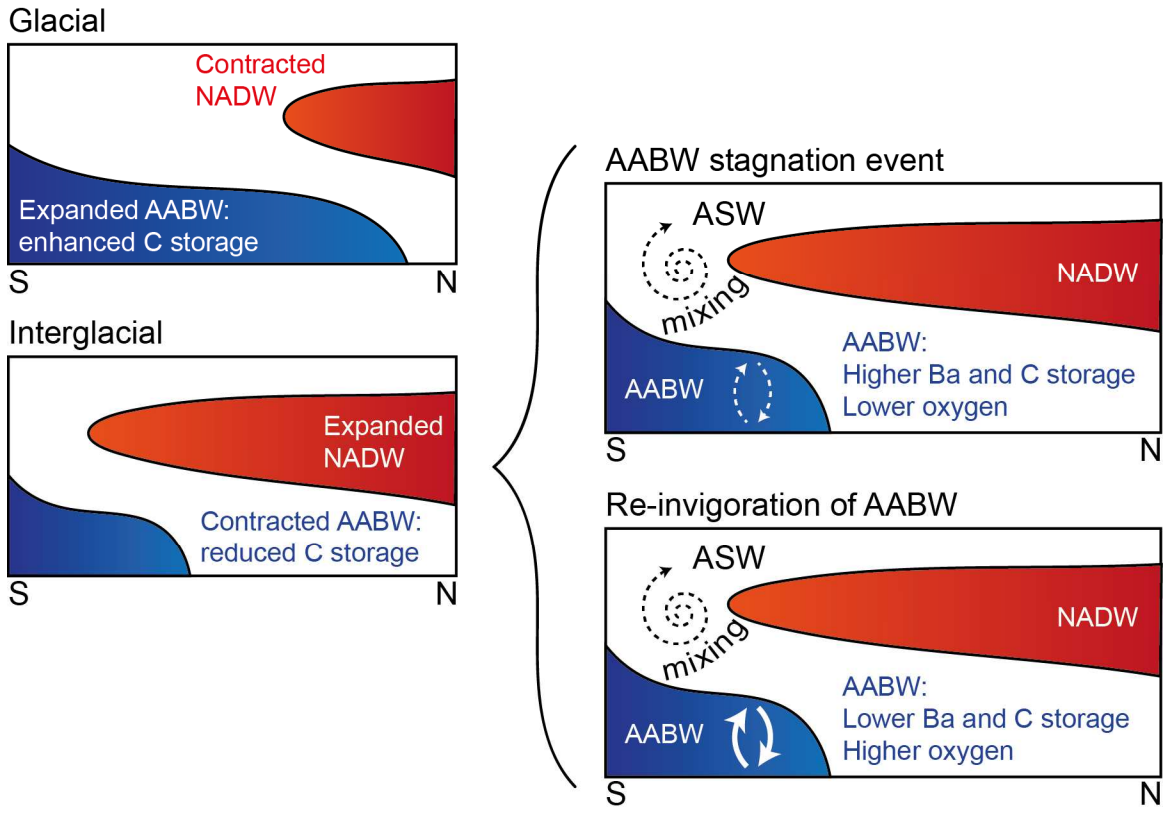

Figure 4.7. Schematic diagram of the glacial-interglacial deep ocean carbon storage mechanism and the stagnation event mechanism which may occur during interglacial periods. A stagnation event occurred during MIS 5e (Hayes et al. 2014) but was absent from the Holocene. A 're-invigoration' of AABW might alternatively refer to the lack of a stagnation event having occurred. Not to scale.

4.5.3.1 Evidence from Mn/Ca ratios

Given that an AABW stagnation event as defined by Hayes et al. 2014 causes dissolved oxygen concentrations to decrease within AABW (Hayes et al. 2014), assuming that changes in AABW are transmitted to ASW via the mechanism described above, this should cause ASW to also become less oxygenated. Mn/Ca ratios are significantly higher on average in MIS 5e than in the Holocene (Figure 4.5; Table 4.2; Table 4.3). Using the Mn/Ca proxy for bottom water oxygenation of McKay et al. 2015 whereby higher Mn/Ca ratios indicate reduced bottom water oxygenation and vice versa, this indicates that dissolved oxygen concentrations were indeed lower during MIS 5e than in the Holocene. This therefore supports the hypothesis that a low-oxygen AABW stagnation event occurred during MIS 5e that was not replicated to the same extent in the Holocene.

Timing considerations can also be applied to dissolved oxygen concentrations. Mn/Ca ratios remain approximately constant throughout ~120 – 125 ka (Figure 4.5), suggesting that bottom water oxygenation also remained unchanged throughout this time (Koho et al. 2015; McKay et al. 2015). This is in agreement with the aU record which indicates that by ~125 ka, pre-stagnation event oxygen concentrations had been regained, remaining relatively constant afterward (Figure 4.6). The agreement between these two records could be confirmed with greater certainty if pre-125 ka Mn/Ca measurements vary in tandem with aU. However, as discussed above, the manifestation of the stagnation event signal in ASW (at the core site) may alternatively lag behind the occurrence of the event in AABW, rather than paralleling it. If the stagnation event is dated to 127 ± 1 ka (Hayes et al. 2014), the Mn/Ca data do not appear to support this hypothesis because they do not show a decrease (indicating a return to higher-oxygen conditions) after ~126 ka. However, using sortable silt size provides an alternative date of ~119 – 121 ka for the end of the stagnation event (Figure 4.6). At ~118 – 120 ka, an increase in Mn/Ca occurs (Figure 4.5) suggesting that bottom water dissolved oxygen concentrations decreased (McKay et al. 2015). This could indicate the flushing out of low-oxygen waters from AABW into ASW after the end of the stagnation event.

The lower dissolved oxygen concentrations of MIS 5e could alternatively be due to higher productivity at this time, caused by the warmer temperatures of MIS 5e compared to the Holocene (independent of the stagnation event) or by greater nutrient concentrations within AABW and hence ASW during MIS 5e (caused by the stagnation event). Similarly, the Mn/Ca increase at ~120 – 118 ka might also be attributed to a change in primary productivity. An independent measure of productivity, such as foraminiferal $\delta^{13}C$, is necessary to differentiate between these scenarios.

4.5.3.2 Evidence from Mg/Ca-derived temperatures

The Mg/Ca-derived temperatures are significantly warmer during MIS 5e than the Holocene by approximately 2 ºC (Figure 4.5; Table 4.2; Table 4.3), in agreement with previous studies (Otto-Bliesner et al. 2006; Kaspar et al. 2005). The MIS 5e stagnation event may have been forced from the

Southern Hemisphere (by warming temperatures, increased ice melting and hence weaker AABW formation) or forced from the Northern Hemisphere (due to strengthened NADW formation which weakened AABW formation) (Hayes et al. 2014). If the stagnation event was forced from a Southern Hemisphere warming, higher temperatures would be expected during this event. If the stagnation event was forced from a Northern Hemisphere strengthening of NADW formation, a temperature increase would also be expected (due to the greater southward transport of heat via NADW). The significantly warmer Mg/Ca-derived temperatures of MIS 5e are in agreement with either of these scenarios. They therefore do not refute the hypothesis that a stagnation event occurred during MIS 5e, but neither can they suggest whether this was forced from the Northern or Southern Hemisphere, and may occur independently of a stagnation event. Nevertheless, the good agreement between these Mg/Ca-derived temperatures and the estimated Holocene-MIS 5e temperature differences of other studies (Otto-Bliesner et al. 2006; Kaspar et al. 2005) lends confidence to the use of *M. barleeanus* Mg/Ca for comparing MIS 5e and Holocene temperatures.

4.5.4 Variability within the Holocene

During most of the presented Holocene record, Ba/Ca remains largely constant. This means that climatic variability associated with sub-epochs such as the mid-Holocene Climatic Optimum, climatic reversal and the Neoglacial cannot be discussed. However, a large Ba/Ca peak occurs at approximately 2.3 ka. The possible causes of this Ba/Ca peak are discussed below. To assist this discussion, the Ba/Ca data are reproduced in Figure 4.8 together with supplementary data measured in sediment core GC528 and at nearby sites.

4.5.4.1 Contamination

A sample may be considered contaminated with metal oxides or clays if it has a high Mn/Ca or Al/Ca ratio, respectively (e.g. Boyle 1983; Ni et al. 2007). During data quality assessment, data points were rejected on these grounds if Mn/Ca was greater than 40 μmol/mol or if Al/Ca was greater than 60 μmol/mol (see Section 2.4 'Quality assurance'). The Ba/Ca data point at the height of the peak at ~2.3 ka is not associated with either a high Mn/Ca or Al/Ca ratio (Mn/Ca = 2.85 ± 0.25 μmol/mol and Al/Ca = 46.38 ± 3.16 μmol/mol) suggesting that if this sample was contaminated, it was not due to metal oxides or clays. A high Ba/Ca ratio may however result from barite contamination. Whilst this cannot be disproven, cleaning tests have shown that the cleaning technique is successful at removing barite (Chapter 3 'Evaluating the Ba/Ca Proxy'; Lea 1990; Lea & Boyle 1993) and this sample was cleaned alongside many other samples which do not show such high Ba/Ca ratios.

An additional data point at 1.8 ka (closed symbol in Figure 4.8, panel A) also has an elevated Ba/Ca ratio relative to the other Holocene measurements. This data point was discarded due to Al/Ca > 60 μmol/mol, but only marginally (Al/Ca = 63 μmol/mol). The presence of this data point provides

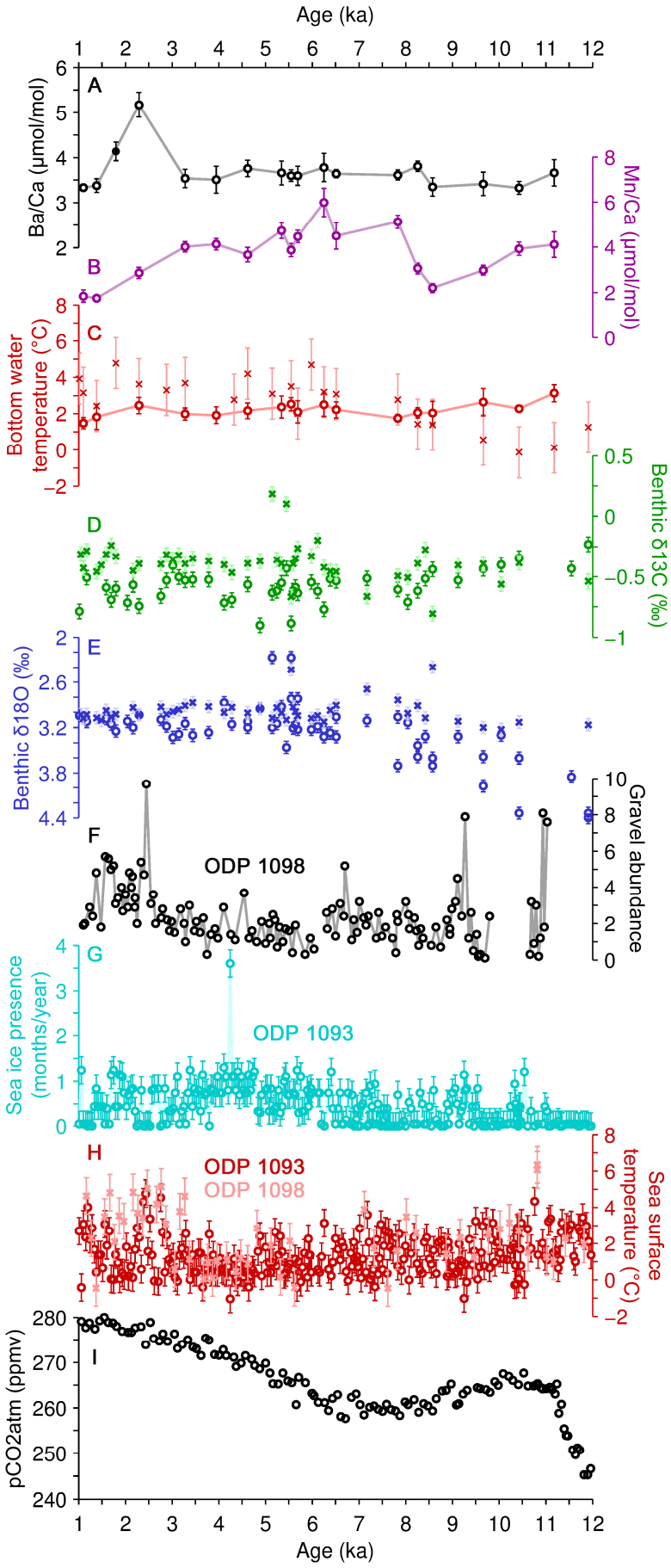

Figure 4.8. Data measured in core GC528 (A – E) and at nearby sites: A) Ba/Ca ± 2σ in *M. barleeanus*, with one data point which failed quality assurance (closed symbol); B) Mn/Ca ± 2σ in *M. barleeanus*; C) estimated bottom water temperatures calculated from *M. barleeanus* Mg/Ca (± 2σ; circle symbols) and *Uvigerina* spp. Mg/Ca (± 1.4 ºC; cross symbols; Roberts et al. 2016); D and E) $\delta^{13}C$ ± 0.06 ‰ and $\delta^{18}O$ ± 0.08 ‰ in *Uvigerina* spp. (circle symbols) and *O. umbonatus* (cross symbols) (Roberts et al. 2016); F) gravel abundance at ODP Site 1098 (Domack et al. 2001); G) sea ice presence ± 0.3 months/year at ODP Site 1093 (Nielsen et al. 2004); H) sea surface temperatures at ODP Site 1093 (± 0.75 ºC; Nielsen et al. 2004) and ODP Site 1098 (± 1 ºC; Shevenell et al. 2007); and I) pCO_{2atm} from Antarctic ice cores (Lüthi et al. 2008; Petit et al. 1999). All GC528 data are plotted using the age model of Roberts et al. 2016. σ = internal precision.

supporting evidence that ambient barium concentrations were elevated at this time. The data points at ~2.3 ka and 1.8 ka were measured on different days so cannot be attributed to a common complication during sample measurement.

Further confidence in the ~2.3 ka data point is provided by details of its measurement via mass spectrometry. The matrix effect associated with this measurement is not high (–3.30 ± 2.35 %) and barium measurements remained stable throughout the run (Figure 4.9), except for instrumental drift which is accounted for by standard-sample bracketing (see Section 2.3.4 'Sequence design'). The measured intensity of the sample (prior to blank-correction) is 92 times higher than the blank and is far above the limit of detection (as defined by Equation 2.19). The relative standard deviation of the sample is 1.21 % (internal precision). There is thus no evidence that this measurement was affected by machine instability or the introduction of a contaminant particle into the apparatus.

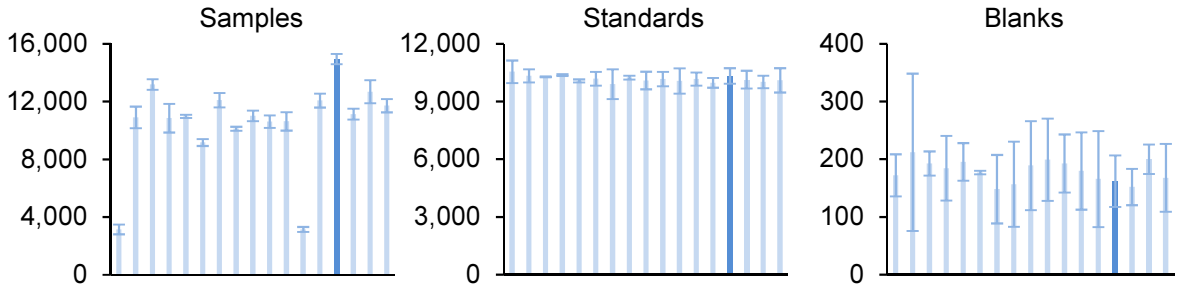

Figure 4.9. ^{138}Ba intensities ± 2SD (cps). Data relating to the ~2.3 ka sample are plotted in dark blue.

4.5.4.2 Microhabitats of infaunal foraminifera

Infaunal benthic foraminifera are known to migrate within sediments in search of optimal growth conditions (Tachikawa & Elderfield 2002). *M. barleeanus* has been observed living at depths ranging from ~1 – 4 cm (Corliss 1985; Corliss 1991; Buzas et al. 1993) and porewater barium concentrations increase rapidly over the top few centimetres of sediment (Figure 4.10; McManus et al. 1998; Paytan & Kastner 1996) due to in situ barite dissolution (McManus et al. 1998; Paytan & Kastner 1996). Therefore, a mass migration of *M. barleeanus* to greater depths would cause their ambient barium concentration, and hence the Ba/Ca ratios they record, to increase. The change in barium concentration recorded by the Ba/Ca peak at ~2.3 ka is approximately 65 – 80 to 100 – 130 nM, which is reasonable given observed porewater barium concentration changes of approximately 175 – 250 nM (McManus et al. 1998), 150 – 200 nM (Paytan & Kastner 1996) and 80 – 100 nM (Figure 4.10) over the top ~4 cm of sediment. However, such a mass migration would be unprecedented and the cause of this migration, followed by a return to their previous habitat, is difficult to imagine. Foraminiferal migrations are opportunistic in response to fleeting changes such as pulses of enhanced food supply (Tachikawa & Elderfield 2002) and are thus ephemeral, whereas this would need to be a prolonged, sustained change of habitat in order for it to be preserved in the sediment record at these timescales,

followed by a return to their previous habitat. There is no known reason for such a perturbation to their behaviour. Furthermore, an enhanced supply of organic matter to the sediments would cause a decrease in $\delta^{13}C$, which is not observed at this time (Figure 4.8). Alternatively, it may be that the ~2.3 ka peak was an extremely short-lived event, which would not require a sustained change in habitat and might instead be explained by a temporary shift to deeper habitats caused by a sudden sedimentation event.

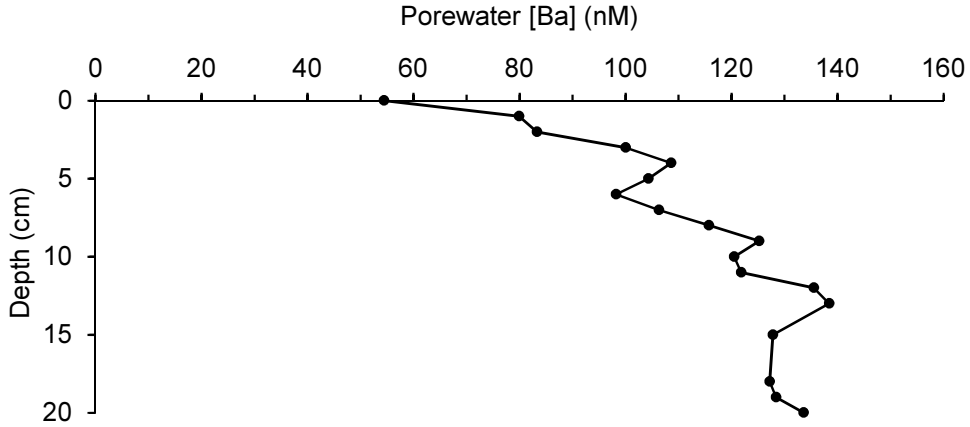

Figure 4.10. Porewater [Ba] in core JC089-07-6M-F, normalised relative to 50 nM, an approximated bottom water [Ba] for its deep Atlantic location (Dr M. Greaves, pers. com. 2015). Absolute values may not be accurate, but relative changes down-core are conserved (Dr M. Greaves, pers. com. 2015).

4.5.4.3 Ice-rafted debris

The Ba/Ca peak at ~2.3 ka coincides with a sharp peak in gravel abundance at ODP Site 1098, in Palmer Deep on the West Antarctic Peninsula, which is also similarly unprecedented within ~0 – 11 ka (Figure 4.8; Domack et al. 2001). The similarity in timing between these two peaks, their lack of repetition within the remainder of the Holocene and their geographic proximity suggest that there may be a link between them. An increased gravel abundance is indicative of enhanced ice rafting at this time. If a large amount of ice-rafted debris was deposited at the GC528 core site, perhaps this material provided a large pulse of barium to sediments, either by dissolving or releasing adsorbed material from clays. Rivers contain high concentrations of dissolved barium due to desorption from clays in the suspended sediment load (Hanor & Chan 1977). There is evidence that icebergs are capable of reaching the latitude of the GC528 core site from iceberg plough-marks found approximately nine degrees north of the site (Figure 4.2; López-Martínez et al. 2011). These icebergs were carried to this location by the Malvinas Current, which flows directly over the GC528 core site (Figure 4.2; Piola & Matano 2009). However, these plough-marks are thought to have originated during glacial periods so this may not be applicable to the Holocene when icebergs are unlikely to have travelled as far north. If a large ice-rafting event occurred, this should coincide with either: a minimum in sea ice extent and maximum in sea surface temperature, indicating enhanced iceberg melting; or a maximum in sea ice extent and

minimum in sea surface temperature, indicative of enhanced iceberg calving and transport (Heinrich 1988). There is no sharp variability observed in either sea surface temperature or sea ice presence at the time of the gravel abundance peak (Figure 4.8). This lack of supporting evidence casts doubt on this mechanism as the cause of the ~2.3 ka Ba/Ca peak. Moreover, the barium composition of ice-rafted debris is not known, and ice-rafted debris may be too insoluble to provide large amounts of barium to sediment porewaters. This idea could be investigated further by measuring ice-rafted debris in additional cores nearby to the GC528 sampling site, both in terms of its abundance and its barium content.

4.5.4.4 A stagnation event

Given that a stagnation event in AABW formation (Hayes et al. 2014) is capable of explaining the higher barium concentrations of MIS 5e compared to the Holocene (see Section 4.5.3 'Comparison of the Holocene with MIS 5e'), perhaps such an event is also capable of explaining this intra-Holocene increase in barium. Short-term (centennial- to millennial-scale) changes in Atlantic Ocean circulation have been observed within interglacial periods (e.g. Oppo et al. 2003; Hall et al. 2004; Ellison et al. 2006; Kleiven et al. 2008; Mayewski et al. 2004) so it is not outside the realms of possibility for such an event to have occurred within the Holocene on this short a timescale. However, such an event would have far-reaching effects and so would be recorded in multiple sediment cores, but there is little evidence in the literature of such an event, except for a minimum in NADW flow at one site in the North Atlantic (Bianchi & Mccave 1999) which is not observed in other nearby records (Thornalley et al. 2013). The seawater barium concentration estimated at the height of the Ba/Ca peak is greater than that of MIS 5e (Figure 4.5), so if this were caused by a stagnation event it would require an event of even greater magnitude than that which occurred during MIS 5e. Given the lack of evidence for this in other sediment cores, the occurrence of such an event at ~2.3 ka seems unlikely. Furthermore, the MIS 5e stagnation event was accompanied by a temporary decrease in atmospheric carbon dioxide of ~13 ppmv (Figure 4.6). No such variability occurs at ~2.3 ka (Figure 4.8), casting further doubt on the occurrence of a stagnation event at this time.

4.5.4.5 The Malvinas Current

An increase in dissolved barium concentration at this site could be caused by enhanced vertical mixing within the Malvinas Current, resulting in the entrainment of deeper, higher-barium waters onto the core site. Vertical mixing in the Malvinas Current partially derives from both barotropic and baroclinic flow. This was determined using current meters moored at various depths within the Malvinas Current: vertical flow within the Malvinas Current was observed both following isobaths (barotropic) and diverging from isobaths (baroclinic flow) (Vivier & Provost 1999). The amount of vertical mixing within the Malvinas Current could therefore be increased by enhancing the temperature-

driven component of vertical baroclinic flow via an increased vertical temperature gradient. Baroclinic vertical flow has been observed at depths up to ~2200 m in the Malvinas Current (Vivier & Provost 1999). At these depths, seawater dissolved barium concentrations reach up to ~100 nM (Figure 4.11) and alkalinity up to ~2380 μequiv/kg (Figure 4.12). These values are consistent with the lower end of the seawater barium and alkalinity estimates in the peak at ~2.3 ka (Figure 4.5). In summary, at ~2.3 ka the Malvinas Current might have experienced enhanced vertical mixing, which increased the influence of deeper, high-barium high-alkalinity waters on the core site.

This increased baroclinic flow within the Malvinas Current could have been caused by a greater contrast in temperature between the surface and depth, resulting in a greater vertical temperature gradient. The lack of a strong change in either Mg/Ca-derived temperature, sea surface temperature or foraminiferal $\delta^{18}O$ (which in benthic environments is indicative of temperature variability rather than freshwater forcing) at ~2.3 ka (Figure 4.8) suggests that the temperature change and enhanced vertical mixing may have occurred upstream of the site. The increased entrainment of deeper waters might be expected to decrease dissolved oxygen concentrations, due to the lower oxygen concentrations of deeper waters (Figure 4.13). However there is no sharp change in Mn/Ca, a proxy for bottom water oxygenation (Koho et al. 2015; McKay et al. 2015), evident at ~2.3 ka. This could be because the Mn/Ca proxy lacks sufficient sensitivity for resolving this small a change in oxygen concentrations, or because changes in primary productivity mitigate the oxygen change. An increase in nutrient concentrations caused by stronger vertical mixing would increase the amount of organic matter production, thereby lowering dissolved oxygen concentrations via remineralisation. In summary, neither temperature evidence nor the Mn/Ca ratios support this hypothesis, but neither do they refute it strongly.

A possible mechanism for enhanced temperature-driven vertical baroclinic flow within the Malvinas Current at ~2.3 ka is unclear, as this process would require a temporary yet millennial-scale change in the vertical temperature gradient within the Malvinas Current. An alternative cause of enhanced vertical mixing is a change in turbulent mixing. Vertical turbulent mixing within the ACC is sensitive to the underlying topography (Sloyan 2005), so either: a) a change in the position of the Malvinas Current relative to the underlying topography; or b) a temporary change in topography whilst the position of the Malvinas Current remained constant would result in a temporary increase in vertical mixing within the Malvinas Current. The location of the Antarctic Polar Front, and by extension the position of the Malvinas Current, is sensitive to the position and strength of local westerly winds (Taylor et al. 1978), whereas a sedimentary mass movement followed by gradual sediment redistribution would facilitate a relatively sudden yet temporary change in topography.

Overall, this mechanism is perhaps one of the more likely causes of the barium peak at ~2.3 ka out of the possibilities considered here. The suddenness of the event could be attributed to the topography of the core site, which is situated near to the shelf break (Figure 4.2) potentially rendering it sensitive to relatively small changes in ocean circulation or topography. Furthermore, such an event would only affect the local area, providing an explanation for why it is so pronounced in this sediment

core yet absent from other Atlantic sediment cores. Unlike most of the other possibilities considered above in Sections 4.5.4.1 to 4.5.4.4, this explanation is therefore capable of explaining not only the sudden, large change in seawater barium concentration at this site, but also the lack of evidence for such an event in regional records. A second possible cause of the ~2.3 ka peak is a sudden sedimentation event which meant that the infaunal foraminifera temporarily lived at greater depths within the sediment, where porewater barium concentrations are higher, before migrating back to their prior habitat. This mechanism requires that the ~2.3 ka event was a very short-lived event, as it is unlikely that the foraminifera would maintain their altered habitat for an extended period of time before returning to their previous habitation depth. To investigate each of these possible mechanisms further, additional measurements from either side of the ~2.3 ka peak could be used to determine whether this was indeed a short-lived event or a more prolonged change which might be more likely attributed to a change in Malvinas Current circulation or broader-scale changes.

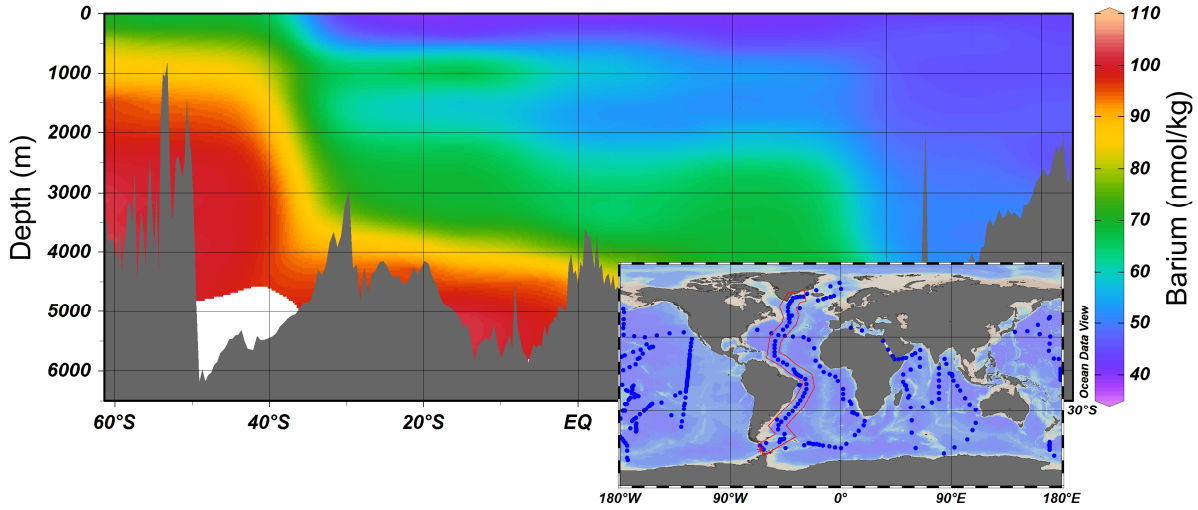

Figure 4.11. GEOSECS seawater barium concentrations in the western Atlantic Ocean.

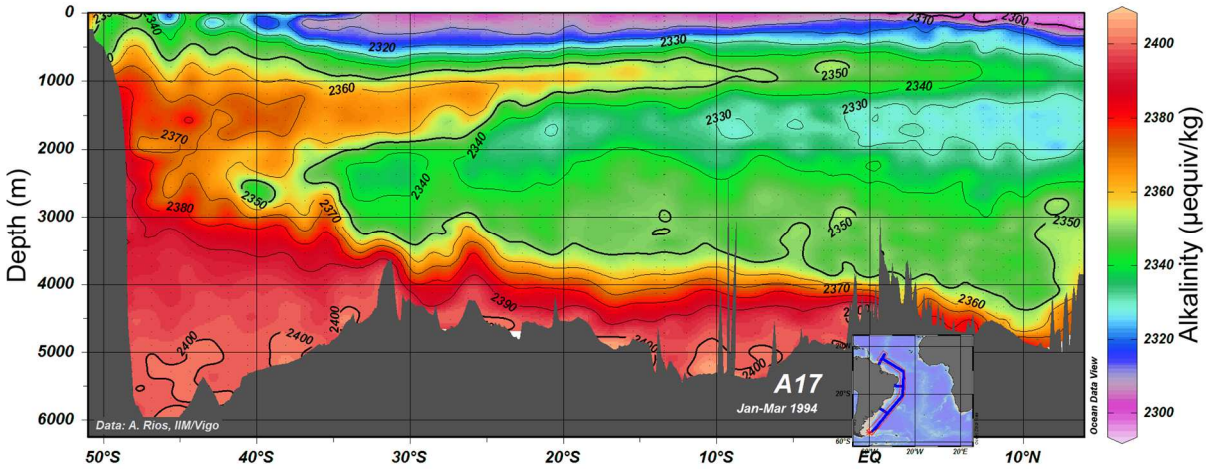

Figure 4.12. Seawater alkalinity in the western Atlantic Ocean. Figure by eWOCE Gallery.

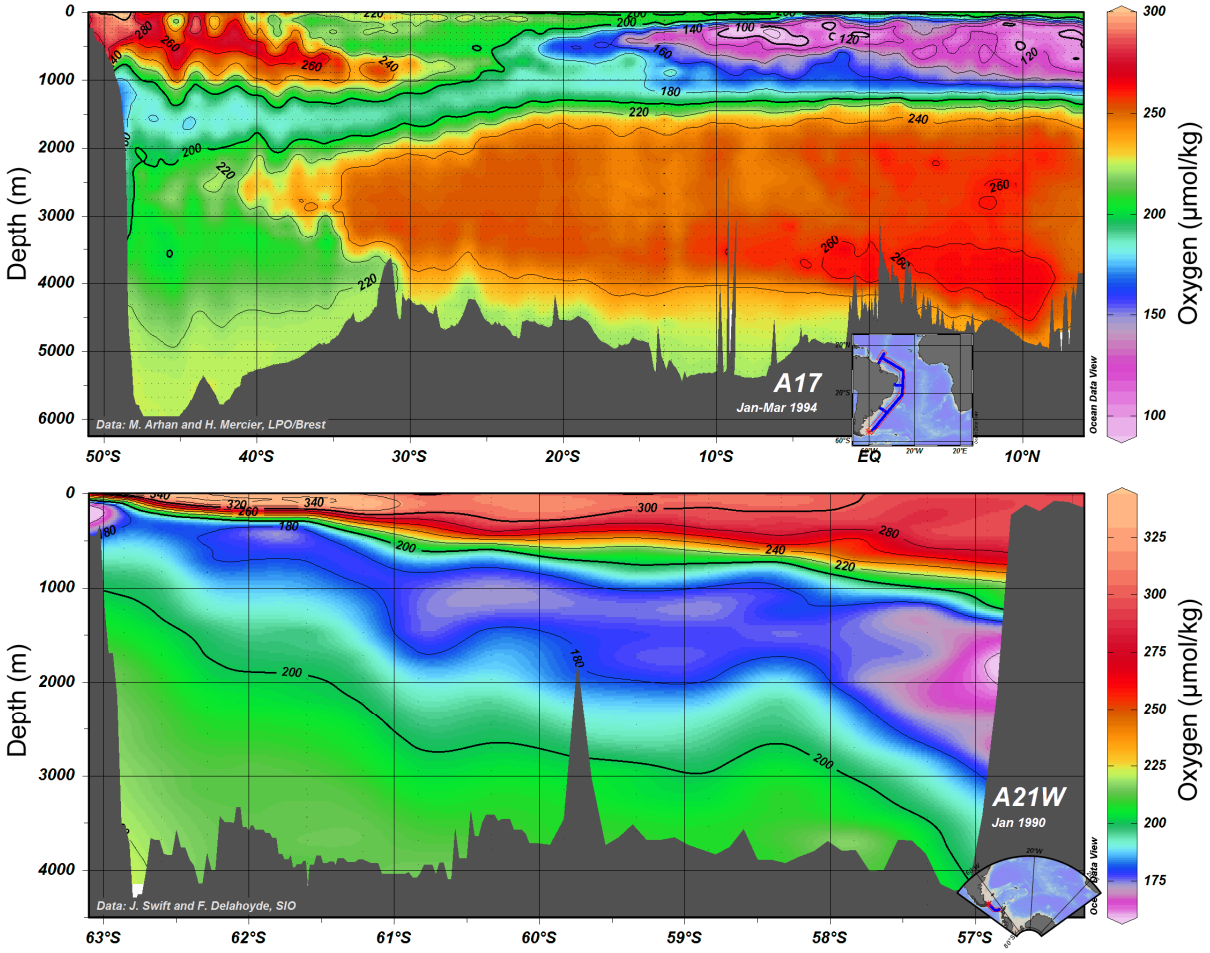

Figure 4.13. Seawater dissolved oxygen concentrations in the vicinity of the core site. Figures by eWOCE Gallery.

4.6 Conclusions

At this site in the southwest Atlantic, foraminiferal Ba/Ca ratios, and by inference seawater barium concentrations and alkalinity, were significantly higher in MIS 5e than during the Holocene (with the exception of a large Ba/Ca peak at ~2.3 ka, which is discussed separately below). The higher seawater barium concentrations of MIS 5e may result from a slowing-down in the formation of AABW, known as a 'stagnation event', at this time (Hayes et al. 2014). An AABW stagnation event during MIS 5e was identified by Hayes et al. 2014, who attribute low oxygen concentrations to this phenomenon and suggest that it may have temporarily increased carbon storage within AABW (Hayes et al. 2014). This mechanism is fundamentally different to the glacial-interglacial mechanism of enhanced AABW formation and carbon storage during glacial periods, because it only invokes a change in chemical water mass properties, rather than a large-scale physical redistribution of water masses. Here, the definition of a stagnation event is extended to include an increase in dissolved barium storage within AABW. These changes in AABW were conveyed to ASW, which bathes the core site, via mixing with NADW which forms ASW through upwelling (Brown et al. 2004). The relative timing between the stagnation event and the results of this study is not certain, however. The precise date at which the event ended is not clear, because variability in sortable silt size, an indicator of flow rate, lags behind changes in authigenic uranium and pCO_{2atm}. The stagnation event may have fully preceded the observations of this study or may have continued to influence water mass properties after the event had ended, partially due to the time required for this change to be transmitted through the ocean. Further measurements could clarify this further. The Mg/Ca-derived temperatures are approximately 2 ºC warmer in MIS 5e than in the Holocene, in agreement with previous authors (Otto-Bliesner et al. 2006; Kaspar et al. 2005). Warmer temperatures during MIS 5e are consistent with an AABW stagnation event during this time. Mn/Ca ratios are also significantly larger during MIS 5e, which may indicate that bottom waters were less oxygenated (McKay et al. 2015), in agreement with the evidence of Hayes et al. 2014. The use of high Mn/Ca ratios as an indicator for low oxygen concentrations in the benthic infaunal species *Melonis barleeanus* suggests that the findings of Koho et al. 2015, who report that high Mn/Ca ratios in this species indicate greater oxygenation of bottom waters, may not always be applicable. Care should therefore be taken to determine the habitation depth of *M. barleeanus* as accurately as possible prior to using this proxy.

Within the Holocene, a large peak in Ba/Ca is observed at approximately 2.3 ka (Figure 4.8). This is incongruous in the context of the Holocene, which elsewise shows little variability in Ba/Ca (Figure 4.8). Several possibilities are discussed for the cause of this Ba/Ca peak. Of these, perhaps the most likely is that enhanced vertical mixing within the Malvinas Current caused increased entrainment of deeper, higher-barium waters at this time. If the peak was caused by a localised event its occurrence would not have strong implications for the wider environment. However, it may nonetheless be important to confirm the origin of this peak with greater certainty in order to increase confidence in the use of foraminiferal Ba/Ca ratios as a proxy for ocean circulation and seawater alkalinity.

In summary, the results presented here provide evidence for important variability both within and between interglacial periods. The MIS 5e stagnation event has implications for the future of the Holocene under anthropogenic warming, because a temperature increase may trigger a similar event within the Holocene. This could result in enhanced carbon storage within AABW, mitigating some of the ongoing pCO_{2atm} rise. Within the Holocene, a peak in Ba/Ca has been observed at ~2.3 ka. Although this event may not have far-reaching implications for the climate system, determining its cause with certainty would nevertheless be beneficial. This could confirm that the methods used here are not susceptible to barite contamination of this magnitude whilst simultaneously revealing a potential new application for Ba/Ca ratios. If the Ba/Ca peak is confirmed to be caused by the entrainment of deeper, high-barium waters, this would suggest that, at certain sites, benthic foraminiferal Ba/Ca is sensitive to changes in vertical mixing and can therefore be used as an upwelling proxy. Further investigations into the hypotheses discussed in this study would therefore be beneficial, both to understanding and thus predicting future Holocene variability and to refining the benthic foraminiferal Ba/Ca proxy itself.

Chapter 5

Barium Isotope Ratios in Foraminifera and Seawater

5.1 Abstract

The distribution of dissolved barium in the oceans is well known, but questions remain about why dissolved barium concentrations are linked to seawater alkalinity and silica concentrations. Several barium-based oceanographic proxies have previously been developed, providing information about ocean circulation, seawater alkalinity, dissolved silica concentrations, river runoff, glacial meltwater discharge, monsoon rains, seawater temperatures, upwelling and marine productivity in the past. The reliability of these proxies depends on a full understanding of oceanic barium dynamics, providing motivation for further study of the processes governing oceanic barium distributions. In this chapter, seawater barium isotope ratios are used to study these processes using samples from the tropical North Atlantic Ocean and southeast Atlantic Ocean. Results suggest that below 'near-surface' depths (approximately 0 – 500 m), barium is largely controlled by conservative mixing of water masses. In the upper 500 m barite cycling asserts a stronger influence than at greater depths, with additional contrasts caused by the depth of the mixed layer in relation to this non-conservative behaviour. Evidence is also presented for non-conservative processes affecting barium within marine sediments. In addition, the possibility of developing foraminiferal barium isotope ratios as a proxy for seawater barium isotope ratios is investigated. Barium isotope ratios are measured in the planktic foraminifer *Orbulina universa* from the tropical North Atlantic Ocean. Foraminiferal barium isotope ratios are isotopically lighter than seawater values. The magnitude of this isotopic offset is variable, which may be due to vital effects associated with different morphotypes of *O. universa*. Overall, the results presented in this chapter provide insights into oceanic barium cycling in the Atlantic which are in agreement with previous studies, and suggest that with further development foraminiferal barium isotope ratios could be used to gain similar insights into the oceans of the past.

5.2 Introduction

Although it has been established that seawater barium concentrations have refractory nutrient-like profiles (e.g. Chan et al. 1977; Jeandel et al. 1996), the reason for this remains uncertain. Barium concentrations are linked to marine productivity by barite precipitation, which occurs within organic matter during remineralisation (Goldberg & Arrhenius 1958; Church 1970; Ganeshram et al. 2003; Bishop 1988; Bernstein et al. 1992; Bernstein et al. 1998; Chow & Goldberg 1960). However, this does not explain why barium has such a strong correlation with dissolved silica and alkalinity and yet not with nitrate and phosphate. This is observed at many locations, not only within diatom-rich regions such as the Southern Ocean (e.g. Chan et al. 1977), so diatom abundance cannot explain this phenomenon. Additionally, the controls on barite formation depths are not well known because although particulate barium peaks in the upper ~500 m (Dehairs et al. 1980; Bishop 1988; Dehairs et al. 1990; Dehairs et al. 1991; Stroobants et al. 1991; Dehairs et al. 1992; Legeleux & Reyss 1996; van Beek et al. 2007) $^{228}Ra/^{226}Ra$ evidence suggests that barite also forms at intermediate depths in the water column (van Beek et al. 2007). The relative contributions of barium from various sources is also not well-established: barium could be released from within organic matter, from the dissolution of barium-bearing minerals such as barite, or from desorption. Quantifying the relative contributions of these sources would aid in determining the mechanistic link between barium and refractory nutrient distributions.

Clarification of the controls on oceanic barium distributions would be beneficial to understanding the mechanisms behind oceanographic proxies based on marine barium, of which there are several. Benthic foraminiferal Ba/Ca ratios have been used as a proxy for ocean circulation, seawater alkalinity and dissolved silica concentrations (Lea & Boyle 1989; Lea & Boyle 1990a; Lea & Boyle 1990b; Lea 1990; Lea 1993; Lea 1995; Hall & Chan 2004b) and this approach has also been applied using corals (Anagnostou et al. 2011; LaVigne et al. 2011). Planktic foraminiferal Ba/Ca can be used to study freshwater inputs such as river runoff, glacial discharge and monsoon rains (Weldeab et al. 2007b; Weldeab et al. 2007a; Weldeab et al. 2014; Weldeab 2012; Sprovieri et al. 2012; Sprovieri et al. 2008; Hall & Chan 2004b; Bahr et al. 2013; Saraswat et al. 2013) or to trace both ocean circulation and river runoff (Lea & Boyle 1991; Lea 1990). Similarly, Ba/Ca ratios in corals and coralline algae have provided information about freshwater inputs (Chan et al. 2011; Horta-Puga & Carriquiry 2012; Grove et al. 2012; Moyer et al. 2012; Montagna et al. 2007) as well as seawater temperatures and upwelling (Lea et al. 1989; Shen et al. 1992; Chen et al. 2011; Fallon et al. 1999; Lea 1990; Montagna et al. 2007; LaVigne et al. 2016). Ba/Ca ratios in saltwater clams and bivalves can also be used to study freshwater inputs as well as marine productivity (Batenburg et al. 2011; Elliot et al. 2009; Hatch et al. 2013; Carroll et al. 2009; Gillikin et al. 2008; Gillikin et al. 2006; Lazareth et al. 2003). Other proxies making use of the link between barium and productivity are based on the properties of marine sediments: accumulation rates of 'excess Ba' (barium which is not lithogenic and so is assumed to come from the water column) can be used to calculate productivity export rates from overlying waters (Dymond et al. 1992; François et al. 1995; Rutsch et al. 1995; Dean et al. 1997; Nürnberg et al. 1997;

Bonn et al. 1998; Bains et al. 2000); a similar approach is used to interpret variations in sedimentary Ba/Ti and Ba/Al ratios as changes in productivity, where Ti and Al are assumed to be purely lithogenic and the lithogenic contribution of Ba is assumed to remain constant, such that any variability is caused by variable production of marine barite (Goldberg & Arrhenius 1958; Murray & Leinen 1996; Reitz et al. 2004; Murray et al. 2000); and sedimentary marine barite abundances can also be measured directly, by isolating barites from sediments using sequential leaching followed by identification using scanning electron microscopy (Paytan 1996; Eagle et al. 2003; Robin et al. 2003; Turchyn & Schrag 2004; Paytan et al. 1996). The accurate use of these barium-based proxies depends on an understanding of barium behaviour in sediments and seawater. It is therefore important that the mechanisms controlling marine barium continue to be investigated.

Barium isotope ratios can provide new insights into seawater barium distributions and sedimentary processes. There are six stable isotopes of barium; the most abundant is ^{138}Ba (71.698 % relative abundance), followed by ^{137}Ba (11.232 %), ^{136}Ba (7.854 %), ^{135}Ba (6.592 %), ^{134}Ba (2.417 %) and ^{130}Ba (0.106 %). In this study, $^{138/134}$Ba barium isotope ratios are reported in delta notation as shown in Equation 5.1. The advantage of using ^{138}Ba is its high abundance, because this reduces the difficulty of measuring barium isotope ratios in very low-barium samples such as seawater (Horner et al. 2015). Some studies have used the isotope ^{137}Ba rather than ^{138}Ba (van Zuilen et al. in press). The advantages of using ^{137}Ba rather than ^{138}Ba are that certain instruments lack the dynamic range required to measure ^{138}Ba alongside other much-less abundant isotopes, and that ^{138}Ba experiences isobaric interference from ^{138}La and ^{138}Ce (Horner et al. 2015). However, the dynamic range of the instrument used by Horner et al. 2015 and this study is sufficient to measure ^{138}Ba alongside other isotopes, and the method corrects for isobaric interferences on ^{138}Ba, allowing ^{138}Ba to be used instead of ^{137}Ba. The measurement of barium isotope ratios is a relatively novel technique and as such a standard notation has not yet been agreed upon (van Zuilen et al. in press). Here, values which were reported by other studies using the $^{137/134}$Ba notation have been converted into $^{138/134}$Ba notation for comparison with the results of this study using a conversion factor as shown in Equation 5.2. All of the barium isotope ratio data presented here (including those of Horner et al. 2015) therefore use the $^{138/134}$Ba notation as shown in Equation 5.1.

$$\delta^{138/134}\mathrm{Ba}\ (‰) = \left(\frac{\left(\frac{^{138}\mathrm{Ba}}{^{134}\mathrm{Ba}}\right)_{\mathrm{sample}}}{\left(\frac{^{138}\mathrm{Ba}}{^{134}\mathrm{Ba}}\right)_{\mathrm{NIST\ SRM\ 3104a}}} - 1 \right) \times 1000 \qquad (5.1)$$

$$\delta^{138/134}\mathrm{Ba} = \frac{\ln\left(\frac{\text{mass of } ^{138}\mathrm{Ba}}{\text{mass of } ^{134}\mathrm{Ba}}\right)}{\ln\left(\frac{\text{mass of } ^{137}\mathrm{Ba}}{\text{mass of } ^{134}\mathrm{Ba}}\right)} \times \delta^{137/134}\mathrm{Ba} = 1.33 \times \delta^{137/134}\mathrm{Ba} \qquad (5.2)$$

Seawater barium isotope ratios have been measured in the southeast Atlantic and South and East China Sea (Horner et al. 2015; Cao et al. 2016). These studies have shown that seawater barium

isotope ratios remain approximately constant over the top 100 m and are heavier at these depths than in deeper waters (Horner et al. 2015; Cao et al. 2016). Horner et al. 2015 and Cao et al. 2016 attribute the heavier barium isotope ratios of shallower waters to productivity-related processes preferentially removing lighter isotopes of barium: barite precipitation (Horner et al. 2015) and adsorption of barium onto diatoms (Cao et al. 2016). In deeper waters, barium isotope ratios appear to be controlled by conservative mixing of water masses (Horner et al. 2015; Cao et al. 2016). The measurement of additional seawater barium isotope ratio profiles will provide further insights into the broad-scale and near-surface controls of marine barium distributions.

As well as aiding the use of the barium-based proxies described above, barium isotope ratios could themselves be developed into a new palaeoceanographic proxy. Barite precipitation is thought to increase seawater barium isotope ratios because barites precipitated in laboratory experiments have lighter barium isotope ratios than the solutions they precipitated from (von Allmen et al. 2010). This fractionation occurs because the ease of desolvation of a dissolved barium ion, and hence the ease of incorporation into a precipitating mineral, is inversely correlated to the isotopic mass of the barium ion (Hofmann et al. 2012). Laboratory-precipitated witherites ($BaCO_3$), the double carbonate $BaMn(CO_3)_2$ and natural marine barites have also been found to preferentially incorporate lighter isotopes of barium (Böttcher et al. 2012a; Böttcher et al. 2012b; Pretet 2013; Pretet et al. 2015; von Allmen et al. 2010; Table 5.1). Barium isotope ratios have also been measured in corals (Pretet 2013; Pretet et al. 2015; Table 5.1). Laboratory-cultured coral samples were isotopically lighter than ambient seawater, with seawater-coral barium isotope ratio offsets ranging from 0 to 0.26 ‰ (Pretet 2013; Pretet et al. 2015; Table 5.1). Barium isotope ratios in corals are highly variable (Pretet 2013; Pretet et al. 2015), which contrasts with relatively consistent barium partition coefficients for corals (Pretet et al. 2015), suggesting that barium isotope ratios in corals experience stronger vital effects than Ba/Ca ratios (Pretet et al. 2015). The variability may also be due to environmental differences (Pretet et al. 2015). If barium isotope ratios in corals could be used to reconstruct seawater barium isotope ratios, this could be used as a proxy for productivity or ocean circulation, depending on the processes controlling seawater barium isotope ratios at the site location. To further explore the possibility of using barium isotope ratios in marine carbonates as a proxy for seawater barium isotope ratios, in this study barium isotope ratios are measured in foraminifera for the first time.

In summary, in this chapter barium isotope ratios and barium concentrations are measured in three new seawater profiles from the tropical North Atlantic Ocean. These are compared to profiles from the southeast Atlantic to build up a picture of the distribution of barium isotope ratios in the Atlantic and to assess what processes might control these distributions at broad scales and within near-surface waters. In addition, foraminiferal barium isotope ratios and Ba/Ca ratios are measured in the planktic foraminifer *Orbulina universa*. These measurements are the first step towards assessing the potential of foraminiferal barium isotope ratios as a new palaeoceanographic proxy.

Table 5.1. Barium isotope ratios in carbonate and sulphate minerals and their relation to barium isotope ratios of their ambient solutions.

Material	$\delta^{138/134}$Ba ± 2SE of carbonate (‰)	Comparison to solution	Reference
Witherite [a]	–0.08 ± 0.04 –0.19 ± 0.07 –0.43 ± 0.07 –0.37 ± 0.01	Carbonates are ~0 – 0.3 ‰ lighter than solution	von Allmen et al. 2010
Barite [a]	–0.32 ± 0.02 –0.36 ± 0.07	Carbonates are ~0.25 – 0.35 ‰ lighter than solution	von Allmen et al. 2010
Barite [b]	–0.68 ± 0.05		von Allmen et al. 2010
$BaMn(CO_3)_2$ [a]	–0.12 ± 0.05	Carbonate is ~0.11 ‰ lighter than solution	Böttcher et al. 2012a; Pretet 2013
Coral (cold-water species) [b] Coral (warm-water species) [b]	0.18 ± 0.03 0.24 ± 0.05 0.59 ± 0.07 0.74 ± 0.04 1.03 ± 0.07 0.54 ± 0.10	Corals are ~0 – 0.26 ‰ lighter than solution	Pretet 2013; Pretet et al. 2015
Coral (warm-water species) [c]	0.45 ± 0.12 0.47 ± 0.12 0.25 ± 0.10 0.54 ± 0.08 0.22 ± 0.08	Corals are ~0 – 0.26 ‰ lighter than solution	Pretet 2013; Pretet et al. 2015

a) experimentally-precipitated; b) natural sample collected from the marine environment; c) cultured in the laboratory using an inflow of seawater. Warm-water coral species are from Florida and the Bahamas; cold-water species are from the Norwegian shelf. Witherite is barium carbonate ($BaCO_3$) and barite is barium sulphate ($BaSO_4$).

5.3 Methods

5.3.1 Sample collection

Sediment and seawater samples were collected from the tropical North Atlantic during cruise JC094 of the RRS *James Cook* (Table 5.2; Figure 5.1). Seawater was sampled using a carousel of Niskin bottles and was filtered (0.2 μm AcroPak filter) and acidified (0.1 % v/v acid using Romil ultra-pure HCl) on board at the time of collection. Sediment sample S0157 was collected via box corer: approximately 16 cm of sediment was recovered, from which sample S0157 was collected as a bulk sample from approximately 10 – 16 cm beneath the sediment-water interface. The remaining sediment samples (S0059, S0066, S0131 and S0177) were taken from the core-tops (0 – 1 cm) of sediment cores collected via megacorer. Sediment and seawater samples were stored under refrigeration during the cruise.

To facilitate a comparison of the North and South Atlantic, previously-published data (Horner et al. 2015) and unpublished data (H. Pryer & Dr T. Horner, pers. com. 2016) from the southeast Atlantic will be plotted alongside tropical North Atlantic data (Table 5.2; Figure 5.1).

Table 5.2. Details of sediment samples and seawater profiles collected in the tropical North Atlantic and previously-published data (CTD025, Horner et al. 2015) and unpublished data (CTD013, H. Pryer & Dr T. Horner, pers. com. 2016) from the southeast Atlantic.

Sample	Location	Cruise	Station	Depth	Latitude	Longitude	Date
Sediment							
S0059	T. N. Atl.	JC094	016	3400 m	7°48.0'N	21°24.0'W	28/10/13
S0066	T. N. Atl.	JC094	019	3428 m	7°26.1'N	21°47.8'W	28/10/13
S0131	T. N. Atl.	JC094	046	4128 m	15°10.4'N	48°15.0'W	18/11/13
S0157	T. N. Atl.	JC094	053	3722 m	14°46.0'N	48°15.0'W	22/11/13
S0177	T. N. Atl.	JC094	061	2713 m	15°27.9'N	50°59.5'W	27/11/13
Seawater							
CTD002	T. N. Atl.	JC094	002	4524 m	9°17.1'N	21°38.0'W	19/10/13
CTD005	T. N. Atl.	JC094	039	5161 m	10°51.8'N	44°29.5'W	11/11/13
CTD006	T. N. Atl.	JC094	044	4183 m	15°16.2'N	48°15.6'W	16/11/13
CTD013	S. E. Atl.	D357	003	4894 m	36°27.3'S	13°23.3'E	23/10/10
CTD025	S. E. Atl.	D357	006	4927 m	39°59.3'S	0°55.0'E	30/10/10

T. N. Atl. = tropical North Atlantic, S. E. Atl. = southeast Atlantic

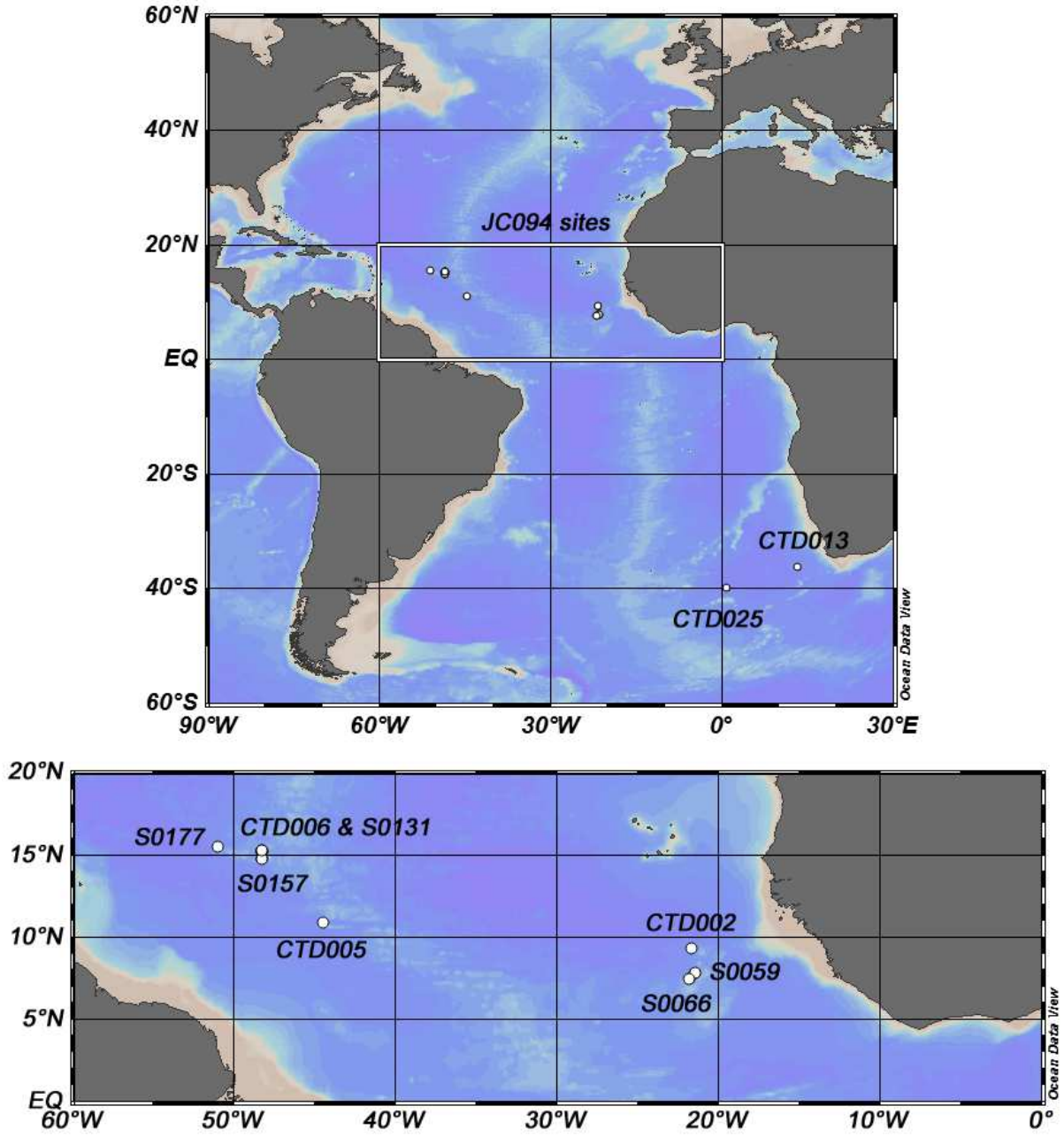

Figure 5.1. Map of sampling sites in the tropical North Atlantic ('CTD' sites = seawater profiles and 'S' sites = sediment samples) and locations of previously-published data (CTD025, Horner et al. 2015) and unpublished data (CTD013, H. Pryer & Dr T. Horner, pers. com. 2016) from the southeast Atlantic. The region surrounded by a white frame is magnified beneath.

5.3.2 Seawater methods

5.3.2.1 Barium isotope ratios and barium concentrations

Seawater barium isotope ratios and barium concentrations were measured at the Department of Marine Chemistry and Geochemistry and the WHOI Plasma Facility at Woods Hole Oceanographic Institution using the double-spiking method of Horner et al. 2015. Firstly, samples were spiked in order to obtain a 1:1 sample to spike ratio in the resulting mixture. Spike volumes were calculated using estimated dissolved barium concentrations obtained using the oceanic relationship between [Ba] and [Si] (Figure 1 in Horner et al. 2015) in combination with previously-made [Si] measurements. A double spike containing ^{135}Ba and ^{136}Ba was used rather than the previously-used ^{135}Ba-^{137}Ba double spike of Horner et al. 2015 to minimise the impact of ^{137}Xe interference (present in the Ar gas) on ^{137}Ba during mass spectrometry. Spiking was performed by adding the spike to empty vials, drying these down and adding 5 ml seawater to the pre-spiked vials. 70 µl ultra-pure 1 M HCl was added to each sample to keep the acidification of seawater samples consistent across both cruises to aid comparisons (JC094 and D357; Table 5.2). These solutions were fluxed overnight at 80 ºC to equilibrate sample and spike. Next, co-precipitation was used as an extra purification step prior to column chemistry. Samples were decanted into 15 ml centrifuge tubes and 50 µl of 1 M Na_2CO_3 was added to each sample seven times, shaking the samples between additions. Samples were then centrifuged at 7197 rcf for 5 minutes to accumulate the precipitate at the bottoms of the centrifuge tubes and the overlying solutions were removed via pipette. The precipitates were then dissolved by adding ~2 ml Milli-Q H_2O and 0.5 ml 6M HCl to each sample, decanting these back into their original vials and then repeating this to give a total sample volume of 5 ml. The samples were then dried down. Next, samples were dissolved in 250 µl 2.3 M HCl and refluxed at 80ºC to prepare them for column chemistry. Columns of ~500 µl AG 50W-X8 cation exchange resin were cleaned with 5 ml 6 M HCl and conditioned with 5 ml 2.3 M HCl. Following this, the samples were loaded onto the columns and non-Ba elements eluted using 5 ml 2.3 M HCl. 250 µl 2 M HNO_3 was then passed through each column before eluting Ba into sample vials using 2750 µl 2 M HNO_3. The samples were then dried down. In addition, in light of two anomalously low barium isotope ratios measured in CTD006, seawater profiles CTD002 and CTD005 were put through column chemistry once more to ensure that matrix effects were minimised. To remove any possible organic contamination originating from the resin, each sample was dissolved in 5 drops of concentrated HNO_3 and then dried down. To prepare them for measurement, samples were then dissolved in 2 ml 2 % HNO_3 and refluxed at 80 ºC overnight before decanting into 2 ml measurement vials.

Samples were run at the Plasma Mass Spectrometry Facility, Woods Hole Oceanographic Institution on a Thermo Finnigan Neptune MC-ICP-MS with a nickel sample cone, nickel 'X' skimmer cone, Elemental Scientific PFA MicroFlow self-aspirating Teflon nebuliser and CETAC Aridus II, with a N_2-Ar gas flow. The following isotopes were measured: ^{135}Ba, ^{136}Ba, ^{137}Ba and ^{138}Ba (to calculate barium isotope ratios and barium concentrations); ^{131}Xe (to correct for ^{136}Xe interference on ^{136}Ba);

^{139}La (to correct for ^{138}La interference on ^{138}Ba); and ^{140}Ce (to correct for ^{138}Ce and ^{136}Ce interferences on ^{138}Ba and ^{136}Ba). Interference corrections were made by calculating the expected abundance of the interfering isotope using the relative abundances of the isotopes of that element (for example, by using the ^{131}Xe measurement to calculate the expected abundance of ^{136}Xe) and then subtracting this expected abundance from the barium isotope in question. Isotope ratios were calculated, with interference corrections applied simultaneously, relative to National Institute of Standards and Technology (NIST) Standard Reference Material 3104a (Equation 5.1). Standards were measured either once at the beginning of each run, for comparison with long-term measurements, or several times within each run using standard-sample bracketing. Barium isotope ratios were calculated via repeated nested iterations as described in Horner et al. 2015. This approach uses a three-dimensional interpretation of double-spiking equations (Siebert et al. 2001) with ^{138}Ba/^{135}Ba on the x axis, ^{137}Ba/^{135}Ba on the y axis and ^{136}Ba/^{135}Ba on the z axis (Figure 5.2). Within this three-dimensional space, three known points – 'S' (the spike), 'm' (the measured sample-spike mixture) and 'n' (the standard) – are used to calculate two unknown points – 'M' (the true (unaffected by instrumental mass fractionation) sample-spike mixture) and 'N' (the sample). The difference between n and N defines the δ^{138}Ba of the sample. Points m, M and S form one curved plane, points n, N and S form another curved plane and the line along which these two planes intersect is a mixing line between S and N upon which M falls (Figure 5.2). An initial value of N (set by δ^{138}Ba = 5000 ‰) is used to calculate M, which is then used to calculate a new N. This is repeated until the δ^{138}Ba of the sample remains constant to the 9th decimal place, which is typically after five iterations. Barium isotope ratios were not blank-corrected because the amount of barium present in the blanks (1 – 3 % of the total barium in a sample) was negligible compared to internal precision (Dr T. Horner, pers. com. 2015). Blanks underwent the same treatment as samples.

Barium isotope ratios were converted from ^{138}Ba/^{135}Ba notation into ^{138}Ba/^{134}Ba notation, as shown in Equation 5.1, by multiplying by a conversion factor as shown below:

$$\delta^{138/134}\mathrm{Ba} = \frac{\ln\left(\frac{\text{mass of } ^{138}\mathrm{Ba}}{\text{mass of } ^{134}\mathrm{Ba}}\right)}{\ln\left(\frac{\text{mass of } ^{138}\mathrm{Ba}}{\text{mass of } ^{135}\mathrm{Ba}}\right)} \times \delta^{138/135}\mathrm{Ba} = 1.34 \times \delta^{138/135}\mathrm{Ba} \qquad (5.3)$$

Seawater barium concentrations were calculated using the following equations:

$$\mathrm{S{:}N} = \frac{S_x}{N_x} = \frac{(S_x+N_x)-N_x}{S_x-(S_x+N_x)} = \frac{M_x-N_x}{S_x-M_x} = \frac{(M_{xy}\times N_y)-N_x}{S_x-(M_{xy}\times S_y)} \qquad (5.4)$$

$$\text{sample [Ba]} = \frac{\text{spike [Ba]}}{\mathrm{S{:}N}} \qquad (5.5)$$

Where S:N is the sample-to-spike ratio, S_x and S_y are the abundances of ^{138}Ba and ^{135}Ba in the spike, N_x and N_y are the abundances of ^{138}Ba and ^{135}Ba in the sample, M_x is the abundance of ^{138}Ba in

the sample-spike mixture which has been corrected for instrumental mass fractionation and M_{xy} is the $^{138}Ba/^{135}Ba$ ratio of the sample-spike mixture corrected for instrumental mass fractionation. This was calculated for samples and blanks separately prior to blank-correcting the samples.

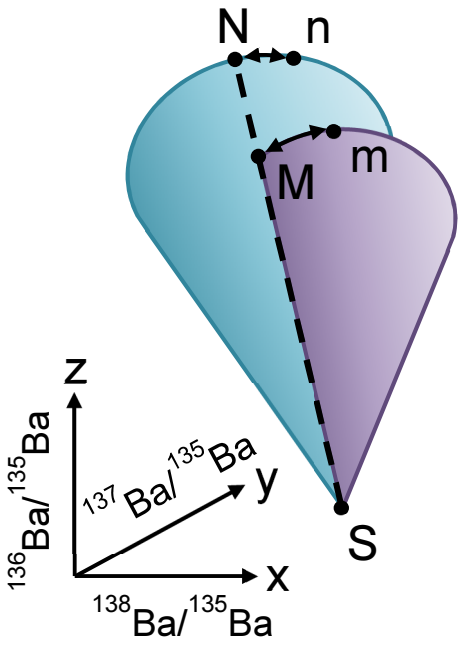

Figure 5.2. Visual representation of a hypothetical solution to the double-spiking equations as used in Horner et al. 2015, based on the three-dimensional approach of Siebert et al. 2001. 'S' is the composition of the spike solution, 'N' is the sample, 'n' is the standard, 'M' is the true (unaffected by instrumental mass fractionation) sample-spike mixture and 'm' is the measured sample-spike mixture. The relationship between 'N' and 'n' defines $\delta^{138}Ba$ and the relationship between 'M' and 'm' is set by instrumental mass fractionation. The dashed line at the intersection of two planes is a mixing line between 'S' and 'N' upon which 'M' falls.

5.3.2.2 Sensor data, nutrients and total alkalinity

Seawater temperature, conductivity (converted to salinity using a Guildline Autosal salinometer and Autosal software), fluorescence and dissolved oxygen were measured in-situ using a Sea-Bird (SBE) 9plus underwater unit fitted with SBE 3 temperature sensors, SBE 4 conductivity sensors, a CTG AquaTracka MKIII fluorimeter and a Sea-Bird 43 dissolved oxygen sensor. In-situ temperature data were converted into potential temperature relative to the sea surface in MatLab (Meyer 2015). Potential density was calculated using potential temperature and salinity data (Maidment 1993). Fluorescence data were baseline-corrected after being converted into relative values via the following equation:

$$F_R = \frac{F - F_{min}}{F_{max} - F_{min}} \qquad (5.6)$$

Where F_R is relative fluorescence, F is the original fluorescence, F_{min} is the minimum F in the seawater profile and F_{max} is the maximum F in the seawater profile.

Seawater silicate, nitrite and combined nitrite and nitrate concentrations were measured in unfiltered seawater samples using a Bran+Luebbe five-channel segmented flow autoanalyser and high-resolution colorimeter (E. M. Woodward, pers. com. 2014). Nitrate concentrations were calculated by subtracting nitrite concentrations from combined nitrite and nitrate concentrations. Total alkalinity was measured via closed-cell titration (Dickson et al. 2007) at the UK Ocean Acidification Research Program Carbonate Chemistry Facility at the National Oceanography Centre, Southampton (A. Griffiths, pers. com. 2015).

5.3.2.3 Si and Ba**

Si* ("Si-star") and Ba* ("Ba-star") were calculated using the following equations (Gruber & Sarmiento 1997; Sarmiento et al. 2004; Horner et al. 2015):

$$N^* = [NO_3^-] - 16[PO_4] \qquad (5.7)$$

$$Si^*(\mu M) = [Si(OH)_4] - [NO_3^-] + \delta \qquad (5.8)$$

$$Ba^*(nM) = [Ba] - 0.6839[Si(OH)_4] - 39.42 \qquad (5.9)$$

Where $\delta = 1$ if $N^* < -3$ μM and $\delta = 0$ if $N^* \geq -3$ μM as a correction for denitrification (Sarmiento et al. 2004). In Equation 5.7, Equation 5.8 and Equation 5.9 all concentrations are in units of μM except for [Ba] which is in nM. Equation 5.9 is based on the equation of Horner et al. 2015, updated to include the [Ba] and [Si] data from this study.

5.3.3 Foraminifer methods

5.3.3.1 Foraminifer picking

Sediment sample S0157 was separated into coarse (> 63 μm) and fine (< 63 μm) fractions via wet sieving and gravity settling, then oven-dried at 45 ºC, at the School of Earth and Ocean Sciences, Cardiff University. The remaining sediment samples were dried and sieved at the Lamont-Doherty Earth Observatory, Columbia University (A. Jacobel, pers. com. 2015). Foraminifera were picked under optical microscope using a brush wetted with RO water at the School of Earth Sciences, University of Bristol. The planktic foraminifer *Orbulina universa* was picked from size fractions 355 – 425 μm and > 425 μm of sediment sample S0157 so that results from different size fractions could be compared. Size fraction > 425 μm was used for the remaining sediment samples because *O. universa* was more plentiful in this size fraction.

This species was selected because several previously-published D_{Ba} values (barium partition coefficients) are available for *O. universa*, facilitating a comparison of the D_{Ba} measured here with those measured by others. Also, a mass of at least 10 ng Ba is required for this method (Dr T. Horner, pers. com. 2015), which is approximately 12 mg of calcium carbonate, given typical seawater [Ba] and D_{Ba}

for this species. *O. universa* was present in plentiful amounts in these sediments and thus able to provide the required masses of calcium carbonate. A further benefit is that *O. universa* is a cosmopolitan species, present between approximately 60 ºN and 50 ºS globally (Gupta 1999), making it a convenient choice for future studies seeking to compare their results with the data presented here.

Foraminifera were picked for: a) barium isotope ratio and Ba/Ca measurement at Woods Hole Oceanographic Institution; b) Ba/Ca measurement at the University of Bristol for interlaboratory comparison (see Section 2.4.6 'Interlaboratory comparison'); c) oxygen and carbon isotope ratios; and d) scanning electron microscopy. The total weights of the foraminifer samples picked for barium isotope ratio and Ba/Ca measurement at Woods Hole Oceanographic Institution are provided in Table 5.3. For the remaining methods, only a few individuals were required per sample. Two visually-distinct types of *O. universa* were seen in the samples: a 'clear' type which was translucent when wet; and an 'opaque' type which was opaque when wet. Because large numbers of foraminifera were required for the barium isotope ratio and Ba/Ca measurements at Woods Hole Oceanographic Institution (Table 5.3), both types were combined together when picking. For the remaining measurements, separate 'clear' and 'opaque' samples were picked to investigate how these two types compare.

Table 5.3. Numbers and total weights of foraminifera picked for barium isotope ratio and Ba/Ca measurement at Woods Hole Oceanographic Institution.

Sediment sample	Size of foraminifera picked (μm)	Number of foraminifera picked	Total weight of foraminifer sample after cleaning (mg) [a]
S0157	355 – 425	800	17.14
S0157	> 425	320	18.81
S0059	> 425	620	20.12
S0066	> 425	620	19.63
S0131	> 425	420	20.69
S0177	> 425	220	13.23

a) All foraminifer samples were cleaned at the School of Earth Sciences, University of Bristol via the methods described in Section 2.2 'Foraminiferal cleaning procedure'.

5.3.3.2 Barium isotope ratios and Ba/Ca

Prior to measurement, foraminifer samples were cleaned at the School of Earth Sciences, University of Bristol using the method described in Section 2.2 'Foraminiferal cleaning procedure'. Ba/Ca ratios in *O. universa* from sediment sample S0157 were measured at the School of Earth Sciences, University of Bristol using the methods described in Chapter 2 'Trace Metal Methods' to facilitate an interlaboratory comparison with Woods Hole Oceanographic Institution (see Section 2.4.6 'Interlaboratory comparison'). Foraminiferal barium isotope ratios and Ba/Ca ratios in the same

samples were measured at the Department of Marine Chemistry and Geochemistry and the WHOI Plasma Facility at Woods Hole Oceanographic Institution. Barium isotope ratios were measured using the seawater method as described in Section 5.3.2 'Seawater methods', excepting that: foraminifera were dissolved in a few drops of concentrated HCl and dried down prior to spiking and spike volumes were calculated to attain a 1:1 sample:spike ratio based on the predicted Ba/Ca of the samples (given seawater [Ba] and foraminiferal D_{Ba}); and instead of the co-precipitation stage, foraminifer samples were fluxed in 6 M HCl at 135 ºC for at least 1 hour to remove nitrogen. The remainder of the method (from column chemistry onwards) was the same as for seawater. Ba/Ca ratios were calculated via:

$$\text{sample Ba mass} = \frac{\text{spike Ba mass}}{\text{S:N}} \qquad (5.10)$$

$$\text{sample Ca mass} = \text{total sample mass} \times \frac{\text{Ca atomic mass}}{\text{CaCO}_3\text{ molecular mass}} \qquad (5.11)$$

$$\text{sample}\frac{\text{Ba}}{\text{Ca}}\text{ratio} = \frac{\text{sample Ba mass}}{\text{sample Ca mass}} \qquad (5.12)$$

Where S:N is the sample-to-spike ratio as calculated by Equation 5.4. The masses of Ba in the samples and blanks were calculated and blank corrections applied before proceeding to calculate Ba/Ca ratios using Equation 5.12. Equation 5.11 makes the assumption that the total weight of each sample (Table 5.3) ≈ the weight of $CaCO_3$ in the sample. Blanks underwent the same treatment as samples, including the foraminiferal cleaning procedure.

5.3.3.3 Seawater-foraminifer barium isotope ratio offsets

Offsets between the barium isotope ratios of foraminifera and those of the ambient seawater were calculated by subtracting foraminiferal barium isotope ratios from seawater barium isotope ratios. Seawater data from the depths most closely resembling the habitat of *O. universa* were used (further details are provided in Section 5.5 'Discussion'). Errors for seawater-foraminifer offsets were propagated using the following equation:

$$\text{SE}_\text{O} = \sqrt{\text{SE}_\text{S}^2 + \text{SE}_\text{F}^2} \qquad (5.13)$$

Where SE_O is the standard error of the seawater-foraminifer offset, SE_S is the standard error of the seawater barium isotope ratio and SE_F is that of the foraminifera.

5.3.3.4 Barium partition coefficients

Foraminiferal barium partition coefficients (D_{Ba}) were calculated via Equation 5.14:

$$\text{D}_\text{Ba} = \left(\frac{\text{Ba}}{\text{Ca}}\right)_\text{f} \times \frac{[\text{Ca}]_\text{sw}}{[\text{Ba}]_\text{sw}} \qquad (5.14)$$

Where $(Ba/Ca)_f$ is the foraminiferal Ba/Ca ratio, $[Ca]_{sw}$ is the calcium concentration of the seawater, assumed to be 10.3 mM (Dickson & Goyet 1994), and $[Ba]_{sw}$ is the barium concentration of the seawater. Seawater barium concentration data from the depths most closely resembling the habitat of *O. universa* were used (further details are provided in Section 5.5 'Discussion').

5.3.3.5 Oxygen and carbon isotope ratios

Approximately 50 – 60 µg of foraminifera per measurement were crushed between two RO water cleaned glass slides under an optical microscope and then placed in acid-cleaned 500 µl microcentrifuge vials. Foraminifer fragments were then ultrasonicated for 5 minutes in approximately 400 – 500 µl methanol and rinsed twice with Milli-Q water. Sample vials were left open under a clean protective guard in a clean fume hood area to dry down completely before measurement. $\delta^{18}O$ and $\delta^{13}C$ were measured at the School of Earth and Ocean Sciences, Cardiff University using a Thermo Scientific Kiel IV Carbonate Device with Thermo Scientific MAT 253 isotope ratio mass spectrometer. This instrument has a long-term precision of $\sigma = 0.040$ ‰ for $\delta^{18}O$ and $\sigma = 0.032$ ‰ for $\delta^{13}C$ ($n = 218$) using a Carrara marble standard (Dr S. Nederbragt, pers. com. 2016). All isotope ratios were calculated relative to Vienna Pee Dee Belemnite (VPDB).

5.3.3.6 Scanning electron microscopy

SEM micrographs of whole shells and fragments of *O. universa* from sediment sample S0157 were taken at the British Ocean Sediment Core Research Facility in the National Oceanography Centre, University of Southampton using a Hitachi TM1000 Tabletop Microscope. No sample coating was required. Samples were mounted on specimen stubs by attaching them to carbon adhesive discs (Leit tabs) using a wetted brush.

5.4 Results

5.4.1 Seawater results

Seawater profiles of potential temperature, salinity, potential density, fluorescence, dissolved oxygen, nitrate, silica, total alkalinity, barium concentration and seawater barium isotope ratios are shown in Figure 5.3, Figure 5.4, Figure 5.5 and Figure 5.6. The data are cropped to depths 0 – 600 m in lower panels for greater visual clarity of near-surface data. Barium concentrations are plotted against silica and total alkalinity in Figure 5.7 and seawater barium isotope ratios are plotted against 1/[Ba] in Figure 5.8 and against [Si]/[Ba] in Figure 5.9. Ba* profiles, Si* profiles and plots of Ba* against seawater barium isotope ratios are presented in Figure 5.10. Figure 5.11 is a guide to interpreting Ba* and Si*. A representative ± 2SE (standard error) error bar (± 0.035 ‰) is shown for the seawater barium isotope data. Typical standard errors were 0.03 – 0.04 ‰. A representative error bar is used in order to aid visual clarity of the figures. Seawater barium concentrations are plotted without error bars because their internal precision was sufficiently small as to be negligible (Dr T. Horner, pers. com. 2015).

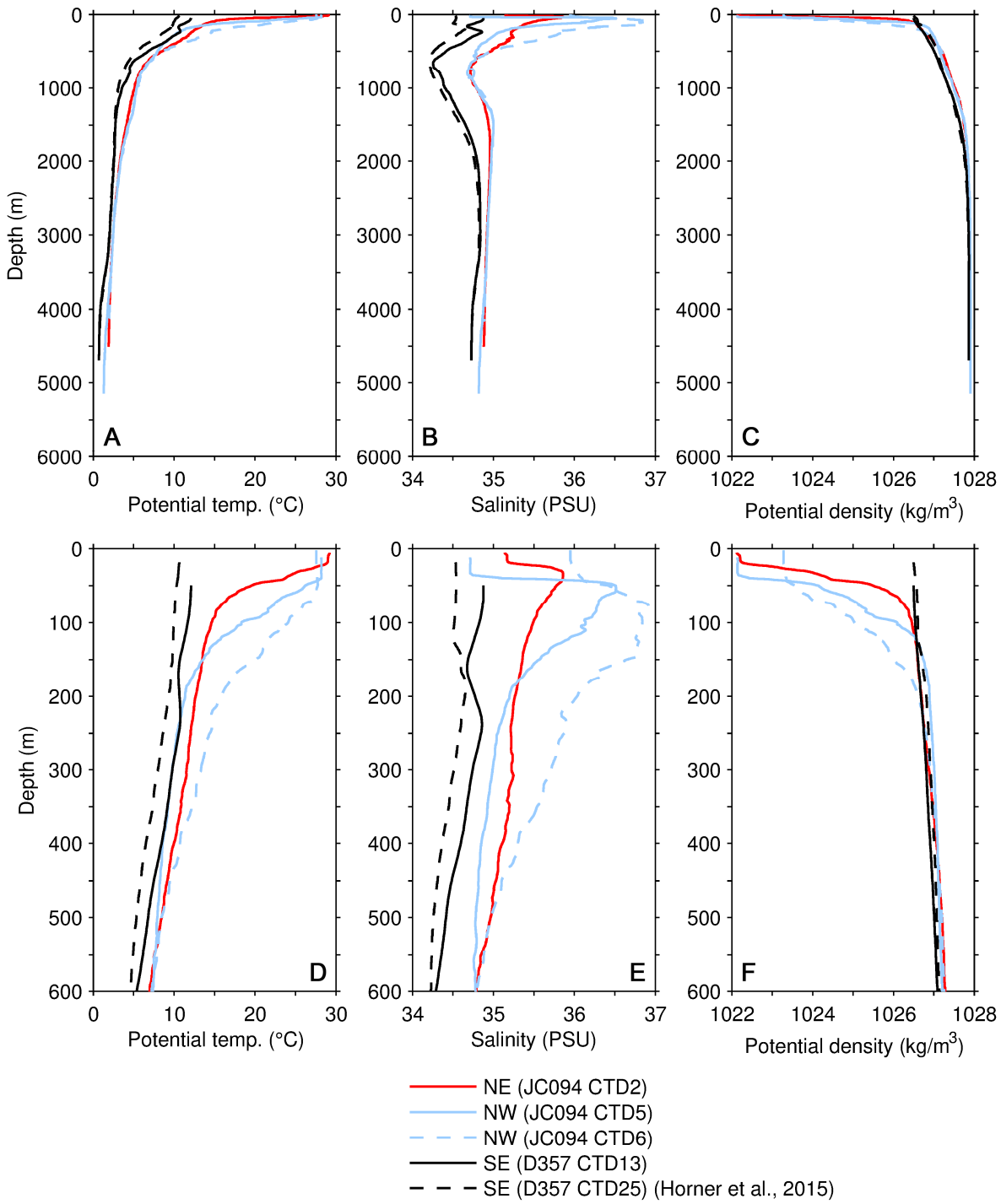

Figure 5.3. Potential temperature (A, D), salinity (B, E) and potential density (C, F) seawater profiles from the tropical North Atlantic and southeast Atlantic.

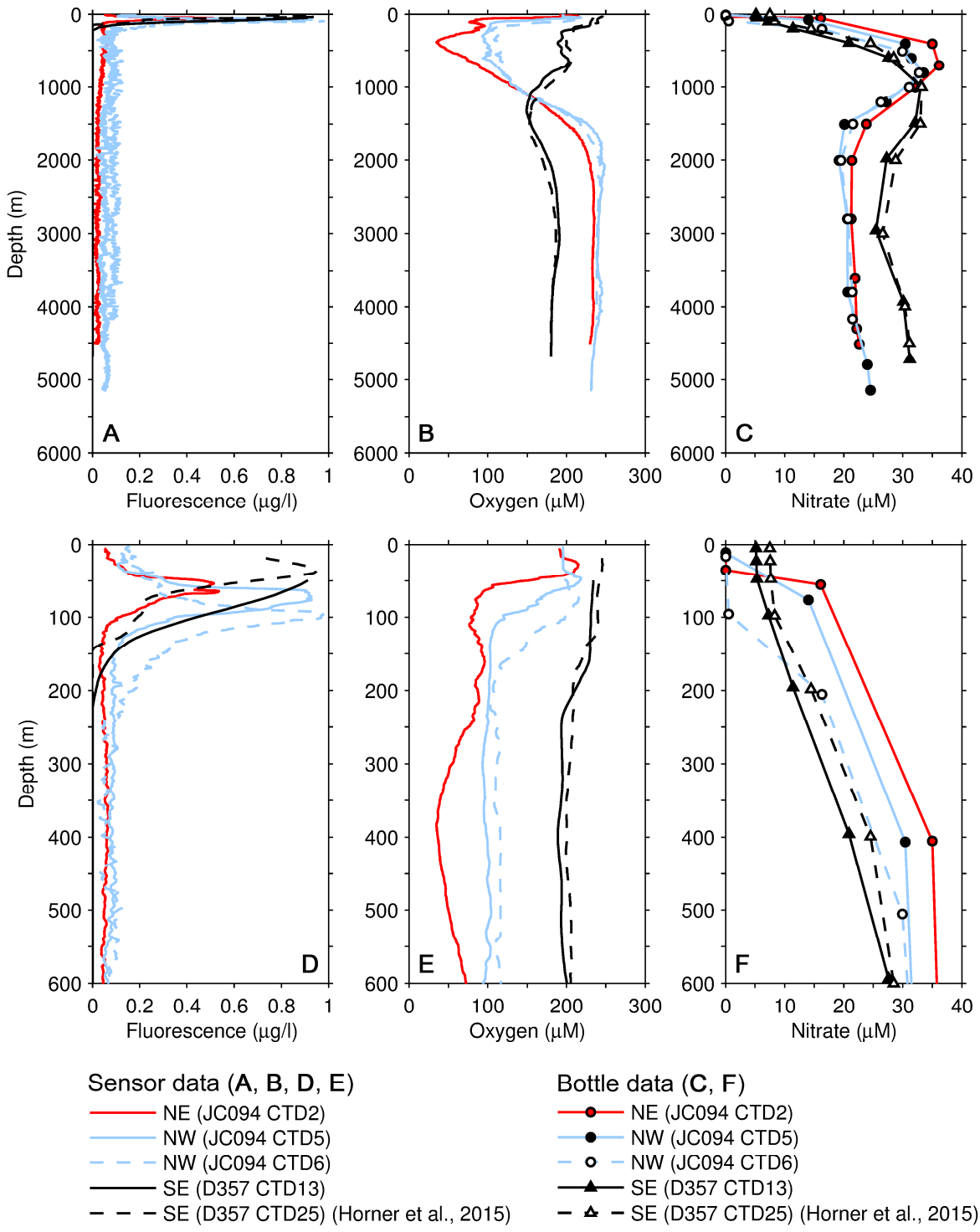

Figure 5.4. Fluorescence (A, D), dissolved oxygen concentration (B, E) and nitrate concentration (C, F) seawater profiles from the tropical North Atlantic and southeast Atlantic.

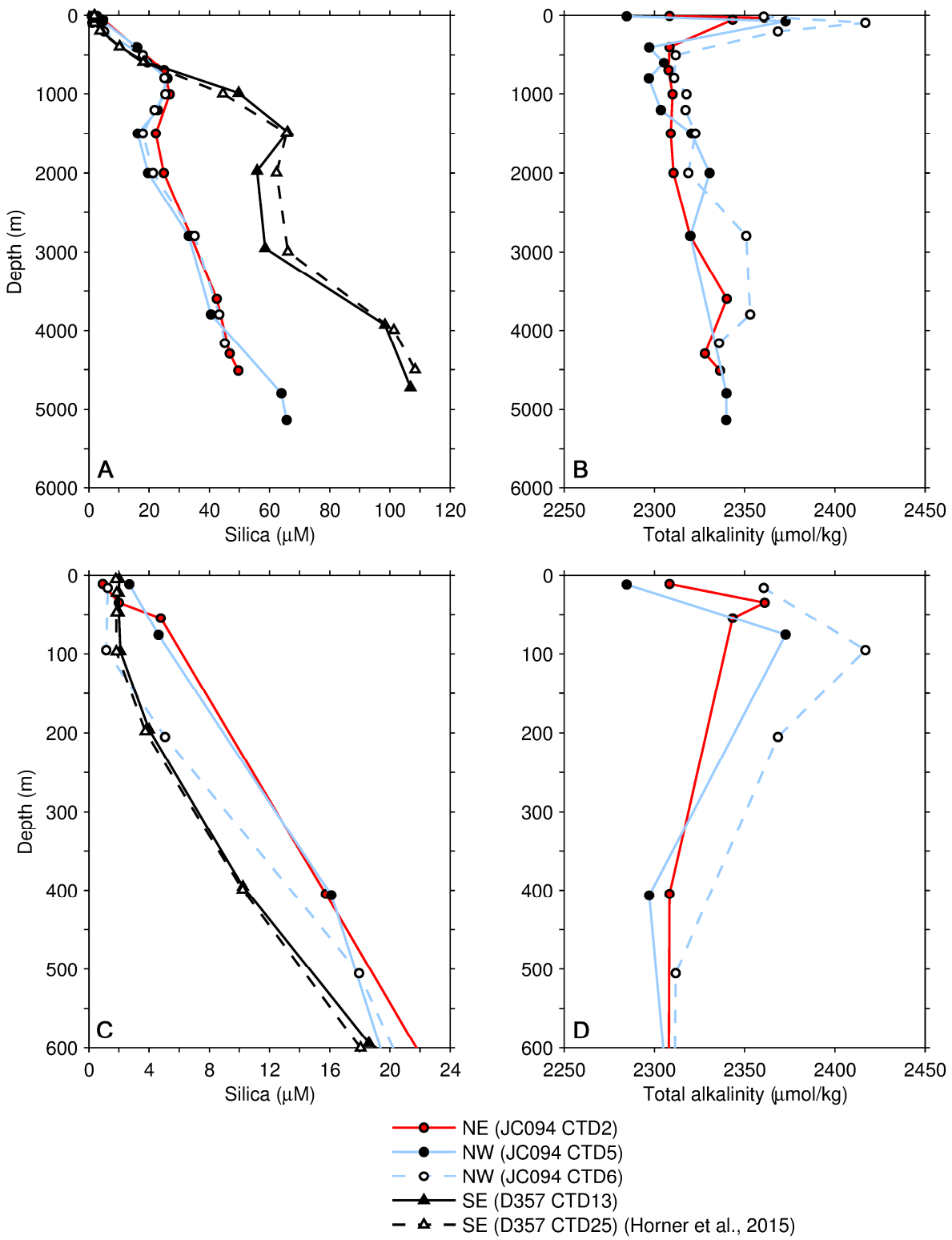

Figure 5.5. Silica concentration (A, C) and total alkalinity (B, D) seawater profiles from the tropical North Atlantic and southeast Atlantic. Total alkalinity data were not available for the southeast Atlantic sites.

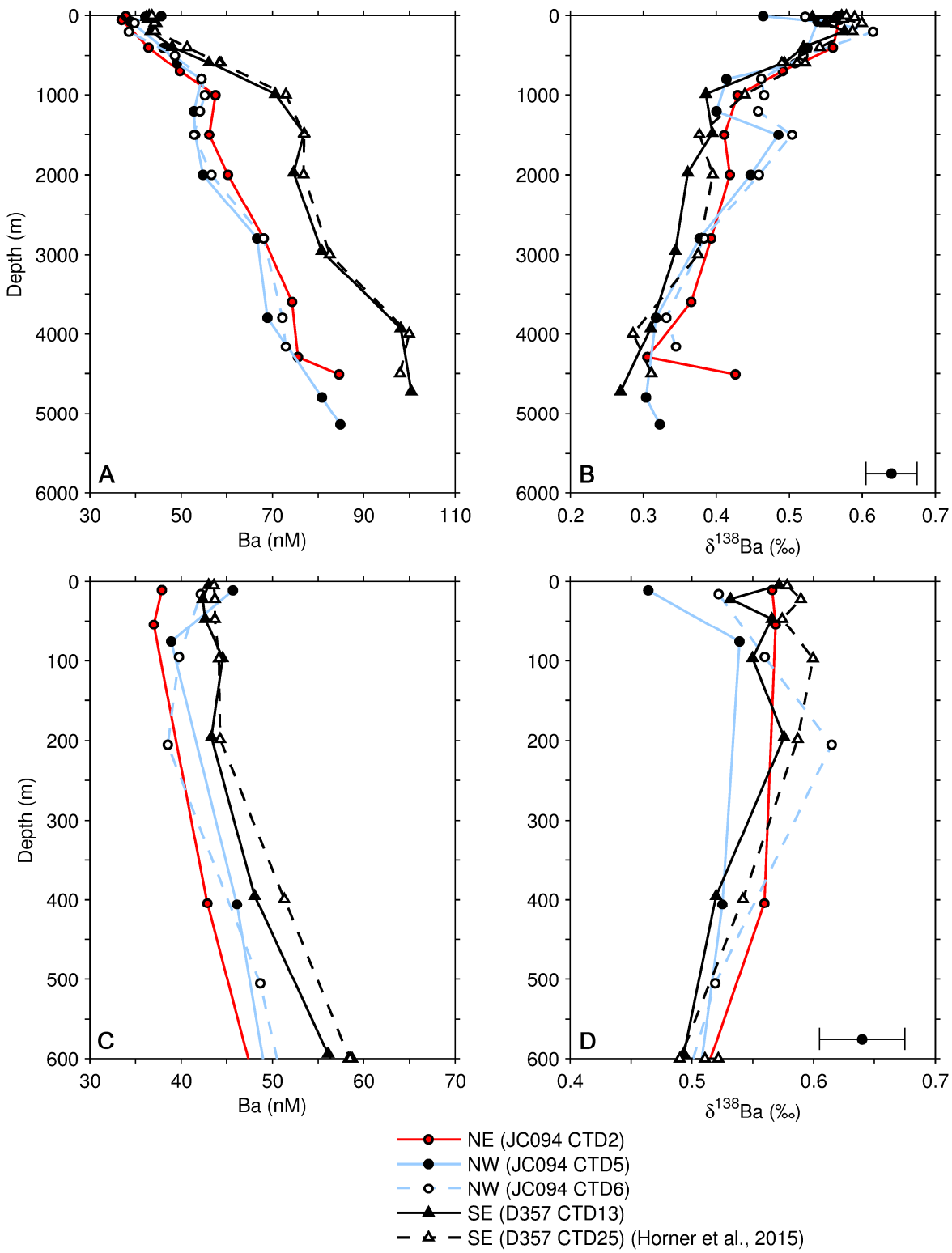

Figure 5.6. Barium concentration (A, C) and barium isotope ratio (B, D) seawater profiles from the tropical North Atlantic and southeast Atlantic. A representative ± 2SE (standard error) error bar (± 0.035 ‰) is shown for the seawater barium isotope data to aid visual clarity; typical standard errors were 0.03 – 0.04 ‰.

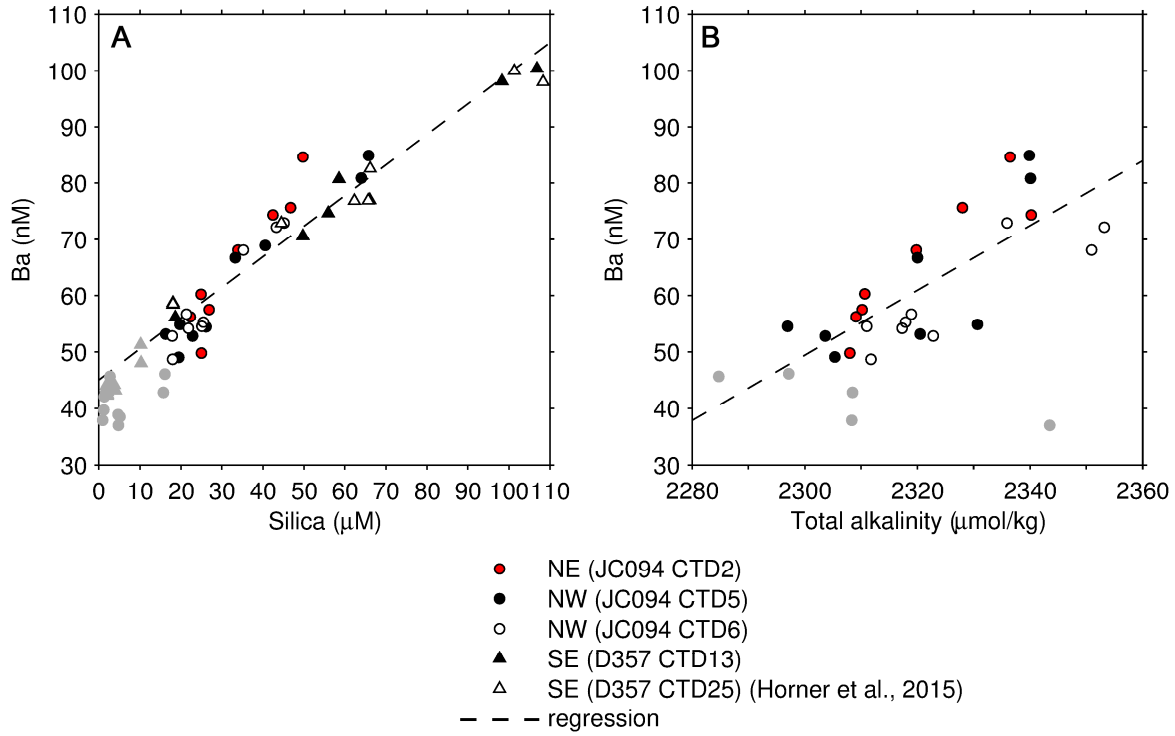

Figure 5.7. Barium concentration plotted against silica concentration (A) and total alkalinity (B) in seawater samples from the tropical North Atlantic and southeast Atlantic. Total alkalinity data were not available for the southeast Atlantic sites. Least-squares linear regressions were calculated using data from > 500 m. Data from < 500 m are plotted in grey. Regression equations are: Ba = 0.55Si + 45.05 (R^2 = 0.92, $p < 0.05$) (A); and Ba = 0.58TA – 1274.58 (R^2 = 0.57, $p < 0.05$) (B).

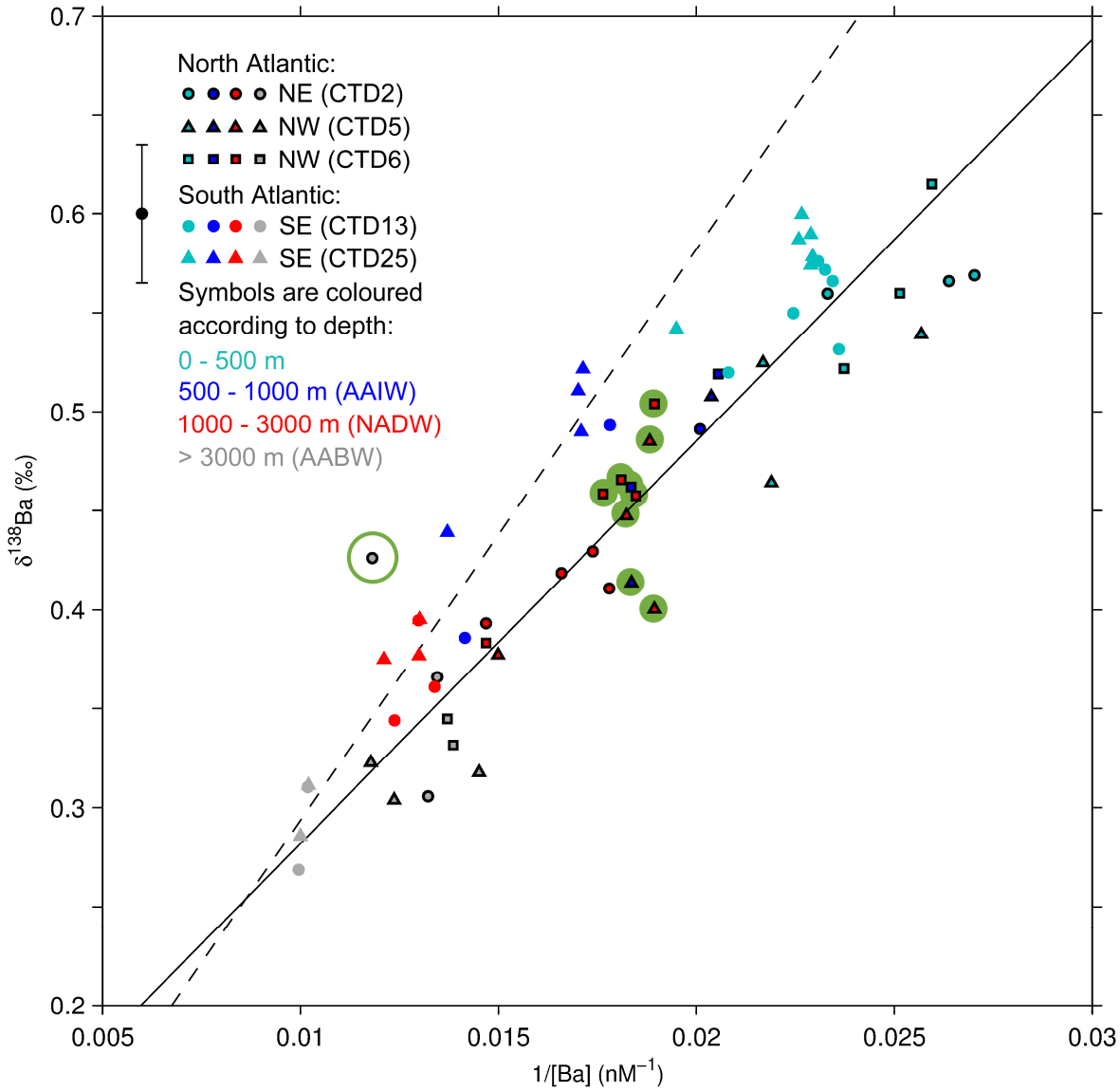

Figure 5.8. Seawater δ^{138}Ba plotted against the inverse of barium concentrations (1/[Ba]). Symbols with a black border are from the tropical North Atlantic: circles are CTD002 (NE), triangles are CTD005 (NW) and squares are CTD006 (NW). Symbols without a border are from the SE Atlantic: circles are CTD013 and triangles are CTD025. Sample depths are colour-coded: light blue is 0 – 500 m (near-surface), dark blue is 500 – 1000 m (AAIW), red is 1000 – 3000 m (NADW) and grey is > 3000 m (AABW). The deepest sample of CTD002 is circled and the samples affected by the DWBC have a shaded green background. The solid line is a linear regression through the tropical North Atlantic data from > 500 m ($y = 20.32x + 0.08$, $R^2 = 0.73$, $p < 0.05$). The dashed line is a linear regression through the SE Atlantic data > 500 m ($y = 28.82x + 0.01$, $R^2 = 0.93$, $p < 0.05$). A representative ± 2SE error bar (± 0.035 ‰) is shown for δ^{138}Ba to aid visual clarity; typical standard errors were 0.03 – 0.04 ‰.

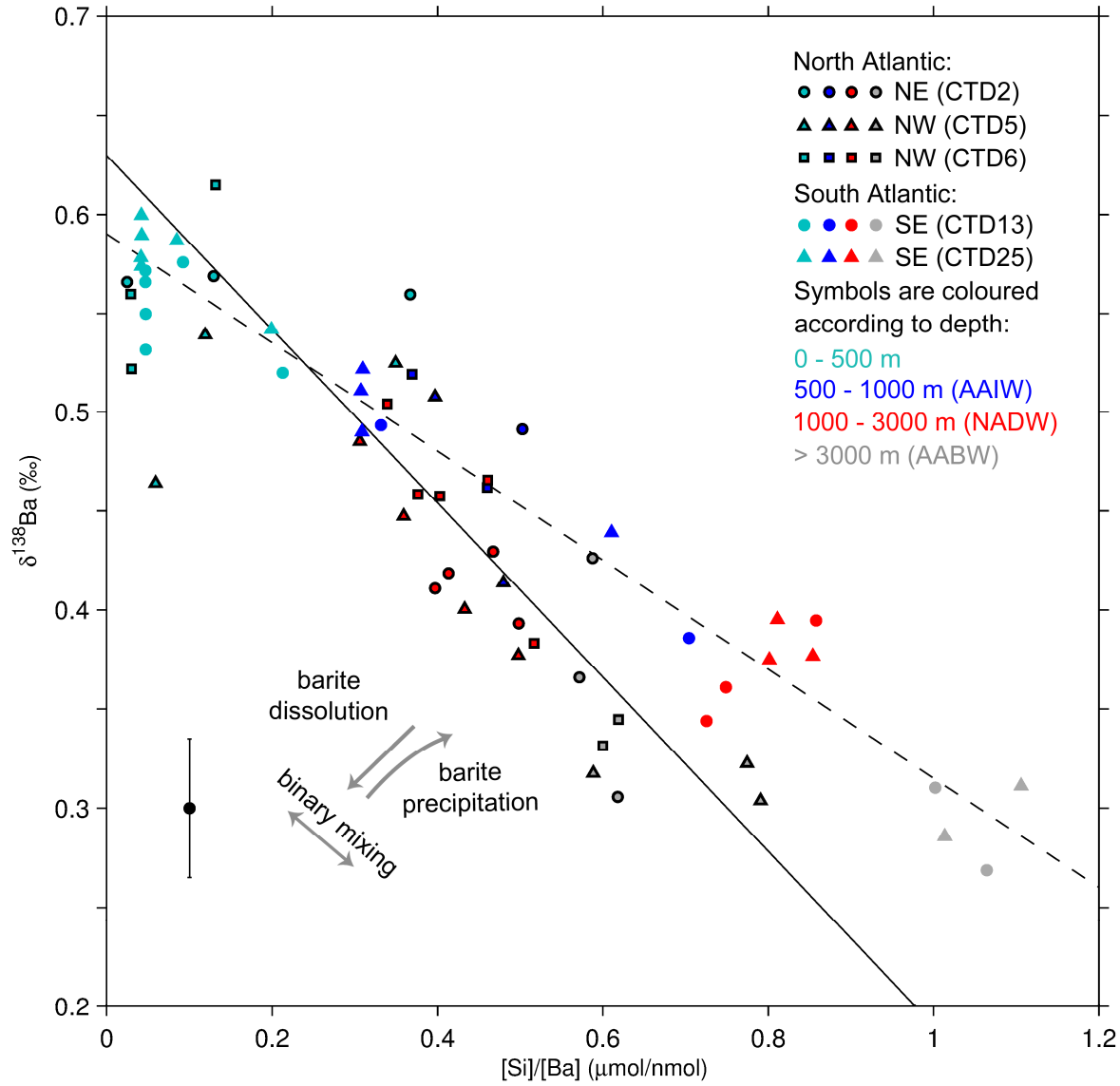

Figure 5.9. Seawater barium isotope ratios plotted against silica divided by barium concentrations. Symbols with a black border are from the tropical North Atlantic: circles are CTD002 (NE), triangles are CTD005 (NW) and squares are CTD006 (NW). Symbols without a border are from the southeast Atlantic: circles are CTD013 and triangles are CTD025. Symbols are coloured according to sample depth: light blue is 0 – 500 m (near-surface), dark blue is 500 – 1000 m (AAIW), red is 1000 – 3000 m (NADW) and grey is > 3000 m (AABW). The solid line is a linear regression through the tropical North Atlantic data from > 500 m ($y = -0.44x + 0.63$, $R^2 = 0.68$, $p < 0.05$). The dashed line is a linear regression through the southeast Atlantic data from > 500 m ($y = -0.28x + 0.59$, $R^2 = 0.91$, $p < 0.05$). A representative ± 2SE (standard error) error bar (± 0.035 ‰) is shown for the seawater barium isotope data to aid visual clarity; typical standard errors were 0.03 – 0.04 ‰.

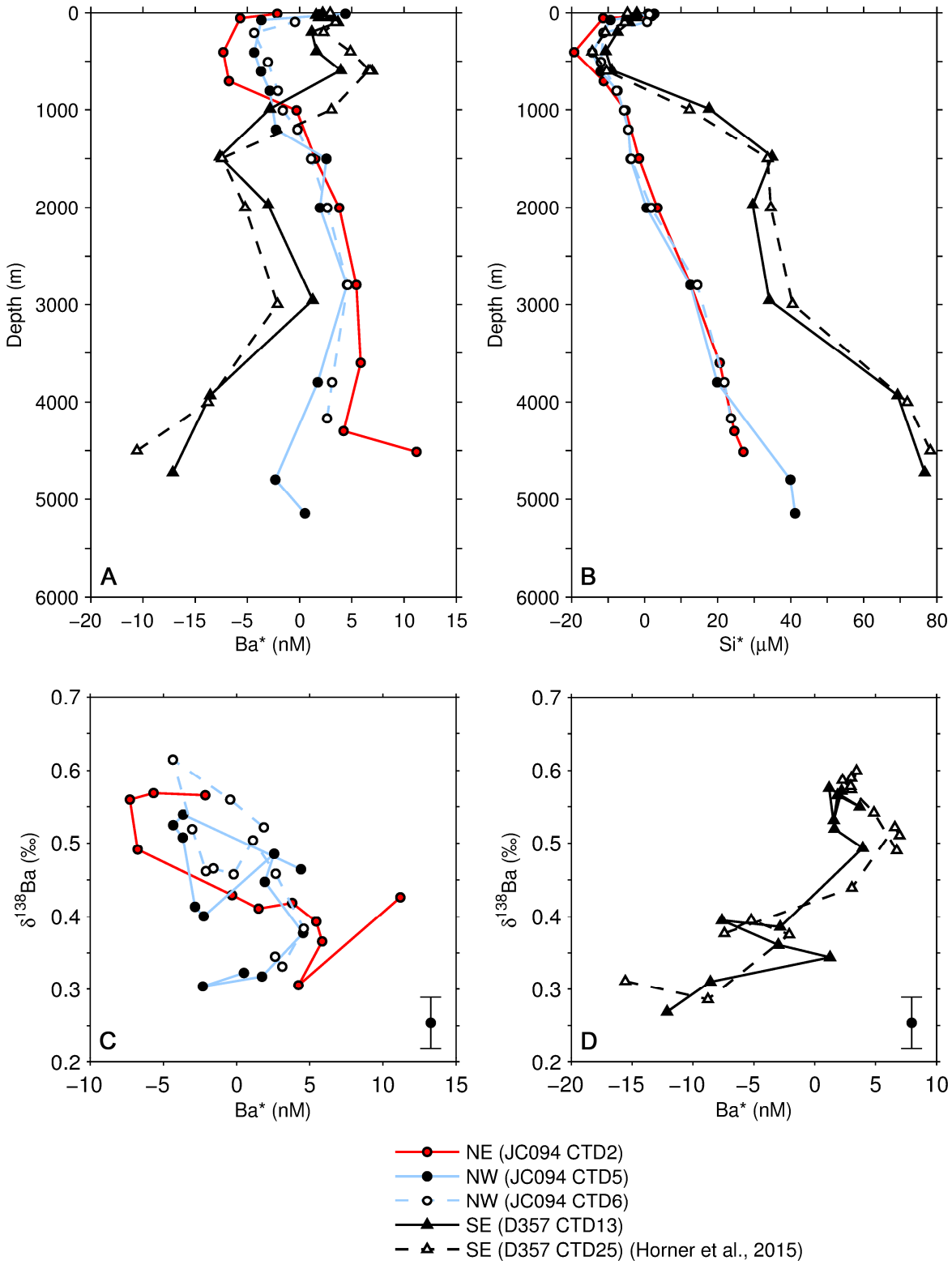

Figure 5.10. Ba* (A), Si* (B) and Ba* plotted against seawater barium isotope ratios (C, D) in seawater samples from the tropical North Atlantic and southeast Atlantic. A representative ± 2SE (standard error) error bar (± 0.035 ‰) is shown for the seawater barium isotope data to aid visual clarity; typical standard errors were 0.03 – 0.04 ‰.

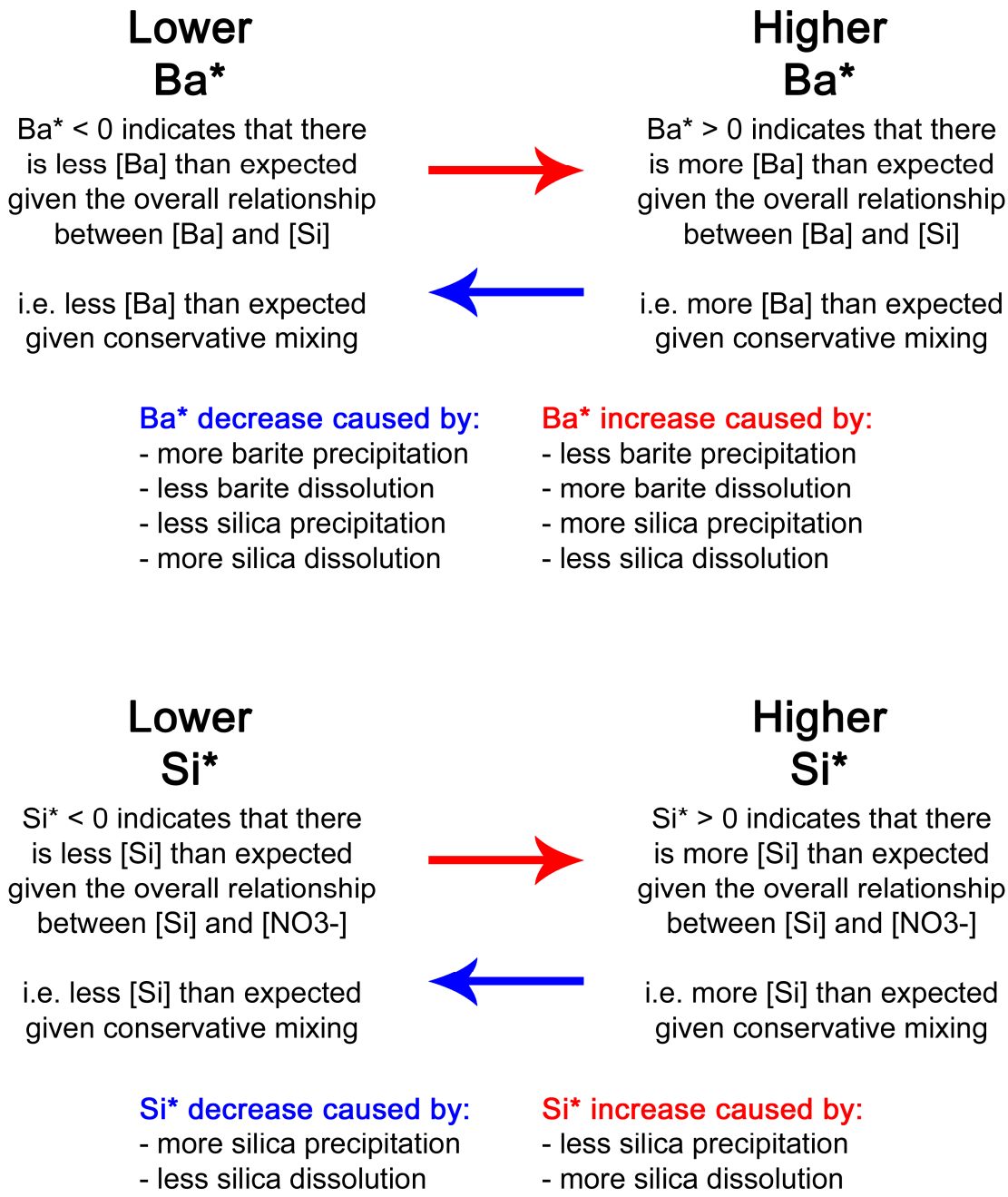

Figure 5.11. A guide to interpreting Ba* and Si*.

5.4.2 Foraminifer results

Foraminiferal barium isotope ratios and Ba/Ca ratios are plotted in Figure 5.12. Ba/Ca ratios measured at Woods Hole Oceanographic Institution compare well with those measured at the University of Bristol (see Section 2.4.6 'Interlaboratory comparison'). ± 2SE error bars are shown for the foraminiferal barium isotope data. Ba/Ca ratios are plotted without error bars because their internal precision was sufficiently small as to be negligible (Dr T. Horner, pers. com. 2015). D_{Ba} values calculated using Ba/Ca ratios and seawater barium concentrations are presented in Table 5.4, along with previously-published D_{Ba} values for *O. universa*. The D_{Ba} values found by this study agree well with those of previous studies (Table 5.4). Seawater-foraminifer barium isotope ratio offsets are plotted in Figure 5.13 and tabulated in Table 5.5. Oxygen isotope ratios and carbon isotope ratios are plotted in Figure 5.14 and Figure 5.15, respectively. Figure 5.16 is a composite SEM micrograph showing whole and fragmented samples of *O. universa* of the two types: 'clear' and 'opaque'.

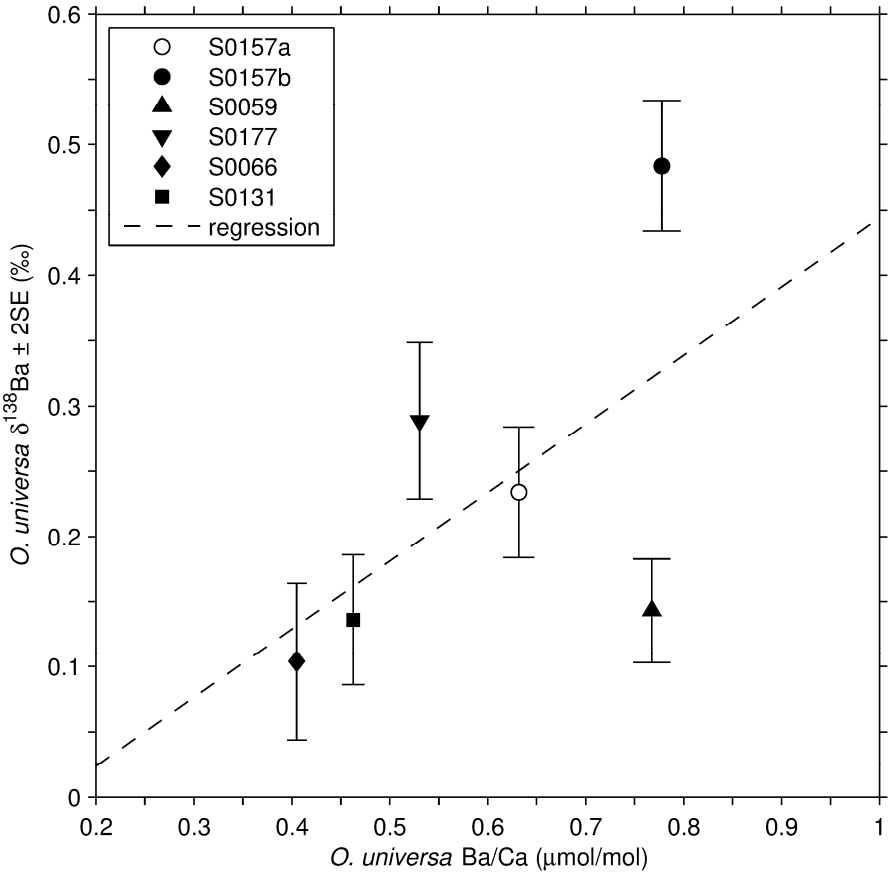

Figure 5.12. Foraminiferal barium isotope ratios plotted against foraminiferal Ba/Ca ratios from the same samples (*O. universa*) with linear regression y = 0.52x – 0.08 (R^2 = 0.34, p = 0.23). Error bars on barium isotope ratios are ± 2SE (standard error). Ba/Ca error bars are not shown because their internal precision was sufficiently small as to be negligible (Dr T. Horner, pers. com. 2015). S0157a is from size fraction 355 – 425 µm; all other samples are > 425 µm.

Table 5.4. D_{Ba} values (barium partition coefficients) for *Orbulina universa*.

This study				
Sediment sample	Ba/Ca (μmol/mol)	Nearest seawater site	Seawater [Ba] (nM)	D_{Ba}
S0059	0.77	CTD002	37.90	0.21
S0066	0.41	CTD002	37.90	0.11
S0131	0.46	CTD006	42.14	0.11
S0157a [a]	0.63	CTD006	42.14	0.15
S0157b	0.78	CTD006	42.14	0.19
S0177	0.53	CTD006	42.14	0.13
Previous studies				
Reference	Species	Method	D_{Ba}	
Lea & Boyle 1991	*Globoquadrina dutertrei, Globigerinoides sacculifer, Orbulina* spp., *Globigerinoides ruber, Globigerinoides conglobatus* (combined)	Core-top calibration	0.19 ± 0.05	
Lea & Spero 1992	*O. universa*	Laboratory culturing	0.15 ± 0.01 (not forced through zero); 0.16 ± 0.01 (forced through zero)	
Lea & Spero 1994	*O. universa*, also applicable to *Globigerinoides sacculifer*	Laboratory culturing	0.134 ± 0.008 (not forced through zero); 0.147 ± 0.004 (forced through zero)	
Hönisch et al. 2011	*O. universa*	Laboratory culturing	0.17 ± 0.02	
Hönisch et al. 2011 (also used data from Lea & Spero 1994)	Applicable to spinose planktic species and *Neogloboquadrina* (but not *Globorotalia*)	Laboratory culturing	0.149 ± 0.05	

a) S0157a is from size fraction 355 – 425 μm; all other samples (this study) are > 425 μm.

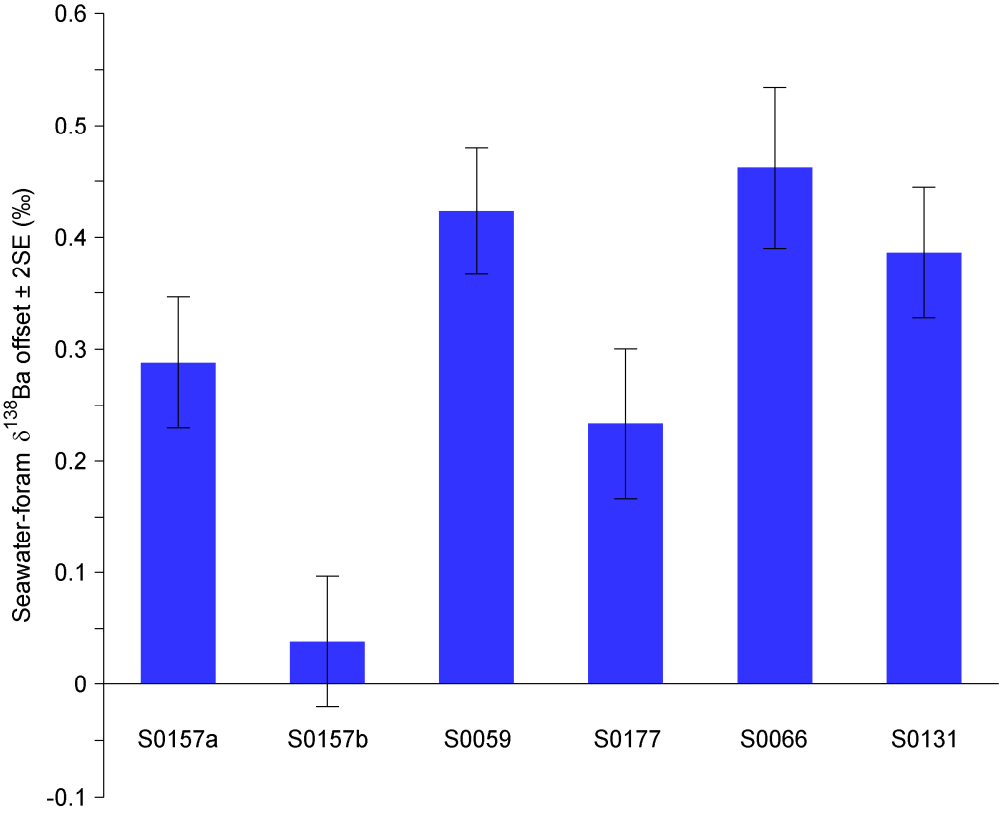

Figure 5.13. Seawater-foraminifer barium isotope ratio offsets. S0157a is from size fraction 355 – 425 µm; all other samples are > 425 µm. All samples are *Orbulina univers*a and each is a mixture of the two types: 'clear' and 'opaque'. Error bars are ± 2SE (standard error) propagated from the uncertainties of the seawater and foraminifera data (Table 5.5).

Table 5.5. Seawater-foraminifer barium isotope ratio offsets.

Sediment sample	Foraminiferal barium isotope ratio (‰)	Seawater barium isotope ratio (‰)	Seawater-foraminifer offset (‰)
S0157a	0.23 ± 0.05	0.52 ± 0.03	0.29 ± 0.06
S0157b	0.48 ± 0.05	0.52 ± 0.03	0.04 ± 0.06
S0059	0.14 ± 0.04	0.57 ± 0.04	0.42 ± 0.06
S0177	0.29 ± 0.06	0.52 ± 0.03	0.23 ± 0.07
S0066	0.10 ± 0.06	0.57 ± 0.04	0.46 ± 0.07
S0131	0.14 ± 0.05	0.52 ± 0.03	0.39 ± 0.06

The closest seawater profile to each sediment site is used (Table 5.4). S0157a is from size fraction 355 – 425 µm; all others are > 425 µm. All samples are mixed 'clear' and 'opaque' *Orbulina univers*a. Uncertainties are propagated using $\sqrt{\sum \sigma^2}$ where σ is 2SE.

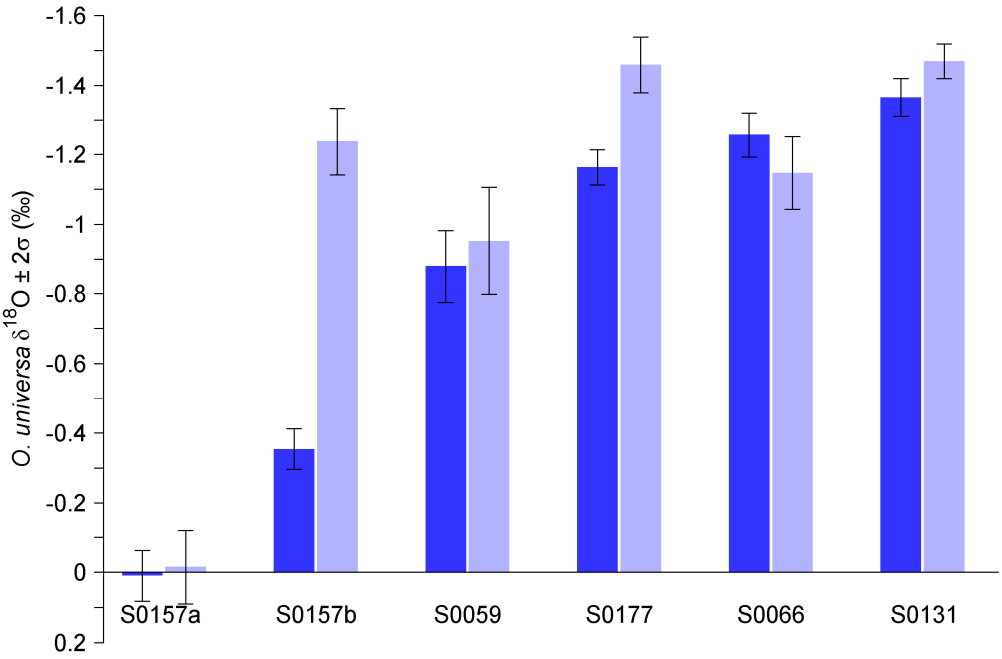

Figure 5.14. Foraminiferal oxygen isotope ratios. S0157a is from size fraction 355 – 425 µm; all other samples are > 425 µm. All samples are *Orbulina univers*a. Samples were separated into 'clear' (light blue) and 'opaque' (dark blue) specimen types. Error bars are ± 2SD (internal precision).

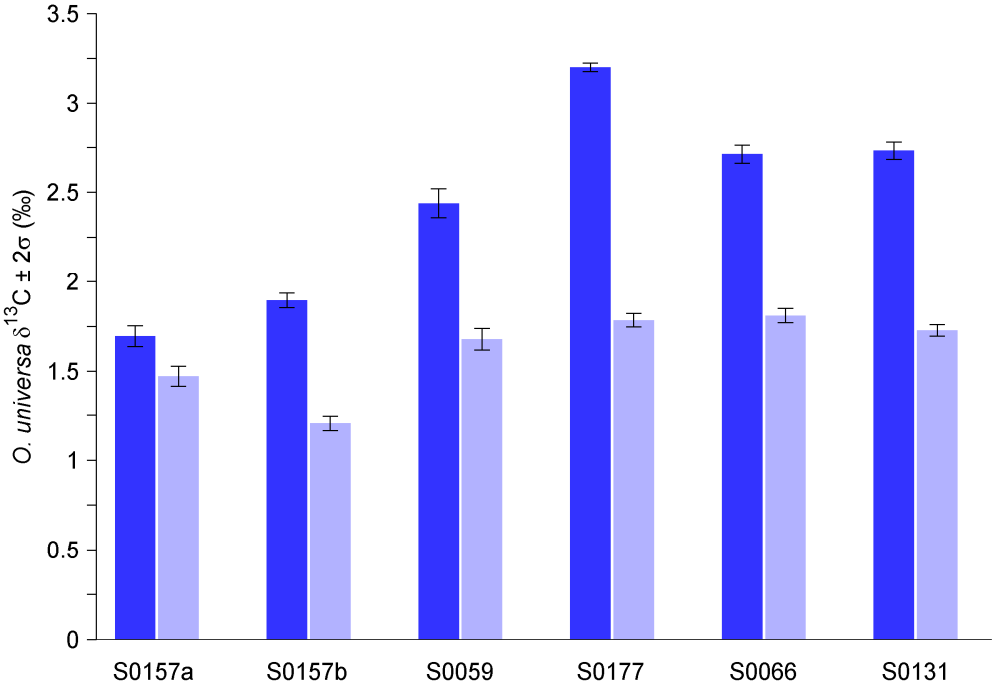

Figure 5.15. Foraminiferal carbon isotope ratios. S0157a is from size fraction 355 – 425 µm; all other samples are > 425 µm. All samples are *Orbulina univers*a. Samples were separated into 'clear' (light blue) and 'opaque' (dark blue) specimen types. Error bars are ± 2SD (internal precision).

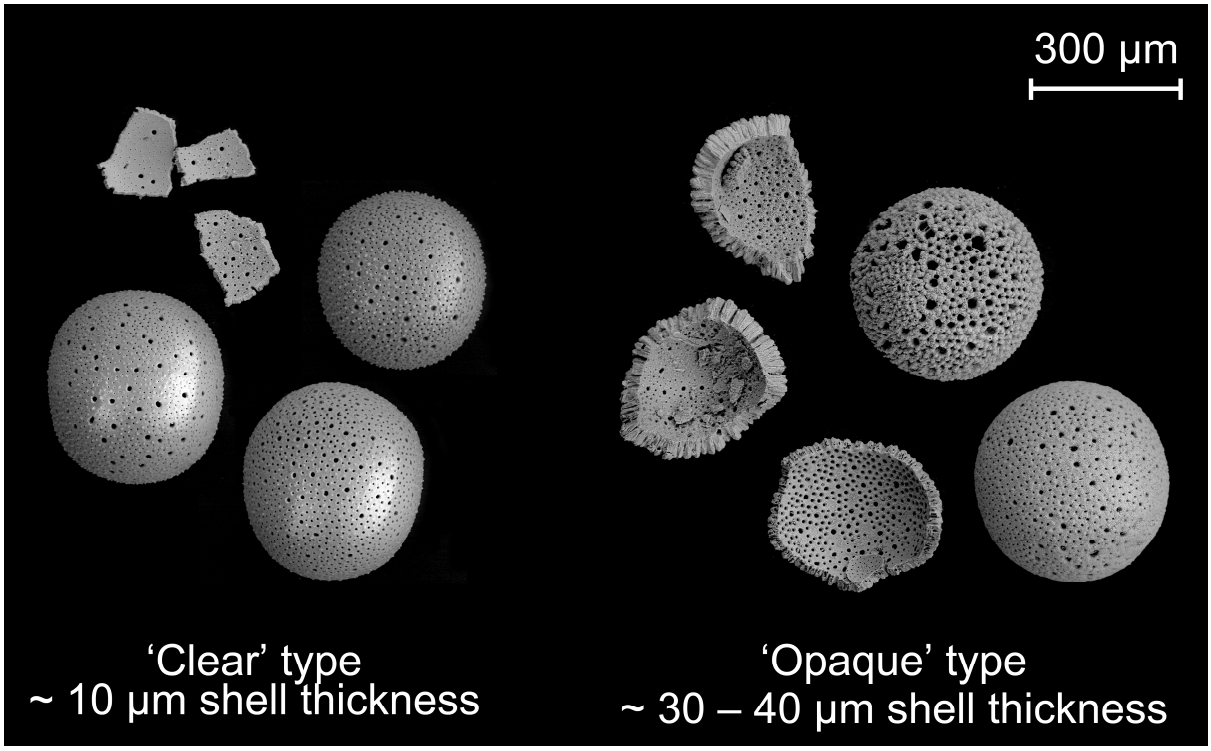

Figure 5.16. SEM micrographs of Orbulina universa (whole and fragmented) from sediment sample S0157. Samples were separated into 'clear' and 'opaque' specimen types. The 'clear' type has a thinner shell wall than the 'opaque' type.

5.5 Discussion

5.5.1 Seawater

Previous studies have shown that intermediate and deep Atlantic barium concentrations are controlled by conservative mixing and that non-conservative processes affect barium at depths nearer the surface (e.g. Chan et al. 1977; Jeandel et al. 1996; Horner et al. 2015; Cao et al. 2015). Because a different set of processes are present in each of these two zones, in Section 5.5.1.1 only the barium data from depths > 500 m are discussed and the data from 0 – 500 m are discussed separately in Section 5.5.1.2 'Near-surface processes (0 – 500 m)'. In addition, a discussion of the deepest samples in the profiles, which may be affected by their proximity to the seafloor, is provided in Section 5.5.1.3 'Seafloor-derived fluxes'.

5.5.1.1 Broad-scale circulation (> 500 m)

In the Atlantic, the following water masses are present at these approximate depths: at 500 – 1000 m, Antarctic Intermediate Water (AAIW) which forms from Antarctic Surface Water sinking below Subantarctic Surface Water at the Antarctic Polar Frontal Zone (approximately 60 ºS), flowing northwards into the Atlantic (Brown et al. 2004); at 1000 – 3000 m, North Atlantic Deep Water (NADW) which forms mainly in the Greenland Sea and Labrador Sea subpolar gyres and moves

southwards, with a higher flow rate in the western Atlantic than the east due to the Deep Western Boundary Current (DWBC) (Brown et al. 2004); and at depths > 3000 m, Antarctic Bottom Water (AABW) which forms on the Antarctic continental shelf and in the deep Antarctic Circumpolar Current and spreads northwards (Brown et al. 2004). Typical barium concentrations of AAIW, NADW and AABW are approximately 70 – 80, 50 – 60 and 90 – 110 nmol/kg, respectively (Figure 5.17). NADW has a lower barium concentration because of stronger biological utilisation of nutrients in its source regions, which removes barium from solution via uptake into organic matter and barite precipitation. Nutrients are relatively less utilised in the source regions of AAIW and AABW (High Nutrient Low Chlorophyll areas) causing them to have higher barium concentrations than NADW. In addition, AABW entrains additional barium from nutrient-rich deep waters resulting in higher barium concentrations than AAIW. Previous studies have shown that the dominant control of barium concentrations below the near-surface is ocean circulation (e.g. Chan et al. 1977) and the barium concentration profiles presented here are in full agreement with this hypothesis, showing the presence of each of these water masses. At 500 – 1000 m barium concentrations increase relative to shallower waters, indicating AAIW (Figure 5.6). This is followed by a slight decrease beneath 1000 m, which is attributable to NADW, then a gradual increase towards the seafloor due to AABW (Figure 5.6). Seawater barium concentrations are linearly correlated with silica concentration and total alkalinity (Figure 5.5; Figure 5.6; Figure 5.7), as observed by previous studies (e.g. Lea 1993; Chan et al. 1977), providing further evidence that barium concentrations are largely controlled by conservative mixing below ~500 m and that these data are in agreement with those of previous studies.

It has been hypothesised that seawater barium isotope ratios below ~500 m are also controlled by ocean circulation (Horner et al. 2015; Cao et al. 2016). Although there are some exceptions, where barium isotope ratios appear to be affected by non-conservative processes even at depths below ~500 m, the data presented here are in broad agreement with this hypothesis. The barium isotope ratios at depths > 500 m display a consistent overall trend of gradually decreasing with depth (Figure 5.6). One possible cause of this is the gradual remineralisation of sinking barite; another is that barium isotope ratios, like barium concentrations, are controlled by conservative mixing below 500 m and the gradual decrease with depth results from the characteristic barium isotope ratios of AAIW, NADW and AABW. To determine which of these processes is dominant, barium isotope ratios are plotted against the inverse of barium concentrations (Figure 5.8). Where the data fall in a straight line, this shows that they are following a mixing line whereby their properties are derived from different amounts of mixing between end-member water masses (the end-members are AAIW, NADW and AABW at their source regions). Where the data plot away from this straight line, they are influenced by non-conservative processes (such as barite dissolution and precipitation). It can be seen that the data below 500 m do indeed follow straight lines with R^2 values of 0.73 and 0.93 ($p < 0.05$) (Figure 5.8), indicating that barium isotope ratios and barium concentrations are both mainly controlled by conservative mixing.

The two regression lines have different gradients (Figure 5.8), which may be because barite dissolves at different rates in the two regions, indicating that in situ barite dissolution does affect barium isotope ratios below 500 m but that this is overprinted by the effect of conservative mixing. To investigate whether different rates of silica remineralisation also occur in the two regions, barium isotope ratios are plotted against silica divided by barium concentrations ([Si]/[Ba]; Figure 5.9). The data from the two regions still follow two different regression lines when plotted against [Si]/[Ba]. In isolation, this observation indicates that there are different extents of silica and/or barite remineralisation during lateral advection within the two regions. In combination with Figure 5.8, it shows that both silica and barite have geographically different regeneration rates. Alternatively it may be that two different gradients are seen because the true end-member water masses have not been sampled at these locations. This hypothesis could be tested by collecting data from sites nearer to the source regions of NADW (in the subpolar North Atlantic) and AAIW (in the Antarctic Polar Frontal Zone): if all of the data from these sites and the tropical North Atlantic and southeast Atlantic data were plotted on one mixing line plot, their combined effect should be to follow one line which represents the true mixing line for the entire Atlantic Ocean. In either case, below ~500 m barium isotope ratios largely follow straight lines when plotted against barium isotope ratios or [Si]/[Ba] and so appear to be dominantly controlled by conservative mixing between water masses.

Differences in silica and barite cycling between the two regions are also evidenced by their contrasting Ba* and Si* profiles (Figure 5.10). Si* is affected by the precipitation and dissolution of silica, whereas Ba* is controlled by silica and/or barite cycling (Equation 5.8; Equation 5.9; Figure 5.11). Therefore, the contrasting Ba* and Si* profiles of the tropical North Atlantic and southeast Atlantic together show that both silica and barite undergo differing amounts of precipitation and/or dissolution in the two regions. At depths ~0 – 1000 m, Ba* is greater in the southeast than in the tropical North Atlantic (Figure 5.10), indicating that there is a larger amount of dissolved barium which is not accounted for by the overall relationship between [Ba] and [Si] in the Atlantic (Equation 5.9). This indicates that more barite dissolution (or less barite precipitation) and/or less silica dissolution (or more silica precipitation) occurs in the southeast than in the tropical North Atlantic at these depths. At depths > ~1000 m the reverse occurs (Figure 5.10), signifying less barite dissolution (or more barite precipitation) and/or more silica dissolution (or less silica precipitation) in the southeast Atlantic. The Si* profiles also reveal differences in silica cycling between the two regions: the larger Si* values of the southeast Atlantic show that a greater amount of silica dissolution (or a lesser amount of silica precipitation) occurs here than in the tropical North Atlantic (Figure 5.10). Therefore together, the Ba* and Si* profiles show that: the differences in the Ba* profiles at depths ~0 – 1000 m are caused by greater barite dissolution (or less barite precipitation) in the southeast Atlantic than in the tropical North Atlantic; and at depths > ~1000 m the differences in the Ba* profiles of the two regions are caused by more silica dissolution (or less silica precipitation) in the southeast Atlantic, possibly accompanied by less barite dissolution (or more barite precipitation) in the southeast. Given that nutrients are less

completely utilised in the southeast Atlantic than in the tropical North Atlantic, it is reasonable for there to be less barite precipitation in the upper ~1000 m of the southeast Atlantic. Similarly, nutrients are more completely utilised in the source regions of tropical intermediate-depth waters than in those of the southeast, which would lead to a greater barite dissolution signal (via in situ barite dissolution during advection) in the tropics than in the southeast Atlantic at depths > ~1000 m. Additionally, at depths > ~1000 m a greater amount of silica dissolution in the southeast Atlantic is in agreement with the greater abundance of diatoms in this region. The importance of barite cycling in the tropical North Atlantic and the relative dominance of silica cycling in the southeast Atlantic can also be seen by plotting Ba* values against seawater barium isotope ratios (Figure 5.10). Given that barite dissolution causes Ba* to increase (Figure 5.11) and seawater barium isotope ratios to decrease, the presence of barite cycling will result in a negative slope on these plots, with greater Ba* at deeper depths. This is seen in the tropical North Atlantic data but not in the southeast Atlantic (Figure 5.10), indicating that in the tropical North Atlantic Ba* is mostly controlled by barite cycling, whereas in the southeast Atlantic silica cycling has a relatively large influence on Ba*, with [Si]-driven changes in Ba* causing a positive slope (increasing [Si] with depth causes Ba* to decrease; Equation 5.9). Collectively, this evidence for regional differences in barite and silica cycling suggests that the regional differences in gradients displayed in Figure 5.8 and Figure 5.9 are caused by differences in barite and silica cycling in the two regions, rather than a lack of end-member seawater samples.

Although barium isotope ratios are dominantly controlled by conservative mixing below 500 m, some exceptions can be seen where non-conservative processes appear to influence barium isotope ratios more heavily than usual. The first of these is that some of the deepest samples display sudden shifts to higher barium isotope ratios; this is discussed in Section 5.5.1.3 'Seafloor-derived fluxes'. The second is that at approximately 1200 – 2000 m in the western tropical North Atlantic profiles (CTD005 and CTD006) barium isotope ratios divert to heavier values before returning to agreement with the other profiles (Figure 5.6). This may be related to the Deep Western Boundary Current (DWBC), which carries NADW southwards along the western margin of the Atlantic (Brown et al. 2004) with the fastest flow centred around approximately 1400 – 1700 m (Molinari et al. 1992; McCartney 1993). The DWBC flows faster than the equivalent current on the eastern side of the Atlantic (e.g. Garzoli et al. 2015), meaning that western tropical North Atlantic waters have travelled more quickly from their source regions than those in the east. Consequently, western waters carry a stronger imprint from the upper 500 m because they have 'aged' less since sinking from shallow to intermediate depths. The location and relatively young 'age' of DWBC waters are clearly displayed by elevated CFC-11 concentrations compared to those at equivalent depths in the east (Figure 5.18). Because DWBC waters are 'younger', barite formed as a result of productivity near the surface has had less time to remineralise, so seawater barium isotope ratios remain high (similar to those just below 500 m) compared to waters at equivalent depths in the east, which have experienced more barite remineralisation during their slower flow, releasing light isotopes of barium back into the seawater. This effect can also be seen in nutrients: at

intermediate depths, phosphate and nitrate concentrations are lower in the west than in the east because they have had less time to replenish after depletion near the surface (Figure 5.19; Figure 5.20). This is supported by dissolved oxygen concentrations which are higher in the west than the east at the depth of the DWBC (Figure 5.21), indicating that less remineralisation of organic matter has occurred in the west. At the depth of the barium isotope anomaly (1200 – 2000 m), barium concentrations are lower in the tropical west than in the tropical east (Figure 5.6) which is in agreement with less barite remineralisation having occurred in the west. The effect of the DWBC can be seen on the mixing line plot (Figure 5.8). By grouping the data points according to water mass, it can be seen that the DWBC causes enhanced mixing between AAIW and NADW compared to in the southeast Atlantic. Some of these data points plot away from the regression line, indicating that non-conservative processes are present. In summary, this shows that the effect of the DWBC can be explained as a combination of enhanced mixing between AAIW and NADW and barite dissolution, resulting in the barium isotope anomaly at 1200 – 2000 m in the western tropical North Atlantic.

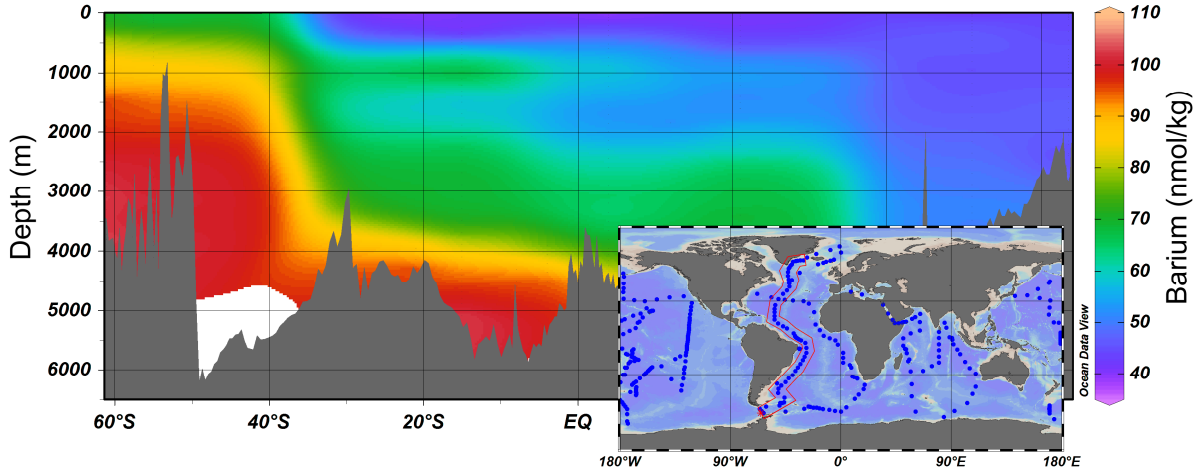

Figure 5.17. GEOSECS seawater barium concentrations in the western Atlantic Ocean.

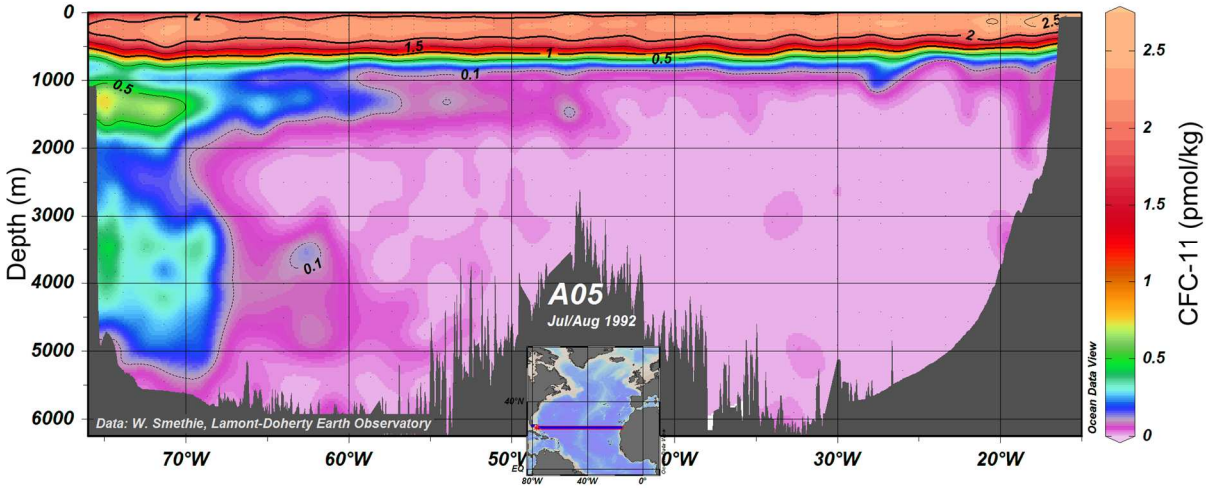

Figure 5.18. CFC-11 concentrations in the tropical Atlantic Ocean. Figure by eWOCE Gallery.

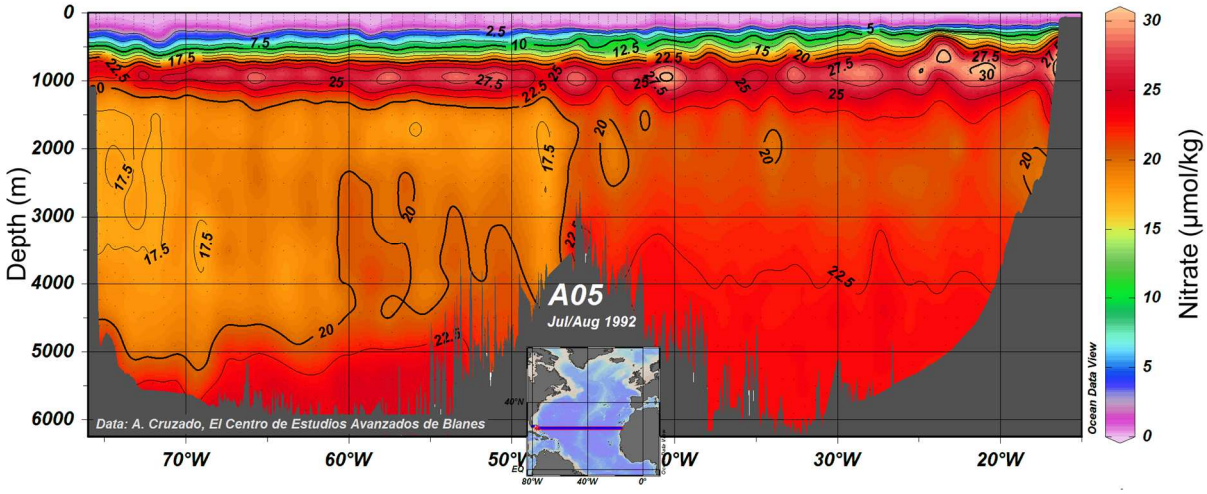

Figure 5.19. Nitrate concentrations in the tropical Atlantic Ocean. Figure by eWOCE Gallery.

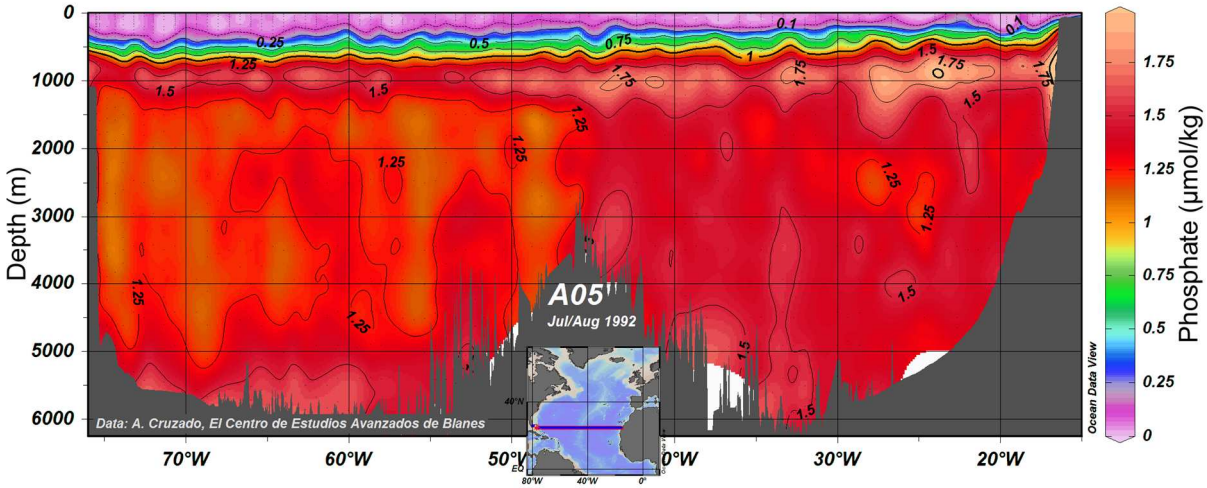

Figure 5.20. Phosphate concentrations in the tropical Atlantic Ocean. Figure by eWOCE Gallery.

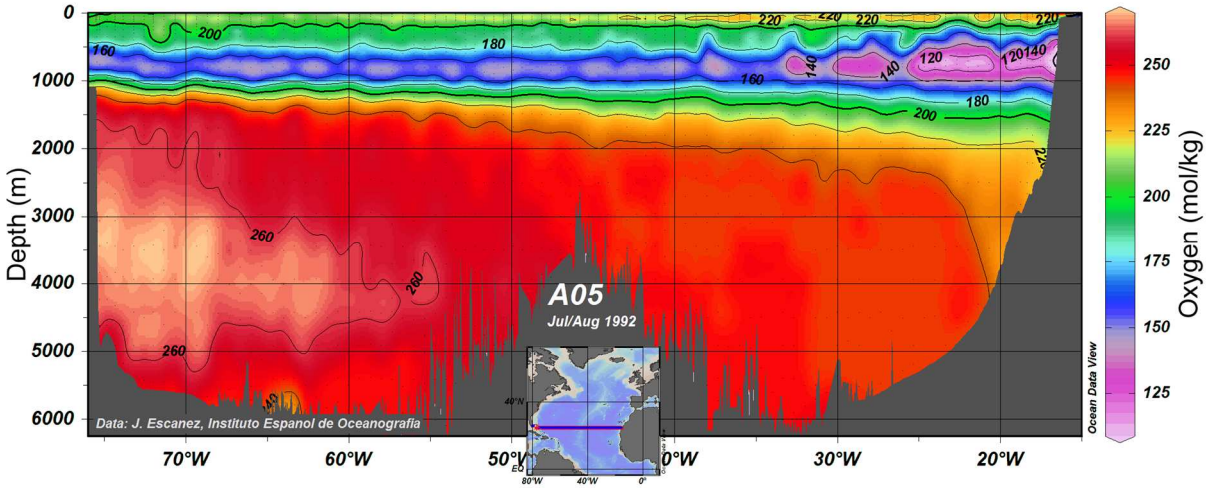

Figure 5.21. Oxygen concentrations in the tropical Atlantic Ocean. Figure by eWOCE Gallery.

5.5.1.2 Near-surface processes (0 – 500 m)

At 'near-surface' depths, defined here as 0 – 500 m, seawater barium isotope profiles in both the tropical North Atlantic and southeast Atlantic show an increase followed by a decrease with depth (Figure 5.6). This variability is likely linked to the formation and dissolution of abiotically-precipitated marine barite (Horner et al. 2015). Depths of maximum barium isotope ratios correspond to depths of maximum barite formation because barites preferentially incorporate lighter isotopes of Ba during precipitation (von Allmen et al. 2010; Hofmann et al. 2012; Böttcher et al. 2012b) causing seawater barium isotope ratios to increase (Horner et al. 2015). The subsequent remineralisation of this barite releases light isotopes of barium thus decreasing seawater barium isotope ratios (Horner et al. 2015). Although much of the oceans are undersaturated with respect to barite, including the Atlantic from 45 ºS to 60 ºN (Monnin et al. 1999), abiotic barite precipitation occurs within barite-oversaturated microenvironments in decaying organic matter (Goldberg & Arrhenius 1958; Bishop 1988; Bernstein et al. 1992; Bernstein et al. 1998; Ganeshram et al. 2003). Previous studies have observed particulate barite maxima at depths 100 – 600 m (Bishop 1988; Stroobants et al. 1991; Dehairs et al. 1991; van Beek et al. 2007). This is in good agreement with the depths of the barium isotope ratio maxima here, which occur at approximately 75 – 200 m. Furthermore, oxygen depletion, indicative of organic matter remineralisation and thus barite precipitation, is also observed at these depths (Figure 5.4), as are decreases in dissolved barium concentrations (Figure 5.6). Fluorescence peaks and nitrate depletions, indicative of productivity, occur at shallower depths than the increases in barium isotope ratios (Figure 5.4; Figure 5.6), which is also commensurate with the aforementioned hypothesis that the barium isotope maxima are due to barite production as a result of productivity higher in the water column. Although these features are present to some degree in all of the profiles, these observations are less defined in the southeast Atlantic profiles which tend to remain fairly constant over 0 – 200 m for reasons discussed below.

The tropical North Atlantic profiles are isotopically lighter at the surface than the southeast Atlantic profiles and show relatively large increases with depth, reaching subsurface maxima at approximately 75 and 200 m in CTD005 and CTD006 (Figure 5.6). The CTD002 profile does not show this pattern, however this may be due to its lower sampling resolution. In contrast to the tropical North Atlantic, the southeast Atlantic profiles have heavier values at the surface and show no such large increases with depth, instead oscillating around a relatively constant value within the top 200 m (Figure 5.6). They show subsurface maxima at approximately 100 and 200 m, but these are only marginally greater than the other isotope ratios within the top 200 m, in contrast to those of the CTD005 and CTD006 which are significantly greater at these depths than at the surface (Figure 5.6). A possible reason for these differences is revealed by comparing the depth of the mixed layer in the two regions. In the tropics, the mixed layer is relatively shallow (approximately 20 – 50 m; Figure 5.3) due to greater precipitation and higher temperatures, which cause the density structure of the upper water column to be stable. In contrast the mixed layer reaches much greater depths in the southeast Atlantic (> 100 m;

Figure 5.3) due to more vigorous vertical mixing (Kara et al. 2003). If the mixed layer depth is shallower than the depth of maximum barite formation, the highest barium isotope ratios are not encapsulated by the mixed layer and so the mixed layer is itself relatively isotopically light and underlain by water which is isotopically heavier. It may be that this is the case in the tropical North Atlantic profiles. In contrast the southeast Atlantic mixed layer depth is great enough to capture more of the seawater in which barite is forming, leading to higher isotope ratios overall and also more homogeneous isotope ratios over the top 200 m than in the tropics (Figure 5.6). This vertical mixing also explains why dissolved oxygen, nitrate and barium concentrations are relatively constant over the top 100 or 200 m in the southeast Atlantic profiles (Figure 5.4; Figure 5.6).

In conclusion, these results provide further evidence that seawater barium isotope ratios can be used to trace productivity through barite precipitation, as suggested by Horner et al. 2015, and that the extent of barium isotope enrichment in the near-surface depends not only on the magnitude of barite precipitation but also on the depth of the mixed layer.

5.5.1.3 Seafloor-derived fluxes

At the deepest sample in all of the seawater profiles except CTD013, increases in barium isotope ratios occur despite decreasing throughout the rest of the water column below 2000 m (Figure 5.6). Comparable features are not seen in other seawater properties (Figure 5.3; Figure 5.4) and AABW is already visible from > 3000 m (Figure 5.8), suggesting that these features are non-conservative rather than related to water mass properties and that they originate from the seafloor. A seafloor source for these features is supported by the distances between the deepest seawater samples and the underlying seafloor (Table 5.6): CTD002 shows this feature most prominently and is closest to the seafloor; whereas CTD005, CTD006 and CTD025 show features of smaller magnitude and are further away from the seafloor. The feature is absent from the CTD013 profile despite it being closer to the seafloor than CTD025 (Figure 5.6; Table 5.6), indicating either that the seafloor source is not ubiquitous throughout the ocean or that its magnitude is variable. As well as having the strongest increase in the barium isotope ratio, CTD002 also displays a prominent increase in barium concentration in its deepest sample (Figure 5.6), supporting the hypothesis that a source of barium from the seafloor is responsible for these features. Two possible sources of this seafloor-derived barium are sedimentary fluxes originating from sediment porewaters and hydrothermal vents; each of these possibilities are discussed below.

Hydrothermal vents provide $2.4 \times 10^8 – 13 \times 10^8$ mol of dissolved barium to the oceans per year (Elderfield & Schultz 1996) which is not insignificant given that the greatest source of barium to the oceans, the riverine flux, is only two orders of magnitude greater at 10^{10} mol/year (Elderfield & Schultz 1996). Vent plumes, containing dissolved trace metals and particulate matter, have been detected at heights of up to 220 – 500 m above the seafloor near the Mid-Atlantic Ridge at similar latitudes to the tropical North Atlantic profiles of this study (Klinkhammer et al. 1985; Klinkhammer et al. 1986; Rona

et al. 1986). Modelling studies agree well with these measured values (e.g. Speer & Rona 1989; Rudnicki & Elderfield 1992). Barium concentrations of 8 x 10^3 – 42.6 x 10^3 nmol/kg have been measured in hydrothermal plumes (Elderfield & Schultz 1996), which are tens to hundreds of times greater than seawater dissolved barium concentrations (Figure 5.17). There are currently no measurements of barium isotope ratios in hydrothermal vent fluids, however strontium isotope ratios are isotopically lighter in hydrothermal fluids than in seawater (Elderfield & Schultz 1996) so the same might be expected of barium isotope ratios. This is in disagreement with the observed features which are isotopically heavier than in overlying waters. Whilst it is possible that the above assumption is not true for barium, considering the behaviour of strontium isotopes, the lack of known hydrothermal vents in the southeast Atlantic (Martin et al. 2008) it seems more likely that the near-seafloor features seen in the seawater profiles are not caused by hydrothermal activity.

An alternative possibility is that the features described above are caused by sedimentary fluxes. In sediment porewaters, barium concentrations are higher than in overlying bottom waters (Figure 5.22; Paytan & Kastner 1996; McManus et al. 1998) resulting in benthic fluxes of dissolved barium from sediments (Paytan et al. 1996; McManus et al. 1999; McManus et al. 1994; Rubin et al. 2003; McManus et al. 1998). Sedimentary fluxes of dissolved barium have been measured in several locations comprising both open-ocean and continental margin settings at depths ranging from approximately 100 to 5000 m (Figure 5.23; Paytan et al. 1996; McManus et al. 1999; McManus et al. 1994; Rubin et al. 2003; McManus et al. 1998). These fluxes are remarkably similar in open-ocean settings versus continental margin settings (Figure 5.23), with the exception of two high values from one localised region on the Southern Californian Margin (McManus et al. 1999). It seems reasonable to conclude that sedimentary fluxes of dissolved barium may be present beneath the seawater profiles of this study, despite their being located in the open ocean. The second question is then whether it is reasonable for these fluxes to affect seawater barium concentrations several metres above the seafloor (Table 5.6). Singh et al. 2013 attribute similar features in their seawater profiles (elevated barium concentrations in bottom waters) to sedimentary fluxes, in samples which are 80 – 330 m away from the seafloor. This suggests that the bottom water samples of the tropical North Atlantic profiles, which are 12 – 18 m away from the seafloor, could be affected by sedimentary fluxes.

In addition to increased barium concentrations, these bottom water samples also have elevated barium isotope ratios (Figure 5.6). To consider the possible causes of these heavy isotope ratios, it is necessary to first determine the processes which cause barium concentrations to be elevated in sediment porewaters relative to overlying bottom waters. With increasing depth from the sediment-water interface, porewater barium concentrations first increase to a maximum concentration at approximately 5 cm (McManus et al. 1998; Figure 5.22) or 0 – 0.5 cm (Paytan et al. 1996) below the sediment-water interface, after which they remain approximately constant with depth (McManus et al. 1998; Paytan & Kastner 1996; Figure 5.22). There is some debate as to whether the sharp increases in barium concentration located immediately below the sediment-water interface, as opposed to those which

increase more gradually to ~5 cm, are in fact artefacts. Paytan & Kastner 1996 suggest that these are real features, because they are observed repeatedly in samples from different locations. Conversely, McManus et al. 1998 propose that these spikes in barium concentration are artefacts because fluxes calculated from those profiles disagree with fluxes measured via benthic landers, whereas profiles showing a more gradual increase to ~5 cm agree well with measured fluxes. If they are artefacts their cause is not known (McManus et al. 1998), although McManus et al. 1998 suggest that it may be related to the length of time between sample collection and measurement. Nevertheless, the high barium concentrations of porewaters compared to overlying bottom waters show that barium is produced in situ within sediments and that sediment porewaters are oversaturated with respect to barite (Paytan et al. 1996; McManus et al. 1998). Furthermore, the persistence of these features in porewater barium profiles shows that the rate of barium input to porewaters must exceed the rate of bioturbation (Paytan et al. 1996). The source of this barium must therefore be capable of releasing barium rapidly and is not the dissolution of pure barite (Paytan et al. 1996; McManus et al. 1998). Several possibilities exist: remineralisation of organic matter (Paytan et al. 1996; McManus et al. 1998); release of adsorbed barium (Paytan et al. 1996); and the dissolution of a different barium-containing mineral with greater solubility than pure barite, such as a celestite-barite solid solution (Paytan et al. 1996), impure barite containing Ca and K (Falkner et al. 1993), or an amorphous form of pure barite (McManus et al. 1998).

Given that extensive barite dissolution is unlikely to occur in sediments because barite oversaturation is consistently observed, it is plausible that a net increase in barite precipitation within sediments compared to in bottom waters could be the cause of the heavy barium isotope ratios in sedimentary fluxes. Two other barium-bearing minerals, witherite and the double carbonate $BaMn(CO_3)_2$, also preferentially incorporate light isotopes of barium (von Allmen et al. 2010; Böttcher et al. 2012a; Böttcher et al. 2012b; Pretet 2013; Table 5.1), so their precipitation could also contribute towards elevating porewater barium isotope ratios. In addition, laboratory experiments have shown that adsorption causes isotopic fractionation of barium (van Zuilen et al. 2016; Pretet et al. 2015), sometimes favouring adsorption of heavier barium isotopes (van Zuilen et al. 2016). The release of barium adsorbed in the water column could raise barium isotope ratios in porewaters. A further consideration is that diffusion through a porous medium has been shown to fractionate in favour of lighter isotopes of barium (van Zuilen et al. 2016). This could occur during the diffusion of sediment porewaters towards the sediment-water interface (van Zuilen et al. 2016). Because it fractionates in favour of lighter isotopes, this process alone could not explain heavy barium isotope ratios in sedimentary fluxes. Instead, it may mean that in situ barium isotope ratios within sediment porewaters are heavier than indicated by sedimentary fluxes. Given that there are a multitude of processes that may affect barium isotope ratios in different ways within sediment porewaters, measurements of barium isotope ratios within sediments would be highly beneficial, particularly of porewaters, organic material and various barium-bearing minerals.

In conclusion, a likely explanation for the elevated barium isotope ratios seen in the deepest seawater samples (with the exception of CTD013; Figure 5.6) is that sedimentary fluxes originating from sediment porewaters have relatively heavy barium isotope ratios compared to NADW and AABW, resulting in heavier barium isotope ratios nearer to the seafloor. Barium isotope ratio measurements of seawater samples collected directly from the sediment-water interface using benthic landers would be beneficial in confirming that this is the source of the elevated barium isotope ratios in the deepest seawater samples. The cause of elevated barium isotope ratios in sedimentary fluxes is not known, but could be investigated by measuring barium isotope ratios in multiple components of marine sediments, including porewaters, organic material and barium-bearing minerals.

Table 5.6. Distances between the deepest seawater samples and the underlying seafloor.

Site	Deepest sample depth (m)	Seafloor depth (m)	Difference (m)
CTD002	4512	4524	12
CTD005	5143	5161	18
CTD006	4168	4183	15
CTD013	4724	4894	170
CTD025	4501	4927	426

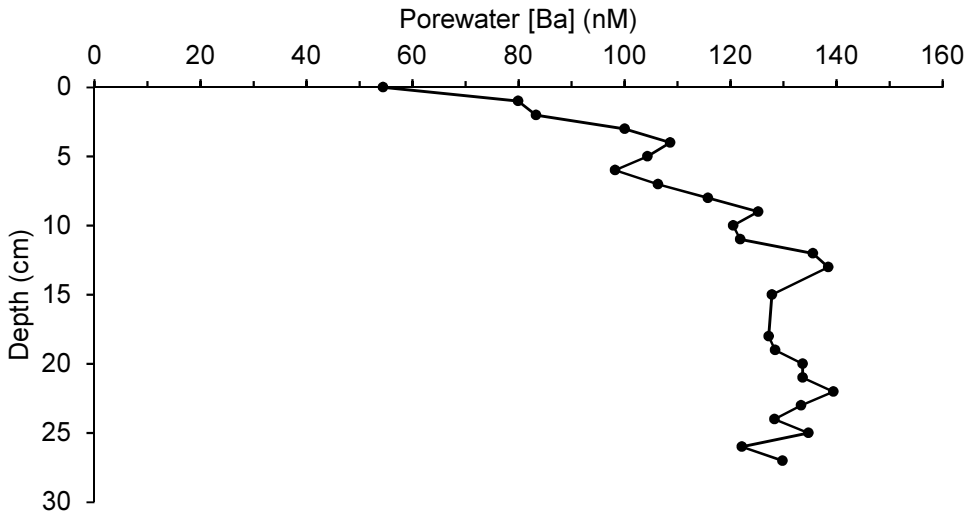

Figure 5.22. Porewater [Ba] in sediment core JC089-07-6M-F, normalised relative to 50 nM, an approximated bottom water [Ba] for its deep Atlantic location (Dr M. Greaves, pers. com. 2015). This approximation means that absolute values may not be accurate, but the relative change in porewater [Ba] down-core is conserved (Dr M. Greaves, pers. com. 2015).

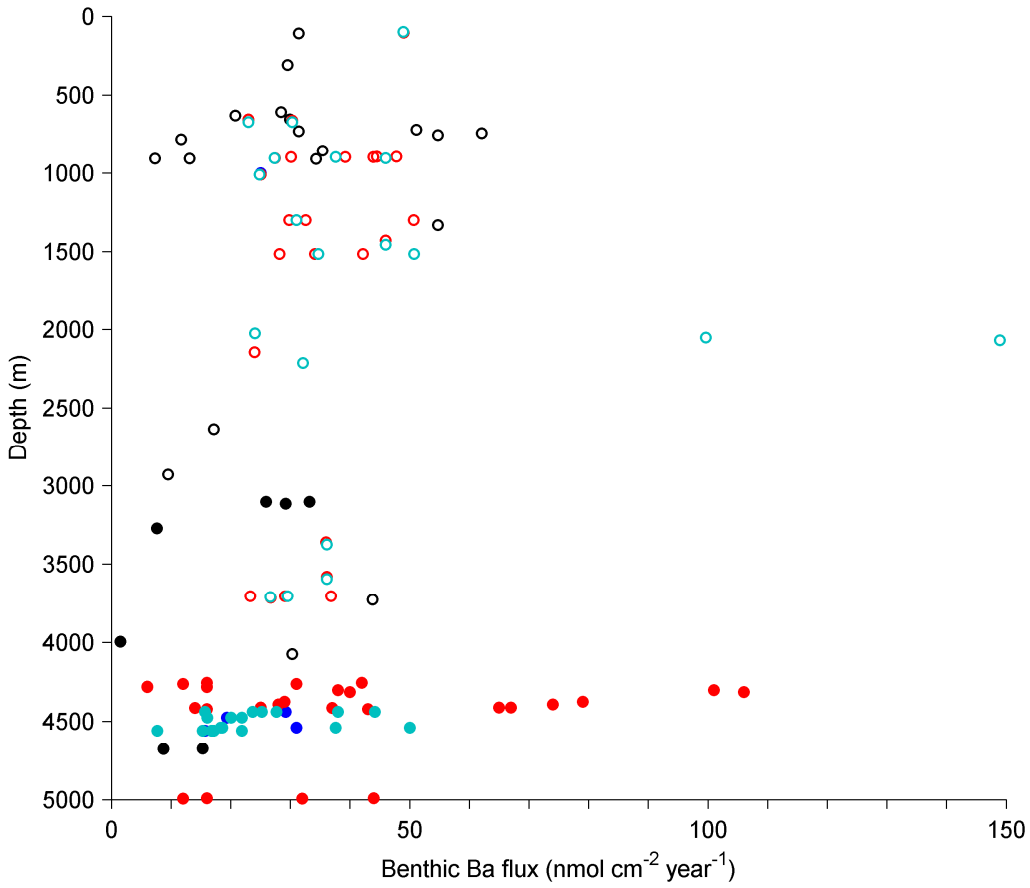

Figure 5.23. Benthic fluxes of dissolved barium from sediments in open-ocean (filled symbols) and margin (open symbols) environments plotted against the depth of the seafloor. Data are from Rubin et al. 2003 (black filled symbols and black open symbols), McManus et al. 1999 (dark blue filled symbols and light blue open symbols), Paytan & Kastner 1996 (red filled symbols), McManus et al. 1998 (light blue filled symbols and red open symbols) and McManus et al. 1994 (dark blue open symbols).

5.5.2 Foraminifera

At near-surface depths (~0 – 500 m), seawater barium isotope ratios are affected by productivity via barite-cycling (e.g. Jeandel et al. 1996; Horner et al. 2015; this study). If foraminifera were to record seawater barium isotope ratios, they could be used to study palaeoproductivity in the upper ~500 m. This would be beneficial for understanding the role of marine productivity in glacial-interglacial CO_2 changes, as well as predicting how phytoplankton communities might respond to future warming. To investigate this, barium isotope ratios were measured in the planktic foraminifer *Orbulina universa* and these measurements paired with seawater barium isotope ratios from nearby profiles. The nearest seawater profile to the site of sediment collection was used in each case (Table 5.4). *Orbulina universa* live in the mixed layer and upper thermocline (Farmer et al. 2007). Therefore, the shallowest sample from each seawater profile was used to estimate the barium isotope ratio of the ambient seawater.

In all cases, the foraminiferal barium isotope ratios are lighter than those of the ambient seawater (Table 5.5; Figure 5.13). Barium uptake into foraminiferal calcium carbonate is thought to

occur via a biologically-mediated process such as seawater vacuolisation (e.g. Erez 2003; Bentov & Erez 2006; Bentov et al. 2009) or trans-membrane transport (e.g. Nehrke et al. 2013). The isotopic fractionation between seawater and foraminifera may therefore be due to biomineralisation. It may also be temperature-dependent, as is the case for foraminiferal calcium isotope ratios (e.g. Griffith et al. 2008). The value of the seawater-foraminifer barium isotope ratio offset varies between samples, from approximately 0.04 to 0.46 ‰ (Table 5.5; Figure 5.13). Although these values are similar to the barium isotopic offsets between other carbonates and their ambient solutions (von Allmen et al. 2010; Böttcher et al. 2012a; Böttcher et al. 2012b; Pretet 2013; Pretet et al. 2015; Table 5.1), this is a large range compared to the variability of barium isotope ratios in seawater (Figure 5.6) and hence would introduce a large amount of uncertainty into seawater barium isotope ratio reconstructions. It is therefore important to determine the cause of this variability in foraminiferal barium isotope ratios. This in turn will aid in determining whether there are any factors which influence foraminiferal barium isotope ratios other than the barium isotope ratio of ambient seawater, such as vital effects and temperature-dependency.

The variability in the foraminiferal barium isotope ratios may be due to the presence of variable proportions of different foraminifer morphotypes in the samples. The foraminifer samples used to measure barium isotope ratios contained a mixture of two 'types' of foraminifer: one which appeared opaque when wetted and one which had a translucent or transparent appearance when wet (a 'clear' type). SEM imaging shows that the opaque and clear types have shell thicknesses of approximately 30 – 40 μm and 10 μm, respectively (Figure 5.16). These shell thicknesses and the appearance of the specimens suggest that they are two different morphotypes of *O. universa* (Marshall et al. 2015; Figure 5.16). If each morphotype records a different barium isotope ratio, which may be due to environmental differences in their habitats or vital effects, different mixtures of these two morphotypes would result in variable barium isotope ratios in samples.

Variability between morphotypes of *O. universa* has been observed in oxygen isotope ratios, suggesting that the same might be true of barium isotope ratios. Marshall et al. 2015 found that a thicker-walled *O. universa* morphotype had heavier oxygen isotope ratios than a thinner-walled *O. universa* morphotype, with an average offset of –0.34 ‰ between them (Marshall et al. 2015). This is attributed largely to temperature differences between the calcification depths of the two morphotypes (Marshall et al. 2015), an effect which is enhanced by greater near-surface stratification leading to larger contrasts in environmental conditions with depth (Marshall et al. 2015). Similar offsets are found by this study: with the exception of S0066, the thicker-walled 'opaque' samples have heavier oxygen isotope ratios than their thinner-walled 'clear' counterparts (Figure 5.14) and the offset between the two morphotypes is –0.21 ± 0.05 ‰ on average (Figure 5.14). Sample S0066 may also fit this pattern within ± 2σ error (Figure 5.14). These results suggest that the two morphotypes observed here also calcify at different depths and under different temperatures. Although sufficiently high-resolution seawater oxygen isotope data are unavailable for the accurate calculation of the calcification temperatures of the two

morphotypes, given a constant seawater oxygen isotope ratio these results indicate that the thicker-shelled 'opaque' morphotype calcifies at a lower temperature and hence greater depth than the 'clear' morphotype (Bemis et al. 1998). Ba/Ca ratios in *O. universa* are unaffected by ambient temperatures (Lea & Spero 1994; Hönisch et al. 2011), but the effect of temperature on barium isotope ratios in foraminifera is unknown. Seawater barium isotope ratio profiles from the tropical North Atlantic and southeast Atlantic suggest that enhanced vertical mixing in the southeast results in relatively constant seawater barium isotope ratios with depth, whereas in the tropical North Atlantic weaker vertical mixing results in shallower mixed layer depths (Kara et al. 2003; Figure 5.3; Figure 5.6). Enhanced stratification in regions such as the tropical North Atlantic may therefore cause greater offsets between the foraminiferal barium isotope ratios of different morphotypes, either by creating greater contrasts in temperature or in seawater barium isotope ratios. This stratification effect has been observed for oxygen isotope ratios in *O. universa* morphotypes (Marshall et al. 2015). Thus the importance of separating foraminifera by morphotype before measuring barium isotope ratios may vary regionally or seasonally depending on the strength of stratification.

Differences in carbon isotope ratios are also observed between *O. universa* morphotypes (Marshall et al. 2015; Figure 5.15). Carbon isotope ratios in thicker-shelled 'opaque' foraminifera are heavier than in the 'clear' morphotype, with an average offset of –0.83 ± 0.03 ‰ (Figure 5.15). This contrasts with the results of Marshall et al. 2015, who find that carbon isotope ratios are lighter in a thicker-shelled *O. universa* morphotype by 0.38 ‰ on average (Marshall et al. 2015). This is attributed to differing light intensities at the calcification depths of the two morphotypes (Marshall et al. 2015): the thicker-shelled morphotype calcifies at greater depths where irradiance is lower; here, the photosynthetic activity of the dinoflagellate symbionts of *O. universa* is weaker; this creates relatively ^{12}C-enriched microenvironments within which the foraminifera calcify, compared to at shallower depths; and this leads to lighter carbon isotope ratios in foraminiferal calcium carbonate (Spero & De Niro 1987). This mechanism cannot explain why heavier carbon isotope ratios are observed in the thicker-shelled, deeper-dwelling foraminifera of this study (Figure 5.15). Foraminiferal carbon isotope ratios are also affected by the carbon isotope ratio of dissolved inorganic carbon in seawater and seawater carbonate ion concentrations (e.g. Spero et al. 1997), however these influences are typically minor in comparison to the impact of symbiont photosynthetic activity and vital effects (e.g. Ravelo & Hillaire-Marcel 2007; Marshall et al. 2015). Although morphotype-specific vital effects have not been found to influence *O. universa* oxygen isotope ratios (Marshall et al. 2015), their influence on carbon isotope ratios has not yet been tested (Marshall et al. 2015). If the observed carbon isotope ratio offsets between morphotypes of *O. universa* (Figure 5.15) are partially due to vital effects, it may be that vital effects are also capable of influencing barium isotope ratios, although the mechanisms affecting carbon and barium are likely to be very different due to the lack of a known biological role for barium. However despite this lack of a known biological function for barium, $\delta^{138}Ba$ vital effects have been observed in corals (Pretet 2013; Pretet et al. 2015).

To investigate whether barium isotope ratios might be affected by temperature (the dominant control of oxygen isotope ratios) or irradiance, which is linked to symbiont photosynthetic activity, or vital effects (the dominant controls of carbon isotope ratios), barium isotope ratios are plotted against oxygen and carbon isotope ratios of foraminifera from the same sediment samples (Figure 5.24) and least-squares regression lines plotted (Figure 5.24; Table 5.7). Because sample S0157b may have an anomalously heavy barium isotope ratio which might create false correlations, regressions are additionally calculated excluding sample S0157b (Figure 5.24; Table 5.7). Only one significant correlation is found, between barium isotope ratios and carbon isotope ratios in the 'clear' morphotype. This relationship is only just significant at a 95 % confidence level ($p = 0.05$) and is no longer significant if sample S0157b is omitted. This weakness or absence of correlations may indicate that barium isotope ratios are not heavily influenced by temperature, irradiance or vital effects. In this case, the dominant control of foraminiferal barium isotope ratios may be the barium isotope ratio of ambient seawater. Differing seawater barium isotope ratios at the calcification depths of different morphotypes would then cause offsets in foraminiferal barium isotope ratios. Alternatively, it may be that the true relationships between oxygen, carbon and barium isotope ratios cannot be distinguished here because mixtures of more than one morphotype were used in the barium isotope ratio samples whereas carbon and oxygen data were measured in single-morphotype samples.

Conversely, Ba/Ca ratios suggest that inter-morphotype barium isotope ratio offsets are not dominantly controlled by seawater barium isotope ratios. In contrast to foraminiferal barium isotope ratios, Ba/Ca ratios do not appear to be significantly affected by the heterogeneous mixing of morphotypes among samples. This is because when combined with seawater barium concentration data, the Ba/Ca ratios provide barium partition coefficients which agree with those of previous studies (Table 5.4) despite geographical variations in morphotype abundances (Morard et al. 2009). Furthermore, during an interlaboratory comparison a foraminifer sample containing 800 individuals was measured at Woods Hole Oceanographic Institution whereas one containing 11 individuals was measured at the University of Bristol. Given their different sample sizes, it is unlikely that morphotypes were present in the same proportions in each of the two samples, yet their Ba/Ca ratios agree well with each other (see Section 2.4.6 'Interlaboratory comparison'). This suggests that differing mixtures of morphotypes among samples does not significantly affect Ba/Ca ratios. When Ba/Ca ratios are plotted against barium isotope ratios measured in the same samples, only a weak positive relationship is found ($R^2 = 0.34$, $p = 0.23$; Figure 5.12). This relationship is heavily dependent on one data point (S0157b), which when removed gives $R^2 = 0.04$ ($p = 0.74$). Additionally, Ba/Ca ratios (indicating a more plentiful supply of dissolved barium to the foraminifera) should have a negative correlation with the barium isotope ratios of the foraminifera (which appear to discriminate in favour of the lighter isotopes of barium, given that their isotope ratios are consistently lighter than those of seawater (Table 5.5)). This casts further doubt on the validity of the apparently positive correlation (Figure 5.12). Foraminiferal Ba/Ca ratios depend on the barium concentration of the ambient seawater (e.g. Lea & Boyle 1989; Lea & Spero 1992; Lea

& Spero 1994; Hönisch et al. 2011) and seawater barium concentrations and barium isotope ratios are highly correlated (e.g. Horner et al. 2015). This weak relationship between foraminiferal Ba/Ca and barium isotope ratios therefore suggests that foraminiferal barium isotope ratios are not controlled solely by the barium isotope ratio of the ambient seawater, because if this were the case foraminiferal barium isotope ratios should be highly correlated with foraminiferal Ba/Ca ratios.

In addition to morphotype effects, barium isotope ratios may also vary with foraminifer size. Oxygen and carbon isotope ratios vary with size due to changes in vital effects, photosynthetic activity and habitation depth during foraminifer growth (e.g. Ravelo & Hillaire-Marcel 2007). The oxygen isotope ratio data suggest that the effect of size fraction can be greater than that of morphotype (Figure 5.14). The barium isotope ratio of sample S0157b (> 425 μm) is 0.25 ± 0.07 ‰ greater than that of sample S0157a (355 – 425 μm) (Table 5.5). This may indicate that barium isotope ratios are heavily influenced by size fraction. However, it may be an artefact produced by the anomalously high barium isotope ratio of sample S0157b compared to the other samples (Figure 5.12; Table 5.5) or the presence of different proportions of morphotypes in these two samples. Sample S0131 (the closest sample site to S0157) only has a difference of 0.09 ± 0.07 ‰ from sample S0157a, suggesting that the effect of size fraction on barium isotope ratios may be minor. This could be investigated further by measuring additional samples of varying size fraction which are also separated by morphotype, in order to determine the separate impacts of foraminifer morphotype and size.

In summary, the variability of foraminiferal barium isotope ratios amongst samples of the same size fraction suggests that they may be morphotype-specific in *O. universa*, although the causes of this remain unclear. The presence of oxygen and carbon isotope ratio offsets between morphotypes suggests that they might also exist in barium isotope ratios. The observed variability of the seawater-foraminifer barium isotope ratio offsets would then arise from variable proportions of two different morphotypes being present within samples. However, barium isotope ratios correlate poorly with oxygen and carbon isotope ratios, suggesting that if inter-morphotype barium isotope ratio offsets exist, they are largely controlled by a different mechanism than oxygen or carbon isotope ratio offsets. A possible candidate for this control is the barium isotope ratio of ambient seawater. Different morphotypes calcifying at different depths may inhabit waters with differing barium isotope ratios, leading to differences in barium isotope ratios between morphotypes. This effect would be exacerbated in regions experiencing strong stratification in the near-surface. However, Ba/Ca ratios only display a weak relationship with barium isotope ratios measured in the same foraminifer samples. If foraminiferal barium isotope ratios were dominantly controlled by seawater barium isotope ratios, a strong correlation between foraminiferal Ba/Ca and barium isotope ratios would be expected. Before using foraminiferal barium isotope ratios as a proxy for seawater barium isotope ratios, barite cycling and productivity, the mechanisms affecting foraminiferal barium isotope ratios should be investigated further. To determine which processes dominantly affect foraminiferal barium isotope ratios, barium isotope ratios could be measured in single-morphotype foraminifer samples collected from sediment traps and these data paired

with seawater measurements taken at their calcification depths. Alternatively, laboratory culturing experiments could be used to test the impact of varying environmental conditions on foraminiferal barium isotope ratios. During these studies, care should be taken to constrain foraminifer samples to one morphotype only, so that morphotype-specific vital effects can also be investigated in addition to environmental controls. This could be achieved using the *O. universa* morphotype-identification method of Marshall et al. 2015 which is non-destructive to foraminiferal calcium carbonate. The influence of foraminifer size on barium isotope ratios should also be investigated further. Once the causes of variability in foraminiferal barium isotope ratios are determined, they could be used to accurately reconstruct the barium isotope ratios of ambient seawater and hence be used as a productivity proxy.

Table 5.7. Details of least-squares linear regressions plotted in Figure 5.24.

X axis	Data in regression	Equation	R^2	p
$\delta^{13}C$ ('opaque')	All	y = –0.10x + 0.48	0.16	0.44
	Excluding S0157b	y = 0.01x + 0.16	< 0.01	0.94
$\delta^{13}C$ ('clear')	All	y = –0.50x + 1.03	0.67	0.05
	Excluding S0157b	y = –0.17x + 0.46	0.08	0.64
$\delta^{18}O$ ('opaque')	All	y = 0.14x + 0.35	0.30	0.26
	Excluding S0157b	y = 0.05x + 0.23	0.16	0.51
$\delta^{18}O$ ('clear')	All	y = –0.02x + 0.21	< 0.01	0.91
	Excluding S0157b	y = 0.02x + 0.20	0.03	0.77

'Opaque' and 'clear' refer to foraminifer morphotype. All y axes are barium isotope ratios.

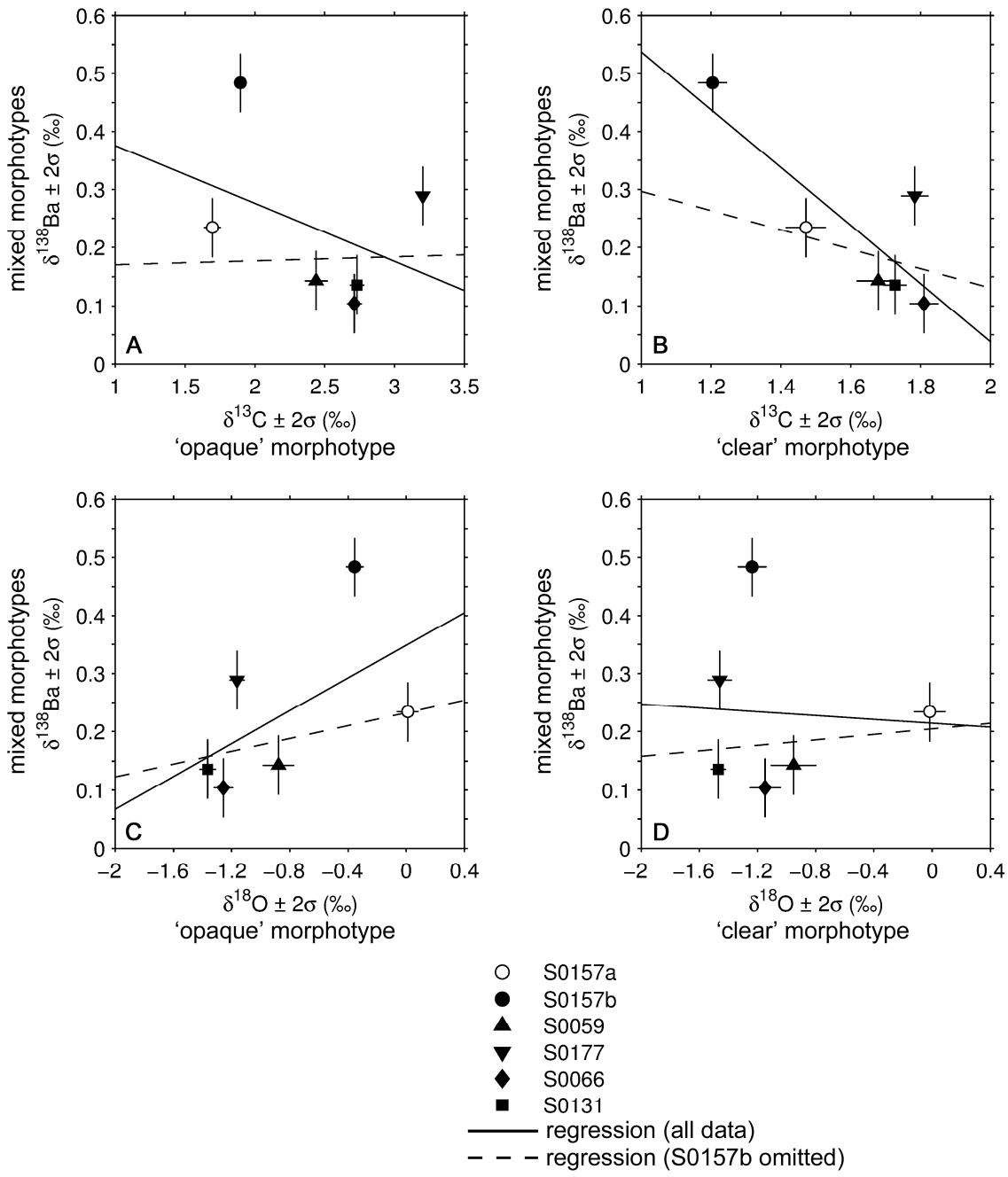

Figure 5.24. Foraminiferal barium isotope ratios (of mixed morphotype) plotted against carbon isotope ratios of 'opaque' morphotype (A), carbon isotope ratios of 'clear' morphotype (B), oxygen isotope ratios of 'opaque' morphotype (C) and oxygen isotope ratios of 'clear' morphotype (D). Least-squares linear regression lines are plotted using all data points (solid lines) and omitting sample S0157b (dashed lines). Details of linear regressions are provided in Table 5.7. Error bars are ± 2SE (standard error) for barium isotope ratios and ± 2SD (internal precision) for carbon and oxygen isotope ratios.

5.6 Conclusions

In conclusion, seawater barium concentrations and seawater barium isotope ratios appear to be controlled by a combination of conservative processes (water mass mixing during ocean circulation) and non-conservative processes (such as barite precipitation and dissolution). In Figure 5.8, data from depths below 500 m fall along a straight line, grouped according to water mass (AAIW is 500 – 1000 m, NADW is 1000 – 3000 m and AABW is > 3000 m), indicating that at depths below 500 m, barium concentrations and barium isotope ratios are mostly controlled by conservative mixing (Figure 5.8). The data from the tropical North Atlantic and southeast Atlantic plot along two different gradients (Figure 5.8; Figure 5.9), which may indicate that different rates of in situ barite and silica dissolution during lateral advection also exert a control (although conservative mixing is dominant), or may be because the true end-member water masses have not been sampled. Ba* and Si* provide evidence for regional differences in barite and silica cycling, suggesting that the former option is likely true (Figure 5.10). In the tropical North Atlantic, the effect of the DWBC can be seen via enhanced mixing between AAIW and NADW data points and also the spread of western data points farther away from the straight line due to ongoing barite dissolution in DWBC-carried waters (Figure 5.8). Data from 0 – 500 m plot further to the side of this straight line in both the tropical North Atlantic and southeast Atlantic (Figure 5.8), indicating that at these depths non-conservative processes exert a stronger influence on barium concentrations and isotope ratios than in deeper waters, due to the link between productivity and barite cycling. Non-conservative processes (such as fluxes from sediment porewaters) might also influence waters near to the seafloor, as shown by the deepest sample of CTD002 plotting far away from the regression line (Figure 5.8). In conclusion, these findings suggest that below 500 m barium concentrations and isotope ratios are mainly controlled by conservative mixing, whereas above 500 m they are more strongly influenced by barite and/or silica cycling (associated with productivity) than at greater depths, in agreement with previous authors (e.g. Chan et al. 1977; Jeandel et al. 1996; Horner et al. 2015; Cao et al. 2015). In addition, sedimentary fluxes appear to influence barium concentrations and barium isotope ratios near to the seafloor (Figure 5.6; Figure 5.8). This has been suggested previously for barium concentrations (Singh et al. 2013) but is the first time that this has been observed in barium isotope ratios. The effect of the DWBC on barium concentrations and isotope ratios has also been shown for the first time (Figure 5.6; Figure 5.8). To build upon these results, further seawater profiles of barium concentrations and isotope ratios could be collected from closer to the source regions of AAIW and NADW, to create a whole-Atlantic view of barium isotope ratios and to further test the hypothesis that barium isotope ratios are largely controlled by conservative mixing at depths below 500 m. The effect of sedimentary fluxes on barium isotope ratios could be further investigated by using benthic landers to measure barium isotope ratio fluxes close to the sediment-water interface and by measuring the barium isotope ratio of the various barium-bearing phases present in ocean sediments, such as labile organic matter, barite and celestite.

There are also further questions to be answered regarding foraminiferal barium uptake. The barium partition coefficients (D_{Ba}) for the planktic foraminifer *Orbulina universa* found by this study are fairly consistent and agree well with those of previous studies (Figure 5.25). Similarly, the barium isotope ratios of *O. universa* are similar to those of other biologically-precipitated carbonates (Figure 5.26), which are isotopically heavier than abiotically-precipitated carbonate and sulphate minerals (Figure 5.26). Compared to the seawater in which it grew, *Orbulina universa* appears to preferentially incorporate light isotopes of barium, evidenced by the lighter barium isotope ratios of these foraminifera compared to those of the ambient seawater (Table 5.5; Figure 5.13). However, there is a large amount of variability observed in the magnitude of this fractionation (expressed as the offset between the seawater barium isotope ratio and the foraminiferal barium isotope ratio) amongst samples of equal size fraction. This could be attributed to heterogeneous mixtures of two different morphotypes of *O. universa*. Morphotype-specific vital effects or differences in ambient seawater barium isotope ratios at their calcification depths may cause variations in barium isotope ratios between morphotypes. If foraminiferal barium isotope ratios were dependent only on those of the ambient seawater, a strong correlation between foraminiferal Ba/Ca and barium isotope ratios would be expected. This has not been observed (Figure 5.12), suggesting that foraminiferal barium isotope ratios are influenced by one or more factors other than ambient seawater barium isotope ratios. Foraminifer size may also influence barium isotope ratios, as is the case for oxygen isotope ratios in *O. universa*. Further foraminiferal barium isotope measurements on different size fractions and morphotypes of *O. universa* and under varied environmental conditions could elucidate the factors which control foraminiferal barium isotope ratios in this species. This would contribute towards the development of foraminiferal barium isotope ratios as a new proxy for palaeoproductivity.

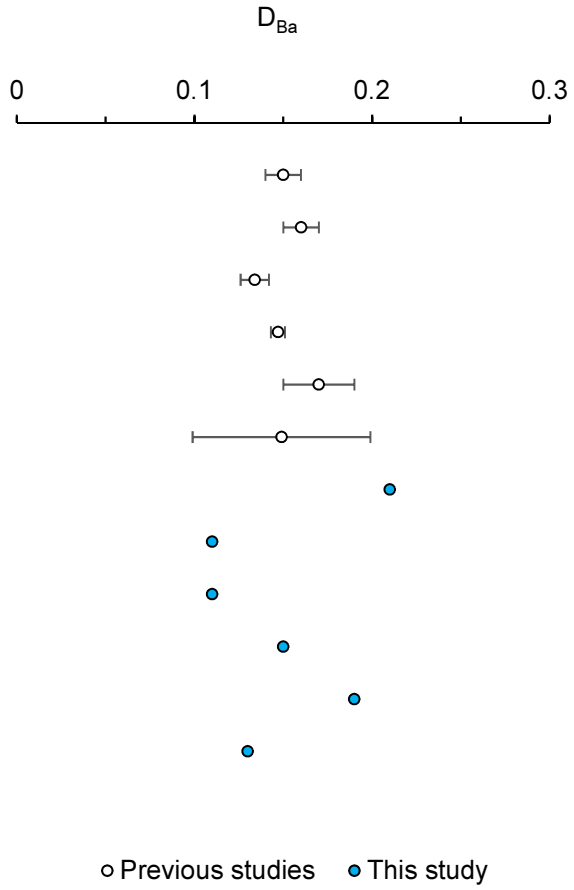

Figure 5.25. Barium partition coefficients (D_{Ba}) for the planktic foraminifer *Orbulina universa* measured by previous studies (as shown in Table 5.4, where references for these data are provided) and this study (also provided in Table 5.4).

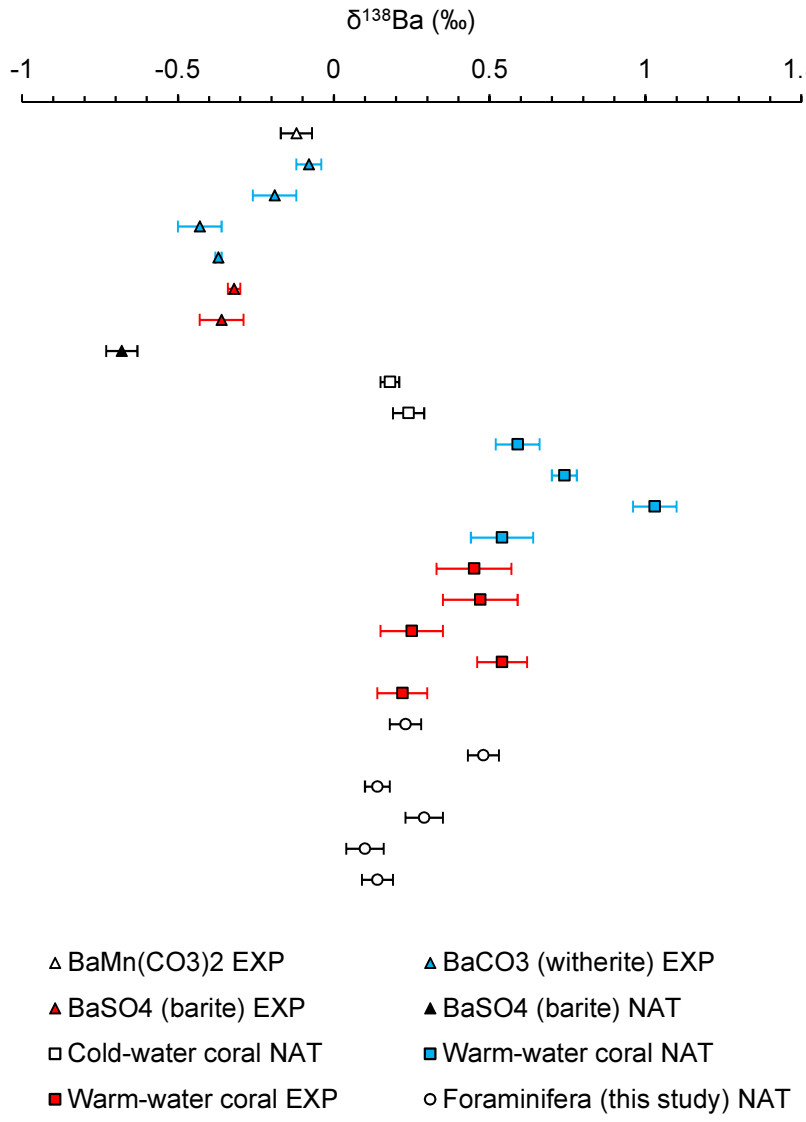

Figure 5.26. Barium isotope ratios ($\delta^{138}Ba$) of carbonates and sulphates measured by previous studies (including coral carbonates as well as abiotically-precipitated minerals, as shown in Table 5.1, where references for these data are provided) and by this study (the planktic foraminifer *Orbulina universa*, as shown in Table 5.5). All values have been converted into $\delta^{138/134}Ba$ notation as shown in Equation 5.1. The error bars on the previously-published data are shown as provided in those studies and the error bars on the data from this study are ± 2SE. EXP indicates that the mineral or coral was experimentally precipitated or cultured in the laboratory; NAT indicates that the samples were collected from the natural environment.

Chapter 6

Conclusions

6.1 Research context

The first steps towards developing foraminiferal Ba/Ca as an oceanographic proxy were made by Lea & Boyle 1989, who noted that Ba/Ca ratios in the benthic foraminifer species *C. wuellerstorfi*, *C. kullenbergi* and *Uvigerina* spp. were linearly related to the concentrations of dissolved barium in ambient seawater. Since then, additional benthic and planktic species have also been confirmed to record seawater [Ba] (Lea & Boyle 1991; Lea & Spero 1992; Lea & Spero 1994; Hall & Chan 2004a; Hönisch et al. 2011; Lea 1993; McCorkle et al. 1995; Havach et al. 2001) and several applications have been developed based upon these findings. The first use of Ba/Ca was to reconstruct the barium concentration of deep ocean water masses (Lea & Boyle 1989) and as a proxy for glacial-interglacial changes in ocean circulation and seawater alkalinity (Lea & Boyle 1990a; Lea & Boyle 1990b; Lea 1990). Planktic Ba/Ca was then deployed to study surface water barium concentrations (Lea & Boyle 1991), followed by further benthic studies (Lea 1993; Lea 1995). Although the use of Ba/Ca attracted a flurry of investigations in the late '80s and early '90s (Lea & Boyle 1989; Lea 1990; Lea & Boyle 1990a; Lea & Boyle 1990b; Lea & Boyle 1991; Lea & Spero 1992; Lea & Spero 1994; Lea 1993; Lea 1995; McCorkle et al. 1995) this field has been left relatively undeveloped in subsequent decades. Because they have been less-utilised relative to some of the more widely-used proxies, and because they have several potential palaeoceanographic uses, there is much scope for further developing Ba/Ca proxies and deploying them to study the oceans in new ways. A recent study has revived the benthic Ba/Ca proxy (Hall & Chan 2004a), others have developed new applications for Ba/Ca (e.g. Hall & Chan 2004b; Weldeab et al. 2007a; Weldeab et al. 2007b; Sprovieri et al. 2008) and more recently barium isotope ratio measurements have opened up new avenues into studying oceanic barium (e.g. Horner et al. 2015), but there are still many questions to be answered in relation to barium-based oceanographic proxies.

Prior to measuring Ba/Ca or δ^{138}Ba in foraminifera, it is necessary to remove barite ($BaSO_4$) from samples. The presence of barite in a sample would elevate its Ba/Ca ratio such that it overestimated the ambient barium concentration in which the foraminifer grew. Furthermore, barite precipitates inorganically except for under rare circumstances (Bertram & Cowen 1997) so is unlikely to have an identical isotope signature to foraminiferal calcium carbonate, which precipitates via biomineralisation (e.g. Elderfield et al. 1996; Erez 2003; de Nooijer et al. 2009). The presence of barite contamination would therefore affect the measured δ^{138}Ba of a foraminifer sample, complicating its interpretation. A barite-removal step which uses DTPA has been incorporated into the foraminiferal cleaning procedure that is routinely used prior to the measurement of trace metal ratios (Lea & Boyle 1993). However, the effect of this cleaning step on foraminifer shells is unclear because Ba/Ca ratios occasionally increase after DTPA is used (Lea & Boyle 1993; Martin & Lea 2002), which cannot be attributed to barite removal. It has been hypothesised that this effect is caused by the preferential dissolution of low-barium regions of the shell (Lea & Boyle 1991; Lea & Boyle 1993), but sequential dissolution experiments have shown barium to be homogeneously-distributed throughout foraminiferal calcium carbonate (Lea

& Boyle 1991; Lea & Boyle 1993). If the effects of the cleaning procedure on foraminifera can be determined with greater certainty, this would help to ensure that Ba/Ca and δ^{138}Ba data are not compromised by either barite contamination or preferential dissolution.

The process by which dissolved, positively-charged ions in ambient water are incorporated into foraminiferal calcium carbonate has not yet been confirmed (e.g. Erez 2003). Foraminiferal barium partition coefficients differ from those of inorganically-precipitated calcium carbonate (Kitano et al. 1971), which suggests that the foraminiferal barium-uptake process occurs during biomineralisation (e.g. Lea 1990; Lea & Boyle 1991; Lea & Spero 1992). Foraminiferal barium isotope ratios might provide new insights into the mechanism by which barium is incorporated by foraminifera, because biologically-mediated processes often preferentially utilise lighter isotopes (e.g. Chang et al. 2004). The effect of temperature on barium uptake also merits further study. Thus far, previous authors have found Ba/Ca ratios to be independent of precipitation temperature (Lea & Spero 1994; Hönisch et al. 2011). This is in contrast to the strong temperature effect on other trace metal ratios such as Mg/Ca (e.g. Lear et al. 2002), so is perhaps unexpected. Further insights might be gained by extending the range of temperatures tested and by investigating the effect of temperature in additional species. Given that a full understanding of the biomineralisation process, including its effect on barium incorporation, is yet to be attained (e.g. Elderfield et al. 1996; Erez 2003; de Nooijer et al. 2009), a practical method for calculating foraminiferal barium uptake is to use a partition coefficient (D_{Ba}) (Boyle 1981). These have been measured in several planktic and benthic species (Lea & Boyle 1991; Lea & Spero 1992; Lea & Spero 1994; Hall & Chan 2004b; Hönisch et al. 2011; Lea & Boyle 1989; Lea 1993; McCorkle et al. 1995; Havach et al. 2001). The measurement of D_{Ba} values in additional species would be beneficial in increasing sample availability and might also provide new insights into how the barium-uptake process varies between species. In addition, a communal D_{Ba} value for certain benthic species could potentially be developed, as it has for planktic foraminifera (e.g. Hönisch et al. 2011).

In seawater, dissolved barium profiles display a minimum near to the surface. The uptake of barium at near-surface depths is primarily controlled by productivity-associated barite precipitation (e.g. Lea 1993; Horner et al. 2015). By comparison, uptake into calcium carbonate only sequesters a minor amount of barium (e.g. Lea 1993; Horner et al. 2015). The global average relationship between barium and alkalinity in seawater might therefore be inapplicable to non-pelagic settings, where productivity (and hence barite precipitation) is likely to surpass that of the open ocean (Rubin et al. 2003). Another environmental control which might perturb the Ba/Ca signal is post-depositional dissolution. Within sediments, foraminifera can experience repeated episodes of dissolution and re-crystallisation, due either to their depth in relation to the lysocline or to diagenetic processes which can alter porewater chemistry (e.g. McCorkle et al. 1995). McCorkle et al. 1995 find that foraminiferal Ba/Ca ratios decrease along a slope of increasing depth. They attribute this effect to the release of barium from calcium carbonate via post-depositional dissolution, caused by increasing exposure to the

lysocline (McCorkle et al. 1995). Such an effect could adversely affect the accuracy of Ba/Ca ratios and so its possible existence merits further investigation.

Although the broad distribution of barium concentrations in the oceans is well-mapped (e.g. Chan et al. 1977), further insights into the mechanisms controlling this distribution would nevertheless be beneficial for providing additional context to barium-based proxies. Seawater barium isotope ratios can be used to study these mechanisms because barite cycling leaves an isotopic signature in seawater (Horner et al. 2015; Cao et al. 2016). In combination with seawater [Ba] measurements, mixing line plots can be constructed to reveal the relative effects of conservative mixing and non-conservative processes (such as barite cycling) on oceanic barium distributions. Thus far, seawater δ^{138}Ba profiles in the southeast Atlantic Ocean and China Sea suggest that in the shallowest ~500 m barite cycling and conservative mixing both affect the distributions of [Ba] and δ^{138}Ba (Horner et al. 2015; Cao et al. 2016), whereas at greater depths these parameters are dominantly controlled by conservative mixing (Horner et al. 2015; Cao et al. 2016). The measurement of additional seawater δ^{138}Ba profiles could expand these findings to the whole Atlantic Ocean or could reveal important regional differences. An additional benefit of mapping the distribution of seawater δ^{138}Ba is that it might allow for a new palaeoceanographic proxy to be developed. If foraminiferal δ^{138}Ba can be used to reconstruct that of the water in which it grew, these measurements could be used to study changes in ocean circulation and near-surface barite cycling (which is related to primary productivity) in the past. Ocean circulation and productivity proxies are valuable tools for investigating past variations in oceanic carbon distributions, which are of great relevance to changes in atmospheric carbon dioxide concentrations.

As well as developing novel proxies in order to provide new insights into current questions, existing proxies can be applied in new ways. The benthic foraminiferal Ba/Ca proxy has previously been used to study glacial-interglacial differences in ocean circulation and alkalinity (Hall & Chan 2004b; Lea & Boyle 1990a; Lea & Boyle 1990b; Lea 1990; Lea 1993; Lea 1995). There is much scope for applying this proxy to other scenarios, for example by comparing interglacial periods, or by studying variability within interglacials. A full understanding of the mechanisms controlling climate variability within and between interglacials may be important for predicting future climate change. As anthropogenic emissions of greenhouse gases into the atmosphere continue, the circulation of the oceans and their associated capacity to store carbon may be important. The Ba/Ca proxy can provide new insights into these processes during interglacial periods, thereby contributing towards predictions of future climatic variability.

6.2 Proxy development

This thesis presents several findings which are of importance for oceanic barium-based palaeoceanographic proxies. As well as providing new insights into existing proxies, they highlight the potential for a new proxy to be developed. These findings are summarised below.

In this study, SEM micrographs taken before and after foraminifera were cleaned using a barite-removal step show that barite which is present prior to cleaning is absent afterward. This suggests that the barite-removal cleaning step is successful at removing barite, but it is not possible to prove that all barite has been removed. Visual inspection of SEM micrographs suggests that the addition of the DTPA step into the cleaning procedure does not result in significant sample degradation. This indicates that if there is preferential dissolution of low-barium regions of the shell, this would occur during the cleaning procedure regardless of whether a DTPA step was used. Foraminiferal trace metal ratios show a variable response to DTPA cleaning: Mg/Ca and Sr/Ca ratios are not affected by the addition of a barite-removal step into the cleaning procedure, whereas Ba/Ca ratios sometimes remain unchanged and other times increase when DTPA cleaning is used. These findings are in agreement with those of previous authors (Lea & Boyle 1993; Martin & Lea 2002). In addition, several possibilities are considered for the source of a relatively large and incongruous peak in Ba/Ca at ~2.3 ka. It is possible that this peak is due to barite contamination, which could have implications for the cleaning procedure.

This thesis also presents the first known foraminiferal $\delta^{138}Ba$ measurements, in the planktic foraminifer *O. universa*. Foraminiferal $\delta^{138}Ba$ ratios are found to be isotopically lighter than those of seawater, but the magnitude of this offset is variable. This variability may be due to vital effects on $\delta^{138}Ba$, leading to morphotype-specific barium isotope ratios. The hypothesis that foraminiferal barium uptake is a biologically-mediated process is supported by this finding. In agreement with previous studies (Lea & Spero 1994; Hönisch et al. 2011), no temperature effect on Ba/Ca ratios is observed. Whilst this is beneficial to the Ba/Ca proxy, this finding cannot reveal new insights into the previously-observed lack of a temperature effect in other species. In addition, new D_{Ba} values are presented for *M. barleeanus*, *O. umbonatus* and *U. peregrina*. The *U. peregrina* D_{Ba} value agrees well with those measured in previous studies (Lea & Boyle 1989; Lea 1993; Havach et al. 2001). There are no known previous measurements of *M. barleeanus* or *O. umbonatus* D_{Ba} values. The D_{Ba} values of the different species are offset from one another, demonstrating the importance of measuring a partition coefficient for each individual species before using it to reconstruct seawater barium concentrations. This suggests that unlike in planktic foraminifera, it may not be appropriate to apply a communal D_{Ba} value to multiple species of benthic foraminifera.

In sediment core BC387-2 from a continental margin site in the southwest Atlantic Ocean, apparent shifts in primary productivity, indicated by $\delta^{13}C$ variability, are unaccompanied by concomitant changes in Ba/Ca. This suggests that the Ba/Ca proxy for ocean circulation remains robust in relatively shallow and productive regions. Due to a lack of dissolution effects in this core, the impact of post-depositional dissolution on Ba/Ca ratios could not be studied.

In combination with data from the southeast Atlantic provided by other authors (Horner et al. 2015; H. Pryer & Dr T. Horner, pers. com. 2016), the tropical North Atlantic seawater δ^{138}Ba profiles presented in this study suggest that seawater δ^{138}Ba is controlled by a combination of conservative and non-conservative processes. At depths greater than ~500 m seawater δ^{138}Ba is dominantly controlled by conservative mixing between water masses. At shallower depths, non-conservative processes such as productivity-associated barite cycling play a more dominant role: barite precipitation sequesters the lighter isotopes of barium, leading to heavier barium isotope ratios in seawater, and the re-dissolution of this barite as it sinks through the water column decreases seawater δ^{138}Ba. These findings are in agreement with previous studies (Horner et al. 2015; Cao et al. 2016). The distribution of seawater δ^{138}Ba in the Atlantic and the mechanisms controlling this distribution are now relatively well understood, providing a backdrop for palaeoceanographic work. Furthermore, seafloor-derived benthic fluxes of dissolved barium which have been observed by previous studies (e.g. McManus et al. 1999; Paytan & Kastner 1996; McManus et al. 1998; McManus et al. 1994; Rubin et al. 2003) appear to have an isotopically heavy δ^{138}Ba signature. In addition to these seawater measurements, the first known foraminiferal δ^{138}Ba measurements are presented, in the planktic foraminifer *O. universa*. These are isotopically lighter than those of seawater, but the magnitude of this offset is variable. This variability may be due to vital effects on δ^{138}Ba which lead to morphotype-specific barium isotope ratios.

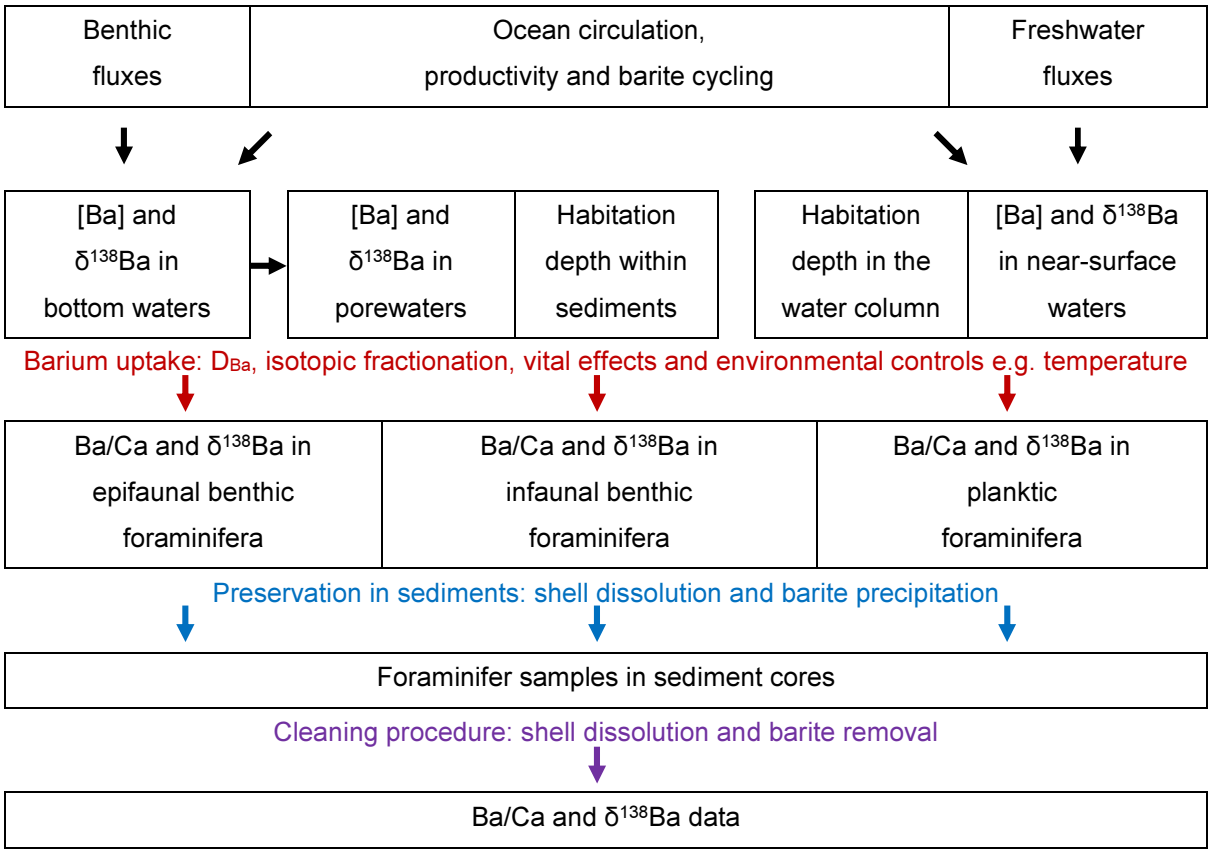

Figure 6.1. Summary of the main factors controlling foraminiferal Ba/Ca and δ^{138}Ba.

6.3 The climate system

As well as providing the aforementioned insights into how the benthic foraminiferal Ba/Ca proxy might be developed, this study makes use of this proxy to provide new information about the climate system. MIS 5e Ba/Ca ratios are on average significantly higher than those of the Holocene, possibly due to a 'stagnation event' in AABW formation during MIS 5e. Such an event may have caused a build-up of dissolved barium within AABW, leading to higher ambient barium concentrations and hence higher Ba/Ca ratios at the core site during this time. This would indicate that some of the mechanisms involved in climatic variability within the last interglacial were different to those of the Holocene thus far. These MIS 5e conditions might manifest from future warming if this triggers a similar stagnation event in the future. Results from sediment core BC387-2 provide further supporting evidence for these conclusions. The trace metal data in core GC528 agree well with those in BC387-2 (Figure 6.2) and the Ba/Ca, Mg/Ca and Mn/Ca offsets previously observed between the Holocene and MIS 5e are also visible when cores BC387-2 and GC642 are compared (Figure 6.2). This suggests that the Holocene-MIS 5e contrasts observed using cores GC528 and GC642 are reproducible in other sediment cores.

In addition, several possibilities are considered for the source of a relatively large peak in Ba/Ca at ~2.3 ka. The most likely explanations for this peak may be that a sedimentation event caused the habitation depth of infaunal foraminifera to temporarily increase to a depth where ambient porewater barium concentrations were significantly higher, or that a fluctuation in the strength of vertical mixing within the Malvinas Current temporarily entrained higher-barium waters onto the site. It is likely that neither of these scenarios would have far-reaching implications for the climate system as they both depend upon relatively localised processes. Nevertheless, if the occurrence of either of these events could be confirmed this would reveal additional information about palaeoceanographic variability during the Holocene and how such variability might impact the Ba/Ca proxy. Alternatively, the ~2.3 ka Ba/Ca peak may be an artefact caused by sample contamination. In the context of results from core BC387-2, this peak appears atypical (Figure 6.2) and thus potentially spurious. BC387-2 was collected from nearby to GC528 (Figure 3.1; Figure 4.2), yet in this core the Ba/Ca peak at ~2.3 ka is absent. This suggests that the ~2.3 ka peak in GC528 may be an artefact rather than an indicator of climatic variability. However, there is considerable uncertainty associated with the age model for BC387-2, with calculated sedimentation rates ranging from 0.01 to 0.21 cm/year (see Section 3.5.1 'BC387-2 age model'). Using an estimated sedimentation rate of 0.21 cm/year gives an age of approximately 120 years to sediments at the base of core BC387-2 (Figure 6.2). Therefore, strong conclusions cannot be drawn about the absence of the ~2.3 ka peak in core BC387-2 unless the ages of these sediments are determined with greater certainty.

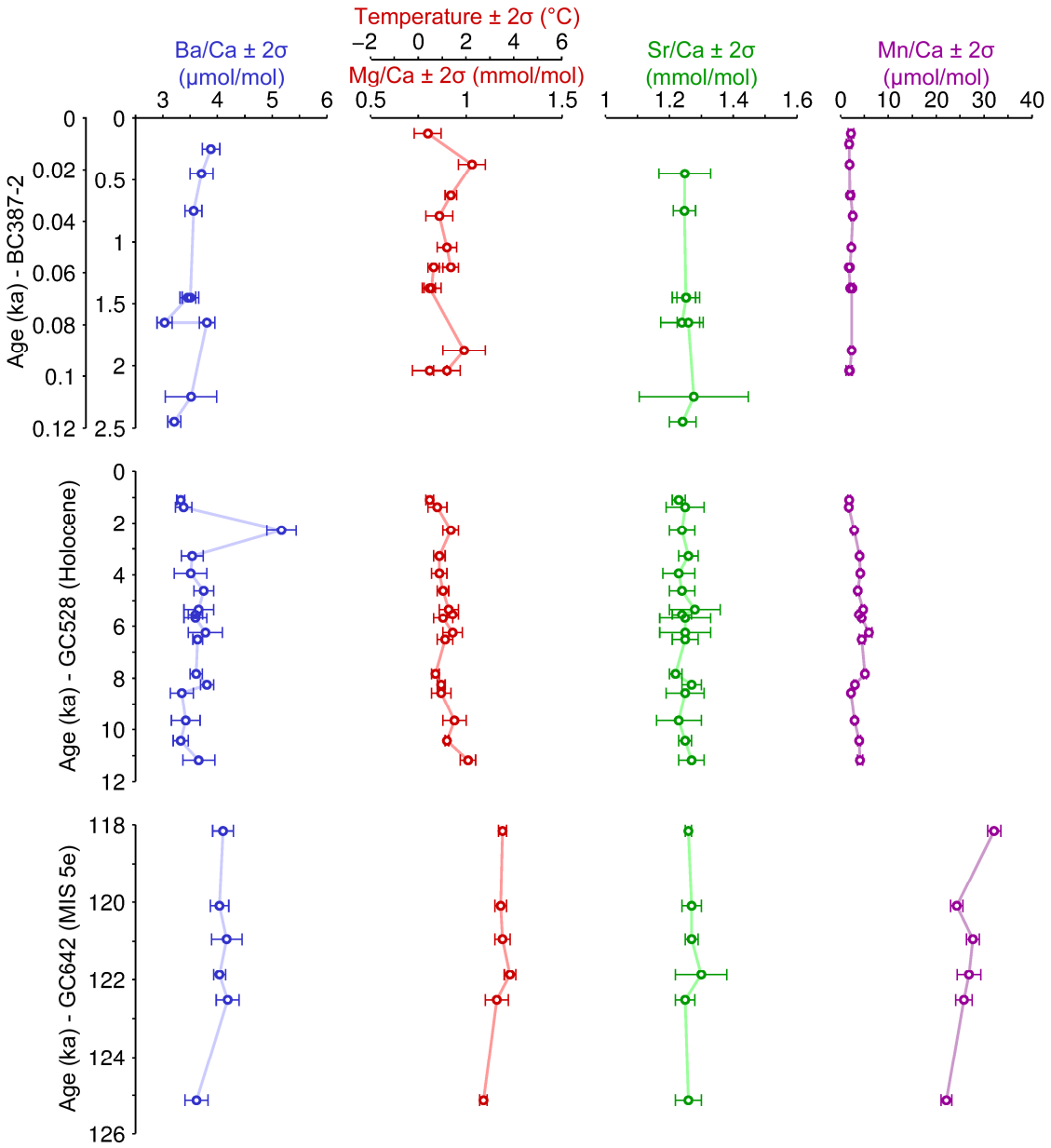

Figure 6.2. All trace metal data measured in *M. barleeanus*, from sediment cores BC387-2 (top), GC528 (middle) and GC642 (bottom): Ba/Ca; Mg/Ca, or Mg/Ca-derived temperature calculated from Mg/Ca using the equation of Kristjánsdóttir et al. 2007; Sr/Ca; and Mn/Ca. Two age axes are presented for sediment core BC387-2, constructed using the two extremes of sedimentation rate that were estimated for this core using ^{210}Pb-dating: 0.21 cm/year (left) and 0.01 cm/year (right). The GC528 and GC642 age models were constructed using radiocarbon dating of *Uvigerina bifurcata* (Roberts et al. 2016; Dr J. Roberts, pers. com. 2015). Error bars (2σ) are internal precision.

6.4 Future work

The findings presented in this thesis raise new questions which invite further study. Although the SEM results suggest that the barite-removal step is effective, the development of a technique for screening out all barite contamination prior to measurement would be ideal. It is difficult to envisage how this might be achieved in multi-specimen samples of dissolved foraminifera, but the use of laser ablation on single specimens (e.g. Hathorne et al. 2003) might preclude the need to remove all barite because barite particles could then be visually avoided. The variable response of foraminiferal Ba/Ca ratios to DTPA cleaning could be investigated further using sequential dissolution experiments or by targeting different regions of the shell using laser ablation (e.g. Hathorne et al. 2003). These experiments would reveal whether barium is heterogeneously spread through the shell. Combining this with visual inspection of partially-dissolved foraminifera would reveal whether low-barium regions of the shell are preferentially dissolved. In addition, the effect of the cleaning procedure on foraminiferal δ^{138}Ba should be investigated, in order to ensure that these results are not affected by the cleaning procedure. As an additional investigation into the cleaning procedure, the source of the Ba/Ca peak at ~2.3 ka should be confirmed, because if it was caused by contamination then the cleaning methods should potentially be adjusted. This could be facilitated by collecting additional sediment cores from nearby to the site of core GC528. If the ~2.3 ka peak is replicated in these cores, this would provide a strong indication that the peak was not caused by contamination. If the peak is not replicated, the possibility of contamination should be reconsidered.

The reason for the isotopically lighter δ^{138}Ba of foraminifera compared to seawater δ^{138}Ba might be determined amid ongoing investigations into the biomineralisation processes, which could reveal the mechanism by which foraminifera incorporate barium. Further insights could also be gained by determining the cause of the observed variability in seawater-foraminifer δ^{138}Ba offsets. To facilitate this, δ^{138}Ba ratios should be measured in single-morphotype samples of *O. universa*. The relationship between foraminifer size and δ^{138}Ba could also be investigated further, by measuring δ^{138}Ba in samples from restricted size fractions. These samples should also be restricted to a single morphotype, to distinguish the effects of size from those of morphotype. Whilst the lack of a temperature effect on Ba/Ca is useful in using Ba/Ca as a proxy for ocean circulation, it is also mysterious. Further studies into the process of biomineralisation, including using foraminiferal δ^{138}Ba, might aid in revealing the reason for the lack of a temperature effect on Ba/Ca. The continued measurement of D_{Ba} values in multiple species of benthic foraminifera will aid in defining the inter-species and intra-species variability in barium uptake, hence improving the accuracy of the Ba/Ca proxy. In addition, D_{Ba} values might be made more accurate by using more closely-paired Ba/Ca and ambient [Ba] measurements, for example by using laboratory culturing experiments, by pairing foraminifera sample collection with porewater measurements from the same sediment core, or in the case of epibenthic species by using benthic landers to measure seawater [Ba] directly above the sediment-water interface. The accuracy of the D_{Ba} values presented here might also be improved by measuring additional samples and then using

a linear regression forced through zero to calculate D_{Ba}, because in theory barium-free water should produce a foraminiferal Ba/Ca ratio of zero (Lea & Spero 1992; Lea & Spero 1994).

The results presented in this study which suggest that the Ba/Ca proxy is robust to changes in productivity may alleviate some of the concern related to using the Ba/Ca proxy in non-pelagic settings. However, further tests would nevertheless be useful for increasing confidence in this finding. The possibility of a dissolution effect on Ba/Ca ratios should also be investigated in future studies. It may be most appropriate to use sediment cores from the open ocean for this purpose, because there is a higher possibility of post-depositional dissolution here and because most palaeoceanographic data are provided from this type of setting. Determining the effects of productivity and post-depositional dissolution on foraminiferal $\delta^{138}Ba$ may also be an important task for future studies, as part of developing this into a new proxy.

The measurement of additional seawater $\delta^{138}Ba$ profiles in the source regions of Atlantic water masses (the subpolar and polar regions) would facilitate the construction of a mixing line for the whole Atlantic Ocean. This could confirm with greater certainty that seawater $\delta^{138}Ba$ (below ~500 m) is controlled by conservative mixing. The source of the observed isotopically-heavy benthic fluxes near to the seafloor could be investigated further by using benthic landers to take measurements from directly above the sediment-water interface. Measuring $\delta^{138}Ba$ ratios in the various barium-bearing phases that are present within seafloor sediments (such as barite, celestite and organic matter) would also be beneficial to this purpose. In addition to these seawater $\delta^{138}Ba$ studies, the determination of a known relationship between foraminiferal $\delta^{138}Ba$ and that of seawater could facilitate its use as a new palaeoceanographic proxy for ocean circulation and primary productivity. This could be achieved via further foraminiferal measurements which separate out the competing effects of species, morphotype and foraminifer size on $\delta^{138}Ba$. The reason for the isotopically lighter $\delta^{138}Ba$ of foraminifera compared to that of seawater might be determined amid ongoing investigations into the biomineralisation processes. This may also aid efforts to determine a reliable relationship between foraminifer and seawater $\delta^{138}Ba$.

In addition to contributing towards the ongoing development of palaeoceanographic proxies, future work could build upon the observations of past climate variability presented in this thesis. Further measurements of high-resolution sediment cores from the South Atlantic and Southern Ocean covering the Holocene and MIS 5e would aid in confirming or denying the existence of a 'stagnation event' during MIS 5e, as well as elucidating its timing. Furthermore, additional Ba/Ca measurements would be useful in confirming that such an event was associated with elevated barium concentrations within AABW. The possibility of a Southern Hemisphere forcing for this mechanism could be investigated by reconstructing past freshwater inputs in regions of AABW formation during MIS 5e and the Holocene using proxies such as planktic oxygen isotopes and by incorporating the stagnation event mechanism into climate models. If foraminiferal $\delta^{138}Ba$ is developed into an established proxy, this could be measured alongside Ba/Ca ratios to provide further insights into Holocene-MIS 5e variability, in

supplement to the results presented here. Within the Holocene, further studies of the Ba/Ca peak at ~2.3 ka could include measuring the barium content of local ice-rafted debris and its ability to release this barium to sediment porewaters. This might reveal whether or not it is feasible to attribute the ~2.3 ka peak to an iceberg rafting event. To investigate whether the Ba/Ca peak resulted from a fluctuation in the Malvinas Current, past variations in this current could be studied using a flow rate indicator such as sortable silt size. The feasibility of a sedimentation event causing infaunal foraminifera to temporarily inhabit greater depths could be investigated by studying such events in the modern day, including their impact on distributions of live foraminifera within sediments.

References

Adams, J.M., Faure, H., Faure-Denard, L., McGlade, J.M. & Woodward, F.I., 1990. Increases in terrestrial carbon storage from the Last Glacial Maximum to the present. *Nature*, 348, pp.711–714.

von Allmen, K., Böttcher, M.E., Samankassou, E. & Nägler, T.F., 2010. Barium isotope fractionation in the global barium cycle: First evidence from barium minerals and precipitation experiments. *Chemical Geology*, 277(1-2), pp.70–77.

Anagnostou, E., Sherrell, R.M., Gagnon, A., LaVigne, M., Field, M.P. & McDonough, W.F., 2011. Seawater nutrient and carbonate ion concentrations recorded as P/Ca, Ba/Ca, and U/Ca in the deep-sea coral Desmophyllum dianthus. *Geochimica et Cosmochimica Acta*, 75, pp.2529–2543.

Anand, P., Elderfield, H. & Conte, M.H., 2003. Calibration of Mg/Ca thermometry in planktonic foraminifera from a sediment trap time series. *Paleoceanography*, 18, p.1050.

Archer, D., 2010. *The Global Carbon Cycle*, Princeton, New Jersey: Princeton University Press.

Bahr, A., Schönfeld, J., Hoffmann, J., Voigt, S., Aurahs, R., Kucera, M., Flögel, S., Jentzen, A. & Gerdes, A., 2013. Comparison of Ba/Ca and $\delta^{18}O_{WATER}$ as freshwater proxies: A multi-species core-top study on planktonic foraminifera from the vicinity of the Orinoco River mouth. *Earth and Planetary Science Letters*, 383, pp.45–57.

Bains, S., Norris, R.D., Corfield, R.M. & Faul, K.L., 2000. Termination of global warmth at the Palaeocene/Eocene boundary through productivity feedback. *Nature*, 407(6801), pp.171–4.

Barker, S., Greaves, M. & Elderfield, H., 2003. A study of cleaning procedures used for foraminiferal Mg/Ca paleothermometry. *Geochemistry, Geophysics, Geosystems*, 4, p.8407.

Barnola, J.-M., Raynaud, D., Korotkevich, Y.S. & Lorius, C., 1987. Vostok ice core provides 160,000-year record of atmospheric CO_2. *Nature*, 329, pp.408–414.

Batenburg, S.J., Reichart, G.-J., Jilbert, T., Janse, M., Wesselingh, F.P. & Renema, W., 2011. Interannual climate variability in the Miocene: High resolution trace element and stable isotope ratios in giant clams. *Palaeogeography, Palaeoclimatology, Palaeoecology*, 306(1-2), pp.75–81.

van Beek, P., François, R., Conte, M., Reyss, J.-L., Souhaut, M. & Charette, M., 2007. $^{228}Ra/^{226}Ra$ and $^{226}Ra/Ba$ ratios to track barite formation and transport in the water column. *Geochimica et Cosmochimica Acta*, 71(1), pp.71–86.

Beerling, D.J., 1999. New estimates of carbon transfer to terrestrial ecosystems between the last glacial maximum and the Holocene. *Terra Nova*, 11, pp.162–167.

Bellemo, S., 1974. Ultrastructures in recent radial and granular foraminifera. *Bulletin of the Geological Institution of the University of Uppsala*, 4, pp.117–122.

Bemis, B.E., Spero, H.J., Bijma, J. & Lea, D.W., 1998. Reevaluation of the oxygen isotopic composition of planktonic foraminifera: Experimental results and revised paleotemperature equations.

Paleoceanography, 13(2), pp.150–160.

Bentov, S., 1997. *Biomineralization processes in the unicellular foraminifera*. The Hebrew University of Jerusalem.

Bentov, S. & Erez, J., 2001. New observations on the calcification mechanisms of foraminifera and implications for trace elements distribution on their shells. *7th International Conference on Paleoceanography*, p.82.

Bentov, S. & Erez, J., 2006. Impact of biomineralization processes on the Mg content of foraminiferal shells: A biological perspective. *Geochemistry, Geophysics, Geosystems*, 7(1).

Bentov, S., Erez, J. & Brownlee, C., 2001. Confocal microscope observations on the calcification processes of the foraminiferan Amphistegina lobifera. *11th International Congress of Protozoology*, p.40.

Bentov, S., Brownlee, C. & Erez, J., 2009. The role of seawater endocytosis in the biomineralization process in calcareous foraminifera. *Proceedings of the National Academy of Sciences of the United States of America*, 106(51), pp.21500–21504.

Berger, A. & Loutre, M.F., 1991. Insolation values for the climate of the last 10 million years. *Quaternary Science Reviews*, 10(1988), pp.297–317.

Bernstein, R.E., Byrne, R.H., Betzer, P.R. & Greco, A.M., 1992. Morphologies and transformations of celestite in seawater: The role of acantharians in strontium and barium geochemistry. *Geochimica et Cosmochimica Acta*, 56(8), pp.3273–3279.

Bernstein, R.E., Byrne, R.H. & Schijf, J., 1998. Acantharians: A missing link in the oceanic biogeochemistry of barium. *Deep-Sea Research Part I: Oceanographic Research Papers*, 45, pp.491–505.

Bertram, M.A. & Cowen, J.P., 1997. Morphological and compositional evidence for biotic precipitation of marine barite. *Journal of Marine Research*, 55, pp.577–593.

Bianchi, G.G. & Mccave, I.N., 1999. Holocene periodicity in North Atlantic climate and deep-ocean flow south of Iceland. *Nature*, 397(5), pp.515–517.

Bishop, J.K.B., 1988. The barite-opal-organic carbon association in oceanic particulate matter. *Nature*, 332, pp.341–343.

Bonn, W.J., Gingele, F.X., Grobe, H., Mackensen, A. & Fütterer, D.K., 1998. Palaeoproductivity at the Antarctic continental margin: Opal and barium records for the last 400 ka. *Palaeogeography, Palaeoclimatology, Palaeoecology*, 139, pp.195–211.

Böttcher, M.E., Geprägs, P., Neubert, N., von Allmen, K., Pretet, C., Samankassou, E. & Nägler, T.F., 2012a. Barium isotope fractionation during experimental formation of the double carbonate BaMn[CO3]2 at ambient temperature. *Isotopes in Environmental and Health Studies*, 48, pp.457–463.

Böttcher, M.E., von Allmen, K., Paytan, A., Neubert, N., Brumsack, H.-J., Samankassou, E. & Nägler, T.F., 2012b. A new look on the barium cycle: Stable barium isotope fractionation in ODP

sediments and calibration experiments. In *Goldschmidt 2012 Conference Abstracts*. p. 1495.

Boyle, E.A., 1981. Cadmium, zinc, copper, and barium in foraminifera tests. *Earth and Planetary Science Letters*, 53, pp.11–35.

Boyle, E.A., 1983. Manganese carbonate overgrowths on foraminifera tests. *Geochimica et Cosmochimica Acta*, 47, pp.1815–1819.

Boyle, E.A. & Keigwin, L.D., 1985. Comparison of Atlantic and Pacific paleochemical records for the last 215,000 years: changes in deep ocean circulation and chemical inventories. *Earth and Planetary Science Letters*, 76(1-2), pp.135–150.

Brandon, M., 2005. *JR112/113 Cruise Report*.

Broecker, W.S. & Peng, T.-H., 1982. *Tracers in the Sea*, Lamont-Doherty Geological Observatory, Columbia University.

Brown, E., Colling, A., Park, D., Phillips, J., Rothery, D., Wright, J., Brandon, M. & James, R., 2004. *Ocean Circulation*, Oxford: Butterworth-Heinemann.

Brown, S.J. & Elderfield, H., 1996. Variations in Mg/Ca and Sr/Ca ratios of planktonic foraminifera caused by postdepositional dissolution: Evidence of shallow Mg-dependent dissolution. *Paleoceanography*, 11, pp.543–551.

Bryan, S.P. & Marchitto, T.M., 2008. Mg/Ca-temperature proxy in benthic foraminifera: New calibrations from the Florida Straits and a hypothesis regarding Mg/Li. *Paleoceanography*, 23(2), pp.1–17.

Burke, A. & Robinson, L.F., 2012. The Southern Ocean's role in carbon exchange during the last deglaciation. *Science*, 335, pp.557–561.

Buzas, M.A., Culver, S.J. & Jorissen, F.J., 1993. A statistical evaluation of the microhabitats of living (stained) infaunal benthic foraminifera. *Marine Micropaleontology*, 20(3-4), pp.311–320.

van Campo, E., Guiot, J. & Peng, C., 1993. A data-based re-appraisal of the terrestrial carbon budget at the last glacial maximum. *Global and Planetary Change*, 8(4), pp.189–201.

Cao, Z., Siebert, C., Hathorne, E.C., Dai, M. & Frank, M., 2016. Constraining the oceanic barium cycle with stable barium isotopes. *Earth and Planetary Science Letters*, 434, pp.1–9.

Carroll, M.L., Johnson, B.J., Henkes, G.A., McMahon, K.W., Voronkov, A., Ambrose Jr., W.G. & Denisenko, S.G., 2009. Bivalves as indicators of environmental variation and potential anthropogenic impacts in the southern Barents Sea. *Marine Pollution Bulletin*, 59, pp.193–206.

Chan, L.H., Edmond, J.M., Stallard, R.F., Broecker, W.S., Chung, Y.C., Weiss, R.F. & Ku, T.L., 1976. Radium and barium at GEOSECS stations in the Atlantic and Pacific. *Earth and Planetary Science Letters*, 32, pp.258–267.

Chan, L.H., Drummond, D., Edmond, J.M. & Grant, B., 1977. On the barium data from the Atlantic GEOSECS expedition. *Deep-Sea Research*, 24, pp.613–649.

Chan, P., Halfar, J., Williams, B., Hetzinger, S., Steneck, R., Zack, T. & Jacob, D.E., 2011. Freshening of the Alaska Coastal Current recorded by coralline algal Ba/Ca ratios. *Journal of Geophysical*

Research: Biogeosciences, 116(1), pp.1–8.

Chang, V.T.-C., Williams, R.J.P., Makishima, A., Belshawl, N.S. & O'Nions, R.K., 2004. Mg and Ca isotope fractionation during $CaCO_3$ biomineralisation. *Biochemical and Biophysical Research Communications*, 323(1), pp.79–85.

Chen, T., Yu, K., Li, S., Chen, T. & Shi, Q., 2011. Anomalous Ba/Ca signals associated with low temperature stresses in Porites corals from Daya Bay, northern South China Sea. *Journal of Environmental Sciences*, 23(9), pp.1452–1459.

Chester, R. & Jickells, T., 2012. *Marine Geochemistry*, Chichester: Wiley-Blackwell.

Chow, T.J. & Goldberg, E.D., 1960. On the marine geochemistry of barium. *Geochimica et Cosmochimica Acta*, 20, pp.192–198.

Church, T.M., 1970. *Marine barite*. University of California.

Ciais, P., Tagliabue, A., Cuntz, M., Bopp, L., Scholze, M., Hoffmann, G., Lourantou, A., Harrison, S.P., Prentice, I.C., Kelley, D.I., Koven, C. & Piao, S.L., 2012. Large inert carbon pool in the terrestrial biosphere during the Last Glacial Maximum. *Nature Geoscience*, 5, pp.74–79.

Cléroux, C., Cortijo, E., Anand, P., Labeyrie, L., Bassinot, F., Caillon, N. & Duplessy, J.-C., 2008. Mg/Ca and Sr/Ca ratios in planktonic foraminifera: Proxies for upper water column temperature reconstruction. *Paleoceanography*, 23(3), pp.1–16.

Coggon, R.M., Teagle, D.A.H., Smith-Duque, C.E., Alt, J.C. & Cooper, M.J., 2010. Reconstructing past seawater Mg/Ca and Sr/Ca from Mid-OCean Ridge flank calcium carbonate veins. *Science*, 327, pp.1114–1117.

Corliss, B.H., 1985. Microhabitats of benthic foraminifera within deep-sea sediments. *Nature*, 314, pp.435–438.

Corliss, B.H., 1991. Morphology and microhabitat preferences of benthic foraminifera from the northwest Atlantic Ocean. *Marine Micropaleontology*, 17(3-4), pp.195–236.

Cortese, G., Abelmann, A. & Gersonde, R., 2007. The last five glacial-interglacial transitions: A high-resolution 450,000-year record from the subantarctic Atlantic. *Paleoceanography*, 22(4), pp.1–14.

Crichton, K., Chappellaz, J., Roche, D., Bopp, L. & Krinner, G., 2013. The effects of increased carbon storage in frozen soils on the carbon cycle in a coupled Earth-system model of intermediate complexity for the glacial and deglaciation timescales. In *Geophysical Research Abstracts*. p. 4398.

Croudace, I.W. & Rothwell, R.G., 2015. *Micro-XRF Studies of Sediment Cores*, Dordrecht: Springer.

Crowley, T.J., 1995. Ice age terrestrial carbon changes revisited. *Global Biogeochemical Cycles*, 9, pp.377–389.

Curry, J.A. & Webster, P.J., 1999. *Thermodynamics of Atmospheres and Oceans*, London: Academic Press.

Dean, W.E., Gardner, J. V. & Piper, D.Z., 1997. Inorganic geochemical indicators of glacial-interglacial

changes in productivity and anoxia on the California continental margin. *Geochimica et Cosmochimica Acta*, 61(21), pp.4507–4518.

Dehairs, F., Chesselet, R. & Jedwab, J., 1980. Discrete suspended particles of barite and the barium cycle in the open ocean. *Earth and Planetary Science Letters*, 49, pp.528–550.

Dehairs, F., Goeyens, L., Stroobants, N., Bernard, P., Goyet, C., Poisson, A. & Chesselet, R., 1990. On suspended barite and the oxygen minimum in the Southern Ocean. *Global Biogeochemical Cycles*, 4, pp.85–102.

Dehairs, F., Stroobants, N. & Goeyens, L., 1991. Suspended barite as a tracer of biological activity in the Southern Ocean. *Marine Chemistry*, 35, pp.399–410.

Dehairs, F., Baeyens, W. & Goeyens, L., 1992. Accumulation of suspended barite at mesopelagic depths and export production in the Southern Ocean. *Science*, 258, pp.1332–1335.

Dickson, J.A.D., 2002. Fossil echinoderms as monitor of the Mg/Ca ratio of Phanerozoic oceans. *Science*, 298, pp.1222–1224.

Dickson, A.G. & Goyet, C., 1994. *Handbook of Methods for the Analysis of Various Parameters of the Carbon Dioxide System in Sea Water*, Washington DC: US Department of Energy.

Dickson, A.G., Sabine, C.L. & Christian, J.R., 2007. Guide to best practices for ocean CO_2 measurements. *PICES Special Publication*, 3, pp.191–210.

Domack, E., Leventer, A., Dunbar, R., Taylor, F., Brachfeld, S. & Sjunneskog, C., 2001. Chronology of the Palmer Deep site, Antarctic Peninsula: A Holocene palaeoenvironmental reference for the circum-Antarctic. *The Holocene*, 11(1), pp.1–9.

Dymond, J., Suess, E. & Lyle, M., 1992. Barium in deep-sea sediment: A geochemical proxy for paleoproductivity. *Paleoceanography*, 7(2), pp.163–181.

Eagle, M., Paytan, A., Arrigo, K., van Dijken, G. & Murray, R.W., 2003. A comparison between excess barium and barite as indicators of carbon export. *Paleoceanography*, 18(1), p.1021.

Edgar, K.M., Pälike, H. & Wilson, P.A., 2013. Testing the impact of diagenesis on the $\delta^{18}O$ and $\delta^{13}C$ of benthic foraminiferal calcite from a sediment burial depth transect in the equatorial Pacific. *Paleoceanography*, 28(3), pp.468–480.

Elderfield, H. & Schultz, A., 1996. Mid-Ocean Ridge Hydrothermal Fluxes and the Chemical Composition of the Ocean. *Annual Review of Earth and Planetary Sciences*, 24(1), pp.191–224.

Elderfield, H., Bertram, C.J. & Erez, J., 1996. Biomineralization model for the incorporation of trace elements into foraminiferal calcium carbonate. *Earth and Planetary Science Letters*, 142(3-4), pp.409–423.

Elderfield, H., Yu, J., Anand, P., Kiefer, T. & Nyland, B., 2006. Calibrations for benthic foraminiferal Mg/Ca paleothermometry and the carbonate ion hypothesis. *Earth and Planetary Science Letters*, 250(3-4), pp.633–649.

Elderfield, H., Greaves, M., Barker, S., Hall, I.R., Tripati, A., Ferretti, P., Crowhurst, S., Booth, L. & Daunt, C., 2010. A record of bottom water temperature and seawater $\delta^{18}O$ for the Southern Ocean

over the past 440 kyr based on Mg/Ca of benthic foraminiferal Uvigerina spp. *Quaternary Science Reviews*, 29(1-2), pp.160–169.

Elliot, M. Welsh, K., Chilcott, C., McCulloch, M., Chappell, J. & Ayling, B., 2009. Profiles of trace elements and stable isotopes derived from giant long-lived Tridacna gigas bivalves: Potential applications in paleoclimate studies. *Palaeogeography, Palaeoclimatology, Palaeoecology*, 280(1-2), pp.132–142.

Ellison, C.R.W., Chapman, M.R. & Hall, I.R., 2006. Surface and deep ocean interactions during the cold climate event 8200 years ago. *Science*, 312(5782), pp.1929–1932.

Erez, J., 2003. The source of ions for biomineralization in foraminifera and their implications for paleoceanographic proxies. *Reviews in Mineralogy and Geochemistry*, 54(1), p.115.

Erez, J. & Bentov, S., 1998. The mechanism of calcification in perforate foraminifera. *International Symposium on Foraminifera*, p.34.

Erez, J. & Bentov, S., 2002. Calcification processes in foraminifera and their paleoceanographic implications. *International Symposium on Foraminifera*, pp.32–33.

Erez, J., Bentov, S., Tishler, C. & Szafranek, D., 1994. Intracellular calcium storage and the calcification mechanism of perforate foraminifera. *Paleobios*, 16(2), p.30.

Erez, J., Bentov, S. & Brownlee, C., 2001. A model for the calcification mechanisms in perforate foraminifera based on seawater vacuolisation. *11th International Congress of Protozoology*, p.40.

Erez, J., Bentov, S., Brownlee, C., Raz, M. & Rinkevich, B., 2002. Biomineralisation mechanisms in foraminifera and corals and their paleoceanographic implications. *Geochimica et Cosmochimica Acta*, 66, p.A216.

Falkner, K.K., Klinkhammer, G.P., Bowers, T.S., Todd, J.F., Lewis, B.L., Landing, W.M. & Edmond, J.M., 1993. The behavior of barium in anoxic marine waters. *Geochimica et Cosmochimica Acta*, 57(3), pp.537–554.

Fallon, S.J., McCulloch, M.T., van Woesik, R. & Sinclair, D.J., 1999. Corals at their latitudinal limits: Laser ablation trace element systematics in Porites from Shirigai Bay, Japan. *Earth and Planetary Science Letters*, 172(3-4), pp.221–238.

Farmer, E.C., Kaplan, A., de Menocal, P.B. & Lynch-Stieglitz, J., 2007. Corroborating ecological depth preferences of planktonic foraminifera in the tropical Atlantic with the stable oxygen isotope ratios of core top specimens. *Paleoceanography*, 22(3), pp.1–14.

Fontanier, C., Mackensen, A., Jorissen, F.J., Anschutz, P., Licari, L. & Griveaud, C., 2006. Stable oxygen and carbon isotopes of live benthic foraminifera from the Bay of Biscay: Microhabitat impact and seasonal variability. *Marine Micropaleontology*, 58(3), pp.159–183.

François, R., Honjo, S., Manganini, S.J. & Ravizza, G.E., 1995. Biogenic barium fluxes to the deep sea: implications for paleoproductivity reconstruction. *Global Biogeochemical Cycles*, 9(2), pp.289–303.

Ganeshram, R.S., François, R., Commeau, J. & Brown-Leger, S.L., 2003. An experimental

investigation of barite formation in seawater. *Geochimica et Cosmochimica Acta*, 67(14), pp.2599–2605.

Garzoli, S.L., Dong, S., Fine, R., Meinen, C.S., Perez, R.C., Schmid, C., van Sebille, E. & Yao, Q., 2015. The fate of the Deep Western Boundary Current in the South Atlantic. *Deep-Sea Research Part I: Oceanographic Research Papers*, 103, pp.125–136.

Gillikin, D.P., Dehairs, F., Lorrain, A., Steenmans, D., Baeyens, W. & André, L., 2006. Barium uptake into the shells of the common mussel (Mytilus edulis) and the potential for estuarine paleo-chemistry reconstruction. *Geochimica et Cosmochimica Acta*, 70(2), pp.395–407.

Gillikin, D.P., Lorrain, A., Paulet, Y.-M., André, L. & Dehairs, F., 2008. Synchronous barium peaks in high-resolution profiles of calcite and aragonite marine bivalve shells. *Geo-Marine Letters*, 28(5-6), pp.351–358.

Goldberg, E.D., 1963. Chemistry – the oceans as a chemical system. In M.N. Hill, eds. *Composition of seawater, comparative and descriptive oceanography*. New York: Interscience Publishers, pp. 3–25.

Goldberg, E.D. & Arrhenius, G.O.S., 1958. Chemistry of Pacific pelagic sediments. *Geochimica et Cosmochimica Acta*, 13(2-3), pp.153–212.

Griffith, E.M., Paytan, A., Kozdon, R., Eisenhauer, A. & Ravelo, A.C., 2008. Influences on the fractionation of calcium isotopes in planktonic foraminifera. *Earth and Planetary Science Letters*, 268(1-2), pp.124–136.

Grove, C.A., Zinke, J., Scheufen, T., Maina, J., Epping, E., Boer, W., Randriamanantsoa, B. & Brummer, G.-J.A., 2012. Spatial linkages between coral proxies of terrestrial runoff across a large embayment in Madagascar. *Biogeosciences*, 9(8), pp.3063–3081.

Gruber, N. & Sarmiento, J.L., 1997. Global patterns of marine nitrogen fixation and denitrification. *Global Biogeochemical Cycles*, 11(2), pp.235–266.

Gupta, B.K.S., 1999. *Modern Foraminifera*, Dordrecht: Kluwer Academic Publishers.

Halicz, L., Galy, A., Belshaw, N.S. & O'Nions, R.K., 1999. High-precision measurement of calcium isotopes in carbonates and related materials by multiple collector inductively coupled plasma mass spectrometry (MC-ICP-MS). *Journal of Analytical Atomic Spectrometry*, 14(12), pp.1835–1838.

Hall, J.M. & Chan, L.H., 2004a. Ba/Ca in benthic foraminifera: Thermocline and middepth circulation in the North Atlantic during the last glaciation. *Paleoceanography*, 19(4), pp.1–13.

Hall, J.M. & Chan, L.H., 2004b. Ba/Ca in Neogloboquadrina pachyderma as an indicator of deglacial meltwater discharge into the western Arctic Ocean. *Paleoceanography*, 19(1), pp.1–9.

Hall, I.R., Bianchi, G.G. & Evans, J.R., 2004. Centennial to millennial scale Holocene climate-deep water linkage in the North Atlantic. *Quaternary Science Reviews*, 23(14-15), pp.1529–1536.

Hanor, J.S. & Chan, L.H., 1977. Non-conservative behavior of barium during mixing of Mississippi River and Gulf of Mexico waters. *Earth and Planetary Science Letters*, 37(2), pp.242–250.

Hansen, H.J. & Reiss, Z., 1972. Scanning electron microscopy of wall structures in some benthonic and

planktonic foraminifera. *Revista Española de Micropaleontología*, 4, pp.169–179.

Harding, D.J., Arden, J.W. & Rickaby, R.E.M., 2006. A method for precise analysis of trace element/calcium ratios in carbonate samples using quadrupole inductively coupled plasma mass spectrometry. *Geochemistry, Geophysics, Geosystems*, 7(6).

Harris, D.C., 2010. *Quantitative Chemical Analysis*, New York: W. H. Freeman & Co.

Hatch, M.B.A., Schellenberg, S.A. & Carter, M.L., 2013. Ba/Ca variations in the modern intertidal bean clam Donax gouldii: An upwelling proxy? *Palaeogeography, Palaeoclimatology, Palaeoecology*, 373, pp.98–107.

Hathorne, E.C., Alard, O., James, R.H. & Rogers, N.W., 2003. Determination of intratest variability of trace elements in foraminifera by laser ablation inductively coupled plasma-mass spectrometry. *Geochemistry, Geophysics, Geosystems*, 4(12).

Havach, S.M., Chandler, G.T., Wilson-Finelli, A. & Shaw, T.J., 2001. Experimental determination of trace element partition coefficients in cultured benthic foraminifera. *Geochimica et Cosmochimica Acta*, 65(8), pp.1277–1283.

Hayes, C.T., Martínez-García, A., Hasenfratz, A.P., Jaccard, S.L., Hodell, D.A., Sigman, D.M., Haug, G.H. & Anderson, R.F., 2014. A stagnation event in the deep South Atlantic during the last interglacial period. *Science*, 346(1514), pp.1514–1517.

Heinrich, H., 1988. Origin and consequences of cyclic ice rafting in the Northeast Atlantic Ocean during the past 130,000 years. *Quaternary Research*, 29(2), pp.142–152.

Hemleben, C., Spindler, M. & Anderson, O.R., 1989. *Modern Planktonic Foraminifera*. New York: Springer-Verlag.

Henderson, G.M., Lindsay, F.N. & Slowey, N.C., 1999. Variation in bioturbation with water depth on marine slopes: A study on the Little Bahamas Bank. *Marine Geology*, 160(1-2), pp.105–118.

Henkel, S., Strasser, M., Schwenk, T., Hanebruth, T.J.J., Hüsener, J., Arnold, G.L., Winkelmann, D., Formolo, M., Tomasini, J., Krastel, S. & Kasten, S., 2011. An interdisciplinary investigation of a recent submarine mass transport deposit at the continental margin off Uruguay. *Geochemistry, Geophysics, Geosystems*, 12(8), pp.1–19.

Hofmann, A.E., Bourg, I.C. & DePaolo, D.J., 2012. Ion desolvation as a mechanism for kinetic isotope fractionation in aqueous systems. *Proceedings of the National Academy of Sciences of the United States of America*, 109(46), pp.18689–94.

Hönisch, B., Allen, K.A., Russell, A.D., Eggins, S.M., Bijma, J., Spero, H.J., Lea, D.W. & Yu, J., 2011. Planktic foraminifers as recorders of seawater Ba/Ca. *Marine Micropaleontology*, 79(1-2), pp.52–57.

Hoogakker, B., Elderfield, H., Oliver, K. & Crowhurst, S., 2010. Benthic foraminiferal oxygen isotope offsets over the last glacial-interglacial cycle. *Paleoceanography*, 25(4), pp.1–11.

Horita, J., Zimmermann, H. & Holland, H.D., 2002. Chemical evolution of seawater during the Phanerozoic: Implications from the record of marine evaporites. *Geochimica et Cosmochimica*

Acta, 66(21), pp.3733–3756.

Horner, T.J., Kinsley, C.W. & Nielsen, S.G., 2015. Barium-isotopic fractionation in seawater mediated by barite cycling and oceanic circulation. *Earth and Planetary Science Letters*, 430, pp.511–522.

Horta-Puga, G. & Carriquiry, J.D., 2012. Coral Ba/Ca molar ratios as a proxy of precipitation in the northern Yucatan Peninsula, Mexico. *Applied Geochemistry*, 27(8), pp.1579–1586.

Housecroft, C.E. & Constable, E.C., 2010. *Chemistry: An Introduction to Organic, Inorganic and Physical Chemistry*, Harlow, Essex: Pearson Education.

IPCC, 2013. *Climate Change 2013: The Physical Science Basis. Contribution of the Working Group I to the Fifth Assessment Report of the Intergovernmental Panel on Climate Change* T. F. Stocker, D. Qin, G.-K. Plattner, M. Tignor, S.K. Allen, J. Boschung, A. Nauels, Y. Xia, V. Bex & P.M. Midgley, eds., Cambridge: Cambridge University Press.

IPCC, 2014. *Climate Change 2014: Impacts, Adaptation and Vulnerability. Part A: Global and Sectoral Aspects. Contribution of Working Group II to the Fifth Assessment Report of the Intergovernmental Panel on Climate Change* C. B. Field, V.R. Barros, D.J. Dokken, K.J. Mach, M.D. Mastrandrea, T.E. Bilir, M. Chatterjee, K.L. Ebi, Y.O. Estrada, R.C. Genova, B. Girma, E.S. Kissel, A.N. Levy, S. MacCracken, P.R. Mastrandrea & L.L. White, eds., Cambridge: Cambridge University Press.

Jeandel, C., Dupré, B., Lebaron, G., Monnin, C. & Minster, J.-F., 1996. Longitudinal distributions of dissolved barium, silica and alkalinity in the western and southern Indian Ocean. *Deep-Sea Research Part I: Oceanographic Research Papers*, 43(1), pp.1–31.

Kara, A.B., Rochford, P.A. & Hurlburt, H.E., 2003. Mixed layer depth variability over the global ocean. *Journal of Geophysical Research*, 108(C3), p.3079.

Kaspar, F., Kühl, N., Cubasch, U. & Litt, T., 2005. A model-data comparison of European temperatures in the Eemian interglacial. *Geophysical Research Letters*, 32(11), pp.1–5.

Kawamura, K., Nakazawa, T., Aoki, S., Sugawara, S., Fujii, Y. & Watanabe, O., 2003. Atmospheric CO_2 variations over the last three glacial-interglacial climatic cycles deduced from the Dome Fuji deep ice core, Antarctica using a wet extraction technique. *Tellus, Series B: Chemical and Physical Meteorology*, 55(2), pp.126–137.

Khalifa, G.M., Kirchenbuechler, D., Koifman, N., Kleinerman, O., Talmon, Y., Elbaum, M., Addadi, L., Weiner, S. & Erez, J., in press. Biomineralization pathways in a foraminifer revealed using a novel correlative cryo-fluorescence-SEM-EDS technique. *Journal of Structural Biology*.

Kitano, Y., Kanamori, N. & Oomori, T., 1971. Measurements of distribution coefficients of strontium and barium between carbonate precipitate and solution - Abnormally high values of distribution coefficients measured at early stages of carbonate formation. *Geochemical Journal*, 4(4), pp.183–206.

Kleiven, H(K).F., Kleiven, F., Kissel, C., Laj, C., Ninnemann, U.S., Richter, T.O. & Cortijo, E., 2008. Reduced North Atlantic deep water coeval with the glacial Lake Agassiz freshwater outburst.

Science, 319(5859), pp.60–64.

Klinkhammer, G.P. & Palmer, M.R., 1991. Uranium in the oceans: Where it goes and why. *Geochimica et Cosmochimica Acta*, 55(7), pp.1799–1806.

Klinkhammer, G., Rona, P., Greaves, M. & Elderfield, H., 1985. Hydrothermal manganese plumes in the Mid-Atlantic Ridge rift valley. *Nature*, 314, pp.727–731.

Klinkhammer, G., Elderfield, H., Greaves, M., Rona, P. & Nelsen, T., 1986. Manganese geochemistry near high-temperature vents in the Mid-Atlantic Ridge rift valley. *Earth and Planetary Science Letters*, 80(3-4), pp.230–240.

Koho, K.A., de Nooijer, L.J. & Reichart, G.J., 2015. Combining benthic foraminiferal ecology and shell Mn/Ca to deconvolve past bottom water oxygenation and paleoproductivity. *Geochimica et Cosmochimica Acta*, 165, pp.294–306.

Kristjánsdóttir, G.B., Lea, D.W., Jennings, A.E., Pak, D.K. & Belanger, C., 2007. New spatial Mg/Ca-temperature calibrations for three Arctic, benthic foraminifera and reconstruction of north Iceland shelf temperature for the past 4000 years. *Geochemistry, Geophysics, Geosystems*, 8(3).

Krueger, S., Leuschner, D.C., Ehrmann, W., Schmiedl, G. & Mackensen, A., 2012. North Atlantic Deep Water and Antarctic Bottom Water variability during the last 200 ka recorded in an abyssal sediment core off South Africa. *Global and Planetary Change*, 80-81, pp.180–189.

LaVigne, M., Hill, T.M., Spero, H.J. & Guilderson, T.P., 2011. Bamboo coral Ba/Ca: Calibration of a new deep ocean refractory nutrient proxy. *Earth and Planetary Science Letters*, 312(3-4), pp.506–515.

LaVigne, M., Grottoli, A.G., Palardy, J.E. & Sherrell, R.M., 2016. Multi-colony calibrations of coral Ba/Ca with a contemporaneous in situ seawater barium record. *Geochimica et Cosmochimica Acta*, 179, pp.203–216.

Lazareth, C.E., Vander Putten, E., André, L. & Dehairs, F., 2003. High-resolution trace element profiles in shells of the mangrove bivalve Isognomon ephippium: A record of environmental spatio-temporal variations? *Estuarine, Coastal and Shelf Science*, 57(5-6), pp.1103–1114.

Lea, D.W., 1990. *Foraminiferal and corraline barium as paleoceanographic tracers*. Massachusetts Institute of Technology and Woods Hole Oceanographic Institution.

Lea, D.W., 1993. Constraints on the alkalinity and circulation of glacial circumpolar deep water from benthic foraminiferal barium. *Global Biogeochemical Cycles*, 7(3), pp.695–710.

Lea, D.W., 1995. A trace metal perspective on the evolution of Antarctic Circumpolar Deep Water chemistry. *Paleoceanography*, 10(4), pp.733–747.

Lea, D. & Boyle, E., 1989. Barium content of benthic foraminifera controlled by bottom-water composition. *Nature*, 338(6218), pp.751–753.

Lea, D.W. & Boyle, E.A., 1990a. A 210,000-year record of barium variability in the deep northwest Atlantic Ocean. *Nature*, 347(6290), pp.269–272.

Lea, D.W. & Boyle, E.A., 1990b. Foraminiferal reconstruction of barium distibutions in water masses

of the glacial oceans. *Paleoceanography*, 5(5), pp.719–742.

Lea, D.W. & Boyle, E.A., 1991. Barium in planktonic foraminifera. *Geochimica et Cosmochimica Acta*, 55(11), pp.3321–3331.

Lea, D.W. & Boyle, E.A., 1993. Determination of carbonate-bound barium in foraminifera and corals by isotope dilution plasma-mass spectrometry. *Chemical Geology*, 103(1-4), pp.73–84.

Lea, D.W. & Spero, H.J., 1994. Assessing the reliability of paleochemical tracers: Barium uptake in the shells of planktonic foraminifera. *Paleoceanography*, 9(3), pp.445–452.

Lea, D.W. & Spero, H.J., 1992. Experimental determination of barium uptake in shells of the planktonic foraminifera Orbulina universa at 22ºC. *Geochimica et Cosmochimica Acta*, 56(7), pp.2673–2680.

Lea, D.W., Shen, G.T. & Boyle, E.A., 1989. Coralline barium records temporal variability in equatorial Pacific upwelling. *Nature*, 340, pp.373–376.

Lear, C.H., Rosenthal, Y. & Slowey, N., 2002. Benthic foraminiferal Mg/Ca-paleothermometry: A revised core-top calibration. *Geochimica et Cosmochimica Acta*, 66(19), pp.3375–3387.

Lear, C.H., Coxall, H.K., Foster, G.L., Lunt, D.J., Mawbey, E.M., Rosenthal, Y., Sosdian, S.M., Thomas, E. & Wilson, P.A., 2015. Neogene ice volume and ocean temperatures: Insights from infaunal foraminiferal Mg/Ca paleothermometry. *Paleoceanography*, 30, pp.1437–1454.

Legeleux, F. & Reyss, J.L., 1996. $^{228}Ra/^{226}Ra$ activity ratio in oceanic settling particles: Implications regarding the use of barium as a proxy for paleoproductivity reconstruction. *Deep-Sea Research Part I: Oceanographic Research Papers*, 43(11-12), pp.1857–1863.

Lipps, J.H., 1993. *Fossil Prokaryotes and Protists*, London: Blackwell Scientific.

Lisiecki, L.E. & Raymo, M.E., 2005. A Pliocene-Pleistocene stack of 57 globally distributed benthic $\delta^{18}O$ records. *Paleoceanography*, 20, p.PA1003.

López-Martínez, J., Muñoz, A., Dowdeswell, J.A., Linés, C. & Acosta, J., 2011. Relict sea-floor ploughmarks record deep-keeled Antarctic icebergs to 45ºS on the Argentine margin. *Marine Geology*, 288(1-4), pp.43–48.

Loubere, P. & Gary, A.C., 1990. Taphonomic process and species microhabitats in the living to fossil assemblage transition of deeper water benthic foraminifera. *Palaios*, 5(4), pp.375–381.

Lüthi, D., Le Floch, M., Bereiter, B., Blunier, T., Barnola, J.-M., Siegenthaler, U., Raynaud, D., Jouzel, J., Fischer, H., Kawamura, K. & Stocker, T.F., 2008. High-resolution carbon dioxide concentration record 650,000-800,000 years before present. *Nature*, 453(7193), pp.379–382.

Maidment, D.R., 1993. Handbook of Hydrology.

Marchitto, T.M., 2006. Precise multielemental ratios in small foraminiferal samples determined by sector field ICP-MS. *Geochemistry, Geophysics, Geosystems*, 7(5).

Marshall, B.J., Thunell, R.C., Spero, H.J., Henehan, M.J., Lorenzoni, L. & Astor, Y., 2015. Morphometric and stable isotopic differentiation of Orbulina universa morphotypes from the Cariaco Basin, Venezuela. *Marine Micropaleontology*, 120, pp.46–64.

Martin, P.A. & Lea, D.W., 2002. A simple evaluation of cleaning procedures on fossil benthic

foraminiferal Mg/Ca. *Geochemistry, Geophysics, Geosystems*, 3(10), pp.1–8.

Martin, W., Baross, J., Kelley, D. & Russell, M.J., 2008. Hydrothermal vents and the origin of life. *Nature Reviews*, 6(11), pp.805–14.

Mayewski, P.A., Rohling, E.E., Stager, J.C., Karlén, W., Maasch, K.A., Meeker, L.D., Meyerson, E.A., Gasse, F., van Kreveld, S., Holmgren, K., Lee-Thorp, J., Rosqvist, G., Rack, F., Staubwasser, M., Schneider, R.P. & Steig, E.J., 2004. Holocene climate variability. *Quaternary Research*, 62(3), pp.243–255.

McCartney, M.S., 1993. Crossing of the Equator by the Deep Western Boundary Current in the Western Atlantic Ocean. *Journal of Physical Oceanography*, 23, pp.1953–1974.

McCorkle, D.C., Martin, P.M., Lea, D.W. & Klinkhammer, G.P., 1995. Evidence of a dissolution effect on benthic foraminiferal shell chemistry: $\delta^{13}C$, Cd/Ca, Ba/Ca, and Sr/Ca results from the Ontong Java Plateau. *Paleoceanography*, 10(4), pp.699–714.

McKay, C.L., Groeneveld, J., Filipsson, H.L., Gallego-Torres, D., Whitehouse, M.J., Toyofuku, T. & Romero, O.E., 2015. A comparison of benthic foraminiferal Mn/Ca and sedimentary Mn/Al as proxies of relative bottom-water oxygenation in the low-latitude NE Atlantic upwelling system. *Biogeosciences*, 12(18), pp.5415–5428.

McManus, J., Berelson, W.M., Klinkhammer, G.P., Kilgore, T.E. & Hammond, D.E., 1994. Remobilization of barium in continental margin sediments. *Geochimica et Cosmochimica Acta*, 58(22), pp.4899–4907.

McManus, J., Berelson, W.M., Klinkhammer, G.P., Johnson, K.S., Coale, K.H., Anderson, R.F., Kumar, N., Burdige, D.J., Hammond, D.E., Brumsack, H.J., McCorkle, D.C. & Rushdi, A., 1998. Geochemistry of barium in marine sediments: implications for its use as a paleoproxy. *Geochimica et Cosmochimica Acta*, 62(21-22), pp.3453–3473.

McManus, J., Berelson, W.M., Hammond, D.E. & Klinkhammer, G.P., 1999. Barium cycling in the North Pacific: Implications for the utility of Ba as a paleoproductivity and paleoalkalinity proxy. *Paleoceanography*, 14(1), pp.53–61.

Meyer, A., 2015. Mixing (MX) oceanographic toolbox for EM-APEX float data.

Molinari, R.L., Fine, R.A. & Johns, E., 1992. The Deep Western Boundary Current in the tropical North Atlantic Ocean. *Deep Sea Research Part A, Oceanographic Research Papers*, 39(11-12), pp.1967–1984.

Monnin, C., Jeandel, C., Cattaldo, T. & Dehairs, F., 1999. The marine barite saturation state of the world's oceans. *Marine Chemistry*, 65(3-4), pp.253–261.

Montagna, P., McCulloch, M., Mazzoli, C., Silenzi, S. & Odorico, R., 2007. The non-tropical coral Cladocora caespitosa as the new climate archive for the Mediterranean: high-resolution (~weekly) trace element systematics. *Quaternary Science Reviews*, 26(3-4), pp.441–462.

Morard, R., Quillévéré, F., Escarguel, G., Ujiie, Y., de Garidel-Thoron, T., Norris, R.D. & de Vargas, C., 2009. Morphological recognition of cryptic species in the planktonic foraminifer Orbulina

universa. *Marine Micropaleontology*, 71(3-4), pp.148–165.

Morse, J.W. & Bender, M.L., 1990. Partition coefficients in calcite: Examination of factors influencing the validity of experimental results and their application to natural systems. *Chemical Geology*, 82, pp.265–277.

Moyer, R.P., Grottoli, A.G. & Olesik, J.W., 2012. A multiproxy record of terrestrial inputs to the coastal ocean sing minor and trace elements (Ba/Ca, Mn/Ca, Y/Ca) and carbon isotopes ($\delta^{13}C$, $\Delta^{14}C$) in a nearshore coral from Puerto Rico. *Paleoceanography*, 27(3), pp.1–14.

Murray, R.W. & Leinen, M., 1996. Scavenged excess aluminum and its relationship to bulk titanium in biogenic sediment from the central equatorial Pacific Ocean. *Geochimica et Cosmochimica Acta*, 60(20), pp.3869–3878.

Murray, W., Knowlton, C., Leinen, M., Mix, A.C. & Polsky, C.H., 2000. Export production and carbonate dissolution in the central equatorial Pacific Ocean over the past 1 Myr. *Paleoceanography*, 15(6), pp.570–592.

Nehrke, G., Keul, N., Langer, G., de Nooijer, L.J., Bijma, J. & Meibom, A., 2013. A new model for biomineralization and trace-element signatures of Foraminifera tests. *Biogeosciences*, 10(10), pp.6759–6767.

Ni, Y., Foster, G.L., Bailey, T., Elliott, T., Schmidt, D.N., Pearson, P., Haley, B. & Coath, C., 2007. A core top assessment of proxies for the ocean carbonate system in surface-dwelling foraminifers. *Paleoceanography*, 22(3).

Nielsen, S.H.H., Koç, N. & Crosta, X., 2004. Holocene climate in the Atlantic sector of the Southern Ocean: controlled by insolation or oceanic circulation? *Geology*, 32(4), pp.317–320.

de Nooijer, L.J., Toyofuku, T. & Kitazato, H., 2009. Foraminifera promote calcification by elevating their intracellular pH. *Proceedings of the National Academy of Sciences of the United States of America*, 106, pp.15374–15378.

Nürnberg, C.C., Bohrmann, G. & Schltiter, M., 1997. Barium accumulation in the Atlantic sector of the Southern Ocean: Results from 190,000-year records. *Paleoceanography*, 12(4), pp.594–603.

O'Leary, M.J., Hearty, P.J., Thompson, W.G., Raymo, M.E., Mitrovica, J.X. & Webster, J.M., 2013. Ice sheet collapse following a prolonged period of stable sea level during the last interglacial. *Nature Geoscience*, 6(9), pp.796–800.

Oppo, D.W., McManus, J.F. & Cullen, J.L., 2003. Deepwater variability in the Holocene epoch. *Nature*, 422, pp.277–278.

Otto-Bliesner, B.L., Marshall, S.J., Overpeck, J.T., Miller, G.H. & Hu, A., 2006. Simulating Arctic climate warmth and icefield retreat in the last interglaciation. *Science*, 311(5768), pp.1751–1753.

Paytan, A., 1996. *Marine barite: A recorder of oceanic chemistry, productivity and circulation*. University of California.

Paytan, A. & Kastner, M., 1996. Benthic Ba fluxes in the central Equatorial Pacific, implications for the oceanic Ba cycle. *Earth and Planetary Science Letters*, 142(3-4), pp.439–450.

Paytan, A., Kastner, M. & Chavez, F.P., 1996. Glacial to interglacial fluctuations in productivity in the equatorial Pacific as indicated by marine barite. *Science*, 274(5291), pp.1355–1357.

Peterson, R.G., 1992. The boundary currents in the western Argentine Basin. *Deep Sea Research Part A, Oceanographic Research Papers*, 39(3-4), pp.623–644.

Petit, R.J., Jouzel, J., Raynaud, D., Barkov, N.I., Barnola, J.-M., Basile, I., Bender, M., Chappellaz, J., Davis, M., Delaygue, G., Delmotte, M., Kotlyakov, V.M., Legrand, M., Lipenkov, V.Y., Lorius, C., Pépin, L., Ritz, C., Saltzman, E. & Stievenard, M., 1999. Climate and atmospheric history of the past 420,000 years from the Vostok ice core, Antarctica. *Nature*, 399, pp.429–413.

Pingitore, N.E., 1986. Modes of coprecipitation of Ba^{2+} and Sr^{2+} with calcite. In J.F. Davis & K.F. Hayes, eds. *Geochemical Processes at Mineral Surfaces*. American Chemical Society, pp. 574–586.

Pingitore, N.E. & Eastman, M.P., 1984. The experimental partitioning of Ba^{2+} into calcite. *Chemical Geology*, 45, pp.113–120.

Piola, A.R. & Gordon, A.L., 1989. Intermediate waters in the southwest South Atlantic. *Deep Sea Research Part A, Oceanographic Research Papers*, 36(1), pp.1–16.

Piola, A.R. & Matano, R.P., 2009. Brazil and Falklands (Malvinas) currents. In J.H. Steele, S.A. Thorpe, & K.K. Turekian, eds. *Ocean Currents: A Derivative of the Encyclopedia of Ocean Sciences*. London: Academic Press, pp. 35–43.

Piola, A.R., Martínez Avellaneda, N., Guerrero, R.A., Jardón, F.P., Palma, E.D. & Romero, S.I., 2010. Malvinas-slope water intrusions on the northern Patagonia continental shelf. *Ocean Science Discussions*, 6(3), pp.2939–2974.

Piola, A.R., Franco, B.C., Palma, E.D. & Saraceno, M., 2013. Multiple jets in the Malvinas Current. *Journal of Geophysical Research: Oceans*, 118(4), pp.2107–2117.

Prentice, I.C., Sykes, M.T., Lautenschlager, M., Harrison, S.P., Denissenko, O. & Bartlen, P.J., 1993. Modelling global vegetation patterns and terrestrial carbon storage at the Last Glacial Maximum. *Global Ecology and Biogeography Letters*, 3(3), pp.67–76.

Pretet, C., 2013. *Non-traditional isotopes (barium and calcium) and elemental ratios in scleractinian coral skeleton: New look into geochemical cycles, environmental proxies and bio-calcification processes*. University of Geneva.

Pretet, C., van Zuilen, K., Nägler, T.F., Reynaud, S., Böttcher, M.E. & Samankassou, E., 2015. Constraints on barium isotope fractionation during aragonite precipitation by corals. *The Depositional Record*, 1(2), pp.118–129.

Putnis, C. V., Kowacz, M. & Putnis, A., 2008. The mechanism and kinetics of DTPA-promoted dissolution of barite. *Applied Geochemistry*, 23(9), pp.2778–2788.

Quattrini, F.J., 1972. Aqueous reactive scale solvent.

Rathburn, A.E. & Corliss, B.H., 1994. The ecology of living (stained) deep-sea benthic foraminifera from the Sulu Sea. *Paleoceanography*, 9(1), pp.87–150.

Ravelo, A.C. & Hillaire-Marcel, C., 2007. The Use of Oxygen and Carbon Isotopes of Foraminifera in Paleoceanography. *Developments in Marine Geology*, 1(7), pp.735–764.

Reiss, Z., 1957. The Bilamellidea, nov. superfam., and remarks on Cretaceous Globorotaliids. *Journal of Foraminiferal Research*, 8, pp.127–145.

Reitz, A., Pfeifer, K., de Lange, G.J. & Klump, J., 2004. Biogenic barium and the detrital Ba/Al ratio: A comparison of their direct and indirect determination. *Marine Geology*, 204(3-4), pp.289–300.

Rickaby, R.E.M., Elderfield, H., Roberts, N., Hillenbrand, C.-D. & Mackensen, A., 2010. Evidence for elevated alkalinity in the glacial Southern Ocean. *Paleoceanography*, 25(1), pp.1–15.

Riedinger, N., Kasten, S., Gröger, J., Franke, C. & Pfeifer, K., 2006. Active and buried authigenic barite fronts in sediments from the Eastern Cape Basin. *Earth and Planetary Science Letters*, 241(3-4), pp.876–887.

Roberts, J., Gottschalk, J., Skinner, L.C., Peck, V.L., Kender, S., Elderfield, H., Waelbroeck, C., Vásquez Riveiros, N. & Hodell, D.A., 2016. Evolution of South Atlantic density and chemical stratification across the last deglaciation. *Proceedings of the National Academy of Sciences of the United States of America*, p.514–519.

Robin, E., Rabouille, C., Martinez, G., Lefevre, I., Reyss, J.L., van Beek, P. & Jeandel, C., 2003. Direct barite determination using SEM/EDS-ACC system: Implication for constraining barium carriers and barite preservation in marine sediments. *Marine Chemistry*, 82(3-4), pp.289–306.

Rohling, E.J., Braun, K., Grant, K., Kucera, M., Roberts, A.P., Siddall, M. & Trommer, G., 2010. Comparison between Holocene and Marine Isotope Stage-11 sea-level histories. *Earth and Planetary Science Letters*, 291(1-4), pp.97–105.

Rona, P.A., Klinkhammer, G., Nelsen, T.A., Trefry, J.H. & Elderfield, H., 1986. Black smokers, massive sulphides and vent biota at the Mid-Atlantic Ridge. *Nature*, 321, pp.33–37.

Rosenthal, Y., Boyle, E.A. & Slowey, N., 1997. Temperature control on the incorporation of magnesium, strontium, fluorine, and cadmium into benthic foraminiferal shells from Little Bahama Bank: Prospects for thermocline paleoceanography. *Geochimica et Cosmochimica Acta*, 61(17), pp.3633–3643.

Rosenthal, Y., Lohmann, G.P., Lohmann, K.C. & Sherrell, R.M., 2000. Incorporation and preservation of Mg in Globigerinoides sacculifer: Implications for reconstructing the temperature and $^{18}O/^{16}O$ of seawater. *Paleoceanography*, 15(1), pp.135–145.

Rosenthal, Y., Lear, C.H., Oppo, D.W. & Linsley, B.K., 2006. Temperature and carbonate ion effects on Mg/Ca and Sr/Ca ratios in benthic foraminifera: Aragonitic species Hoeglundina elegans. *Paleoceanography*, 21(1), pp.1–14.

Rubin, S.I., King, S.L., Jahnke, R.A. & Froelich, P.N., 2003. Benthic barium and alkalinity fluxes: Is Ba an oceanic paleo-alkalinity proxy for glacial atmospheric CO_2? *Geophysical Research Letters*, 30(17), p.1885.

Ruddiman, W.F., 2001. *Earth's Climate Past and Future*, New York: W. H. Freeman & Co.

Rudnicki, M.D. & Elderfield, H., 1992. Theory applied to the Mid-Atlantic ridge hydrothermal plumes: the finite-difference approach. *Journal of Volcanology and Geothermal Research*, 50(1-2), pp.161–172.

Rutsch, H.J., Mangini, A., Bonani, G., Dittrich-Hannen, B., Kubik, P.W., Suter, M. & Segl, M., 1995. ^{10}Be and Ba concentrations in West African sediments trace productivity in the past. *Earth and Planetary Science Letters*, 133(1-2), pp.129–143.

Saraswat, R., Lea, D.W., Nigam, R., Mackensen, A. & Naik, D.K., 2013. Deglaciation in the tropical Indian Ocean driven by interplay between the regional monsoon and global teleconnections. *Earth and Planetary Science Letters*, 375, pp.166–175.

Sarmiento, J.L., Gruber, N., Brzezinski, M.A. & Dunne, J.P., 2004. High-latitude controls of thermocline nutrients and low latitude biological productivity. *Nature*, 427(6969), pp.56–60.

Schejter, L., Rimondino, C., Chiesa, I., Díaz de Astarloa, J.M., Doti, B., Elías, R., Escolar, M., Genzano, G., López-Gappa, J., Tatián, M., Zelaya, D.G., Cristobo, J., Perez, C.D., Cordeiro, R.T. & Bremec, C.S., 2016. Namuncurá Marine Protected Area: An oceanic hot spot of benthic biodiversity at Burdwood Bank, Argentina. *Polar Biology*, pp.1–14.

Schmiedl, G. & Mackensen, A., 2006. Multispecies stable isotopes of benthic foraminifers reveal past changes of organic matter decomposition and deepwater oxygenation in the Arabian Sea. *Paleoceanography*, 21(4), pp.1–14.

Schweizer, M., 2006. *Evolution and molecular phylogeny of Cibicides and Uvigerina (Rotaliida, Foraminifera)*. Utrecht University.

Schweizer, M., Pawlowski, J., Duijnstee, I.A.P., Kouwenhoven, T.J. & van der Zwaan, G.J., 2005. Molecular phylogeny of the foraminiferal genus Uvigerina based on ribosomal DNA sequences. *Marine Micropaleontology*, 57(3-4), pp.51–67.

Shackleton, N.J., Fernanda Sánchez-Goñi, M., Pailler, D. & Lancelot, Y., 2003. Marine isotope substage 5e and the Eemian interglacial. *Global and Planetary Change*, 36(3), pp.151–155.

Shannon, R.D., 1976. Revised effective ionic radii and systematic studies of interatomic distances in halides and chalcogenides. *Acta Crystallographica Section A*, 32(5), pp.751–767.

Shen, G.T., Cole, J.E., Lea, D.W., Linn, L.J., McConnaughey, T.A. & Fairbanks, R.G., 1992. Surface ocean variability at Galapagos from 1936–1982: Calibration of geochemical tracers in corals. *Paleoceanography*, 7(5), p.563.

Shevenell, A.E., Ingalls, A.E. & Domack, E.W., 2007. Orbital and atmospheric forcing of western Antarctic Peninsula climate in the Holocene: The TEX_{86} paleotemperature record of Palmer Deep. In *10th International Symposium on Antarctic Earth Sciences*. p. 131.

Siebert, C., Nägler, T.F. & Kramers, J.D., 2001. Determination of molybdenum isotope fractionation by double-spike multicollector inductively coupled plasma mass spectrometry. *Geochemistry, Geophysics, Geosystems*, 2(7), pp.1032–16.

Siegenthaler, U., Stocker, T.F., Monnin, E., Lüthi, D., Schwander, J., Stauffer, B., Raynaud, D.,

Barnola, J.-M., Fischer, H., Masson-Delmotte, V. & Jouzel, J., 2005. Stable carbon cycle-climate relationship during the late Pleistocene. *Science*, 310, pp.1313–1317.

Sigman, D.M. & Boyle, E.A., 2000. Glacial/interglacial variations in atmospheric carbon dioxide. *Nature*, 407(6806), pp.859–869.

Sigman, D.M., Hain, M.P. & Haug, G.H., 2010. The polar ocean and glacial cycles in atmospheric CO_2 concentration. *Nature*, 466(7302), pp.47–55.

Singh, S.P., Singh, S.K. & Bhushan, R., 2013. Internal cycling of dissolved barium in water column of the Bay of Bengal. *Marine Chemistry*, 154, pp.12–23.

Sloyan, B.M., 2005. Spatial variability of mixing in the Southern Ocean. *Geophysical Research Letters*, 32(18), pp.1–5.

Speer, K.G. & Rona, P.A., 1989. A model of an Atlantic and Pacific hydrothermal plume. *Journal of Geophysical Research*, 94(C5), p.6213.

Spero, H.J. & De Niro, M.J., 1987. The influence of symbiont photosynthesis on the $\delta^{18}O$ and $\delta^{13}C$ values of planktonic foraminiferal calcite. *Symbiosis*, 4, pp.213–228.

Spero, H.J., Bijma, J., Lea, D.W. & Bemis, B.E., 1997. Effect of seawater carbonate concentration on foraminiferal carbon and oxygen isotopes. *Nature*, 390, pp.497–500.

Sprovieri, M., Ribera d'Alcalà, M., Salvagio Manta, D., Bellanca, A., Neri, R., Lirer, F., Taberner, C., Josè Pueyo, J. & Sammartino, S., 2008. Ba/Ca evolution in water masses of the Mediterranean late Neogene. *Paleoceanography*, 23(3), pp.1–17.

Sprovieri, M., Di Stefano, E., Incarbona, A., Salvagio Manta, D., Pelosi, N., Ribera d'Alcalà, M. & Sprovieri, R., 2012. Centennial- to millennial-scale climate oscillations in the Central-Eastern Mediterranean Sea between 20,000 and 70,000 years ago: Evidence from a high-resolution geochemical and micropaleontological record. *Quaternary Science Reviews*, 46, pp.126–135.

Stroobants, N., Dehairs, F., Goeyens, L., Vanderheijden, N. & Van Grieken, R., 1991. Barite formation in the Southern Ocean water column. *Marine Chemistry*, 35(1-4), pp.411–421.

Tachikawa, K. & Elderfield, H., 2002. Microhabitat effects on Cd/Ca and $\delta^{13}C$ of benthic foraminifera. *Earth and Planetary Science Letters*, 202, pp.607–624.

Taylor, H., Gordon, A. & Molinelli, E., 1978. Climatic characteristics of the Antarctic Polar Front zone. *Journal of Geophysical Research*, 83(C9), pp.4572–4578.

Teal, L.R., Bulling, M.T., Parker, E.R. & Solan, M., 2008. Global patterns of bioturbation intensity and mixed depth of marine soft sediments. *Aquatic Biology*, 2(3), pp.207–218.

Thermo Finnigan, 2001. Element 2 Operating Manual.

Thornalley, D.J.R., Blaschek, M., Davies, F.J., Praetorius, S., Oppo, D.W., McManus, J.F., Hall, I.R., Kleiven, H., Renssen, H. & McCave, I.N., 2013. Long-term variations in Iceland-Scotland overflow strength during the Holocene. *Climate of the Past*, 9(5), pp.2073–2084.

Tsumune, D., Aoyama, M., Hirose, K., Bryan, F.O., Lindsay, K. & Danabasoglu, G., 2011. Transport of ^{137}Cs to the Southern Hemisphere in an ocean general circulation model. *Progress in*

Oceanography, 89(1-4), pp.38–48.

Turchyn, A. V. & Schrag, D.P., 2004. Oxygen isotope constraints on the sulfur cycle over the past 10 million years. *Science*, 303, pp.2004–2007.

Tzedakis, P., Raynaud, D., McManus, J.F., Berger, A., Brovkin, V. & Kiefer, T., 2009. Interglacial diversity. *Nature Geoscience*, 2(11), pp.751–755.

Vivier, F. & Provost, C., 1999. Direct velocity measurements in the Malvinas Current. *Journal of Geophysical Research*, 104(C9), pp.21083–21103.

Wanner, H., Beer, J., Bütikofer, J., Crowley, T.J., Cubasch, U., Flückiger, J., Goosse, H., Grosjean, M., Joos, F., Kaplan, J.O., Küttel, M., Müller, S.A., Prentice, I.C., Solomina, O., Stocker, T.F., Tarasov, P., Wagner, M. & Widmann, M., 2008. Mid- to Late Holocene climate change: an overview. *Quaternary Science Reviews*, 27(19-20), pp.1791–1828.

Weldeab, S., 2012. Bipolar modulation of millennial-scale West African monsoon variability during the last glacial (75,000-25,000 years ago). *Quaternary Science Reviews*, 40, pp.21–29.

Weldeab, S., Lea, D.W., Schneider, R.R. & Andersen, N., 2007a. 155,000 years of West African monsoon and ocean thermal evolution. *Science*, 316, pp.1303–1307.

Weldeab, S., Lea, D.W., Schneider, R.R. & Andersen, N., 2007b. Centennial scale climate instabilities in a wet early Holocene West African monsoon. *Geophysical Research Letters*, 34(24), pp.1–6.

Weldeab, S., Menke, V. & Schmiedl, G., 2014. The pace of East African monsson evolution during the Holocene. *Geophysical Research Letters*, 41, pp.1724–1731.

Yu, J., Day, J., Greaves, M. & Elderfield, H., 2005. Determination of multiple element/calcium ratios in foraminiferal calcite by quadrupole ICP-MS. *Geochemistry, Geophysics, Geosystems*, 6(8), pp.1–9.

Yu, J., Elderfield, H., Jin, Z., Tomascak, P. & Rohling, E.J., 2014. Controls on Sr/Ca in benthic foraminifera and implications for seawater Sr/Ca during the late Pleistocene. *Quaternary Science Reviews*, 98, pp.1–6.

van Zuilen, K., Müller, T., Nägler, T.F., Dietzel, M. & Küsters, T., 2016. Experimental determination of barium isotope fractionation during diffusion and adsorption processes at low temperatures. *Geochimica et Cosmochimica Acta*, 186, pp.226–241.

van Zuilen, K., Nägler, T.F. & Bullen, T.D., in press. Barium Isotopic Compositions of Geological Reference Materials. *Geostandards and Geoanalytical Research*.

List of Abbreviations

AABW – Antarctic Bottom Water

AAIW – Antarctic Intermediate Water

ACC – Antarctic Circumpolar Current

ASW – Antarctic Surface Water

CDW – Circumpolar Deep Water

CFC-11 - Trichlorofluoromethane

DIC – Dissolved Inorganic Carbon

DTPA – Diethylenetriaminepentaacetic Acid

DWBC – Deep Western Boundary Current

EDS – Energy-Dispersive X-Ray Spectroscopy

eWOCE – Electronic Atlas of the World Ocean Circulation Experiment

GEOSECS – Geochemical Ocean Sections Study

HR-ICP-MS – High Resolution Inductively Coupled Plasma Mass Spectrometry

LGM – Last Glacial Maximum

MC-ICP-MS – Multiple Collector Inductively Coupled Plasma Mass Spectrometry

MIS – Marine Isotope Stage

MNADW – Middle North Atlantic Deep Water

N/A – Not Applicable

NADW – North Atlantic Deep Water

NIST – National Institute of Standards and Technology

ODP – Ocean Drilling Program

PMCC – Product Moment Correlation Coefficient

RGB – Red Green Blue Colour Model

RO – Reverse Osmosis Purified

RSD – Relative Standard Deviation

SD – Standard Deviation

SE – Standard Error

SEM – Scanning Electron Microscopy

SRM – Standard Reference Material

TA – Total Alkalinity

UNADW – Upper North Atlantic Deep Water

VPDB – Vienna Pee Dee Belemnite

XRF – X-Ray Fluorescence

Appendix A

Full Suite of XRF Data

Table A.1. Elemental abundances in sediment core BC387-2 measured via XRF, averaged per sediment horizon. Counts per second = cps.

Depth (cm)	Al (cps)	Si (cps)	S (cps)	Cl (cps)	K (cps)	Ca (cps)	Ti (cps)	Cr (cps)	Mn (cps)	Rh (cps)
1 – 2	3109	11,706	3227	12,334	3982	55,157	2294	579	472	11,169
2 – 3	3308	10,942	3565	14,495	4199	57,307	2474	514	644	11,345
3 – 4	3823	13,063	4252	17,511	4964	68,998	2852	563	668	13,600
4 – 5	4325	17,106	4682	19,204	6222	85,010	3520	577	825	16,049
5 – 6	4367	16,201	4804	21,387	6094	84,423	3181	621	765	16,358
6 – 7	4454	17,851	4763	20,764	6448	83,663	3480	627	843	17,055
7 – 8	4558	18,762	4852	20,693	6818	87,188	3758	626	802	16,973
8 – 9	4750	20,617	4764	19,626	7137	91,689	3776	640	820	17,143
9 – 10	4778	20,752	4842	20,392	7369	89,796	4072	652	980	17,030
10 – 11	4780	20,863	4964	19,926	7301	94,623	3950	712	914	17,108
11 – 12	4725	20,920	4875	19,499	7186	90,696	3860	611	793	16,811
12 – 13	4698	20,152	4817	19,026	6937	84,673	3868	719	945	16,500
13 – 14	4654	20,167	4816	19,611	7001	86,902	3896	672	881	16,400
14 – 15	4708	20,751	4772	19,745	6980	96,192	3859	633	915	16,954
15 – 16	4649	20,454	4675	18,390	7268	91,548	3621	636	902	17,133
16 – 17	4418	17,258	4701	18,885	6217	85,242	3428	661	824	15,791
17 – 18	4492	18,919	4822	19,254	6878	89,412	3598	593	927	16,913
18 – 19	4454	18,225	4893	22,255	6959	92,426	3737	716	911	18,279
19 – 20	4418	17,544	4948	25,009	6988	95,263	3893	614	822	19,129
20 – 21	4299	16,430	4965	25,178	6714	89,401	3850	770	920	19,610
21 – 22	4264	15,627	5061	27,205	6690	87,238	3590	660	956	19,887
22 – 23	4418	18,045	4906	24,011	7125	99,237	3766	621	977	19,496
23 – 24	4231	14,622	5197	26,652	6428	87,409	3667	715	955	18,433

Table A.2. Elemental abundances in sediment core BC387-2 measured via XRF, averaged per sediment horizon. Counts per second = cps.

Depth (cm)	Fe (cps)	Cu (cps)	Zn (cps)	Br (cps)	Rb (cps)	Sr (cps)	Zr (cps)	Pb (cps)	Ni (cps)	Sn (cps)	Ba (cps)
1 – 2	40,165	504	767	2779	1467	10,675	3564	639	281	1067	990
2 – 3	41,561	458	790	2660	1330	10,739	3763	568	262	1042	1174
3 – 4	41,824	509	780	2757	1369	11,317	3920	488	250	1023	1156
4 – 5	44,150	483	775	2879	1523	11,635	3803	530	254	1062	1227
5 – 6	44,901	516	808	2981	1436	11,990	4068	543	262	1099	1228
6 – 7	45,437	521	801	3059	1587	11,917	4206	578	251	1052	1374
7 – 8	46,240	490	801	3115	1529	12,101	4310	510	275	1087	1292
8 – 9	48,734	530	847	2831	1670	12,189	4515	542	279	1069	1345
9 – 10	48,863	485	856	2755	1560	12,285	4559	529	254	1104	1355
10 – 11	49,736	489	841	2935	1601	12,347	4249	597	273	1087	1320
11 – 12	48,064	459	770	2829	1503	11,920	4365	509	276	1146	1321
12 – 13	49,122	490	815	2680	1732	11,926	4438	580	259	1118	1284
13 – 14	48,692	490	833	2590	1560	11,793	4312	585	245	1157	1398
14 – 15	46,809	476	872	2703	1627	12,609	4520	506	266	1124	1354
15 – 16	49,124	492	838	2355	1733	12,450	4577	658	260	1118	1404
16 – 17	46,865	532	841	2391	1644	12,567	4675	544	248	1173	1417
17 – 18	48,227	521	829	2444	1647	12,718	4355	603	262	1155	1385
18 – 19	49,218	462	836	2492	1632	12,998	4964	567	265	1181	1487
19 – 20	49,658	482	834	2456	1648	13,114	4784	510	262	1128	1442
20 – 21	49,282	466	832	2649	1653	13,117	4432	561	253	1178	1467
21 – 22	50,594	495	876	2513	1699	13,399	4882	542	243	1182	1512
22 – 23	52,398	520	870	2455	1831	13,869	4477	573	263	1171	1384
23 – 24	51,002	414	861	2544	1580	13,036	4674	526	274	1083	1302

Appendix B

EDS Spectra Results

Table A.3. Results of EDS spectra collected from barite-like particles located upon a specimen of *Oridorsalis umbonatus*. EDS spectra results collected from the shell of this foraminifer are provided in Table A.4. Repeat measurements were taken from the same position to ensure that the EDS spectra are representative.

	Ca (wt %)	Al (wt %)	Si (wt %)
Results shown in Figure 3.9			
Initial results	86.0	14.0	0.0
Repeat 1	84.2	15.8	0.0
Repeat 2	83.3	16.7	0.0
Additional barite-like particle A			
Initial results	89.5	10.5	0.0
Repeat 1	90.5	9.5	0.0
Repeat 2	90.2	9.8	0.0
Additional barite-like particle B			
Initial results	88.4	10.4	1.2 [a]
Repeat 1	87.1	11.5	1.4 [a]
Repeat 2	88.5	11.5	0.0
Repeat 3	85.7	12.3	2.0
Repeat 4	82.6	15.1	2.3
Repeat 5	82.5	15.3	2.2

a) Results < 2 % are likely to be spurious (Dr S. MacLachlan, pers. com. 2015). wt % = weight %.

Table A.4. Results of EDS spectra collected from the calcium carbonate shell surfaces of *Oridorsalis umbonatus* and *Melonis barleeanus*. EDS spectra results collected from barite-like particles located upon *O. umbonatus* are provided in Table A.3. Repeat measurements were taken from the same position to ensure that the EDS spectra are representative.

	Ca (wt %)	Al (wt %)	Si (wt %)	Cu (wt %)
Results shown in Figure 3.9				
Initial results	92.3	7.7	0.0	0.0
Repeat 1	89.3	10.7	0.0	0.0
Repeat 2	86.4	11.2	2.3	0.0
	Ca (wt %)	Al (wt %)	Si (wt %)	Cu (wt %)
Repeat 3	84.6	12.5	2.8	0.0
Additional *O. umbonatus* site (same specimen as above)				
Initial results	86.0	14.0	0.0	0.0
Repeat 1	85.1	14.9	0.0	0.0
Repeat 2	85.0	15.0	0.0	0.0
M. barleeanus				
Initial results	92.4	7.6	0.0	0.0
Repeat 1	87.9	8.5	2.1	1.5 [a]
Repeat 2	88.5	9.3	2.2	0.0

a) Results < 2 % are likely to be spurious (Dr S. MacLachlan, pers. com. 2015). wt % = weight %.

Appendix C

Additional SEM Images

The following SEM images of uncleaned, fully-cleaned (cleaned using the full cleaning procedure described in Section 2.2 'Foraminiferal cleaning procedure') and non-DTPA-cleaned (cleaned without using the DTPA step for barite-removal) foraminifera are presented:

Figure A.1. Uncleaned *M. barleeanus* (core BC387-2)
Figure A.2. Uncleaned *O. umbonatus* (core BC387-2)
Figure A.3. Uncleaned *U. peregrina* (core BC387-2)
Figure A.4. Uncleaned *U. peregrina* (core BC387-2)

Figure A.5. Non-DTPA-cleaned *M. barleeanus* (core BC387-2)
Figure A.6. Non-DTPA-cleaned *M. barleeanus* (core BC387-2)
Figure A.7. Non-DTPA-cleaned *O. umbonatus* (core BC387-2)
Figure A.8. Non-DTPA-cleaned *O. umbonatus* (core BC387-2)
Figure A.9. Non-DTPA-cleaned *U. peregrina* (core BC387-2)
Figure A.10. Non-DTPA-cleaned *U. peregrina* (core BC387-2)
Figure A.11. Non-DTPA-cleaned *U. peregrina* (core BC387-2)

Figure A.12. Fully-cleaned *M. barleeanus* (core BC387-2)
Figure A.13. Fully-cleaned *O. umbonatus* (core BC387-2)
Figure A.14. Fully-cleaned *U. peregrina* (core BC387-2)

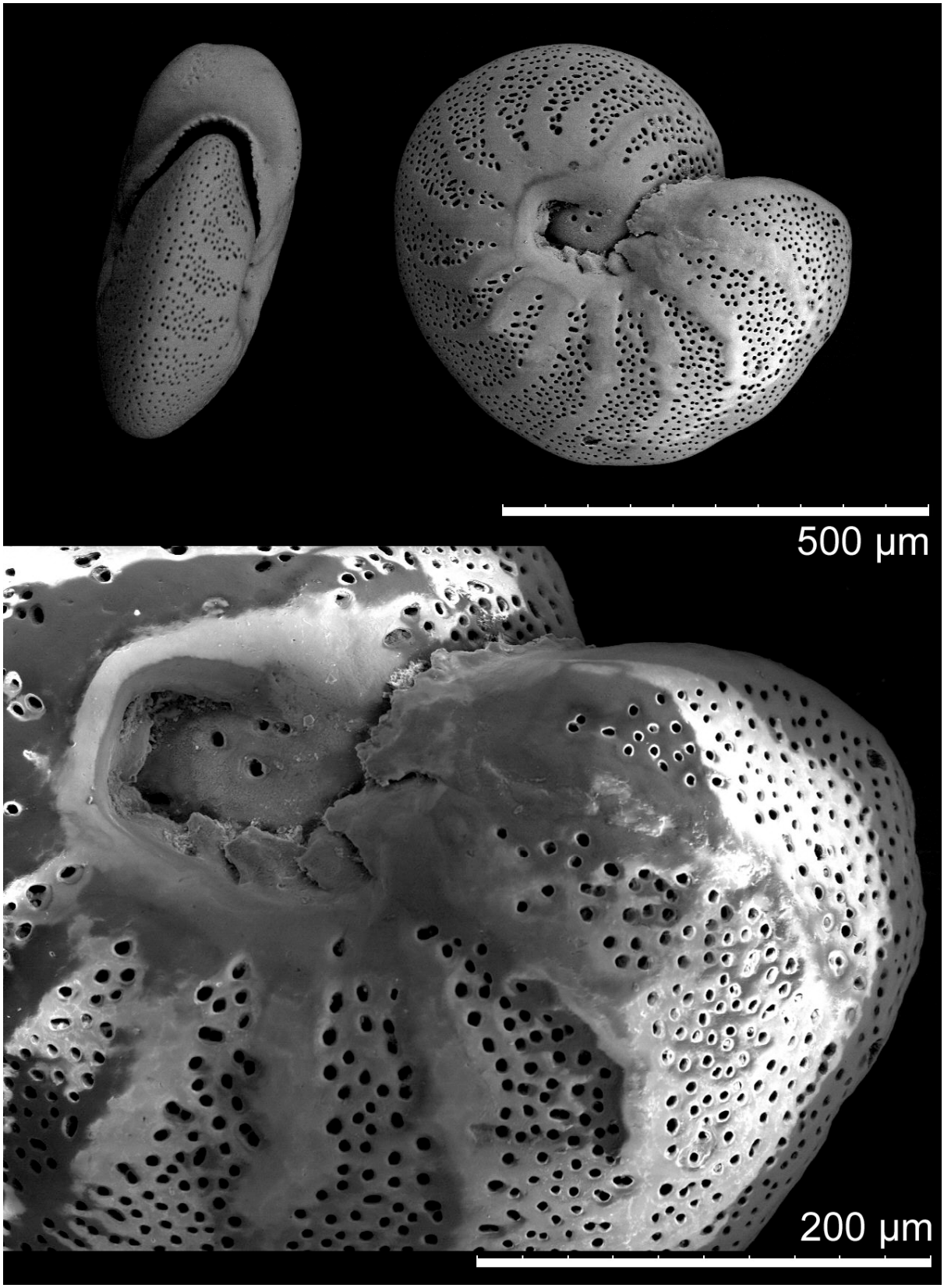

Figure A.1. Uncleaned *M. barleeanus* (core BC387-2).

Figure A.2. Uncleaned *O. umbonatus* (core BC387-2).

Figure A.3. Uncleaned *U. peregrina* (core BC387-2).

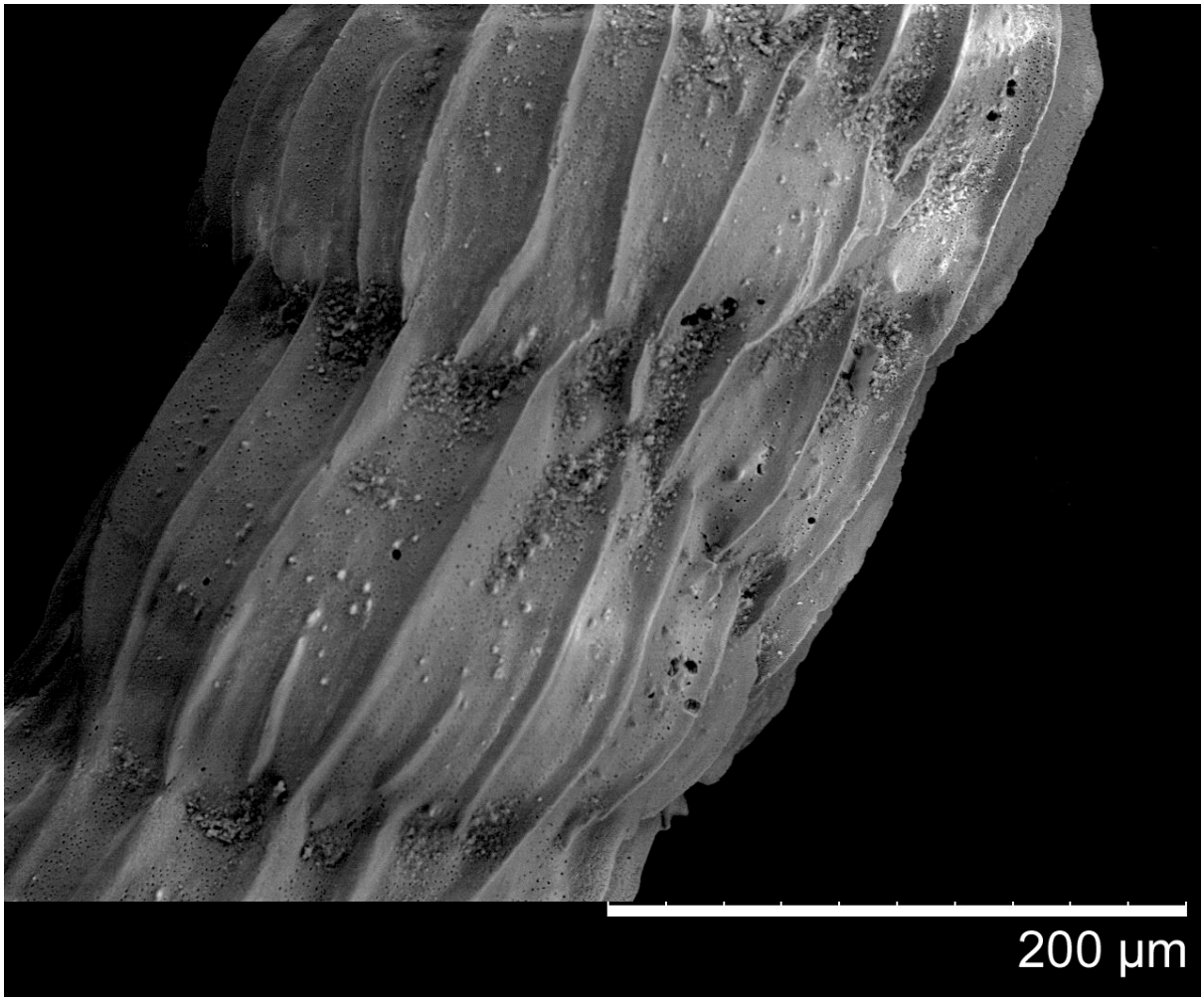

Figure A.4. Uncleaned *U. peregrina* (core BC387-2).

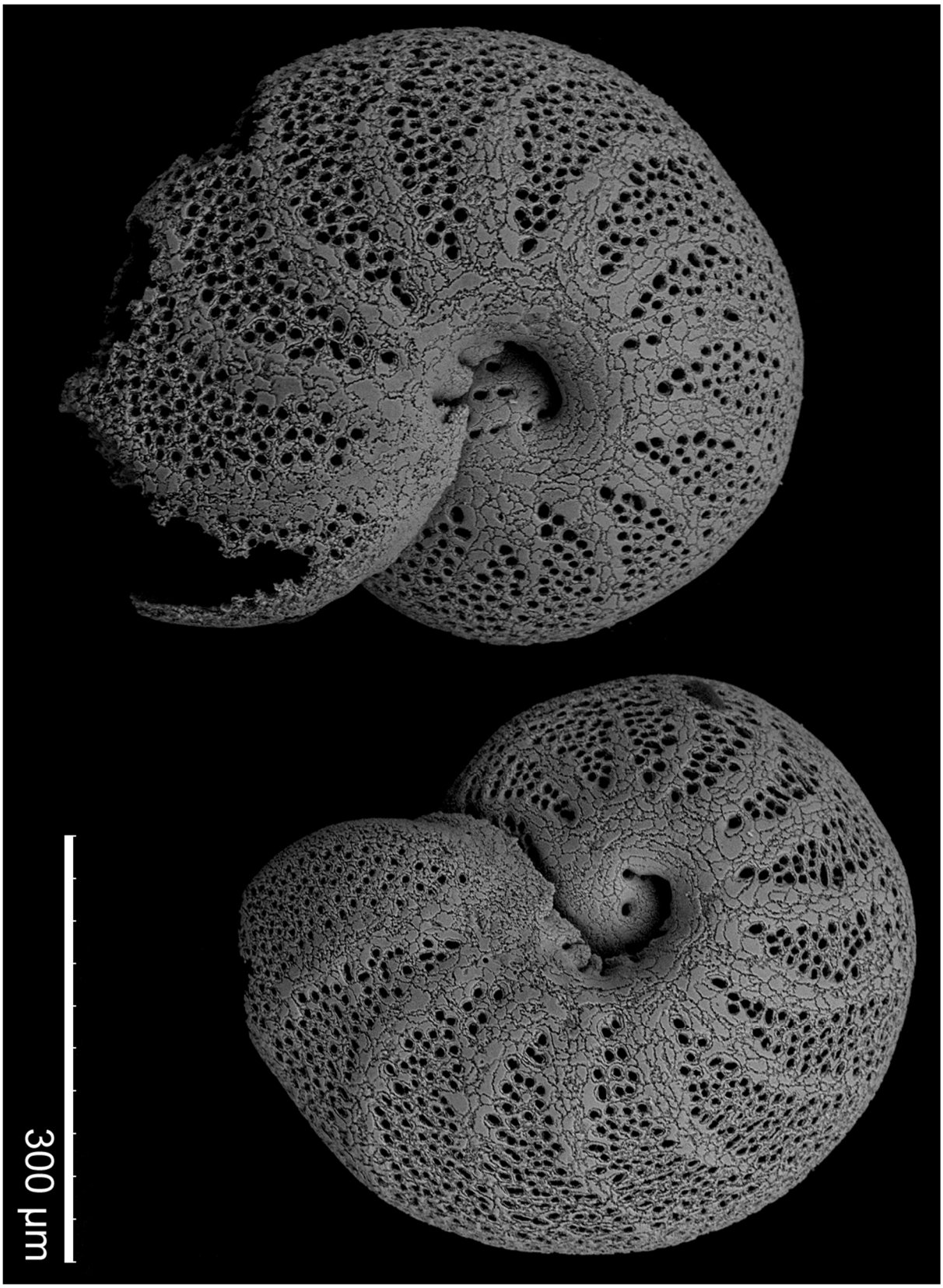

Figure A.5. Non-DTPA-cleaned *M. barleeanus* (core BC387-2).

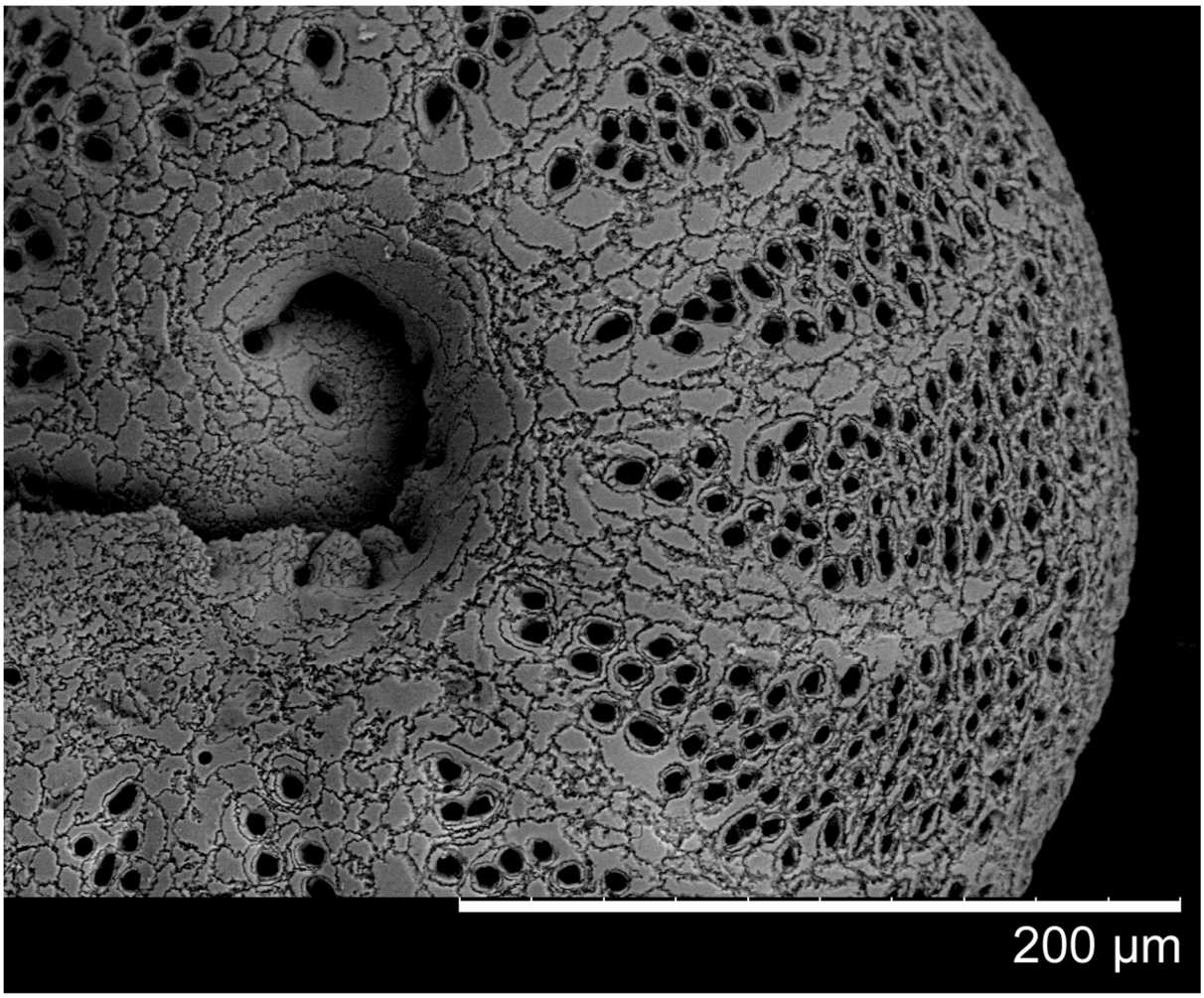

Figure A.6. Non-DTPA-cleaned *M. barleeanus* (core BC387-2).

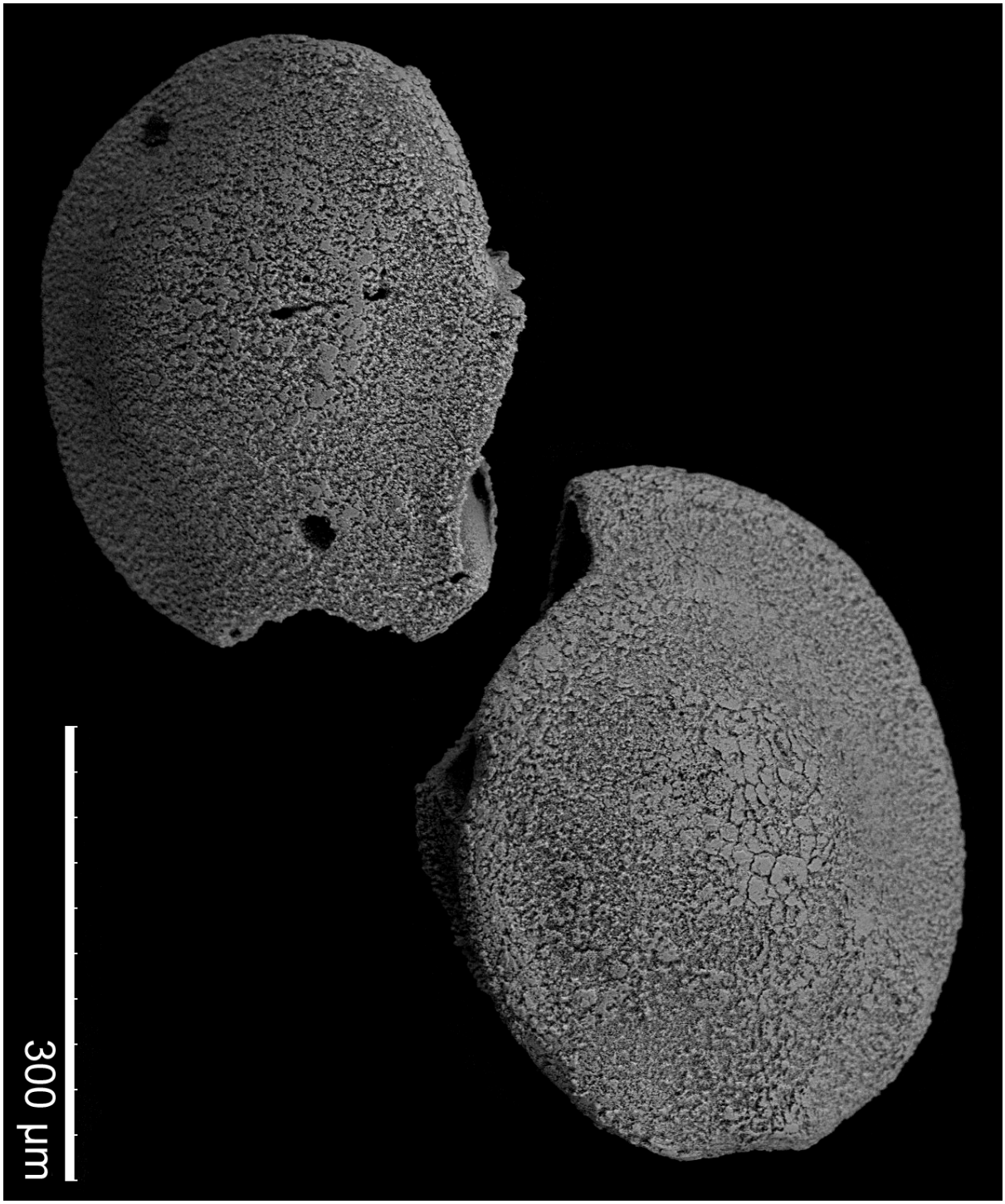

Figure A.7. Non-DTPA-cleaned *O. umbonatus* (core BC387-2).

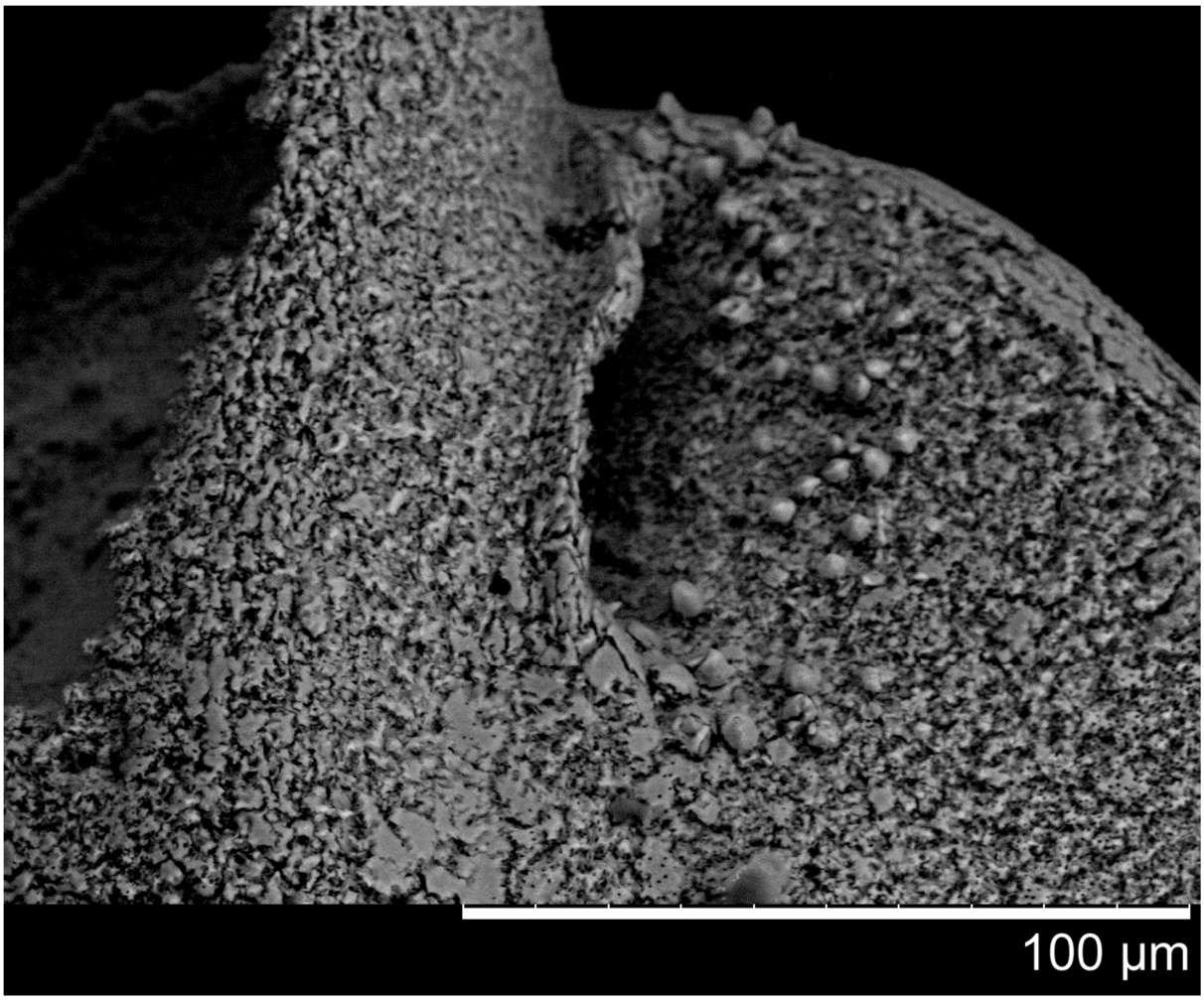

Figure A.8. Non-DTPA-cleaned *O. umbonatus* (core BC387-2).

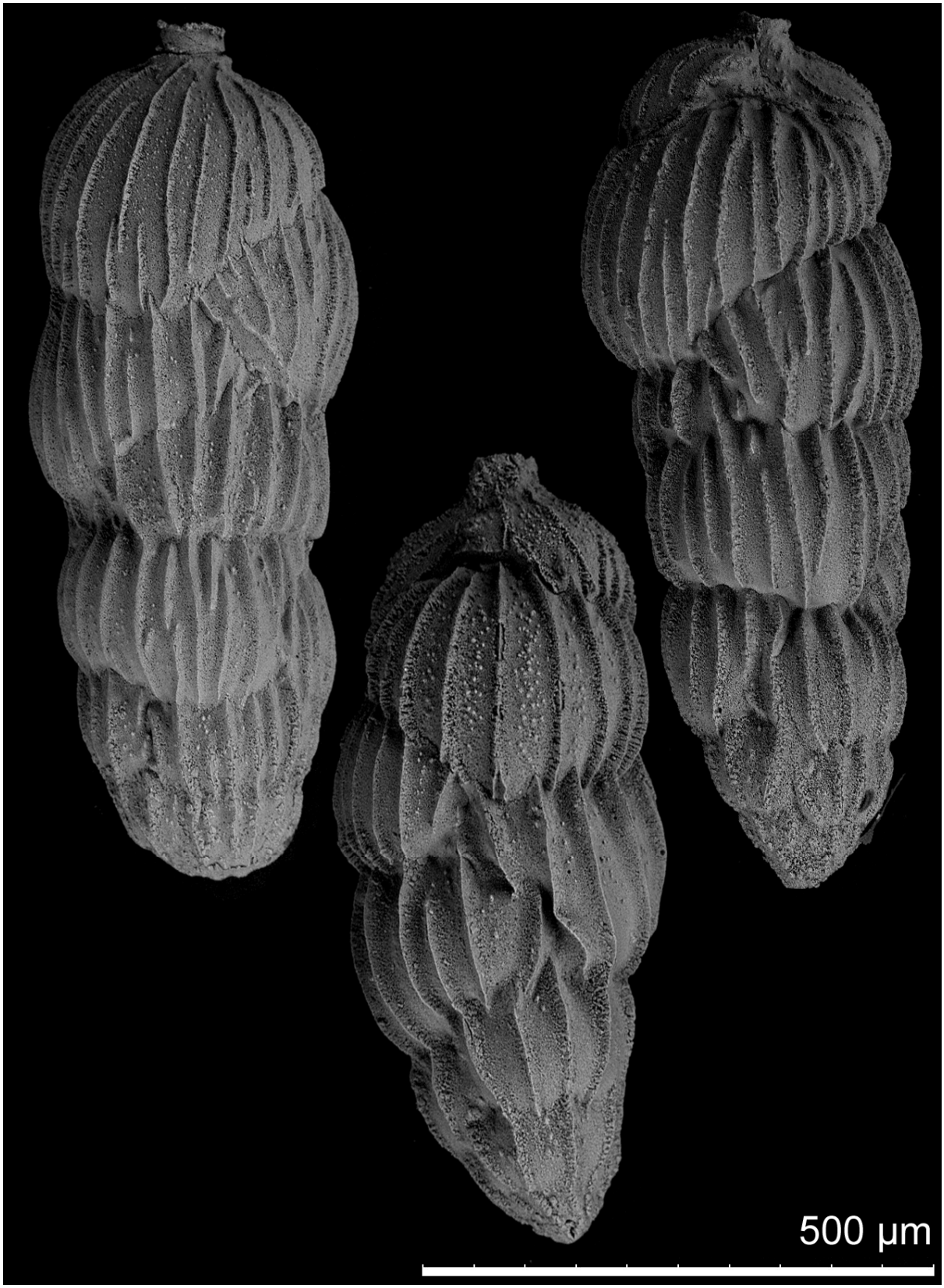

Figure A.9. Non-DTPA-cleaned *U. peregrina* (core BC387-2).

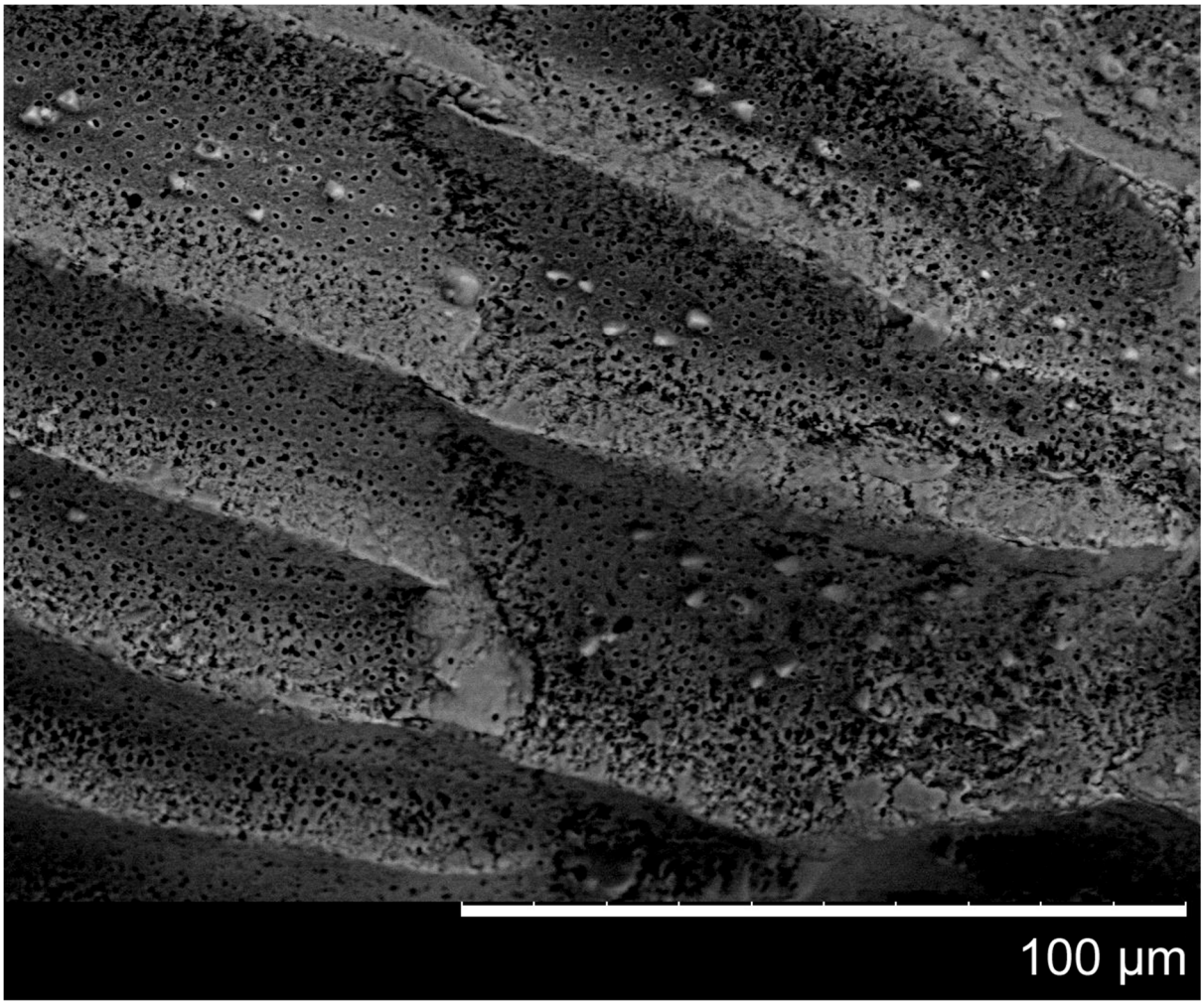

Figure A.10. Non-DTPA-cleaned *U. peregrina* (core BC387-2).

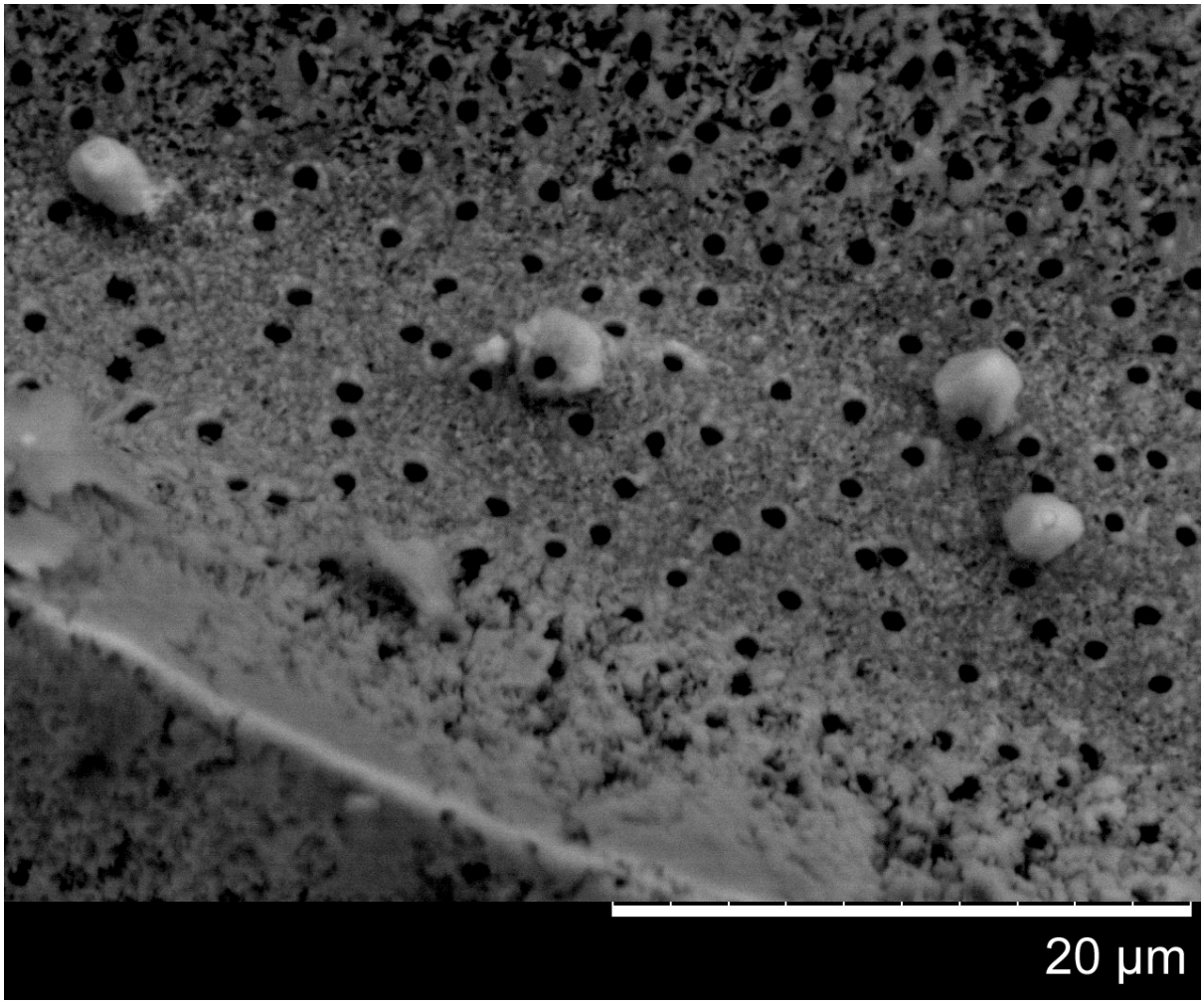

Figure A.11. Non-DTPA-cleaned *U. peregrina* (core BC387-2).

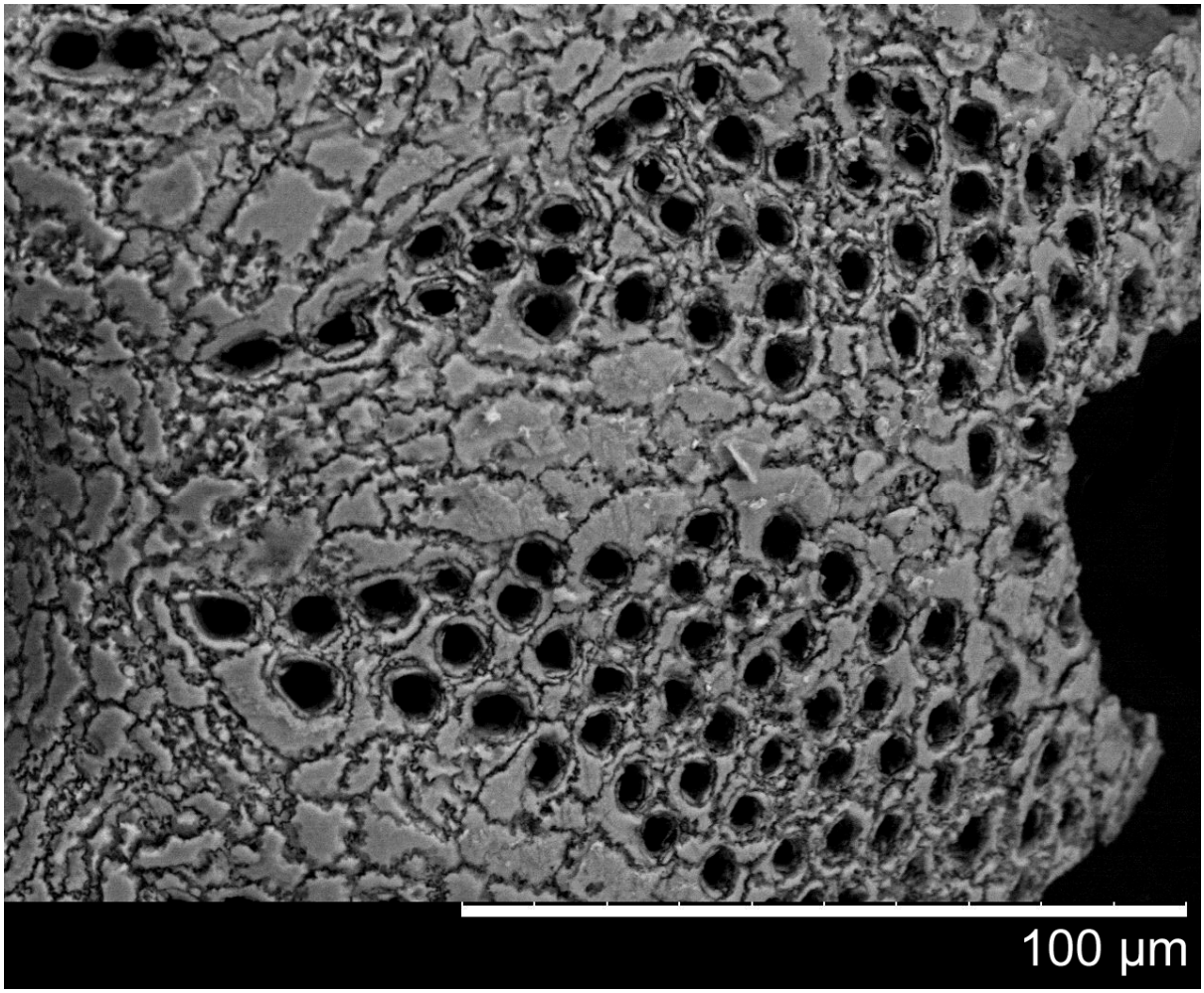

Figure A.12. Fully-cleaned *M. barleeanus* (core BC387-2).

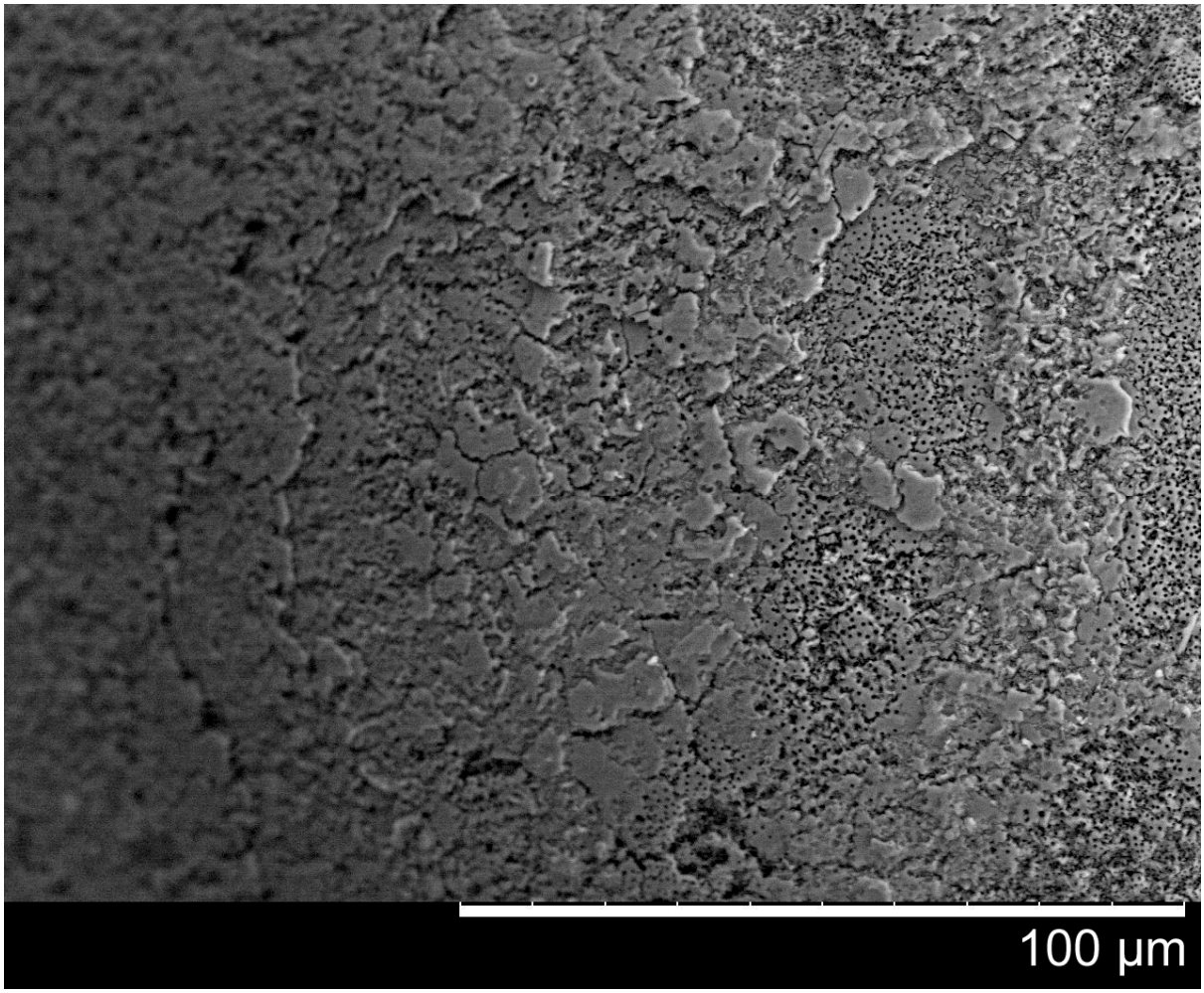

Figure A.13. Fully-cleaned *O. umbonatus* (core BC387-2).

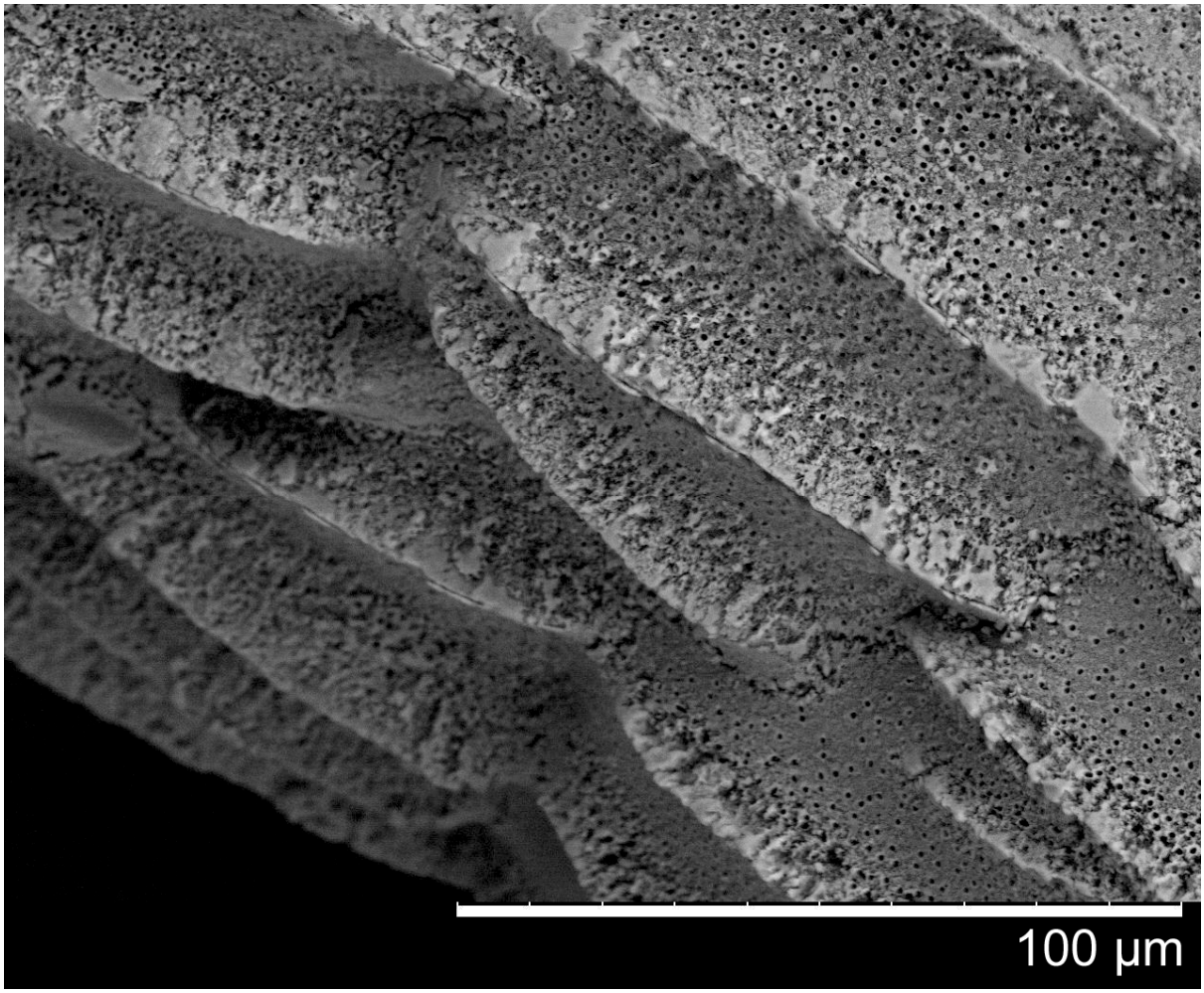

Figure A.14. Fully-cleaned *U. peregrina* (core BC387-2).

Appendix D

Data Tables

Data tables are presented for figures in Chapters 2 to 6, except for where these are included in the main text. Data provided by other authors are not shown. Also omitted are datasets of very high resolution: RGB colour data for sediment core BC387-2 (Figure 3.2); and CTD sensor data (Figure 5.3; Figure 5.4). The following calculated datasets are also not included because they can be regenerated using the equations provided: age-depth plots for various sedimentation rates (Figure 3.10); the effect of D_{Ba} on calculated seawater [Ba] and alkalinity (Figure 3.13); and the effect of seawater [Ba] on calculated D_{Ba} (Figure 3.17).

Table A.5. Data plotted in Figure 2.2.

Measured $^{43}Ca \pm 2\sigma$ (cps)	Solution [Ca] (ppm)
$3.39 \times 10^5 \pm 8.35 \times 10^3$	1
$1.69 \times 10^6 \pm 1.24 \times 10^4$	5
$3.96 \times 10^6 \pm 1.29 \times 10^4$	10
$8.16 \times 10^6 \pm 9.34 \times 10^4$	20
σ = internal precision.	

Table A.6. Data plotted in Figure 2.6.

Depth (cm)	Ba/Ca ± 2σ (µmol/mol)	Mn/Ca ± 2σ (µmol/mol)	Al/Ca ± 2σ (µmol/mol)	Matrix effect ± 2σ for Ba/Ca (%)
Sediment core BC387-2, *M. barleeanus*				
2.5	3.88 ± 0.16	1.82 ± 0.56	54.81 ± 3.38	–0.91 ± 2.55
4.5	3.71 ± 0.21	1.92 ± 0.12	17.74 ± 1.96	–3.00 ± 3.79
7.5	3.56 ± 0.16	2.11 ± 0.60	43.04 ± 2.73	5.82 ± 3.61
14.5	3.51 ± 0.15	2.01 ± 0.23	1.90 ± 1.85	–3.00 ± 1.98
14.5	3.46 ± 0.14	1.80 ± 0.28	43.35 ± 2.59	–0.26 ± 1.97
16.5	3.04 ± 0.14	2.04 ± 0.23	< LoD	1.00 ± 3.44
16.5	3.81 ± 0.14	2.51 ± 0.41	41.33 ± 2.33	5.25 ± 3.08
22.5	3.52 ± 0.47	2.33 ± 0.34	33.56 ± 3.87	5.00 ± 8.39
24.5	3.21 ± 0.12	2.01 ± 0.33	< LoD	–1.00 ± 2.34
Sediment core BC387-2, *O. umbonatus*				
0.5	1.91 ± 0.07	1.24 ± 0.20	34.22 ± 2.65	–4.00 ± 1.52

Depth (cm)	Ba/Ca ± 2σ (μmol/mol)	Mn/Ca ± 2σ (μmol/mol)	Al/Ca ± 2σ (μmol/mol)	Matrix effect ± 2σ for Ba/Ca (%)
2.5	1.86 ± 0.10	1.25 ± 0.20	30.72 ± 3.26	–2.00 ± 2.10
4.5	1.84 ± 0.05	1.47 ± 0.17	< LoD	–4.00 ± 0.63
8.5	2.15 ± 0.20	1.98 ± 0.18	4.20 ± 0.92	6.00 ± 6.57
8.5	1.88 ± 0.18	1.29 ± 0.27	7.05 ± 1.49	8.62 ± 5.40
12.5	1.87 ± 0.09	1.73 ± 0.17	< LoD	5.00 ± 1.80
16.5	1.90 ± 0.06	1.67 ± 0.19	< LoD	–2.00 ± 0.71
16.5	2.01 ± 0.18	1.80 ± 0.38	8.37 ± 1.65	–4.72 ± 4.71
20.5	1.88 ± 0.14	1.90 ± 0.47	5.34 ± 1.46	8.68 ± 1.93
Sediment core BC387-2, *U. peregrina*				
5.5	2.32 ± 0.13	1.27 ± 0.50	4.76 ± 1.71	2.61 ± 1.39
7.5	2.46 ± 0.09	1.59 ± 0.10	3.11 ± 1.01	6.56 ± 1.88
9.5	2.37 ± 0.13	2.16 ± 0.36	5.69 ± 0.77	–0.87 ± 2.98
11.5	2.45 ± 0.11	1.65 ± 0.46	4.75 ± 1.53	7.73 ± 1.68
15.5	2.42 ± 0.08	1.46 ± 0.57	6.36 ± 2.17	3.13 ± 1.29
17.5	2.49 ± 0.14	1.15 ± 0.48	4.82 ± 1.51	1.78 ± 4.18
18.5	2.53 ± 0.14	1.12 ± 0.16	< LoD	17.00 ± 4.33
23.5	2.40 ± 0.10	1.46 ± 0.43	4.13 ± 1.46	12.37 ± 3.32
Sediment core GC528, *M. barleeanus*				
4.5	3.33 ± 0.07	1.84 ± 0.28	28.15 ± 3.20	1.94 ± 1.09
8.5	3.38 ± 0.15	1.75 ± 0.12	34.04 ± 1.88	21.67 ± 3.24
16.5	5.17 ± 0.27	2.85 ± 0.25	46.38 ± 3.16	–3.30 ± 2.35
24.5	3.54 ± 0.20	4.01 ± 0.24	42.59 ± 1.35	1.68 ± 0.97
28.5	3.51 ± 0.30	4.12 ± 0.26	34.01 ± 1.85	15.99 ± 3.95
32.5	3.75 ± 0.18	3.66 ± 0.33	45.62 ± 2.27	–16.76 ± 2.27
36.5	3.66 ± 0.27	4.72 ± 0.35	45.26 ± 3.38	19.39 ± 5.61
38.5	3.60 ± 0.13	3.86 ± 0.29	37.74 ± 1.80	4.54 ± 1.71
41.5	3.60 ± 0.21	4.46 ± 0.27	48.05 ± 1.75	9.17 ± 4.23
44.5	3.78 ± 0.31	5.98 ± 0.62	40.75 ± 2.95	14.13 ± 5.70
46.5	3.64 ± 0.09	4.49 ± 0.58	27.93 ± 2.19	3.15 ± 2.06
48.5	3.61 ± 0.11	5.12 ± 0.29	25.08 ± 0.46	5.22 ± 0.94
52.5	3.81 ± 0.12	3.05 ± 0.24	34.52 ± 1.16	21.70 ± 2.21
54.5	3.35 ± 0.21	2.19 ± 0.20	27.94 ± 1.86	18.79 ± 4.89
56.5	3.42 ± 0.26	2.97 ± 0.22	41.44 ± 2.03	23.74 ± 6.39
58.5	3.33 ± 0.14	3.92 ± 0.29	26.56 ± 1.52	4.73 ± 0.81

Depth (cm)	Ba/Ca ± 2σ (μmol/mol)	Mn/Ca ± 2σ (μmol/mol)	Al/Ca ± 2σ (μmol/mol)	Matrix effect ± 2σ for Ba/Ca (%)
62.5	3.66 ± 0.29	4.10 ± 0.57	34.09 ± 1.80	9.20 ± 2.50
Sediment core GC642, *M. barleeanus*				
22.5	4.10 ± 0.19	32.12 ± 1.40	54.84 ± 2.24	3.17 ± 2.99
26.5	4.04 ± 0.17	24.29 ± 1.26	37.78 ± 1.87	–6.51 ± 1.51
28.5	4.17 ± 0.28	27.70 ± 1.35	43.51 ± 1.42	–0.04 ± 1.94
30.5	4.04 ± 0.11	26.86 ± 2.48	48.10 ± 3.04	–4.09 ± 2.11
32.5	4.19 ± 0.21	25.81 ± 1.74	45.15 ± 2.04	–7.76 ± 0.52
38.5	3.62 ± 0.21	22.15 ± 1.13	48.43 ± 2.16	3.76 ± 1.24

σ = internal precision. < LoD = below limit of detection. Depths are mid-points (± 0.5 cm).

Table A.7. Data plotted in Figure 2.7.

Depth (cm)	Mg/Ca ± 2σ (mmol/mol)	Mn/Ca ± 2σ (μmol/mol)	Al/Ca ± 2σ (μmol/mol)	Matrix effect ± 2σ for Mg/Ca (%)
Sediment core BC387-2, *M. barleeanus*				
1.5	0.80 ± 0.07	2.23 ± 0.61	< LoD	–12.00 ± 3.88
4.5	1.03 ± 0.07	1.92 ± 0.12	17.74 ± 1.96	–3.00 ± 3.79
7.5	0.92 ± 0.03	2.00 ± 0.49	42.36 ± 2.03	5.34 ± 2.39
9.5	0.86 ± 0.07	2.57 ± 0.33	< LoD	12.00 ± 6.52
12.5	0.90 ± 0.05	2.29 ± 0.13	30.82 ± 3.92	–16.00 ± 2.57
14.5	0.92 ± 0.04	2.01 ± 0.23	1.90 ± 1.85	–3.00 ± 1.98
14.5	0.83 ± 0.03	1.80 ± 0.28	43.35 ± 2.59	–0.26 ± 1.97
16.5	0.82 ± 0.05	2.04 ± 0.23	< LoD	1.00 ± 3.44
16.5	0.81 ± 0.03	2.51 ± 0.41	41.33 ± 2.33	5.25 ± 3.08
22.5	0.99 ± 0.11	2.33 ± 0.34	33.56 ± 3.87	5.00 ± 8.39
24.5	0.90 ± 0.07	2.01 ± 0.33	< LoD	–1.00 ± 2.34
24.5	0.81 ± 0.09	1.84 ± 0.65	< LoD	13.00 ± 6.44
Sediment core BC387-2, *O. umbonatus*				
0.5	1.45 ± 0.04	1.24 ± 0.20	34.22 ± 2.65	–4.00 ± 1.52
2.5	1.38 ± 0.05	1.25 ± 0.20	30.72 ± 3.26	–2.00 ± 2.10
4.5	1.32 ± 0.04	1.47 ± 0.17	< LoD	–4.00 ± 0.63
8.5	1.47 ± 0.12	1.98 ± 0.18	4.20 ± 0.92	6.00 ± 6.57
8.5	1.45 ± 0.11	1.53 ± 0.25	6.70 ± 0.62	3.62 ± 3.48

Depth (cm)	Mg/Ca ± 2σ (mmol/mol)	Mn/Ca ± 2σ (µmol/mol)	Al/Ca ± 2σ (µmol/mol)	Matrix effect ± 2σ for Mg/Ca (%)
12.5	1.58 ± 0.07	1.73 ± 0.17	< LoD	5.00 ± 1.80
16.5	1.38 ± 0.05	1.67 ± 0.19	< LoD	–2.00 ± 0.71
16.5	1.39 ± 0.08	1.97 ± 0.56	8.38 ± 2.42	2.42 ± 4.07
20.5	1.38 ± 0.06	1.90 ± 0.47	5.34 ± 1.46	8.68 ± 1.93
22.5	1.43 ± 0.09	2.23 ± 0.20	17.99 ± 3.10	–16.00 ± 0.95
Sediment core BC387-2, *U. peregrina*				
0.5	0.99 ± 0.05	2.47 ± 0.17	< LoD	–4.00 ± 1.93
5.5	1.01 ± 0.04	1.27 ± 0.50	4.76 ± 1.71	2.61 ± 1.39
6.5	0.97 ± 0.03	1.15 ± 0.12	< LoD	–4.00 ± 1.21
7.5	1.09 ± 0.02	1.37 ± 0.24	3.23 ± 2.60	–0.19 ± 0.79
9.5	1.04 ± 0.09	2.16 ± 0.36	5.69 ± 0.77	–0.87 ± 2.98
10.5	1.03 ± 0.07	1.61 ± 0.26	7.30 ± 0.98	–5.00 ± 4.84
11.5	1.04 ± 0.04	1.83 ± 0.44	5.63 ± 0.24	1.23 ± 1.82
15.5	1.13 ± 0.05	1.46 ± 0.57	6.36 ± 2.17	3.13 ± 1.29
17.5	0.93 ± 0.04	1.12 ± 0.59	4.87 ± 1.23	–5.50 ± 0.77
18.5	1.09 ± 0.05	1.12 ± 0.16	< LoD	17.00 ± 4.33
23.5	1.05 ± 0.04	1.31 ± 0.17	3.16 ± 1.47	10.69 ± 4.10
Sediment core GC528, *M. barleeanus*				
4.5	0.81 ± 0.02	1.84 ± 0.28	28.15 ± 3.20	1.94 ± 1.09
8.5	0.85 ± 0.05	1.75 ± 0.12	34.04 ± 1.88	21.67 ± 3.24
16.5	0.92 ± 0.04	2.85 ± 0.25	46.38 ± 3.16	–3.30 ± 2.35
24.5	0.86 ± 0.03	4.01 ± 0.24	42.59 ± 1.35	1.68 ± 0.97
28.5	0.86 ± 0.04	4.12 ± 0.26	34.01 ± 1.85	15.99 ± 3.95
32.5	0.88 ± 0.03	3.66 ± 0.33	45.62 ± 2.27	–18.32 ± 2.33
36.5	0.91 ± 0.05	4.72 ± 0.35	45.26 ± 3.38	19.39 ± 5.61
38.5	0.93 ± 0.03	3.86 ± 0.29	37.74 ± 1.80	–0.06 ± 1.72
41.5	0.88 ± 0.05	4.46 ± 0.27	48.05 ± 1.75	9.17 ± 4.23
44.5	0.93 ± 0.05	5.98 ± 0.62	40.75 ± 2.95	10.75 ± 4.74
46.5	0.89 ± 0.04	4.49 ± 0.58	27.93 ± 2.19	3.15 ± 2.06
48.5	0.84 ± 0.02	5.12 ± 0.29	25.08 ± 0.46	5.22 ± 0.94
52.5	0.87 ± 0.02	3.05 ± 0.24	34.52 ± 1.16	17.83 ± 1.10
54.5	0.87 ± 0.05	2.19 ± 0.20	27.94 ± 1.86	22.20 ± 1.72
56.5	0.94 ± 0.06	2.97 ± 0.22	41.44 ± 2.03	24.00 ± 4.86
58.5	0.90 ± 0.01	3.92 ± 0.29	26.56 ± 1.52	4.73 ± 0.81

Depth (cm)	Mg/Ca ± 2σ (mmol/mol)	Mn/Ca ± 2σ (µmol/mol)	Al/Ca ± 2σ (µmol/mol)	Matrix effect ± 2σ for Mg/Ca (%)
62.5	1.01 ± 0.04	4.10 ± 0.57	34.09 ± 1.80	9.20 ± 2.50
Sediment core GC642, *M. barleeanus*				
22.5	1.19 ± 0.02	32.12 ± 1.40	54.84 ± 2.24	–0.91 ± 0.74
26.5	1.18 ± 0.03	24.29 ± 1.26	37.78 ± 1.87	–6.51 ± 1.51
28.5	1.19 ± 0.04	27.70 ± 1.35	43.51 ± 1.42	–3.99 ± 2.02
30.5	1.23 ± 0.03	26.86 ± 2.48	48.10 ± 3.04	–4.09 ± 2.11
32.5	1.16 ± 0.06	25.81 ± 1.74	45.15 ± 2.04	–7.76 ± 0.52
38.5	1.09 ± 0.02	22.15 ± 1.13	48.43 ± 2.16	3.76 ± 1.24

σ = internal precision. < LoD = below limit of detection. Depths are mid-points (± 0.5 cm).

Table A.8. Data plotted in Figure 2.8.

Depth (cm)	Sr/Ca ± 2σ (mmol/mol)	Mn/Ca ± 2σ (µmol/mol)	Al/Ca ± 2σ (µmol/mol)	Matrix effect ± 2σ for Sr/Ca (%)
Sediment core BC387-2, *M. barleeanus*				
4.5	1.25 ± 0.08	1.92 ± 0.12	17.74 ± 1.96	–3.00 ± 3.79
7.5	1.25 ± 0.04	2.00 ± 0.49	42.36 ± 2.03	5.34 ± 2.39
14.5	1.25 ± 0.04	2.01 ± 0.23	1.90 ± 1.85	–3.00 ± 1.98
14.5	1.25 ± 0.03	1.80 ± 0.28	43.35 ± 2.59	–0.26 ± 1.97
16.5	1.24 ± 0.07	2.04 ± 0.23	< LoD	1.00 ± 3.44
16.5	1.26 ± 0.03	2.38 ± 0.46	41.80 ± 3.40	5.61 ± 2.09
22.5	1.28 ± 0.17	2.33 ± 0.34	33.56 ± 3.87	5.00 ± 8.39
24.5	1.24 ± 0.04	2.01 ± 0.33	< LoD	–1.00 ± 2.34
Sediment core BC387-2, *O. umbonatus*				
0.5	1.00 ± 0.02	1.24 ± 0.20	34.22 ± 2.65	–4.00 ± 1.52
2.5	1.00 ± 0.03	1.25 ± 0.20	30.72 ± 3.26	–2.00 ± 2.10
4.5	0.99 ± 0.01	1.47 ± 0.17	< LoD	–4.00 ± 0.63
8.5	0.99 ± 0.10	1.98 ± 0.18	4.20 ± 0.92	6.00 ± 6.57
8.5	0.99 ± 0.04	1.53 ± 0.25	6.70 ± 0.62	3.62 ± 3.48
12.5	0.99 ± 0.03	1.73 ± 0.17	< LoD	5.00 ± 1.80
16.5	0.99 ± 0.01	1.67 ± 0.19	< LoD	–2.00 ± 0.71
16.5	0.96 ± 0.05	1.97 ± 0.56	8.38 ± 2.42	2.42 ± 4.07
20.5	1.01 ± 0.03	1.90 ± 0.47	5.34 ± 1.46	8.68 ± 1.93

Depth (cm)	Sr/Ca ± 2σ (mmol/mol)	Mn/Ca ± 2σ (µmol/mol)	Al/Ca ± 2σ (µmol/mol)	Matrix effect ± 2σ for Sr/Ca (%)
22.5	1.02 ± 0.07	2.23 ± 0.20	17.99 ± 3.10	–16.00 ± 0.95
Sediment core BC387-2, *U. peregrina*				
0.5	1.03 ± 0.03	2.47 ± 0.17	< LoD	–4.00 ± 1.93
5.5	1.06 ± 0.03	1.27 ± 0.50	4.76 ± 1.71	2.61 ± 1.39
6.5	1.02 ± 0.02	1.15 ± 0.12	< LoD	–4.00 ± 1.21
7.5	1.05 ± 0.04	1.37 ± 0.24	3.23 ± 2.60	–0.19 ± 0.79
9.5	1.05 ± 0.05	2.16 ± 0.36	5.69 ± 0.77	–0.87 ± 2.98
10.5	1.09 ± 0.07	1.61 ± 0.26	7.30 ± 0.98	–5.00 ± 4.84
11.5	1.07 ± 0.03	1.83 ± 0.44	5.63 ± 0.24	1.23 ± 1.82
15.5	1.06 ± 0.02	1.46 ± 0.57	6.36 ± 2.17	3.13 ± 1.29
17.5	1.03 ± 0.03	1.12 ± 0.59	4.87 ± 1.23	–5.50 ± 0.77
18.5	1.05 ± 0.06	1.12 ± 0.16	< LoD	17.00 ± 4.33
23.5	1.03 ± 0.04	1.46 ± 0.43	4.13 ± 1.46	12.37 ± 3.32
Sediment core GC528, *M. barleeanus*				
4.5	1.23 ± 0.02	1.84 ± 0.28	28.15 ± 3.20	1.94 ± 1.09
8.5	1.25 ± 0.06	1.75 ± 0.12	34.04 ± 1.88	21.67 ± 3.24
16.5	1.24 ± 0.04	2.85 ± 0.25	46.38 ± 3.16	–3.30 ± 2.35
24.5	1.26 ± 0.03	4.01 ± 0.24	42.59 ± 1.35	1.68 ± 0.97
28.5	1.23 ± 0.05	4.12 ± 0.26	34.01 ± 1.85	10.96 ± 4.18
32.5	1.24 ± 0.04	3.66 ± 0.33	45.62 ± 2.27	–18.32 ± 2.33
36.5	1.28 ± 0.08	4.72 ± 0.35	45.26 ± 3.38	17.59 ± 5.13
38.5	1.24 ± 0.03	3.86 ± 0.29	37.74 ± 1.80	4.54 ± 1.71
41.5	1.25 ± 0.08	4.46 ± 0.27	48.05 ± 1.75	4.05 ± 2.23
44.5	1.25 ± 0.08	5.98 ± 0.62	40.75 ± 2.95	14.13 ± 5.70
46.5	1.25 ± 0.04	4.49 ± 0.58	27.93 ± 2.19	3.15 ± 2.06
48.5	1.22 ± 0.02	5.12 ± 0.29	25.08 ± 0.46	–0.40 ± 1.39
52.5	1.27 ± 0.03	3.05 ± 0.24	34.52 ± 1.16	17.83 ± 1.10
54.5	1.25 ± 0.06	2.19 ± 0.20	27.94 ± 1.86	23.93 ± 3.41
56.5	1.23 ± 0.07	2.97 ± 0.22	41.44 ± 2.03	24.00 ± 4.86
58.5	1.25 ± 0.02	3.92 ± 0.29	26.56 ± 1.52	4.73 ± 0.81
62.5	1.27 ± 0.04	4.10 ± 0.57	34.09 ± 1.80	9.20 ± 2.50
Sediment core GC642, *M. barleeanus*				
22.5	1.26 ± 0.01	32.12 ± 1.40	54.84 ± 2.24	–0.91 ± 0.74
26.5	1.27 ± 0.03	24.29 ± 1.26	37.78 ± 1.87	–6.51 ± 1.51

Depth (cm)	Sr/Ca ± 2σ (mmol/mol)	Mn/Ca ± 2σ (µmol/mol)	Al/Ca ± 2σ (µmol/mol)	Matrix effect ± 2σ for Sr/Ca (%)
28.5	1.27 ± 0.02	27.70 ± 1.35	43.51 ± 1.42	0.91 ± 0.82
30.5	1.30 ± 0.08	26.86 ± 2.48	48.10 ± 3.04	–4.09 ± 2.11
32.5	1.25 ± 0.03	25.81 ± 1.74	45.15 ± 2.04	–7.76 ± 0.52
38.5	1.26 ± 0.04	22.15 ± 1.13	48.43 ± 2.16	3.76 ± 1.24

σ = internal precision. < LoD = below limit of detection. Depths are mid-points (± 0.5 cm).

Table A.9. Consistency standard measurements plotted in Figure 2.9, Figure 2.10, Figure 2.11, Figure 2.12 and Figure 2.13. The short- and long-term precision calculated from these values are provided in Table 2.5 and Table 2.6.

	Start of run	Middle of run	End of run
21st March 2015			
Ba/Ca ± 2σ (µmol/mol)	N/A	N/A	1.20 ± 0.06
Mg/Ca ± 2σ (mmol/mol)	N/A	N/A	4.49 ± 0.17
Sr/Ca ± 2σ (mmol/mol)	N/A	N/A	1.26 ± 0.05
29th March 2015			
Ba/Ca ± 2σ (µmol/mol)	1.05 ± 0.10	N/A	1.07 ± 0.03
Mg/Ca ± 2σ (mmol/mol)	4.44 ± 0.31	N/A	4.42 ± 0.11
Sr/Ca ± 2σ (mmol/mol)	1.25 ± 0.09	N/A	1.26 ± 0.03
19th April 2015			
Ba/Ca ± 2σ (µmol/mol)	1.23 ± 0.29	1.11 ± 0.20	1.14 ± 1.14
Mg/Ca ± 2σ (mmol/mol)	4.63 ± 1.06	4.45 ± 0.99	4.46 ± 4.46
Sr/Ca ± 2σ (mmol/mol)	1.26 ± 0.25	1.25 ± 0.24	1.26 ± 1.26
24th May 2015			
Mg/Ca ± 2σ (mmol/mol)	4.49 ± 0.21	N/A	4.53 ± 1.06
Sr/Ca ± 2σ (mmol/mol)	1.26 ± 0.11	N/A	1.17 ± 0.89
26th June 2015			
Mg/Ca ± 2σ (mmol/mol)	4.60 ± 2.78	4.60 ± 0.52	4.48 ± 0.59
Sr/Ca ± 2σ (mmol/mol)	1.26 ± 0.74	1.27 ± 0.18	1.27 ± 0.19
11th July 2015			
Mg/Ca ± 2σ (mmol/mol)	4.41 ± 0.42	4.41 ± 0.19	4.49 ± 0.21
18th November 2015			
Ba/Ca ± 2σ (µmol/mol)	1.36 ± 0.18	1.38 ± 0.10	1.32 ± 0.09

	Start of run	Middle of run	End of run
Mg/Ca ± 2σ (mmol/mol)	4.54 ± 0.13	4.46 ± 0.14	4.50 ± 0.17
Sr/Ca ± 2σ (mmol/mol)	1.26 ± 0.03	1.26 ± 0.02	1.28 ± 0.03
23rd November 2015			
Ba/Ca ± 2σ (µmol/mol)	1.54 ± 0.18	1.67 ± 0.27	1.61 ± 0.11
Mg/Ca ± 2σ (mmol/mol)	4.28 ± 0.48	4.56 ± 0.46	4.50 ± 0.13
Sr/Ca ± 2σ (mmol/mol)	1.25 ± 0.16	1.34 ± 0.16	1.26 ± 0.07
4th February 2016			
Ba/Ca ± 2σ (µmol/mol)	1.17 ± 0.11	1.24 ± 0.12	1.23 ± 0.12
Mg/Ca ± 2σ (mmol/mol)	4.49 ± 0.20	4.54 ± 0.15	4.40 ± 0.25
Sr/Ca ± 2σ (mmol/mol)	1.27 ± 0.04	1.27 ± 0.04	1.27 ± 0.07

σ = internal precision.

Table A.10. Interlaboratory comparison measurements plotted in Figure 2.14.

	Ba/Ca ± 2σ (µmol/mol) [a]	Ba/Ca ± 2σ (µmol/mol) [b]	Mg/Ca ± 2σ (mmol/mol) [b]	Sr/Ca ± 2σ (mmol/mol) [b]
Measured at the Bristol Isotope Group in the School of Earth Sciences, University of Bristol				
	0.67 ± 0.12	2.15 ± 0.07	1.47 ± 0.06	1.01 ± 0.04
Measured at the School of Earth and Ocean Sciences, Cardiff University				
		2.12 ± 0.10	1.43 ± 0.07	0.99 ± 0.04
Measured at the Department of Marine Chemistry and Geochemistry, Woods Hole Oceanographic Institution				
	0.63 [c]			

a) *Orbulina universa* (S0157); b) *Oridorsalis umbonatus* (BC387-2)

c) No error bar is shown for this measurement because the internal precision resulting from this technique was sufficiently small as to be negligible (Dr T. Horner, pers. com. 2015).

See Table 2.7 for further details of measurement techniques.

Table A.11. Data plotted in Figure 3.5, Figure 3.14, Figure 3.18 and Figure 6.2.

Depth (cm)	Ba/Ca ± 2σ (μmol/mol)	Mg/Ca ± 2σ (mmol/mol)	Sr/Ca ± 2σ (mmol/mol)	Temperature ± 2σ (° C)	$\delta^{18}O$ ± 2σ (‰)	$\delta^{13}C$ ± 2σ (‰)
Sediment core BC387-2, *M. barleeanus*						
1.5		0.80 ± 0.07		1.44 ± 1.01	2.34 ± 0.05	–1.10 ± 0.04
2.5	3.88 ± 0.16					
3.5					2.42 ± 0.08	–0.98 ± 0.03
4.5	3.71 ± 0.21	1.03 ± 0.07	1.25 ± 0.08	3.26 ± 0.70	2.48 ± 0.05	–0.63 ± 0.02
5.5					2.52 ± 0.07	–0.94 ± 0.03
7.5	3.56 ± 0.16	0.92 ± 0.03	1.25 ± 0.04	2.48 ± 0.32		
8.5					2.44 ± 0.08	–0.75 ± 0.02
9.5		0.86 ± 0.07		1.98 ± 0.94		
11.5					2.52 ± 0.07	–0.59 ± 0.06
12.5		0.90 ± 0.05		2.29 ± 0.63		
14.5	3.51 ± 0.15	0.92 ± 0.04	1.25 ± 0.04	2.46 ± 0.42	2.40 ± 0.06	–0.75 ± 0.05
14.5	3.46 ± 0.14	0.83 ± 0.03	1.25 ± 0.03	1.71 ± 0.40		
16.5	3.04 ± 0.14	0.82 ± 0.05	1.24 ± 0.07	1.61 ± 0.71		
16.5	3.81 ± 0.14	0.81 ± 0.03	1.26 ± 0.03	1.51 ± 0.47		
17.5					2.51 ± 0.10	–0.61 ± 0.06
20.5				2.98 ± 1.18	2.44 ± 0.10	–0.67 ± 0.05
22.5	3.52 ± 0.47	0.99 ± 0.11	1.28 ± 0.17			
23.5					2.46 ± 0.06	–0.67 ± 0.06
24.5	3.21 ± 0.12	0.90 ± 0.07	1.24 ± 0.04	2.32 ± 0.88		
24.5		0.81 ± 0.09		1.51 ± 1.25		

Depth (cm)	Ba/Ca ± 2σ (μmol/mol)	Mg/Ca ± 2σ (mmol/mol)	Sr/Ca ± 2σ (mmol/mol)	Temperature ± 2σ (° C)	$\delta^{18}O$ ± 2σ (‰)	$\delta^{13}C$ ± 2σ (‰)
Sediment core BC387-2, *O. umbonatus*						
0.5	1.91 ± 0.07	1.45 ± 0.04	1.00 ± 0.02	3.01 ± 0.23 [a] or 2.02 ± 0.32 [b]		
1.5					2.94 ± 0.05	–0.63 ± 0.06
2.5	1.86 ± 0.10	1.38 ± 0.05	1.00 ± 0.03	2.55 ± 0.31 [a] or 1.41 ± 0.42 [b]		
3.5					2.85 ± 0.06	–0.71 ± 0.03
4.5	1.84 ± 0.05	1.32 ± 0.04	0.99 ± 0.01	2.17 ± 0.28 [a] or 0.91 ± 0.36 [b]	3.07 ± 0.09	–0.63 ± 0.06
5.5					2.99 ± 0.07	–0.34 ± 0.04
8.5	2.15 ± 0.20	1.47 ± 0.12	0.99 ± 0.10	3.11 ± 0.72 [a] or 2.17 ± 1.04 [b]	3.08 ± 0.12	–0.48 ± 0.05
8.5	1.88 ± 0.18	1.45 ± 0.11	0.99 ± 0.04	2.99 ± 0.62 [a] or 1.99 ± 0.89 [b]		
11.5					3.03 ± 0.09	–0.46 ± 0.06
12.5	1.87 ± 0.09	1.58 ± 0.07	0.99 ± 0.03	3.77 ± 0.39 [a] or 3.12 ± 0.60 [b]		
14.5					2.99 ± 0.06	–0.31 ± 0.04
16.5	1.90 ± 0.06	1.38 ± 0.05	0.99 ± 0.01	2.57 ± 0.32 [a] or 1.43 ± 0.44 [b]		
16.5	2.01 ± 0.18	1.39 ± 0.08	0.96 ± 0.05	2.65 ± 0.47 [a] or 1.53 ± 0.64 [b]		
17.5					2.88 ± 0.07	–0.33 ± 0.06
20.5	1.88 ± 0.14	1.38 ± 0.06	1.01 ± 0.03	2.59 ± 0.36 [a] or 1.46 ± 0.50 [b]	2.99 ± 0.07	–0.37 ± 0.05
22.5		1.43 ± 0.09	1.02 ± 0.07	2.85 ± 0.55 [a] or 1.81 ± 0.78 [b]		

Depth (cm)	Ba/Ca ± 2σ (μmol/mol)	Mg/Ca ± 2σ (mmol/mol)	Sr/Ca ± 2σ (mmol/mol)	Temperature ± 2σ (° C)	$\delta^{18}O$ ± 2σ (‰)	$\delta^{13}C$ ± 2σ (‰)
23.5					2.84 ± 0.05	–0.36 ± 0.04
Sediment core BC387-2, *U. peregrina*						
0.5		0.99 ± 0.05	1.03 ± 0.03	1.82 ± 0.70 [c] or 1.22 ± 0.77 [d]		
1.5					3.06 ± 0.06	–0.90 ± 0.05
3.5					3.15 ± 0.05	–0.63 ± 0.03
4.5					2.98 ± 0.06	–0.62 ± 0.03
5.5	2.32 ± 0.13	1.01 ± 0.04	1.06 ± 0.03	2.17 ± 0.54 [c] or 1.60 ± 0.59 [d]	3.12 ± 0.10	–1.02 ± 0.03
6.5		0.97 ± 0.03	1.02 ± 0.02	1.60 ± 0.39 [c] or 0.98 ± 0.42 [d]		
7.5	2.46 ± 0.09	1.09 ± 0.02	1.05 ± 0.04	3.30 ± 0.28 [c] or 2.83 ± 0.31 [d]		
8.5					3.08 ± 0.06	–0.97 ± 0.04
9.5	2.37 ± 0.13	1.04 ± 0.09	1.05 ± 0.05	2.56 ± 1.26 [c] or 2.03 ± 1.37 [d]		
10.5		1.03 ± 0.07	1.09 ± 0.07	2.44 ± 1.04 [c] or 1.89 ± 1.14 [d]		
11.5	2.45 ± 0.11	1.04 ± 0.04	1.07 ± 0.03	2.55 ± 0.50 [c] or 2.02 ± 0.55 [d]	3.10 ± 0.09	–0.56 ± 0.03
14.5					2.98 ± 0.14	–0.60 ± 0.05
15.5	2.42 ± 0.08	1.13 ± 0.05	1.06 ± 0.02	3.75 ± 0.69 [c] or 3.32 ± 0.75 [d]		
17.5	2.49 ± 0.14	0.93 ± 0.04	1.03 ± 0.03	0.97 ± 0.56 [c] or 0.29 ± 0.61 [d]	3.10 ± 0.10	–0.71 ± 0.04
18.5	2.53 ± 0.14	1.09 ± 0.05	1.05 ± 0.06	3.30 ± 0.64 [c] or 2.83 ± 0.70 [d]		

Depth (cm)	Ba/Ca ± 2σ (μmol/mol)	Mg/Ca ± 2σ (mmol/mol)	Sr/Ca ± 2σ (mmol/mol)	Temperature ± 2σ (° C)	$\delta^{18}O$ ± 2σ (‰)	$\delta^{13}C$ ± 2σ (‰)
20.5					3.05 ± 0.08	–0.63 ± 0.04
23.5	2.40 ± 0.10	1.05 ± 0.04	1.03 ± 0.04	2.61 ± 0.58 [c] or 2.08 ± 0.64 [d]	3.10 ± 0.06	–0.59 ± 0.05

Sediment core BC387-2, XRF ratios (normalised) [e]

Depth (cm)	Fe/Al	Cu/Al	S/Al	Ca/Al	Si/Al	Ba/Al
1.5	2.40	3.29	–0.65	–1.46	–0.74	0.53
2.5	1.98	1.71	0.03	–1.80	–2.08	2.01
3.5	0.05	1.34	0.62	–1.22	–1.76	–0.12
4.5	–0.82	–0.11	0.11	0.08	–0.18	–0.88
5.5	–0.73	0.33	0.41	–0.18	–0.90	–0.98
6.5	–0.83	0.25	–0.11	–0.62	–0.03	0.12
7.5	–0.89	–0.39	–0.20	–0.35	0.29	–0.89
8.5	–0.76	–0.12	–1.25	–0.21	0.95	–0.91
9.5	–0.80	–0.79	–1.07	–0.62	0.96	–0.89
10.5	–0.58	–0.74	–0.64	0.19	1.02	–1.19
11.5	–0.86	–1.10	–0.76	–0.29	1.20	–1.05
12.5	–0.52	–0.61	–0.87	–1.24	0.80	–1.30
13.5	–0.52	–0.55	–0.71	–0.71	0.93	–0.21
14.5	–1.13	–0.83	–1.07	0.71	1.15	–0.73
15.5	–0.39	–0.51	–1.20	0.11	1.12	–0.14
16.5	–0.34	0.47	–0.20	–0.21	–0.32	0.63
17.5	–0.19	0.19	–0.04	0.28	0.57	0.12
18.5	0.18	–0.65	0.39	0.96	0.22	1.16
19.5	0.41	–0.28	0.75	1.62	–0.14	0.85
20.5	0.67	–0.33	1.35	1.00	–0.57	1.46
21.5	1.15	0.19	1.90	0.73	–1.03	2.00
22.5	1.15	0.30	0.59	2.34	0.20	0.32
23.5	1.38	–1.05	2.61	0.89	–1.65	0.10

Sediment core BC387-2, XRF ratios (not normalised) [e]

1.5	12.92	0.16	1.04	17.74	3.77	0.32
2.5	12.56	0.14	1.08	17.32	3.31	0.35
3.5	10.94	0.13	1.11	18.05	3.42	0.30
4.5	10.21	0.11	1.08	19.65	3.95	0.28

Depth (cm)	Fe/Al	Cu/Al	S/Al	Ca/Al	Si/Al	Ba/Al
5.5	10.28	0.12	1.10	19.33	3.71	0.28
6.5	10.20	0.12	1.07	18.78	4.01	0.31
7.5	10.14	0.11	1.06	19.13	4.12	0.28
8.5	10.26	0.11	1.00	19.30	4.34	0.28
9.5	10.23	0.10	1.01	18.79	4.34	0.28
10.5	10.41	0.10	1.04	19.80	4.37	0.28
11.5	10.17	0.10	1.03	19.19	4.43	0.28
12.5	10.46	0.10	1.03	18.02	4.29	0.27
13.5	10.46	0.11	1.03	18.67	4.33	0.30
14.5	9.94	0.10	1.01	20.43	4.41	0.29
15.5	10.57	0.11	1.01	19.69	4.40	0.30
16.5	10.61	0.12	1.06	19.30	3.91	0.32
17.5	10.74	0.12	1.07	19.91	4.21	0.31
18.5	11.05	0.10	1.10	20.75	4.09	0.33
19.5	11.24	0.11	1.12	21.56	3.97	0.33
20.5	11.46	0.11	1.15	20.80	3.82	0.34
21.5	11.87	0.12	1.19	20.46	3.66	0.35
22.5	11.86	0.12	1.11	22.46	4.08	0.31
23.5	12.05	0.10	1.23	20.66	3.46	0.31

Sediment core BC387-2, *M. barleeanus* Mn/Ca ± 2σ (µmol/mol) in Figure 6.2.

Depth (cm)	Mn/Ca	Depth (cm)	Mn/Ca	Depth (cm)	Mn/Ca
1.5	2.23 ± 0.61	9.5	2.57 ± 0.33	16.5	2.51 ± 0.41
2.5	1.82 ± 0.56	12.5	2.29 ± 0.13	16.5	2.38 ± 0.46
4.5	1.92 ± 0.12	14.5	2.01 ± 0.23	22.5	2.33 ± 0.34
7.5	2.00 ± 0.49	14.5	1.80 ± 0.28	24.5	2.01 ± 0.33
7.5	2.11 ± 0.60	16.5	2.04 ± 0.23	24.5	1.84 ± 0.65

σ = internal precision. Depths are mid-points (± 0.5 cm). *M. barleeanus* temperatures were calculated from Mg/Ca using the equation of Kristjánsdóttir et al. 2007. *O. umbonatus* temperatures were calculated from Mg/Ca using either: a) the exponential equation of Lear et al. 2015; or b) the linear equation of Lear et al. 2015. *U. peregrina* temperatures were calculated from Mg/Ca using either: c) the equation of Bryan & Marchitto 2008; or d) the equation of Elderfield et al. 2006.
e) XRF data normalisation was achieved per dataset by first subtracting the mean and then dividing by the standard deviation.

Table A.12. Data plotted in Figure 3.6.

	No DTPA [a]	DTPA [b]
Sediment core BC387-2, *O. umbonatus*		
Ba/Ca ± 2σ (μmol/mol)	2.06 ± 0.01	2.21 ± 0.03, 2.21 ± 0.06
Mg/Ca ± 2σ (mmol/mol)	1.35 ± 0.002	1.38 ± 0.01, 1.42 ± 0.02
Sr/Ca ± 2σ (mmol/mol)	1.01 ± 0.01	0.99 ± 0.02, 0.99 ± 0.01
Sediment core BC387-2, *U. peregrina*		
Ba/Ca ± 2σ (μmol/mol)	2.69 ± 0.02, 2.55 ± 0.13	2.56 ± 0.17
Mg/Ca ± 2σ (mmol/mol)	1.06 ± 0.09, 1.19 ± 0.07	1.03 ± 0.07
Sr/Ca ± 2σ (mmol/mol)	1.06 ± 0.07, 1.06 ± 0.07	1.09 ± 0.07

a) Cleaned using the full procedure including a DTPA step for barite removal.

b) The DTPA step was omitted during cleaning.

σ = internal precision.

Table A.13. Trace metal data plotted in Figure 4.5, Figure 4.8 and Figure 6.2 (see Table A.14 for other data in these figures).

Depth (cm)	Ba/Ca ± 2σ (μmol/mol)	Mg/Ca ± 2σ (mmol/mol)	Sr/Ca ± 2σ (mmol/mol)	Mn/Ca ± 2σ (μmol/mol)
Sediment core GC528, *M. barleeanus*				
4.5	3.33 ± 0.07	0.81 ± 0.02	1.23 ± 0.02	1.84 ± 0.28
8.5	3.38 ± 0.15	0.85 ± 0.05	1.25 ± 0.06	1.75 ± 0.12
16.5	5.17 ± 0.27	0.92 ± 0.04	1.24 ± 0.04	2.85 ± 0.25
24.5	3.54 ± 0.20	0.86 ± 0.03	1.26 ± 0.03	4.01 ± 0.24
28.5	3.51 ± 0.30	0.86 ± 0.04	1.23 ± 0.05	4.12 ± 0.26
32.5	3.75 ± 0.18	0.88 ± 0.03	1.24 ± 0.04	3.66 ± 0.33
36.5	3.66 ± 0.27	0.91 ± 0.05	1.28 ± 0.08	4.72 ± 0.35
38.5	3.60 ± 0.13	0.93 ± 0.03	1.24 ± 0.03	3.86 ± 0.29
41.5	3.60 ± 0.21	0.88 ± 0.05	1.25 ± 0.08	4.46 ± 0.27
44.5	3.78 ± 0.31	0.93 ± 0.05	1.25 ± 0.08	5.98 ± 0.62
46.5	3.64 ± 0.09	0.89 ± 0.04	1.25 ± 0.04	4.49 ± 0.58
48.5	3.61 ± 0.11	0.84 ± 0.02	1.22 ± 0.02	5.12 ± 0.29
52.5	3.81 ± 0.12	0.87 ± 0.02	1.27 ± 0.03	3.05 ± 0.24
54.5	3.35 ± 0.21	0.87 ± 0.05	1.25 ± 0.06	2.19 ± 0.20
56.5	3.42 ± 0.26	0.94 ± 0.06	1.23 ± 0.07	2.97 ± 0.22

Depth (cm)	Ba/Ca ± 2σ (μmol/mol)	Mg/Ca ± 2σ (mmol/mol)	Sr/Ca ± 2σ (mmol/mol)	Mn/Ca ± 2σ (μmol/mol)
58.5	3.33 ± 0.14	0.90 ± 0.01	1.25 ± 0.02	3.92 ± 0.29
62.5	3.66 ± 0.29	1.01 ± 0.04	1.27 ± 0.04	4.10 ± 0.57
Sediment core GC642, *M. barleeanus*				
22.5	4.10 ± 0.19	1.19 ± 0.02	1.26 ± 0.01	32.12 ± 1.40
26.5	4.04 ± 0.17	1.18 ± 0.03	1.27 ± 0.03	24.29 ± 1.26
28.5	4.17 ± 0.28	1.19 ± 0.04	1.27 ± 0.02	27.70 ± 1.35
30.5	4.04 ± 0.11	1.23 ± 0.03	1.30 ± 0.08	26.86 ± 2.48
32.5	4.19 ± 0.21	1.16 ± 0.06	1.25 ± 0.03	25.81 ± 1.74
38.5	3.62 ± 0.21	1.09 ± 0.02	1.26 ± 0.04	22.15 ± 1.13

σ = internal precision. Depths are mid-points (± 0.5 cm).

Table A.14. Calculated data plotted in Figure 4.5, Figure 4.8 and Figure 6.2 (see Table A.13 for other data in these figures).

Depth (cm)	Temperature ± 2σ (ºC)	Seawater [Ba] ± 2σ (nM)	Seawater alkalinity ± 2σ (μequiv/kg)
Sediment core GC528, *M. barleeanus*			
4.5	1.48 ± 0.31	81.76 ± 1.75 [a] or 62.44 ± 1.33 [b]	2379.70 ± 2.53 [c] or 2351.70 ± 1.93 [d]
8.5	1.83 ± 0.69	82.87 ± 3.63 [a] or 63.28 ± 2.77 [b]	2381.30 ± 5.27 [c] or 2352.90 ± 4.02 [d]
16.5	2.46 ± 0.45	126.89 ± 6.70 [a] or 96.89 ± 5.11 [b]	2445.10 ± 9.70 [c] or 2401.60 ± 7.41 [d]
24.5	1.98 ± 0.33	86.72 ± 4.96 [a] or 66.22 ± 3.79 [b]	2386.90 ± 7.19 [c] or 2357.20 ± 5.49 [d]
28.5	1.92 ± 0.46	85.98 ± 7.37 [a] or 65.66 ± 5.63 [b]	2385.80 ± 10.68 [c] or 2356.30 ± 8.16 [d]
32.5	2.16 ± 0.43	92.06 ± 4.53 [a] or 70.30 ± 3.46 [b]	2394.60 ± 6.56 [c] or 2363.10 ± 5.01 [d]
36.5	2.37 ± 0.60	89.71 ± 6.58 [a] or 68.50 ± 5.03 [b]	2391.20 ± 9.54 [c] or 2360.50 ± 7.28 [d]
38.5	2.53 ± 0.35	88.21 ± 3.16 [a] or 67.36 ± 2.41 [b]	2389.00 ± 4.58 [c] or 2358.80 ± 3.50 [d]

Depth (cm)	Temperature ± 2σ (ºC)	Seawater [Ba] ± 2σ (nM)	Seawater alkalinity ± 2σ (μequiv/kg)
41.5	2.10 ± 0.61	88.19 ± 5.15 [a] or 67.34 ± 3.93 [b]	2389.00 ± 7.46 [c] or 2358.80 ± 5.70 [d]
44.5	2.49 ± 0.64	92.63 ± 7.70 [a] or 70.73 ± 5.88 [b]	2395.40 ± 11.16 [c] or 2363.70 ± 8.52 [d]
46.5	2.22 ± 0.44	89.29 ± 2.21 [a] or 68.19 ± 1.69 [b]	2390.60 ± 3.21 [c] or 2360.00 ± 2.45 [d]
48.5	1.76 ± 0.21	88.58 ± 2.79 [a] or 67.64 ± 2.13 [b]	2389.60 ± 4.04 [c] or 2359.20 ± 3.09 [d]
52.5	2.05 ± 0.28	93.31 ± 2.85 [a] or 71.26 ± 2.18 [b]	2396.40 ± 4.13 [c] or 2364.50 ± 3.15 [d]
54.5	2.05 ± 0.64	82.06 ± 5.08 [a] or 62.66 ± 3.88 [b]	2380.10 ± 7.36 [c] or 2352.00 ± 5.62 [d]
56.5	2.64 ± 0.75	83.77 ± 6.33 [a] or 63.97 ± 4.84 [b]	2382.60 ± 9.18 [c] or 2353.90 ± 7.01 [d]
58.5	2.28 ± 0.16	81.62 ± 3.43 [a] or 62.32 ± 2.62 [b]	2379.50 ± 4.97 [c] or 2351.50 ± 3.80 [d]
62.5	3.13 ± 0.46	89.81 ± 7.11 [a] or 68.58 ± 5.43 [b]	2391.30 ± 10.31 [c] or 2360.60 ± 7.87 [d]
Sediment core GC642, *M. barleeanus*			
22.5	4.30 ± 0.22	100.52 ± 4.56 [a] or 76.76 ± 3.48 [b]	2406.90 ± 6.60 [c] or 2372.40 ± 5.04 [d]
26.5	4.25 ± 0.25	99.08 ± 4.06 [a] or 75.66 ± 3.10 [b]	2404.80 ± 5.88 c or 2370.80 ± 4.49 [d]
28.5	4.33 ± 0.35	102.29 ± 6.93 [a] or 78.11 ± 5.29 [b]	2409.40 ± 10.04 [c] or 2374.40 ± 7.66 [d]
30.5	4.57 ± 0.29	99.08 ± 2.70 [a] or 75.66 ± 2.06 [b]	2404.80 ± 3.92 [c] or 2370.80 ± 2.99 [d]
32.5	4.15 ± 0.55	102.71 ± 5.25 [a] or 78.43 ± 4.01 [b]	2410.00 ± 7.60 [c] or 2374.80 ± 5.81 [d]
38.5	3.66 ± 0.22	88.87 ± 5.22 [a] or 67.87 ± 3.99 [b]	2390.00 ± 7.57 [c] or 2359.50 ± 5.78 [d]

σ = internal precision. Depths are mid-points (± 0.5 cm). Temperatures calculated from the Mg/Ca ratios in Table A.12 (Kristjánsdóttir et al. 2007). a) Calculated using D_{Ba} = 0.42; b) Calculated using D_{Ba} = 0.55; c) Calculated from seawater [Ba] 'a'; d) Calculated from seawater [Ba] 'b'

Table A.15. Data plotted in Figure 4.9.

^{138}Ba intensity (cps)	Standard deviation (cps)	Relative standard deviation (%)	Sample name
Samples			
3150.10	171.30	5.44	Consistency STD
10905.90	373.50	3.42	42.5 cm (GC528)
13180.90	185.70	1.41	18.5 cm (GC642)
10850.30	494.60	4.56	38.5 cm (GC528)
10978.30	53.70	0.49	46.5 cm (GC528)
9167.20	120.00	1.31	32.5 cm (GC528)
12094.90	247.40	2.05	28.5 cm (GC642)
10121.40	69.10	0.68	4.5 cm (GC528)
11010.70	180.90	1.64	38.5 cm (GC642)
10614.70	217.00	2.04	24.5 cm (GC528)
10627.80	318.80	3.00	48.5 cm (GC528)
3149.20	86.20	2.74	Consistency STD
12068.00	239.50	1.98	22.5 cm (GC642)
14948.70	178.40	1.19	16.5 cm (GC528)
11132.20	185.40	1.67	40.5 cm (GC642)
12681.90	396.90	3.13	52.5 cm (GC528)
11710.90	228.20	1.95	62.5 cm (GC528)
Standards			
10544.30	294.00	2.79	
10332.90	169.70	1.64	
10280.90	10.60	0.10	
10372.70	22.60	0.22	
10075.00	38.60	0.38	
10182.60	177.70	1.75	
9902.60	385.70	3.89	
10245.70	50.10	0.49	
10092.70	228.90	2.27	
10165.00	185.80	1.83	
10066.80	329.80	3.28	
10166.80	171.40	1.69	
9972.10	126.70	1.27	

^{138}Ba intensity (cps)	Standard deviation (cps)	Relative standard deviation (%)
10330.10	201.50	1.95
10140.00	230.50	2.27
10018.50	160.10	1.60
10101.00	316.10	3.13
Blanks		
172.20	18.20	10.57
212.00	68.20	32.17
192.60	10.50	5.45
184.30	28.00	15.19
195.40	16.30	8.34
176.90	1.60	0.90
148.10	29.70	20.05
156.50	36.90	23.58
188.90	38.60	20.43
199.10	35.70	17.93
192.60	25.20	13.08
179.60	33.50	18.65
165.70	41.60	25.11
162.00	22.30	13.77
151.90	15.80	10.40
200.00	12.70	6.35
167.60	29.40	17.54

Measurements related to the sample at ~2.3 ka in Figure 4.5 and Figure 4.8 are highlighted in grey. Consistency STD = consistency standard. Sample depths are mid-points (± 0.5 cm).

Table A.16. Data plotted in Figure 5.5, Figure 5.6, Figure 5.7, Figure 5.8, Figure 5.9 and Figure 5.10.

Depth (m)	δ^{138}Ba ± 2σ (‰)	[Ba] (nM)	1/[Ba] (nM^{-1})	[Si] (µM)	[Si]/[Ba] (µM/nM)
CTD002					
4512	0.43 ± 0.04	84.61	1.18×10^{-2}	49.71	0.59
4299	0.31 ± 0.04	75.62	1.32×10^{-2}	46.75	0.62
3600	0.37 ± 0.04	74.32	1.35×10^{-2}	42.47	0.57

Depth (m)	δ^{138}Ba ± 2SE (‰)	[Ba] (nM)	1/[Ba] (nM^{-1})	[Si] (μM)	[Si]/[Ba] (μM/nM)
2800	0.39 ± 0.04	68.06	1.47 x 10^{-2}	33.92	0.50
2002	0.42 ± 0.04	60.24	1.66 x 10^{-2}	24.90	0.41
1502	0.41 ± 0.03	56.16	1.78 x 10^{-2}	22.30	0.40
1005	0.43 ± 0.03	57.49	1.74 x 10^{-2}	26.87	0.47
705	0.49 ± 0.04	49.75	2.01 x 10^{-2}	25.01	0.50
405	0.56 ± 0.04	42.88	2.33 x 10^{-2}	15.75	0.37
55	0.57 ± 0.07	37.00	2.70 x 10^{-2}	4.78	0.13
11	0.57 ± 0.04	37.90	2.64 x 10^{-2}	0.93	0.02
CTD005					
5143	0.32 ± 0.04	84.90	1.18 x 10^{-2}	65.76	0.77
4798	0.30 ± 0.04	80.85	1.24 x 10^{-2}	63.96	0.79
3799	0.32 ± 0.04	68.89	1.45 x 10^{-2}	40.55	0.59
2800	0.38 ± 0.03	66.68	1.50 x 10^{-2}	33.21	0.50
2002	0.45 ± 0.04	54.82	1.82 x 10^{-2}	19.70	0.36
1503	0.49 ± 0.04	53.11	1.88 x 10^{-2}	16.26	0.31
1204	0.40 ± 0.04	52.78	1.89 x 10^{-2}	22.84	0.43
805	0.41 ± 0.03	54.44	1.84 x 10^{-2}	26.13	0.48
606	0.51 ± 0.03	49.06	2.04 x 10^{-2}	19.48	0.40
407	0.52 ± 0.04	46.11	2.17 x 10^{-2}	16.12	0.35
76	0.54 ± 0.06	38.93	2.57 x 10^{-2}	4.64	0.12
12	0.46 ± 0.04	45.66	2.19 x 10^{-2}	2.69	0.06
CTD006					
4168	0.34 ± 0.03	72.93	1.37 x 10^{-2}	45.15	0.62
3798	0.33 ± 0.03	72.15	1.39 x 10^{-2}	43.30	0.60
2800	0.38 ± 0.03	68.07	1.47 x 10^{-2}	35.19	0.52
2002	0.46 ± 0.03	56.66	1.76 x 10^{-2}	21.31	0.38
1503	0.50 ± 0.03	52.79	1.89 x 10^{-2}	17.91	0.34
1203	0.46 ± 0.03	54.13	1.85 x 10^{-2}	21.79	0.40
1004	0.47 ± 0.03	55.23	1.81 x 10^{-2}	25.45	0.46
804	0.46 ± 0.03	54.48	1.84 x 10^{-2}	25.08	0.46
505	0.52 ± 0.04	48.66	2.06 x 10^{-2}	17.96	0.37
205	0.61 ± 0.04	38.53	2.60 x 10^{-2}	5.07	0.13
95	0.56 ± 0.03	39.77	2.51 x 10^{-2}	1.15	0.03
16	0.52 ± 0.03	42.14	2.37 x 10^{-2}	1.26	0.03

Table A.17. Data plotted in Figure 5.5, Figure 5.7 and Figure 5.10, as well as [PO_4] and N*.

Depth (m)	[$NO3^-$] (µM)	[PO_4] (µM)	N* (µM)	Si* (µM)	Ba* (nM)	TA (µmol/kg)
CTD002						
4512	22.67	1.38	0.59	27.04	11.20	2336.45
4299	22.21	1.23	2.45	24.54	4.22	2328.04
3600	21.94	1.36	0.08	20.54	5.85	2340.26
2800	21.28	1.32	0.15	12.64	5.44	2319.86
2002	21.38	1.40	–1.04	3.52	3.79	2310.72
1502	23.83	1.47	0.48	–1.53	1.49	2309.10
1005	32.11	2.00	0.16	–5.23	–0.31	2310.23
705	36.15	2.28	–0.31	–11.14	–6.77	2308.01
405	35.04	2.01	2.87	–19.30	–7.31	2308.49
55	16.13	1.01	–0.44	–11.36	–5.69	2343.49
11	0.00	0.01	–0.15	0.93	–2.15	2308.39
CTD005						
5143	24.55	1.70	–2.71	41.22	0.50	2339.93
4798	23.99	1.67	–2.67	39.97	–2.32	2340.09
3799	20.70	1.41	–1.90	19.85	1.74	2320.06
2800	20.63	1.39	–1.68	12.58	4.55	2330.70
2002	19.19	1.29	–1.43	0.50	1.93	2320.54
1503	20.13	1.33	–1.19	–3.87	2.57	2303.67
1204	27.25	1.85	–2.31	–4.40	–2.26	2296.97
805	33.57	2.27	–2.80	–7.44	–2.85	2305.35
606	31.47	2.12	–2.41	–12.00	–3.68	2297.20
407	30.45	1.95	–0.81	–14.33	–4.34	2372.76
76	14.01	0.82	0.83	–9.37	–3.67	2284.77
12	0.00	0.02	–0.31	2.69	4.40	2339.93
CTD006						
4168	21.48	1.48	–2.19	23.67	2.63	2335.92
3798	21.46	1.47	–2.04	21.83	3.12	2353.21
2800	20.74	1.41	–1.80	14.45	4.59	2350.94
2002	19.53	1.30	–1.35	1.79	2.67	2318.93
1503	21.57	1.45	–1.56	–3.66	1.12	2322.81
1203	26.28	1.78	–2.24	–4.48	–0.20	2317.30
1004	31.09	2.11	–2.70	–5.65	–1.59	2317.90

Depth (m)	[$NO3^-$] (µM)	[PO_4] (µM)	N* (µM)	Si* (µM)	Ba* (nM)	TA (µmol/kg)
804	32.76	2.21	–2.66	–7.68	–2.09	2311.03
505	29.94	2.02	–2.32	–11.98	–3.05	2311.79
205	16.32	0.97	0.77	–11.24	–4.36	2368.47
95	0.49	0.04	–0.32	0.66	–0.43	2416.95
16	0.00	0.02	–0.31	1.26	1.86	2360.70

TA = total alkalinity.

Table A.18. Data plotted in Figure 5.12, Figure 5.14, Figure 5.15 and Figure 5.24.

Sample	Ba/Ca ± 2σ (µmol/mol)	δ^{138}Ba ± 2σ (‰)	δ^{18}O ± 2σ (‰)	δ^{13}C ± 2σ (‰)
S0157a, M	0.63	0.23 ± 0.05		
S0157a, O			0.01 ± 0.07	1.70 ± 0.06
S0157a, C			–0.02 ± 0.11	1.47 ± 0.06
S0157b, M	0.78	0.48 ± 0.05		
S0157b, O			–0.35 ± 0.06	1.90 ± 0.04
S0157b, C			–1.24 ± 0.10	1.21 ± 0.04
S0059, M	0.77	0.14 ± 0.04		
S0059, O			–0.88 ± 0.10	2.44 ± 0.08
S0059, C			–0.95 ± 0.15	1.68 ± 0.06
S0177, M	0.53	0.29 ± 0.06		
S0177, O			–1.16 ± 0.05	3.20 ± 0.02
S0177, C			–1.46 ± 0.08	1.78 ± 0.04
S0066, M	0.41	0.10 ± 0.06		
S0066, O			–1.26 ± 0.06	2.71 ± 0.05
S0066, C			–1.15 ± 0.10	1.81 ± 0.04
S0131, M	0.46	0.14 ± 0.05		
S0131, O			–1.37 ± 0.05	2.73 ± 0.05
S0131, C			–1.47 ± 0.05	1.73 ± 0.03

C = 'clear', thinner-shelled *O. universa*; 'O' = 'opaque', thicker-shelled *O. universa*;
M = a mixture of the two types. Sample S0157a is from size fraction 355 – 425 µm; all others are > 425 µm. σ = internal precision.